Femtosecond-laser-written Type A modifications : Application to X-ray spatially-resolved dosimetry and volume Bragg gratings

Joelle Harb

université de BORDEAUX

THÈSE PRÉSENTÉE

POUR OBTENIR LE GRADE DE

DOCTEUR DE

L'UNIVERSITÉ DE BORDEAUX

ÉCOLE DOCTORALE DES SCIENCES PHYSIQUES ET DE L'INGÉNIEUR SPÉCIALITÉ : LASERS, MATIÈRE ET NANOSCIENCES

Par **Joelle HARB**

Inscription laser femtoseconde des modifications de Type-A: Application à la dosimétrie résolue spatialement des rayons X et aux réseaux de Bragg volumiques

Femtosecond-laser-written Type A modifications: Application to X-ray spatially-resolved dosimetry and volume Bragg gratings

Sous la direction de : **Lionel CANIONI**
Co-directeur : **Yannick PETIT**

Soutenue le 04 Décembre 2023

Membre de Jury:

Prof. Bruno Capoen	Université de Lille	Rapporteur
Prof. Sylvain Lecler	Université de Strasbourg	Rapporteur
Prof. Emmanuel D'Humières	Université de Bordeaux	Président Examinateur
Prof. Nathalie Destouches	Université Jean-Monnet - Saint Etienne	Examinatrice
Prof. Lionel Canioni	Université de Bordeaux	Directeur
Dr. Yannick Petit	Université de Bordeaux	Co-directeur
Dr. Adriana Morana	Université Jean-Monnet - Saint Etienne	Invité

Abstract

Direct Laser Writing (DLW) has seen remarkable growth as a research field over the past two decades, based on the process of multiphoton absorption. This technique, known for its reliability and efficiency, enables the formation of permanent and confined modification in glasses, inducing complex 3D optical structures down to sub-micrometer dimensions. Over the years, researchers have delved deeply into femtosecond (fs) DLW across a diverse range of glass material families. In particular, the phosphate glass family represents numerous advantageous characteristics, especially with the addition of photosensitive substances, such as silver. Thus, the fs interaction enables the clustering of silver ions, inducing the creation of fluorescent silver clusters Ag_m^{x+} at the vicinity of the interaction voxel. Based on silver clusters, a distinct type of refractive index modification was demonstrated, labeled as Type-A (with A referring to Argentum). In this project, we take advantage of Type-A modifications in order to create new types of optical components through their fluorescence and refractive index change properties. The research presented in this manuscript has a dual objective. On one hand, we investigate the potential of the 3D distributed fluorescent structures created by laser inscription in spatially-distributed X-ray dosimetry. Within this context, a novel technique combining radiophotoluminescence and fs laser irradiation is employed in our glasses. Our study shows that the ensemble of the spectroscopic experiments highlights the resilience of laser-induced silver clusters, these species acting as local probes of the depth-dependent deposited doses and potentially behaving as in-depth local probes of the X-ray energy deposition. Additionally, in-situ measurements were carried out on waveguides supporting fs-induces silver cluster distribution.

On the other hand, this work reports on the fabrication of periodic optical gratings based on Type-A refractive index change which have been exploited for the realization of transmission Volume Bragg Gratings (VBGs). The Type-A VBGs are presented using several techniques, from multi-layer using standard Gaussian beam geometry to the phase mask approach. Consequently, Type-A VBGs have been successfully realized for the very first time. A noteworthy outcome of this research is the inscription of a single plane grating inscribed with a Gaussian-Bessel fs beam. This approach yielded a remarkable and high diffraction efficiency of 95% Thus, this work opens the avenue for highly effective femtosecond-written VBGs suitable for industrial applications.

Keywords: Femtosecond laser inscription, silver-containing glasses, silver clusters, Type-A modifications, X-ray irradiation, spatially-resolved dosimetry, Volume Bragg Gratings.

General introduction

Since the discovery of lasers in the mid-20th century, the field of laser-matter interaction has evolved into boundless possibilities and established new frontiers across numerous disciplines. Hence, laser technology is experiencing rapid growth in industries and laboratories. Among the uses in laboratory, femtosecond (fs) laser technology is now a preferred tool for structuring transparent materials at a sub-micron scale.

The applications of photonics are exceptionally diverse, ranging from telecommunications and information technology to healthcare, manufacturing, and beyond. Photonics has not only transformed how we communicate through optical fibers and high-speed data transmission but has also revolutionized medical diagnostics and treatments through lasers and imaging technologies. In manufacturing, photonics plays a pivotal role in precision cutting, welding, and three-dimensional (3D) printing. In advanced manufacturing and materials science, the technique known as Direct Laser Writing (DLW) stands as a powerful and precise tool that has revolutionized the ability to manipulate matter at the nanoscale range. DLW enables the creation of complex and three-dimensional structures by multiphoton absorption of a focused femtosecond laser source in the voxel of interaction. This exhibits many advantages such as record precision, versatility, single-step fabrication with respect to two-dimensional (2D) structuring by lithography. It thus becomes possible in a single step to obtain a multifunctional optical system within a transparent bulk material.

This PhD study took place in collaborative interdisciplinary environment between different universities and groups (Laboratory Hubert Curien of University Jean Monnet -Saint-Etienne, France and Centre d'Optique, Photonique et Laser of University Laval, Québec). My research project was principally hosted at the University of Bordeaux, specifically within the Short-pulse Lasers: Applications & Materials (SLAM) group in CELIA (Centre Lasers Intenses et Applications) and in the Institut de Chimie de la Matière Condensée de Bordeaux (ICMCB) laboratory. The SLAM group is renowned for its expertise in the femtosecond laser inscription of materials, encompassing both bulk materials and fibers, for photonics applications. Additionally, the group "Chimie et photonique des matériaux oxide de fluores" at the ICMCB has acquired substantial knowledge through the development of materials containing photosensitive ions like silver, enabling the localized generation of optical properties without damaging the surrounding ion matrix.
This project relies on research activities, conducted in both research groups, focusing on femtosecond infrared laser inscription in silver-containing phosphate glasses. The introduction of silver ions inside the glass matrix results in unique responses from the glass following DLW

such as the formation of silver clusters. These clusters exhibit outstanding properties exploited by the group for many applications such as fluorescence, second order optical nonlinearity and refractive index modification. Notably, this interaction leads to a positive refractive index change linked to the formation of silver clusters independent of the modification of the glass matrix. This particular modification is known as Type-A, named for Argentum. In this project, we took advantage of Type-A modifications to create new types of optical components through their fluorescence and refractive index properties for X-ray dosimetry and optical filters.

The manuscript is divided into four distinct chapters, as follows.

The first chapter provides an overview, covering essential background information on glasses and the fundamentals of laser-material interaction. The initial section is dedicated to glasses, involving discussions on their structural and optical characteristics, as well as the methods employed for their production. Following that, the chapter delves into the field of laser-material interaction, offering a comprehensive examination of nonlinear absorption mechanisms associated with femtosecond laser pulses in glasses. This includes an in-depth discussion of the underlying physical processes and various laser writing regimes. Lastly, fundamental concepts related to femtosecond beam engineering and delivering were introduced such as the Gaussian and the Gaussian-Bessel beam.

The second chapter is dedicated to Direct Laser Writing in glasses. It delves into the different types of photo-induced modifications that occur as a result of laser-matter interaction. Specifically, the chapter focuses on Direct Laser Writing in silver-containing phosphate glasses, highlighting the choice of this material and discussing the optical properties of the pristine glasses. Furthermore, it provides a comprehensive examination of the interaction between silver-containing glasses and femtosecond lasers. The chapter details the physical mechanism behind the formation of induced silver clusters and describes their characteristics. This specific interaction leads to Type-A refractive index modifications, which are thoroughly explained along with the presentation of significant results and applications achieved by our research group.

The third chapter introduces an exploration of the potential application for X-ray spatially-distributed dosimetry based on three-dimensional distributed highly fluorescent laser-inscribed structures. Within this section, a novel technique combining radiophotoluminescence and femtosecond laser irradiation is employed in our glasses to investigate their potential as indicators of deposited radiation doses. This section begins with a comprehensive introduction to the radiative environment, followed by an in-depth exploration of the impact of radiation on optical materials. Furthermore, it provides a state-of-the-art review of radiophotoluminescence dosimeters. The first experimental part focuses on a post-X-ray study conducted across three different glass compositions, encompassing an analysis of the pristine glasses before and after irradiation. Furthermore, Monte Carlo Geant4

simulations are utilized to explore the dose deposited at various depths within the glass's thickness. Moreover, the study of the spectroscopic properties of femtosecond laser-written silver species exposed to X-ray irradiation were conducted, assessing their stability and resilience under X-ray irradiation. Lastly, information about the dosimetry behavior of these glasses has been extracted thanks to the photo-inscribed patterns. The second experimental part is dedicated to real-time measurements aimed at studying the behavior of silver clusters when exposed to in-situ X-ray irradiation. It includes findings from radioluminescence and radiation-induced attenuation measurements conducted on the photo-inscribed structures, which are then compared to the properties observed in bulk glasses.

This work was a collaboration with the MOPERE team (Materials for Optics and Photonics in Extreme Radiation Environments) of Laboratory Hubert Curien of University Jean Monnet (Saint-Etienne, France), specifically with Adriana Moroana, Youcef Ouerdane, Aziz Boukenter, Sylvain Girard, with additional assistance provided by Arnaud Meyer and Timoté Allanche.

The fourth chapter focuses on the creation of volume Bragg gratings (VBGs) employing the unique Type-A refractive index modification. An essential aspect addressed in this chapter is the enhancement of throughput fabrication of VBGs with fs lasers. This is a crucial factor that opens doors for industrial applications. The current state of the art regarding volume Bragg gratings is succinctly presented, offering insights into their diverse applications, the materials employed for their fabrication, and the various manufacturing techniques involved. In this chapter, we investigate advanced beam shaping for laser processing. In particular, the Gaussian beam, the Gaussian-Bessel beam, the light sheet combined with/without phase mask are detailed. Furthermore, complete modeling and characterization is presented. The phase mask experiment was carried out at the COPL laboratory (Centre d'Optique, Photonique et Laser, University Laval, Québec) in collaboration with Lauris Talbot and Martin Bernier.

Introduction générale

Depuis la découverte des lasers au milieu du XXe siècle, le domaine de l'interaction laser-matière a évolué vers des possibilités illimitées et a établi de nouvelles frontières dans de nombreuses disciplines. Ainsi, la technologie laser connaît une croissance rapide dans les industries et les laboratoires. Parmi les utilisations en laboratoire, la technologie laser femtoseconde est désormais un outil privilégié pour la structuration de matériaux transparents à l'échelle submicronique.

Les applications de la photonique sont exceptionnellement diverses, allant des télécommunications et de la technologie de l'information aux soins de santé, à la fabrication, et au-delà. La photonique a non seulement transformé notre manière de communiquer grâce aux fibres optiques et à la transmission de données à haute vitesse, mais a également révolutionné les diagnostics médicaux et les traitements grâce aux lasers et aux technologies d'imagerie. Dans la fabrication, la photonique joue un rôle central dans la découpe de précision, le soudage et l'impression tridimensionnelle. Dans la fabrication avancée et la science des matériaux, la technique appelée écriture laser directe est un outil puissant et précis qui a révolutionné la capacité de manipuler la matière à l'échelle nanométrique. Cette technique permet la création de structures complexes et tridimensionnelles par absorption multiphotonique d'une source laser femtoseconde focalisée dans le voxel d'interaction. Cela présente de nombreux avantages tels que la précision record, la polyvalence, la fabrication en une seule étape par rapport à la structuration bidimensionnelle par lithographie. Il devient ainsi possible en une seule étape d'obtenir un système optique multifonctionnel à l'intérieur d'un matériau transparent.

Cette thèse s'est déroulée dans un environnement interdisciplinaire collaboratif entre différentes universités et groupes (Laboratoire Hubert Curien de l'Université Jean Monnet - Saint-Étienne, France et Centre d'optique, de photonique et de laser de l'Université Laval, Québec). Mon projet de recherche a principalement été accueilli à l'Université de Bordeaux, plus précisément au sein du groupe Lasers à impulsions courtes : Applications & Matériaux (SLAM) au sein de CELIA (Centre Lasers Intenses et Applications) et au laboratoire Institut de Chimie de la Matière Condensée de Bordeaux (ICMCB). Le groupe SLAM est renommé pour son expertise dans l'inscription laser femtoseconde de matériaux, englobant à la fois les matériaux massifs et les fibres, pour des applications photoniques. De plus, le groupe "Chimie et photonique des matériaux oxydes de fluores" à l'ICMCB a acquis une connaissance substantielle grâce au développement de matériaux contenant des ions photosensibles tels que l'argent, permettant la génération localisée de propriétés optiques sans endommager la matrice ionique environnante. Ce projet repose sur des activités de recherche menée dans les deux groupes de recherche, se concentrant sur l'inscription laser femtoseconde infrarouge

dans des verres de phosphate contenant de l'argent. L'introduction d'ions d'argent à l'intérieur de la matrice en verre donne lieu à des réponses uniques du verre suite à l'inscription laser directe, telle que la formation des agrégats d'argent. Ces agrégats présentent des propriétés exceptionnelles exploitées par le groupe pour de nombreuses applications telles que la fluorescence, la non-linéarité optique du second et troisième ordre et la modification de l'indice de réfraction. En particulier, cette interaction conduit à une modification positive de l'indice de réfraction liée à la formation des agrégats d'argent indépendante de la modification de la matrice vitreuse. Cette modification particulière est connue sous le nom de modification de Type-A, nommée d'après le mot latin Argentum. Dans ce projet, nous avons profité des modifications de Type-A pour créer de nouveaux types de composants optiques grâce à leurs propriétés de fluorescence et d'indice de réfraction pour la dosimétrie des rayons X et les filtres optiques.

Le manuscrit est divisé en quatre chapitres distincts, comme suit.

Le premier chapitre donne un aperçu, couvrant des informations de base essentielles sur les verres et les fondements de l'interaction laser-matière. La première section est consacrée aux verres, impliquant des discussions sur leurs caractéristiques structurales et optiques, ainsi qu'aux méthodes utilisées pour leur production. Ensuite, le chapitre plonge dans le domaine de l'interaction laser-matière, offrant une étude complète des mécanismes d'absorption non linéaire associés aux impulsions laser femtosecondes dans les verres. Cela comprend une discussion approfondie des processus physiques sous-jacents et des différents régimes d'écriture laser. Enfin, des concepts fondamentaux liés à l'ingénierie et à la propagation des faisceaux femtosecondes ont été introduits, tels que ceux associés à la forme transversale des faisceaux (faisceau Gaussien et faisceau Gaussien-Bessel).
Le deuxième chapitre est dédié à l'écriture laser directe dans les verres. Il se penche sur les différents types de modifications photo-induites qui surviennent en raison de l'interaction laser-matière. Plus précisément, le chapitre se concentre sur l'écriture laser directe dans les verres phosphate contenant de l'argent, mettant en évidence le choix de ce matériau et discutant des propriétés optiques des verres vierges. De plus, il offre une étude complète de l'interaction entre les verres contenant de l'argent et les lasers femtosecondes. Le chapitre détaille le mécanisme physique derrière la formation des agrégats d'argent induites et décrit leurs caractéristiques. Cette interaction spécifique conduit à des modifications de l'indice de réfraction de Type-A, qui sont expliquées en détail avec la présentation des résultats significatifs et des applications obtenues par notre groupe de recherche.
Le troisième chapitre introduit une exploration de l'application potentielle pour la dosimétrie résolue spatialement des rayons X basée sur des structures fluorescentes, tridimensionnelles et distribuées inscrites au laser. Dans cette section, une nouvelle technique combinant la radiophotoluminescence et l'irradiation laser femtoseconde est utilisée dans nos verres pour

étudier leur potentiel en tant que sondes locales de la dose de radiation déposée. Cette section commence par une introduction complète à l'environnement radiatif, suivie d'une exploration approfondie de l'impact des radiations sur les matériaux optiques. De plus, elle offre une revue de l'état de l'art des dosimètres de radiophotoluminescence. La première partie expérimentale se concentre sur une étude post-rayons X réalisée sur trois compositions de verre différentes, englobant une analyse des verres vierges avant et après l'irradiation. De plus, des simulations Monte-Carlo Geant4 sont utilisées pour explorer la dose déposée à différentes profondeurs à l'intérieur de l'épaisseur du verre. De plus, l'étude des propriétés spectroscopiques des espèces d'argent inscrites au laser femtoseconde exposées à l'irradiation par des rayons X a été réalisée, évaluant leur stabilité et leur résistance sous l'irradiation. Enfin, des informations sur le comportement dosimétrique de ces verres ont été extraites grâce aux motifs photo-inscrits. La deuxième partie expérimentale est dédiée aux mesures en temps réel visant à étudier le comportement des agrégats d'argent exposées à l'irradiation aux rayons X in situ. Elle inclut les résultats des mesures de radioluminescence et d'atténuation induite par les radiations effectuées sur les structures photo-inscrites, qui sont ensuite comparées aux propriétés observées dans les verres vierges. Ce travail a été réalisé en collaboration avec l'équipe MOPERE (Matériaux pour l'Optique et la Photonique dans les Environnements de Radiations Extrêmes) du Laboratoire Hubert Curien de l'Université Jean Monnet (Saint-Étienne, France), en particulier avec Adriana Moroana, Youcef Ouerdane, Aziz Boukenter, Sylvain Girard, avec l'assistance supplémentaire d'Arnaud Meyer et Timoté Allanche.

Le quatrième chapitre se concentre sur la création des réseaux de Bragg volumiques en utilisant la modification unique de l'indice de réfraction de Type-A. Un aspect essentiel abordé dans ce chapitre est l'amélioration du débit de fabrication des VBG avec des lasers femtosecondes. Il s'agit d'un facteur crucial qui ouvre des portes pour des applications industrielles. L'état actuel de l'art concernant les réseaux de Bragg volumiques est présenté de manière concise, offrant des informations sur leurs diverses applications, les matériaux utilisés pour leur fabrication et les différentes techniques de fabrication impliquées. Dans ce chapitre, nous examinons la mise en forme avancée du faisceau pour le traitement laser. En particulier, le faisceau Gaussien, le faisceau Gaussien-Bessel, le feuillet de lumière combinée avec/sans masque de phase sont détaillés. De plus, une modélisation et une caractérisation complète des réseaux inscrits sont présentées. L'expérience du masque de phase a été réalisée au laboratoire COPL (Centre d'Optique, Photonique et Laser, Université Laval, Québec) en collaboration avec Lauris Talbot et Martin Bernier.

Résumé de la thèse

Les investigations actuelles dans le domaine des matériaux vitreux et de leur interaction avec le laser offrent la perspective de manipuler ces matériaux au moyen du laser, créant ainsi de nouvelles fonctionnalités et ouvrant la voie à un large éventail d'applications envisageables. Cela signifie qu'il devient possible de manière simplifiée de concevoir un système optique multifonctionnel à l'intérieur d'un matériau massif et transparent. Ces méthodes présentent un potentiel considérable pour la fabrication de composants dans divers domaines, notamment la micro-optique, les télécommunications, l'imagerie, la biophotonique, et bien d'autres encore.

Au fil des années, la réduction progressive de la taille des systèmes informatiques a été à l'origine d'avancées technologiques majeures ayant un impact considérable dans un large éventail de secteurs d'activité, parmi lesquels figurent la médecine, l'agroalimentaire, le transport, le commerce. Dans le domaine des technologies photoniques, la miniaturisation est un aspect essentiel de leur évolution. L'inscription laser directe à l'intérieur de matériaux transparents constitue un sujet de recherche d'un intérêt soutenu depuis plus de vingt ans. Cette technique simple repose sur les principes de l'optique non linéaire et permet d'adresser directement des modifications localisées en 3D à l'intérieur de matériaux transparents, atteignant des échelles submicrométriques. Elle présente de nombreux avantages par rapport aux techniques de lithographie qui se limitent à une structuration en 2D et impliquent de nombreuses étapes, ce qui rend la technique d'inscription directe hautement compatible avec un traitement plus rapide des matériaux et un transfert technologique futur vers la fabrication industrielle avancée. Cette technique induit dans les verres une modification locale permanente de l'indice de réfraction. En contrôlant à la fois les paramètres du laser et la composition du verre, la modification du verre peut être adaptée et est généralement classée en trois régimes d'inscription laser (Type I, Type II et Type III) en fonction de la nature précise de la modification. Le Type I correspond à un changement lisse, isotrope et continu de la densité du matériau et donc de son indice de réfraction. Le Type II est associé à la formation de structures nanopériodiques biréfringentes, tandis que le Type III concerne les structures de type vide résultant d'explosions coulombiennes. Cette avancée a ouvert de nouvelles possibilités pour le développement de microsystèmes optiques intégrés et compacts directement au sein des matériaux transparents, que ce soit sous forme de volume ou de fibres optiques.

Au départ, cette technique était principalement utilisée sur des matériaux vitreux silicatés. Mais au fil du temps, les chercheurs ont largement exploré l'écriture laser directe

femtoseconde dans un large éventail de familles de verre, à savoir la silice, le borate, le fluorure, le chalcogénure, le phosphate, le germanate etc. révélant l'universalité de ce traitement du verre induit par laser. En élaborant des matériaux amorphes qui renferment des ions photosensibles, comme l'argent, il devient envisageable de créer localement des propriétés optiques sans altérer la structure environnante de ces ions.

Les recherches présentées dans ce mémoire s'inscrivent dans une expertise scientifique et technologique développée à Bordeaux sur une période de plus de dix ans. Cette expertise se concentre sur l'utilisation de l'inscription laser femtoseconde infrarouge dans des verres phosphates contenant de l'argent. L'incorporation des ions argent en tant qu'agents photosensibles déclenche une modification exotique basée uniquement sur la photochimie des ions d'argent. Les mécanismes d'oxydoréduction des ions argent Ag^+ joue un rôle essentiel dans ces processus, impliquant directement la formation de défauts électroniques ($Ag^+ + e^- \rightarrow Ag^0$) et de défauts de type trous ($Ag^+ + h^+ \rightarrow Ag^{2+}$). Par le biais de migrations des espèces $Ag^+ et\, Ag^0$, il est possible de générer des espèces avec une nucléarité et une charge plus élevée, conduisant à la formation de clusters d'argent Ag_m^{x+}. En outre, les espèces d'argent générées par photo-induction présentent des propriétés de fluorescence et sont associées à un changement d'indice de réfraction positif, connu sous le nom de Type-A, d'après le mot latin Argentum. Le Type-A ne résulte pas d'une modification de la structure de la matrice vitreuse. Cette distinction d'indice positive s'avère particulièrement bénéfique dans le domaine des applications liées au guidage d'ondes, ce qui a permis la conception de guides d'ondes à l'argent, de guides d'ondes de surface, ainsi que d'un capteur d'indice de réfraction, etc. Notre groupe a aussi examiné les effets de l'absorption cumulative des impulsions laser sur la modification de l'indice de réfraction induite lors de l'inscription multiscan des modifications de Type-A. Cette étude vise à tirer parti du régime athermique pour atteindre un contraste d'indice de réfraction élevé. Les résultats de cette étude montrent qu'il est possible d'obtenir un indice de réfraction de Type-A significativement élevé, pouvant atteindre jusqu'à 2×10^{-2}. Il faut noter que les modifications laser de Type-A sont déclenchées à de faibles densités de puissance laser, généralement deux ordres de grandeur inférieurs au seuil du régime de Type I dans de tels verres photosensibles.

Dans le cadre de ce projet, nous avons profité des modifications de Type-A pour développer de nouveaux types de composants optiques en exploitant leurs caractéristiques de fluorescence et de modification de l'indice de réfraction. Par conséquent, cette recherche envisage l'exploration des agrégats d'argent photo-induits pour deux applications distinctes.

Un premier axe de recherche profite des agrégats d'argent fluorescents pour étudier le potentiel de l'utilisation de ses structures, préalablement obtenues par irradiation laser, pour la dosimétrie des rayons X résolue spatialement. Cet axe est basé sur des résultats antérieurs

du groupe. Notre groupe a récemment démontré la génération d'espèces d'argent dans des verres sodo-gallophosphates contenant de l'argent fortement photosensible exposé aux rayons X. Ce verre de phosphate avait une influence décisive sur la photosensibilité aux rayons X et sur la formation d'espèces d'argent luminescentes, notamment les ions Ag^{2+} piège à trous et les agrégats d'argent Ag_m^{x+}. De plus, des espèces moléculaires inscrites au laser femtoseconde telles que les agrégats d'argent fluorescents montrent leur subsistance sous irradiation aux rayons X. Pour ces raisons, les techniques de radiophotoluminescence et d'inscription laser directe femtoseconde sont combinées pour évaluer le potentiel de ces structures inscrites au laser en tant que sondes locales des doses de radiation déposées. Deux localisations en profondeur différentes d'agrégats d'argent identiques sont générées par inscription directe par laser femtoseconde dans des verres de phosphate contenant une concentration élevée d'oxyde d'argent. Les propriétés spectroscopiques des verres vierges ont été étudiées après irradiation aux rayons X à différentes doses afin d'évaluer leur potentiel dosimétrique. En plus, la dose déposée dépendant de la profondeur dans l'épaisseur du verre a été évaluée à l'aide d'une simulation Monte-Carlo Geant4. Ensuite, l'impact des rayons X sur les agrégats d'argent inscrits en trois dimensions a été analysé à l'aide de plusieurs méthodes spectroscopiques. Ces analyses ont mis en évidence la résilience de ces structures inscrites pouvant agir comme des sondes locales de la dose déposée. Cette étude peut démontrer que ces verres inscrits permettent de définir une gamme et une sensibilité de doses de rayons X et d'envisager la réalisation de dosimètres résolus spatialement.
Compte tenu de la remarquable stabilité des structures photo-inscrites suite aux rayons X, on s'est concentré ensuite sur une étude en temps-réel des agrégats d'argent inscrits au laser pour étudier leur comportement lorsqu'ils sont exposés aux rayons X. Dans ce contexte, un guide d'onde a été précisément inscrit sous la surface du verre, s'étendant sur toute la longueur du matériau. Il a ensuite été relié des deux côtés à l'aide de fibres résistantes aux radiations, ce qui permet la collecte en temps réel de données de radioluminescence et d'atténuation induite par les rayonnements à partir des structures inscrites. En comparant ces données à celles de l'échantillon non inscrit au laser, nous avons observé que les signaux de radioluminescence mesurés provenaient de la matrice irradiée plutôt que des agrégats d'argent eux-mêmes. Donc, ces structures inscrites au laser n'exprimaient aucune réaction aux rayons X lors de la mesure en temps réel de la radioluminescence. Malheureusement, ces sondes locales résistantes ne peuvent pas être utilisées pour des applications de dosimétrie de luminescence en temps réel.

Un deuxième axe de recherche tire parti de la modification de l'indice de réfraction du Type-A induite dans ces matériaux pour la fabrication de réseaux de Bragg volumiques (VBG). Ces derniers ont suscité un intérêt croissant au cours des dernières décennies, principalement en tant qu'éléments de stabilisation de longueur d'onde pour les diodes laser, ainsi comme combineurs de faisceau pour les lasers haute puissance. Jusqu'à présent, les VBGs ont été

réalisés en utilisant la photoinscription de verres photothermoréfractifs avec de la lumière UV, ainsi que divers autres matériaux en utilisant des impulsions laser femtosecondes. En effet, il existe un intérêt croissant pour l'inscription de VBG dans des matrices de verre plus photosensibles, ce qui permet de générer des modifications plus importantes de l'indice de réfraction et d'accélérer le temps d'enregistrement du processus d'inscription. En raison de plusieurs facteurs, notre choix s'est orienté vers l'inscription de réseaux de Bragg en volume basés sur la modification de l'indice de réfraction de Type-A. Ainsi, plusieurs techniques expérimentales ont été présentées pour leur réalisation. Initialement, nous avons exploré la fabrication de réseaux multicouches à l'aide de faisceaux gaussiens. Bien que cette approche ait donné lieu à une efficacité de diffraction relativement faible, elle a permis d'obtenir une modification significative de l'indice de réfraction effective. Cependant, le débit était faible, et le contrôle précis de la période inscrite était difficile. Pour résoudre ces problèmes, nous avons envisagé d'utiliser un faisceau Gaussien-Bessel. Cela se traduit par une zone de modification de l'indice de réfraction, induite par l'apparition des agrégats d'argent, s'étendant sur une profondeur beaucoup plus grande que celle obtenue avec des faisceaux gaussiens standards. Cependant, en inscrivant une seule couche avec le faisceau Gaussien-Bessel, nous avons démontré des VBG atteignant une efficacité de diffraction élevée allant jusqu'à 95 % à 632.8 nm, avec une période de 2 µm et une épaisseur effective de 150 µm, ce qui correspond à une modulation de l'indice de réfraction de 1.78×10^{-3} selon la simulation. Cette simulation utilise l'analyse de Kogelnik basée sur la théorie des ondes couplées. La sélectivité spectrale a également été étudiée et montre une bonne concordance avec la modélisation numérique. En plus, l'efficacité de diffraction des VBG a été analysée à 1.55 µm et montre une modulation élevée de l'indice de réfraction de 1.37×10^{-3}. Nous avons également exploré la formation d'un faisceau en forme de feuillet de lumière pour améliorer le débit d'inscription. Les tests préliminaires ont révélé que le réseau inscrit se comportait comme un réseau de surface optiquement mince, plutôt qu'un réseau de Bragg volumique. Cependant, des optimisations supplémentaires seront nécessaires pour obtenir les résultats souhaités. De plus, nous avons étudié l'approche de masque de phase qui offrait un débit élevé. Cette méthode démontre la nécessité d'utiliser un laser à plus haute fréquence de répétition (>1 kHz) pour favoriser davantage la création des agrégats d'argent. Ces études démontrent, pour la première fois, la réalisation de VBG de Type-A, ouvrant la voie à des applications industrielles.

Table of contents

List of figures

List of Table

Acknowledgment

This PhD has been completed between two labs in France: the Centre des Lasers Intenses et ses Applications (CELIA) and the Institut des Chimie de la Matière Condensée de Bordeaux (ICMCB).

I would like to thank Pr. Bruno Capoen, Pr. Sylvain Lecler, Pr. Nathalie Destouches, Pr. Emmanuel D'Hummières and Dr. Adriana Morana for agreeing to be part of my thesis jury. I appreciate your time, expertise, and valuable feedback during the defense of my thesis. Your constructive evaluations have greatly enriched my work.

To my PhD supervisors, Prof. Lionel Canioni and Dr. Yannick Petit, I express my heartfelt gratitude for selecting me for this PhD journey. Your unwavering support, understanding, and assistance was invaluable during the most challenging phases of my doctoral studies. Thank you sincerely for your guidance. To Lionel Canioni, your constant optimism and determination have been a crucial source of inspiration that significantly contributed to the success of my research project. Your ability to maintain a positive attitude, even in the face of the most complex challenges, has had a transformative impact on my own mindset. Your energy and contagious enthusiasm have encouraged me to persevere, even in the most difficult moments. You've taught me to adopt a positive perspective, to recognize the constructive aspects of every progress, even when things weren't perfect after several attempts. To my co-director Yannick Petit, I am deeply grateful for your attentive pedagogical approach and unwavering commitment to my academic development. I wanted to express my sincere gratitude for your exceptional support throughout my thesis, especially during the challenging periods of the COVID-19 pandemic. Your ability to stay connected and available despite the collective challenges we faced created a supportive environment that I will always remember with gratitude. I am deeply thankful for the opportunity to work under your guidance, and I sincerely thank you for your constant presence, understanding, and support. Also, I really appreciate the coffee breaks and lunch breaks with both of you.

I'd like to express my gratitude to all my colleagues within the SLAM group. I appreciate the assistance and the enjoyable moments we shared. Being a member of the SLAM group feels like being part of a family, and I genuinely appreciate the welcoming atmosphere. Thank you to the SLAM colleagues: Bruno Bousquet, Inka Mannek-Honninger, Alain Abou Khalil, Laura Loi, Sabrina Benhamouche, Raphael Hazem, Elize Clave, Yann Serre, Mathis Carpentier, Rybal Beyrouthi. Thank you to the colleagues at ICMCB: Thierry Cardinal, Veronique Jubera, Alexander Fargues, Sylvain Danto, Fouad AlAssani, Olivier Nguyen, Rayan Zaiter, Georges ElDib, Théo Guérineau for providing samples, for helping in the polishing of the samples and

the realization of some mechanical pieces for my project. I also thank you for the interesting discussions during the meetings. I also want to extend my appreciation to my colleagues at CELIA, particularly Laurent Merzeau and Rodrigue Bouillard, for their assistance with the mechanical components. Many thanks to the colleagues in the ISM (Institut des Sciences Moléculaires) laboratory: Guillaume Rafy and André Del Guerzo for their help in the FLIM measurements. Special thanks to Argolight Company by Kevin Bourhis and Arnaud Royon for providing me samples for this project.

Moreover, I want to extend my appreciation for the warm reception and collaborative spirit within the Hubert Curien Laboratory group in St-Étienne. My sincere thanks go to Sylvain Girard, Aziz Boukenter, and Youcef Ouerdane. A special acknowledgment is reserved for Adriana Morana, who steadfastly supported me throughout my experimental work, dedicating a full week from 9 am to 9 pm. I am truly grateful for all the insightful discussions and the considerable time you devoted to assisting me with my research. I would like to express my gratitude to the colleagues in this laboratory who warmly welcomed me during my work and helped when needed. Special thanks to Arnaud Meyer for his collaboration in the simulation work and to Thimote Allanche for his invaluable help in the experimental part.

Furthermore, I want to express my gratitude for the collaboration with the COPL laboratory in Quebec. It was a pleasure working with Lauris Talbot when he visited our laboratory. Subsequently, during my collaboration with COPL, I also worked alongside Martin Bernier. I gained valuable insights from your both expertise, and I appreciate the positive atmosphere Lauris Talbot brought to the long experimental days. You're also deserving of thanks for introducing me to the Québécois culture!

Also, thank you to Céline, Sophie, Sonia, Vanessa, Clara, Pamela, Frederique, Cecilia and so on.. for all the administrative help that you provided.

Of course, I would like to thank my funding sponsor, the Sciences Aquitaine Transfer and Bordeaux University for the funding and for the equipment bought and used during this project. Many funding also has been collaborated in this project, I would like to thank the Funglass project, the ANR and the European commission.

Finally, I would like to express my gratitude to everyone who has contributed, directly or indirectly, to the realization of this project: Patrick Mounaix, Giorgio Santarelli, Roopa Prakash, Bruno Courtinade, Lucie Desclaux, Marie Fleureau, Marc Casting, Michael Berisset.

On a personal note, I would like to dedicate this PhD to my parents. I appreciate their sacrifices, their patience, and above all, for their unconditional love. A special thanks to my

sister who stood next to me in every step. I would also like to thank my friends from France and Lebanon for supporting me and helping me during this Phd.

Finally, I thank my boyfriend for his presence, love, and encouragement. Thank you for your understanding during the times when I was absorbed in my research, and for celebrating each milestone of this journey with me. I appreciate your patience, unconditional love, and for being the extraordinary person that you are.

I General background on glass and laser-matter interaction

This chapter provides a comprehensive understanding of the detailed processes of ultrafast laser-matter interactions offering an overview of both glasses and laser beam engineering and delivering.

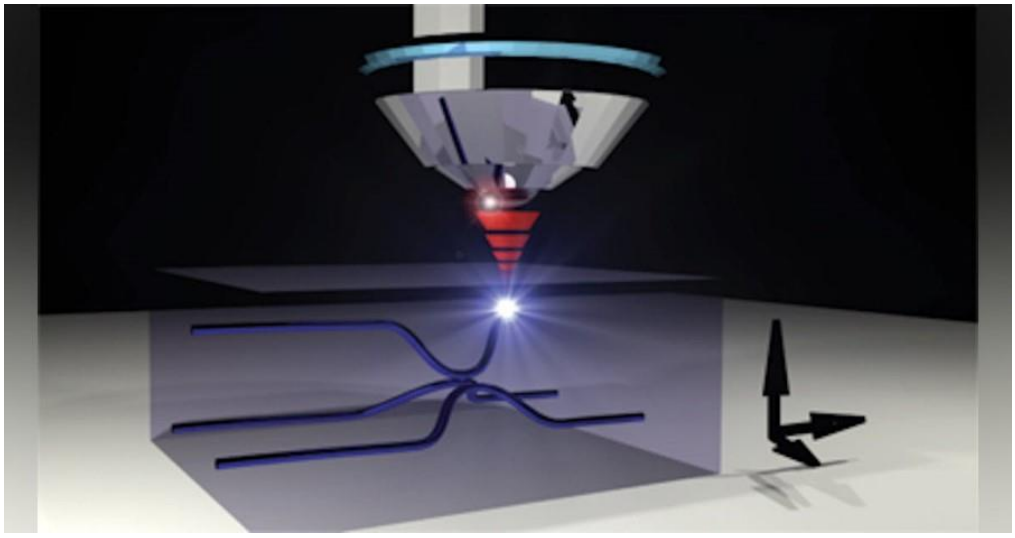

Taken from [1].

I.1.Introduction

Laser-matter interaction is a diverse and dynamic research field that spans numerous scientific and practical applications across various domains. It involves the interaction between laser beams and different types of materials, including gases, liquids, solids, and even plasmas. Also, it has become an essential tool in numerous fields. Understanding how lasers interact with matter is essential for using their potential across a wide range of industrial and scientific research activities. Indeed, every material interacts with laser irradiation in a specific way. In this work, we will concentrate on glasses for several reasons. They exhibit exceptional optical properties, which are dependent on their specific composition and their atomic-level structure. Additionally, these materials possess interesting thermomechanical properties, which make them capable of achieving both high stability and uniformity in the production process. In particular, they are highly suitable for photonics applications. For this reason, a brief overview of glasses and their production techniques are presented in the first part of this chapter. Additionally, their main optical properties are discussed. In the second part of this chapter, the laser-matter interaction is introduced starting with a brief history of the laser followed by the different physical phenomena that occur subsequently the interaction of femtosecond (fs) lasers with glasses. Finally, basic notions of focused Gaussian and Gaussian-Bessel beam are recalled understanding the experimental sections related to this part.

I.2.Glasses

The history of glasses is a fascinating journey through centuries of human creativity and technological advancement. The earliest known glass objects were created in Mesopotamia and Egypt around 3500 BC. These objects were primarily beads and small vessels made using a technique called core-forming. Early glass objects were created by melting a combination of silica (sand), soda, and lime. The Romans refined glassmaking techniques, introducing glassblowing in the first century BC. This innovation revolutionized glass production, making it more accessible. Byzantine glassmakers further developed this art, creating complex glass mosaics and vessels. Islamic civilization made significant contributions to glassmaking, perfecting techniques like lusterware, which involved metallic glazes. Later, Venice became a center of glass production in the 13th century, thanks to its skilled artisans. Murano glassmakers developed techniques for producing fine glassware and mirrors.

Furthermore, advances in science and optics led to a better understanding of glass. The Dutch inventor Anton van Leeuwenhoek used glass lenses to create the first microscope in the late 17th century. In the 19th century, the Industrial Revolution brought significant advancements in glass production. Mass-produced window glass, glass bottles, and glassware became widespread. Then, the development of precision optical instruments, like telescopes

and microscopes, drove innovations in optical glass manufacturing. The 20th century brought further innovations in glass production, such as the development of tempered glass, laminated glass, and the float glass process. Various types of specialty glasses are developed, including borosilicate glass (Pyrex), safety glass, and fiber optics. These innovations made glass safer, more durable, and more versatile, leading to its use in architectural applications, automotive windshields, and consumer electronics.

Advances in materials science led to the development of glasses with specific properties. Examples include Gorilla Glass for smartphone screens and smart glasses with augmented reality capabilities. Contemporary glass artists and architects continue to push the boundaries of glass as a medium for artistic expression and structural design. Ongoing research explores the potential of glasses in various fields, including nanotechnology, energy storage, and flexible electronics.

The history of glasses reflects the evolution of human knowledge, craftsmanship, and technological expertise. From ancient beads to modern optical fibers, glasses have played a pivotal role in shaping our world. Nowadays, many industrial glass companies exist such as Corning, Saint-Gobain, Pilinkgton, Asahi Glass Co, etc. and they master the art of glass making.

I.2.1.Definition and properties of glasses

Numerous definitions proposed by scientists in the past twenty years, as outlined in references [1–3], have contributed to the understanding of the concept of glass. Any material, regardless of whether it's inorganic, organic, or metal, produced through any method that involves a glass transition, can be categorized as a glass [5]. Consequently, a comprehensive description of glass involves viewing it as a supercooled liquid existing in a metastable state, characterized by a glass transition region accompanied by long-range atomic disorder. Due to the irregular arrangement of atoms, glasses are recognized as amorphous substances that possess a liquid-like structure, lacking long-range molecular order. Despite this, their mechanical properties resemble those of solids.

In contrast to the ordered atomic structure found in crystals (depicted in Figure I-1(a)), glasses show an unordered atomic arrangement (as shown in Figure I-1(b)).

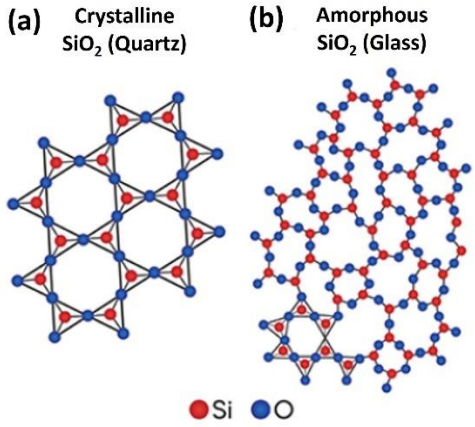

Figure I-1: Schematic of silica molecule: variation in the structural configuration in both its (a) crystalline and (b) glass forms. Taken from [6].

Glass is a non-crystalline solid that demonstrates the phenomenon of glass transition. Once a liquid is cooled below its melting temperature T_L, it undergoes a thermodynamical state known as a metastable liquid. Below the melting temperature, there are two potential outcomes: the cooled liquid can either crystallize into a solid crystal structure or transform into a glassy state. In situations where there is a favorable thermodynamic ability to promote nucleation, a significant discontinuity in volume occurs within the system. This leads to the formation of a crystal, as depicted in Figure I-2. On the other hand, if nucleation doesn't occur, the liquid remains in a state of metastable equilibrium below T_L. In this scenario, the thermal contraction coefficient remains consistent, and there's no substantial alteration in the system's volume. As the temperature drops below T_L, atomic mobility decreases, causing atoms to become immobilized in fixed positions. This transition takes place across a temperature range known as the glass transition region, marking the initiation of glass formation. A discontinuity in specific volume and enthalpy is then observed at a new characteristic temperature called the glass transition temperature T_g. Generally, T_g is the temperature range at which an amorphous material changes from soft to hard and vice versa, which is the intersection of the extrapolated lines from the glass and metastable liquid ranges shown in Figure I-2. The crystallization phase can be avoided if the cooling process is sufficiently fast since the nucleation process is triggered at higher temperatures than the glass transition temperature and for specific conditions of the melt's kinetic parameters and pressure.

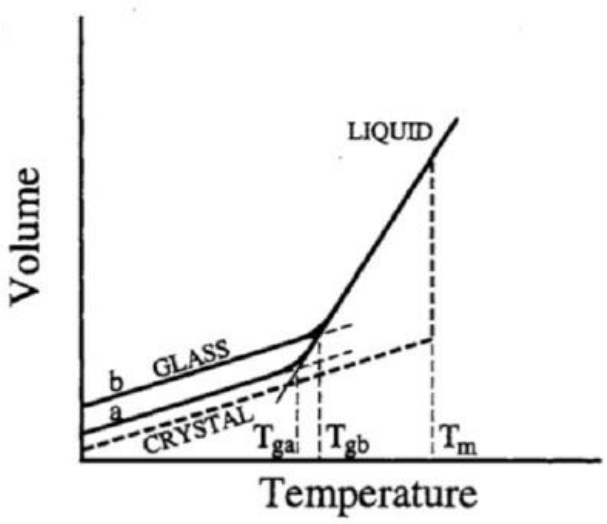

Figure I-2: Volume variation as a function of the temperature while cooling a liquid to form a crystal or a glass. Taken from [7].

Presently, various glass categories exist, including oxide glasses, metallic glasses, fluoride glasses, chalcogenide glasses, organic and inorganic glasses. For the last category, namely the inorganic glasses, the classification is made on the type of anion forming the glass. In the case of oxide glasses, the anions are oxygen elements, while halide and chalcogenide glasses are based on fluorine (or chlorine) and sulfur (or selenium or tellurium), respectively.

Back in 1926, scientists introduced certain criteria for the formation of glass that could potentially apply in specific instances. However, this aspect will not be extensively covered in this document. For those who wish to delve deeper into this topic, additional information can be found in the following references [8]–[12]. The focus of the present PhD manuscript will be on oxide glasses. There are two approaches to explain why a chemical compound can give rise to glass formation. Readers are invited to check the PhD of Théo Guérineau (University of Bordeaux, CNRS, ICMCB, 2020) for deeper details [13].

Zachariasen's classification categorized the oxides utilized in glass production into three distinct groups: formers, modifiers, intermediates [8].

- ***Glass formers:*** they are elements that can form a glass network. The most common elements are silicon (SiO_2), boron (B_2O_3), phosphorus (P_2O_5), germanium (GeO_2) and arsenic (As_2O_3).
- ***Modifiers:*** they cannot form a glass network alone under normal cooling conditions. Their addition to formers leads to a reduction of the melting temperature and liquid viscosity. They are also added to reduce the structural cohesion, such as Li_2O, Na_2O, BaO.
- ***Intermediates:*** they can act as glass formers or modifiers but are not able to form the glass network by themselves. The main intermediate elements in oxide glasses are aluminum, zinc, iron and titanium. Examples of intermediate glass constituents are: Al_2O_3, ZnO, Ga_2O_3, TiO_2, PbO, ZnO or CdO.

I.2.2.Methods of glass production

Numerous methods are employed in the fabrication of glasses, depending each on variables such as the type of glass, its composition, the desired final structure, and the intended purpose of the resulting product. Glass can be produced from plasma through chemical vapor deposition, from liquids through the sol-gel and the melt-quenching method or from solids through decomposition. In this context, our focus will be on the melt-quenching method consisting of two approaches. The first one involves float glass, an industrial and preferred method employed for producing large glass quantities under a continuous steady-state production process. The second approach, termed the lab technique, is a homemade method for research applications.

I.2.2.a.Melt-Quenching Technique

In this work, the melt-quenching method is used to synthesize the glasses at the ICMCB laboratory (Institut de Chimie de la Matière Condensée de Bordeaux, UMR 5026) by different colleagues from group 3. The process begins with the selection and measurement of the appropriate mix of powdered materials required for creating the glass at the desired composition with respect to the molar fraction of each involved oxide. Such materials are grinded into powders using a ball mill. Then, the powders are transferred into a platinum crucible and this assembly is heated in a furnace up to the melting temperature of 1200°C for a duration of ~12 hours. At that temperature, the mixed powder is transformed into a melted liquid. Hence, the crucible is taken out of the furnace and promptly quenched to form the glass, thereby preventing any crystallization from occurring. Subsequently, the glass undergoes an annealing process at a typical temperature of 40°C lower than the glass transition temperature for a minimum duration of 4 hours to release the stress. This step is crucial to eliminate by relaxation any mechanical stress that may have been embedded in the quenching step within the glass structure. Finally, the glass is removed from the furnace. The cutting and polishing of the manufactured glass are carried out after allowing it to stabilize at room temperature. The melt-quenching technique is shown in Figure I-3.

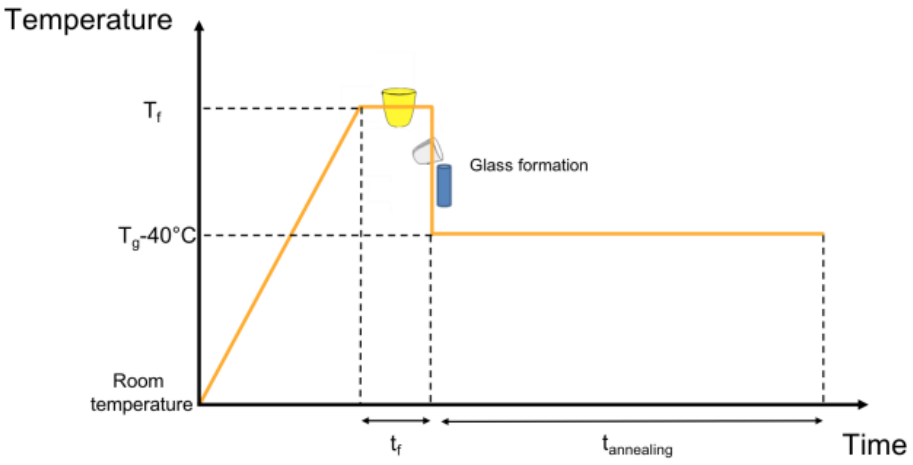

Figure I-3: Schematic representation of the melt-quenching technique.

I.2.2.b.Float glass process

The float glass process was developed during the 1950s to address the urgent requirement for a cost-effective technique to produce flat glass suitable for both automobile and architectural uses. Figure I-4 illustrates the float glass production process. A glass ribbon is floated on a molten tin bath, resulting in the natural creation of a smooth surface. The process begins with the preparation of a batch of raw materials, which is then introduced into a horizontal furnace. To ensure good chemical homogeneity, the glass is initially heated to around 1550–1600°C within the furnace. It is subsequently cooled down to approximately 1100–1200°C in the forehearth. During the glass's movement across the tin bath, the thickness of the glass sheet is regulated by managing the flow at the entry point and the lateral edges of the bath. The glass then proceeds through a channel, flowing over a refractory lipstone or spout onto the tin bath. As it flows, the glass's temperature decreases, leading to increased viscosity. At the end of the tin bath, the glass is gradually cooled to a temperature near its glass transition temperature. Then, it enters the annealing lehr for controlled gradual cooling down. Ultimately, the formed glass is further subjected to annealing to eliminate any accumulated stress and mechanical constraints. The glass exhibits flat and polished surfaces, attributed to its flotation on the high-quality nonporous metal bath, the high quality of these surfaces inherently results from the thermodynamical stabilization of the curve between two liquid interfaces.

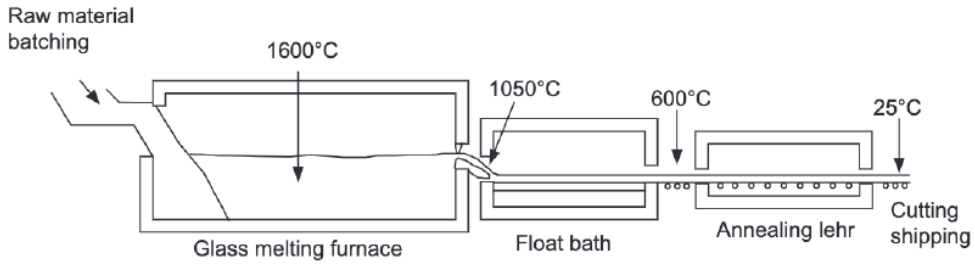

Figure I-4: Schematic illustration depicting the procedure of the float glass technique. Taken from [14].

I.3.Optical properties

I.3.1.Transparency window

The optical characteristics of a glass are determined by the elements that compose the glass itself. The optical transmission window of a transparent material corresponds to the spectral range where no significant absorption is observed for different wavelengths. Only the refractive properties come into play, influencing the propagation of an electromagnetic wave. Based on the transmission of the glass, the absorption coefficient is calculated using the Lambert-beer law as depicted in Equation C-1 in Appendix.

Oxide glasses, as well as chalcogenide and halide glasses, have an optical transmission window bounded by two major absorption phenomena: the multi-phonon absorption at longer wavelengths in the infrared range (IR) and the absorption related to electronic transitions (due to the absorption of an electron in the valence band to be promoted in the conduction band) at shorter wavelengths (in the ultraviolet (UV) range) [15]. However, the absorption in the infrared is linked to the molecular vibrations at this wavelength range and the associated phonon energy. Typical oxide glasses demonstrate significant transparency in the visible and near-infrared (NIR) regions with a typical common IR-cutoff around 2.9 µm (depending on the considered sample's length) due to the absorption of hydroxyl groups, but they exhibit high absorption in the UV range. On the other hand, different types of glasses such as chalcogenide glasses can display extended transmission in the IR region while demonstrating reduced transmission in the visible spectrum, due to the present of heavier cations than those in oxide glasses which leads to lower vibration frequencies and thus larger IR transparency [16]. Figure I-5 depicts the typical comparison of the optical transmission between different glasses families, including silica glasses, fluoride glasses and chalcogenide glasses.

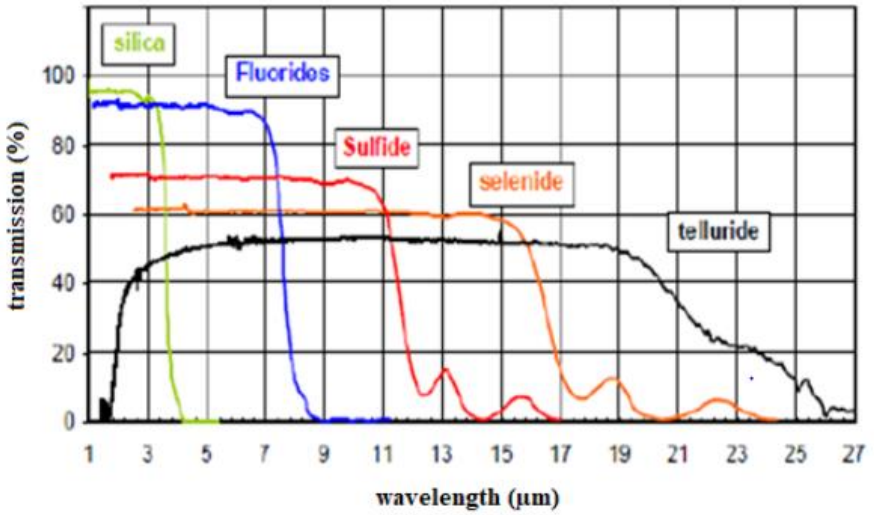

Figure I-5: Absorption spectrum of silica, fluoride and chalcogenide glasses. Taken from [17].

As already known, when an incident light passes through a bulk glass, a fraction of light is reflected, scattered, absorbed and the rest is transmitted. Fresnel reflection is known as the phenomenon of reflected light from one facet of a glass. The losses associated to Fresnel reflection at the input and output interfaces of the material should be taken into consideration while experimentally measuring transmission of glasses. The percentage of reflected light depends on the refractive index change between the considered glass and the surrounding medium. As an example, in the case of the silver-containing phosphate glass employed in this PhD manuscript, the refractive index is ~1.6. Thus, the calculated Fresnel reflection stands at around 5%. This calculation is achieved using the following standard formula:

$$R = \left(\frac{n_1 - n_2}{n_1 + n_2}\right)^2 \qquad \text{I-1}$$

I.3.2.Refractive index

When producing glasses for photonic applications, it is crucial to regulate the material's optical characteristics. For instance, controlling the dependence of refractive and absorption properties with wavelength is a key objective, and this is accomplished by tailoring the composition of the glass.

In general, the optical index can be considered as a complex number $\hat{n}$, consisting of a real part n and an imaginary part κ, respectively dealing with the refractive and absorbent behaviors [18]:

$$\hat{n} = n - i\kappa \qquad \text{I-2}$$

where κ depends on the absorption coefficient α and the wavelength using the following equation:

$$\alpha = \frac{4\pi\kappa}{\lambda} \qquad \text{I-3}$$

The dependence of the refractive index change with the wavelength is generally expressed using the dispersion formula given by the Sellmeier equation:

$$n^2(\lambda) - 1 = \sum_{i=1}^{3} \frac{A_i \lambda^2}{\lambda^2 - B_i^2} \qquad \text{I-4}$$

where the three terms reported in the sum represent three harmonic oscillators with amplitudes A_i and resonance wavelengths B_i, with i = 1, 2, 3. Two of the resonance wavelengths in the UV correspond to electronic transitions while the third one in the IR spectral range corresponds to ionic vibrations and photonic absorption. Moreover, the refractive index of the glass is critically dependent on the cooling process of the glass from the liquid to the solid state [19].

I.4.Laser-matter interaction

A laser is a device that produces a coherent and collimated beam of light through a process called "Light Amplification by Stimulated Emission of Radiation." It operates based on the principles of quantum mechanics and involves the emission of photons through the stimulated emission process introduced by Einstein in 1917. Thus, this results in a concentrated and well-defined beam of light. Indeed, laser is a photonic system designed to produce or amplify temporally and spatially coherent electromagnetic radiation with dedicated wavelengths ranging from ultraviolet to microwaves, including the visible and infrared spectra. They have a wide range of applications in various fields, including technology, industrial communications, medicine, manufacturing, research, spectroscopy, interferometry and more. Presently, there is a broad spectrum of laser types available, spanning different technologies such as solid-state [20], dye [21], semiconductor [22], gas [23], fiber [24], free electron [25], and X-ray lasers [26]. These lasers exhibit the capability to operate in both continuous and pulsed modes. The first application of the stimulated emission process for amplifying a radiation field resulted in the achievement of MASER: Microwave Amplification by Stimulated Emission of Radiation. It was developed independently in 1954 by the research team of Charles Townes at Columbia University (USA) to amplify microwaves. The jump from masers to lasers occurred when Theodore Maiman developed the first working laser in the visible range using a ruby crystal as the gain medium. In 1960, Maiman demonstrated the first successful operation of a pulsed laser, generating coherent red light out of a ruby crystal pumped by a flash tube. The 1980s saw the advent of high-power solid-state lasers and advancements in laser technology. Researchers worked on improving laser efficiency, increasing power outputs, and developing new laser materials.

To optimize interactions between lasers and materials, the primary focus is on maximizing laser intensity, which represents the photon flux per unit of time and surface area. While efforts have been made to boost the average power of continuous-wave lasers, this approach

faces limitations due to the size and thermal constraints of these large systems. One alternative is to operate in pulsed modes, such as relaxed or triggered modes, which allow the system to cool down between each pulse. A significant advancement was made with the implementation of short triggering in Q-switched mode, leading to shorter laser pulses and consequently higher intensity, achieved by concentrating photons within a shorter time frame. Lastly, the mode-locked approach enables the attainment of femtosecond laser regimes, resulting in the ultimate temporal concentration. Current femtosecond laser sources combine short pulses with very high repetition rates, yielding substantial average power and making them the optimal choice for laser-material interactions.

In the context of this project, well-established commercial lasers are employed to create photonic components by inscribing them inside glass materials. The lasers used for direct laser writing are mode-locked lasers. The emitted wavelength is determined by the gain medium, specifically through the atomic or molecular transitions occurring between the energy levels of the atoms. Several references provide comprehensive explanations of the principles of lasers and cover various aspects of laser physics, from the underlying theory to practical applications [27]–[29].

Over the past two decades, there has been extensive research into the interaction between femtosecond lasers and materials [30]–[34]. Focused femtosecond lasers generate ultra-high peak power pulses, leading to a fundamentally different interaction between the laser and matter compared to conventional long-pulse lasers. This interaction involves nonlinear absorption phenomena, including multiphoton processes (as discussed in references [31], [32]) as further detailed in the following section. This has opened new and exciting opportunities for customizing the interaction between the laser and matter, providing exceptional spatial resolution and paved the way for three-dimensional fabrication techniques.

I.4.1. Nonlinear absorption mechanism in glasses

In dielectric materials or semiconductors, linear absorption based on electric dipolar transitions occurs when a single photon carries enough energy to surpass the material's band gap. This energy prompts the transition of an electron from the valence band (VB) to the conduction band (CB) through single-photon absorption, as depicted in Figure I-6(a). However, under the influence of high-density photons flux as it is often the case with very intense ultrashort laser pulses, an electron can be elevated to an excited state through the simultaneous absorption of two or more lower-energy photons. This occurs through intermediate virtual states, where the combined energy of these photons exceeds the band gap energy E_g, as illustrated in Figure I-6(b). This multi-photon absorption (MPA)

phenomenon is inherently a nonlinear process. In dielectric materials, the E_g is generally higher than the energy of one photon with commonly used laser sources. Therefore, for the electrons to pass to the conduction band, the nonlinear absorption process is a must.

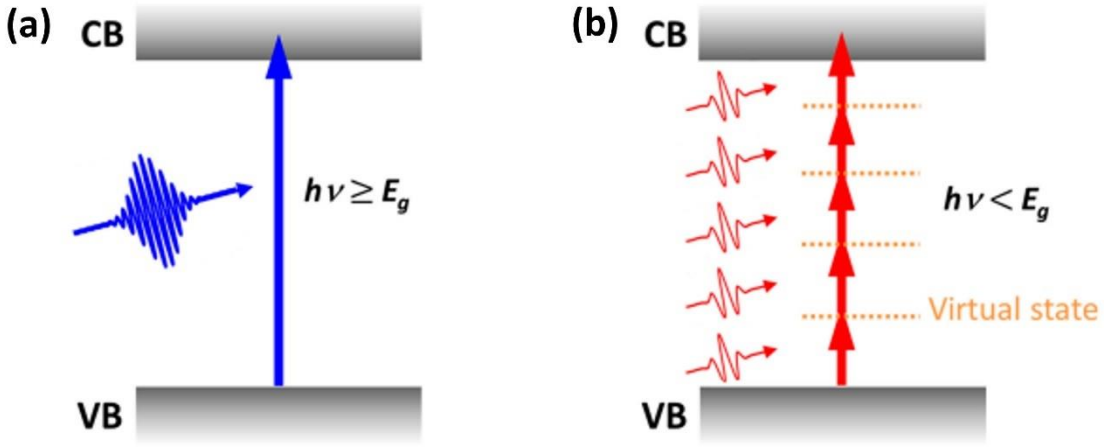

Figure I-6: Illustration depicting the process of (a) single-photon absorption and (b) multi-photon absorption. Taken from [35].

This nonlinear light-matter interaction takes place exclusively in the vicinity of the focal volume, where the laser's peak intensity is sufficiently high to induce substantial multi-photon absorption process in relationship with the low associated multi-photon absorption cross-section. Indeed, Figure I-7 shows the difference in terms of extension of the interaction zone in the case of linear (Figure I-7(a-b)) and multi-photon absorption (Figure I-7(c-d)), respectively. In particular, the images reported in Figure I-7(b) and Figure I-7(d) show the fluorescence emitted by the excitation of a dye solution in interaction with a laser source in the two above-mentioned cases: for the case of multi-photon absorption, the excitation is achieved only in the focal volume, as already explained.

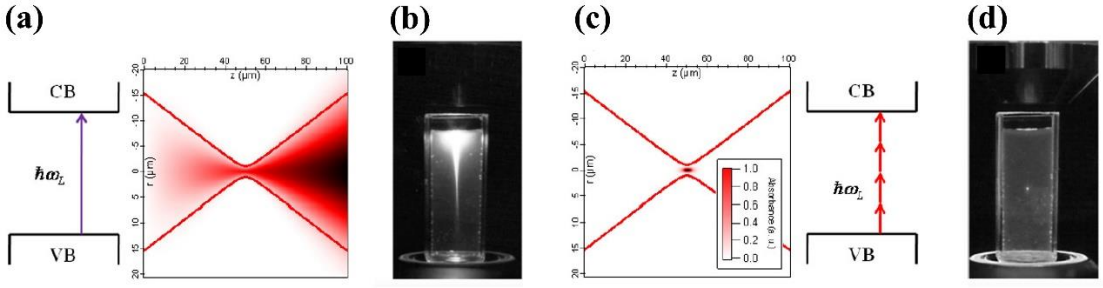

Figure I-7: Interaction zones for the case of (a-b) linear absorption and (c-d) multi-photon absorption. Taken from [36], [37].

As already mentioned, focused femtosecond laser pulses, operating within the visible or near-

infrared wavelengths, lack the necessary photon energy for linear absorption in glasses. Instead, nonlinear photoionization promotes valence electrons to the conduction band. When using ultrashort laser pulses, such as a femtosecond pulses, three primary elementary processes can lead to electron generation, depending on the laser frequency and intensity [31], [32]: multiphoton ionization, tunnel ionization, and avalanche ionization. The first two processes are considered as direct photoionization of the medium. Avalanche ionization is an indirect process where electrons are promoted to the conduction band due to the collision between free electrons accelerated by the electric field. The three processes are depicted in Figure I-8. Keldysh introduced a parameter to describe the transition between the processes, referred to as the Keldysh parameter [38]:

$$\gamma = \frac{w}{e}\left(\frac{mcn\varepsilon_0 E_g}{I}\right)^{\frac{1}{2}} = \frac{w}{e}\frac{\left(2mE_g\right)^{\frac{1}{2}}}{F} \qquad \text{I-5}$$

where w is the laser pulsation, c is the velocity of light, n is the refractive index change of the medium, ε_0 is the permittivity in the vacuum, m and e are the reduced mass and charge of the electron and I is the laser intensity and F the related electric field amplitude.

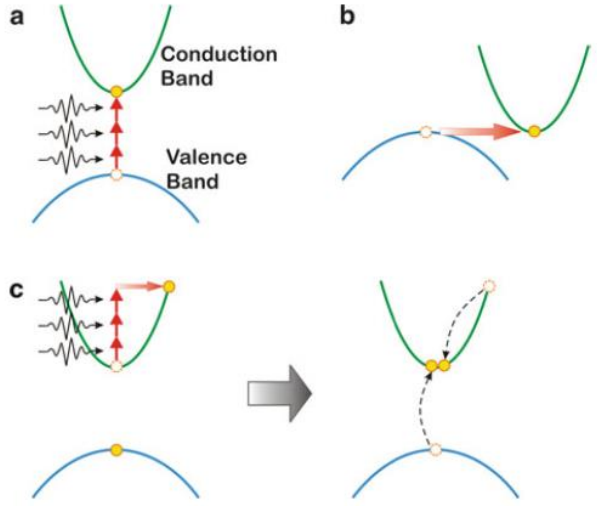

Figure I-8: Schematic representation of the nonlinear processes involved during femtosecond laser irradiation:(a) multiphoton ionization, (b) tunneling ionization, and (c) avalanche ionization. Taken from [39].

Multiphoton ionization: this process involves the simultaneous absorption of several photons (two or more), promoting an electron from the valence band to the conduction band (Figure I-8(a)). For multiphoton ionization to occur, the number of photons k required to bridge the band gap must satisfy $kh\nu > E_g$, where E_g is the band gap energy and ν is the frequency of light.

For pulses with relatively low laser irradiance and high frequency, where the Keldysh

parameter satisfies γ >1, the multiphoton ionization dominates the process. The photoionization rate highly depends on laser intensity, given by [31], [32], [40]:

$$P(I) = \sigma_k I^k \quad \text{I-6}$$

where σ_k represents the multiphoton absorption coefficient for the absorption of k photons, and I stands for the laser intensity.

In the context of the silver-containing phosphate glasses used in this study, their band gap ranges from 4.5 eV to 4.8 eV, depending on the concentration of silver ions within the glass [41]. Therefore, when employing a 1030 nm laser with a photon energy of 1.2 eV, a four-photon absorption process becomes necessary to attain ionization. In our context, the estimated value of the Keldysh parameter is slightly greater than 1 (γ ~1.3). Thus, the regime of the multiphoton ionization process is considered to dominantly take place in our case.

Tunnel ionization: For γ<1, corresponding to higher irradiance and low laser frequency, tunnel ionization takes place. This phenomenon is characterized by the elimination of the Coulomb potential well due to the strong electric field produced by the laser intensity, enabling an electron to traverse a barrier and to become liberated, as depicted in Figure I-8(b). However, when γ is ~1, a combination of both multiphoton ionization and tunneling ionization processes occurs (known as the intermediate regime [32]).

Avalanche ionization: In the case of high intensity of the laser field, avalanche ionization occurs. This leads to the acceleration of free electrons in the conduction band. Such free electrons absorb photons until their energy surpasses the material's band gap. Electrons acquiring enough kinetic energy can collide and excite other atoms from the valence band to the conduction band. These electrons can sporadically collide with another atom, resulting in the ionization of one of its electrons from the valence band to the conduction band, resulting in two excited electrons at the conduction band minimum. These two electrons can undergo free carrier absorption and impact ionization and the process can repeat itself if the laser field is present and strong enough, giving rise to an electron avalanche. Figure I-8(c) illustrates this process.

I.4.2.Physical processes (time scale)

It is important to understand the physical processes associated with laser-matter interaction as well as their associated characteristic times. This has been widely studied during the last two decades and it depends on the investigated material and on the irradiation regime. Figure I-9 depicts certain fundamental processes involved in laser-matter interactions.

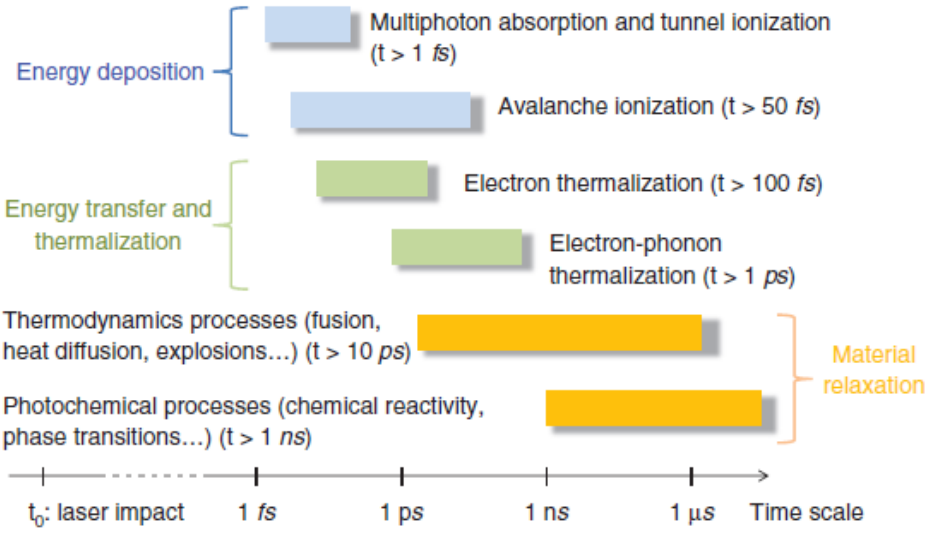

Figure I-9: Time scales of the physical phenomena occurring during the interaction of a focused beam in the matter. Taken from [42].

In the initial phase, the incident ultrafast laser pulses are partially absorbed in the first few fs, resulting in energy deposition into the material and the generation of photoelectrons. Subsequently, these photoelectrons transfer their kinetic energy to the lattice over a picosecond (ps) time scale. Ultimately, heat diffusion takes place to homogenize the temperature distribution. This can lead to material melting, fusion, or even material fragmentation, depending on the threshold modification of the material and consequently enables chemical reactions. Finally, if the temperature within the interaction voxel exceeds the material's melting point during pulse absorption, rapid localized melting occurs, succeeded by a re-solidification process occurring within the microsecond (µs) time frame. Beyond one nanosecond (ns), photochemical processes such as redox reactions and nucleation can occur due to thermal activation, divided into three major categories (energy deposition, thermalization, and energy transfer), followed by relaxation and material modification. Material modification will be discussed in detail in chapter II.

I.4.3.Repetition rate, heat accumulation and laser writing regimes

Generally, a laser can operate in continuous mode, emitting light continuously and without interruption. In this case, the laser doesn't have a repetition rate and the material does not have time to cool down as steady state irradiation takes place. Alternatively, lasers can also operate in pulsed mode where emitted pulses are separated by a specific time interval determined by its repetition rate. The pulses exhibit a pulse duration T_0 and are separated by a period of T which is determined by the laser repetition rate $\tau = \frac{1}{T}$. Indeed, in this case, thermal relaxation is eventually available between successive pulses and material may have time to cool down depending on the repetition rate as well as the thermal properties of the

material. One approach to control the overall thermalization of a material is to increase the laser repetition rate, particularly to activate photochemical processes. Indeed, the higher the laser repetition rate, the shorter the time between two pulses, allowing the material less time to thermally relax. Over numerous pulses, the glass experiences heating and melting in a volume larger than the initial focal volume. Once the pulse train is stopped, the glass undergoes cooling and re-solidification in a manner distinct from the initial state. When the repetition rate is sufficiently high, the material's temperature cannot return to its original value through diffusion between pulses. If the temperature increase per pulse is non-negligible, this initiates a significant pulse-after-pulse heat accumulation, possibly leading the material to undergo phase transition from solid to liquid phases, followed then by ultrafast cooling and re-solidification when laser irradiation stops. Figure I-10 represents the pulse shape, power and the temperature as a function of time for both regimes [43].

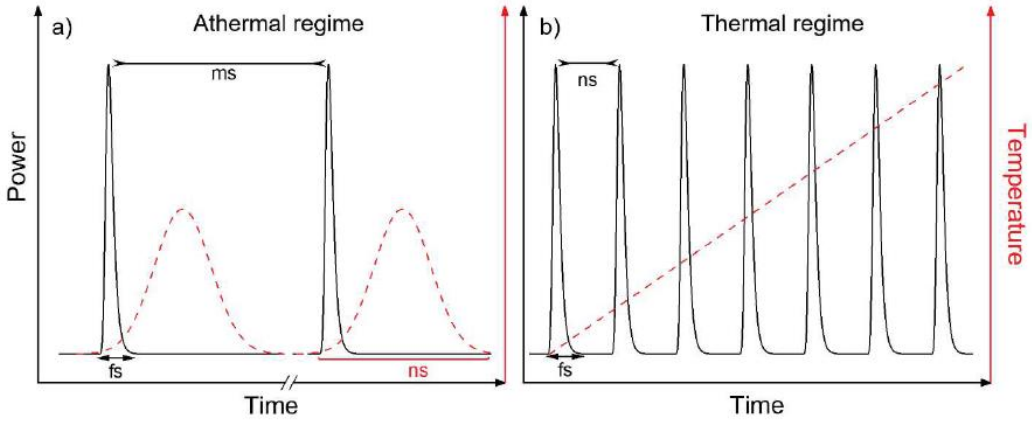

Figure I-10: Comparison of the schematic evolution of temperature over time in a material irradiated by a femtosecond laser: a) athermal regime, b) thermal regime.

The form of the energy deposit in the material is a not an easy task, and it was already explained in details in the Phd manuscript of Papon Gautier, in reference [44].

It should be noted that for weak repetition rate ($\frac{1}{f} \gg 2\,\tau_{th}$, τ_{th} being the thermal diffusion time in the focal volume and f is the pulse repetition frequency), there is practically no heat accumulation between two consecutive laser pulses. When the pulse energy rises, the maximum temperature achieved at the laser focal point also rises, while the spatial heat distribution remains constant.

When $\frac{1}{f} < 2\,\tau_{th}$, the width of the temperature distribution profile increases. This results in a temperature profile leading to the observed spatial widening of laser-textured tracks.

If we take the case of an initial distribution due to a single pulse coming from a Gaussian beam of size w_{NL} , the temperature will be diffused out of the voxel in time τ! of the order of

$$\tau_D = \frac{w_{NL}^2}{4D_{th}} \quad \text{I-7}$$

where w_{NL} is the non-linear equivalent waist equal to $\frac{W_0}{\sqrt{N}}$ with N is the number of photons required for absorption and D_{th} is the thermal diffusion coefficient.

The thermal regime is associated to a sufficiently high repetition rate (f_{rep} > 1 MHz) with pulse energy in the nJ regime. It is directly linked to the heat accumulation process. In this process, the subsequent pulses are so close in time that the glass has no time to cool down. Therefore, the cumulative effect of the many-pulse absorption leads to an increase in the temperature and to heat accumulation in the interaction voxel. In a more precise manner, the increase in the temperature also depends on many other experimental conditions such as the voxel size, the thermodynamic properties of the material, the conditions for energy deposition and so on. As a result, a rearrangement of the glass matrix will occur in the interaction voxel. Finally, the induced material modifications present a symmetrical geometry as a result of the heat diffusion from the interaction voxel to the surrounding glass, and their volume is dependent on the heat-affected zone, which is inevitably larger than the size of the focused laser beam. Normally, such symmetrical geometry is more complex when the thermodynamic properties vary with temperature or when we move the beam at constant velocity.

While the athermal regime is associated to low repetition rate f_{rep} < 250 kHz with low pulse energy in the µJ range. In this case, the regime remains non-cumulative for pulse energies since the pulses are widely spaced so the glass has the time to cool down and the temperature does not build up. The time between two consecutive pulses is long enough to allow for the diffusion of the heat accumulated during the pulse absorption out of the interaction voxel. It is crucial to emphasize that a non-cumulative regime doesn't automatically imply athermal conditions, as the temperature can exceed the glass transition temperature (T_g) even for a single pulse. In 2019, Abou Khalil *et al*. demonstrated that even with irradiation at 10 MHz, the irradiation regime corresponds to a athermal accumulation regime with almost no pulse-to-pulse temperature increase (limited to a few tens of degrees) because of the very low energy deposition per pulse: in laser irradiation in such photosensitive glasses, the high repetition rate irradiation behaves as an athermal regime with minor temperature increase so that the glass stood far below the glass transition temperature [45].

Many researchers have conducted studies concerning the heating process following the interaction of femtosecond laser with glasses [46], [47]. Eaton and Zhang have proposed a numerical model concerning the heat accumulation effects for different repetition rates in a borosilicate glass (Schott, AF45) [48]. Figure I-11 depicts the results for the three repetition rates values taken into consideration of 100 kHz, 500 kHz and 1 MHz. The horizontal dashed black line represents the glass's annealing temperature. This temperature marks the point at

which the glass begins to melt and undergo structural changes.

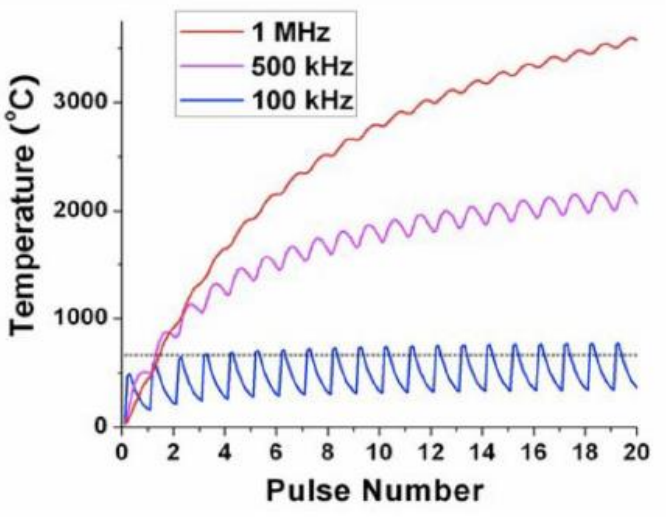

Figure I-11: Numerical simulations illustrating the accumulation of heat within glass following laser irradiation of consecutive laser pulses at different repetition rates: 100 kHz, 500 kHz, and 1 MHz, with an absorbed laser energy of 201 nJ. Taken from [48].

In the case of the 100 kHz repetition rate, the overall temperature stays below the simulated melting point of the glass: it increases roughly above the annealing temperature after the first pulse and decreases well below this temperature before the next pulse. Heat accumulation starts to occur for the 500 kHz and 1 MHz repetition rate: the temperature rises exhibiting a steeper slope with higher repetition rates. As already explained, after the first pulse, the glass temperature increases above the annealing temperature, while the second pulse arrives quickly so that the glass does not have time to cool down and the temperature continues to build up.

I.4.4.Femtosecond laser pulse propagation

I.4.4.a.Focused Gaussian beam

Generally, most of the output laser modes are TEM_{00} Gaussian modes, which is the case also in this work. A Gaussian beam is a solution of the Paraxial Wave Equation:

$$\frac{\partial^2 u}{\partial x} + \frac{\partial^2 u}{\partial y^2} - 2ik\frac{\partial u}{\partial z} = 0 \qquad \text{I-8}$$

where u is a complex scalar wave amplitude describing the transverse profile of a beam propagating along the z axis. Equation I-9 is an approximation of the scalar Helmholtz wave equation:

$$[\nabla^2 + k^2]E(x,y,z) = 0 \qquad \text{I-9}$$

and it is used for describing the propagation of an electromagnetic field $E(x,y,z) = u(x,y,z)e^{ikz}$ whose transversal variation $u(x,y,z)$ along the propagation direction z is slow compared to the plane wave e^{ikz} variation in the z direction.

Figure I-12 presents the intensity distribution of a simple Gaussian beam at the waist position, given by:

$$I = I_0 e^{-\frac{2r^2}{w_0^2}} \quad \text{I-10}$$

where I_0 is the maximum intensity, w_0 is the beam waist at 13.6% of the intensity maximum, and where the diameter $2w_0$ contains 86.5% of the beam energy.

In general, the Gaussian beam is characterized by the intensity profile, the beam waist, the Rayleigh length, the depth of focus, the beam divergence, and the beam wavefront curvature. For a reference plane typically set at $z = 0$, it is characterized by a spot size radius known as the beam waist located at the position of propagation corresponding to its minimum dimension. In addition, it exhibits a planar wavefront with an infinite radius of curvature $R_0 = \infty$. For a distance $\pm z$ from the beam waist, the beam propagates in a non-collinear way.

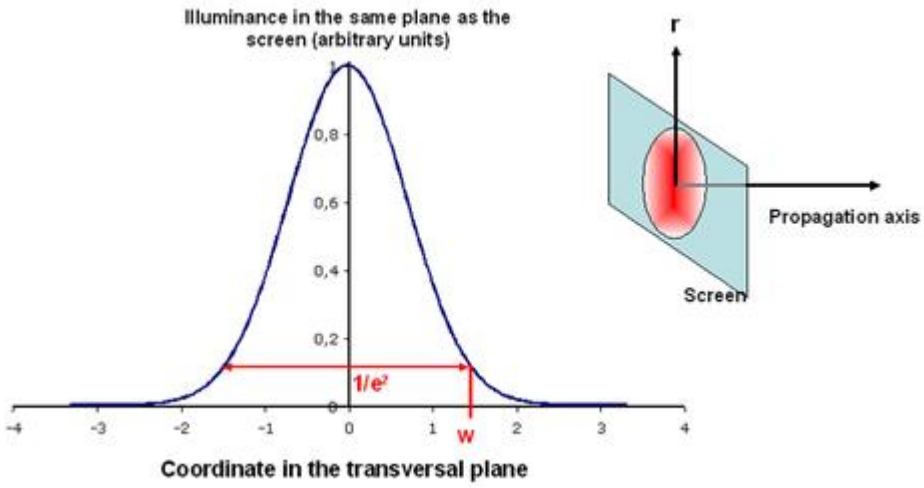

Figure I-12:Intensity profile distribution of a Gaussian beam as a function of r. Taken from [49].

Figure I-13 illustrates the progression of the Gaussian beam along the z-axis as it diverges from its waist.

Its following parameters are described as follows:

$$w(z) = w_0 \sqrt{1 + \left(\frac{z}{z_R}\right)^2} \quad \text{I-11}$$

$$R(z) = z + \frac{z_R^2}{z} \quad \text{I-12}$$

$$\theta_0 = \frac{\lambda}{\pi w_0} \quad \text{I-13}$$

$$w_0 = \sqrt{\frac{\lambda z_R}{\pi}} \quad \text{I-14}$$

$$b = 2z_R = 2\frac{\pi w_0^2}{\lambda} \qquad \text{I-15}$$

where z_R is the Rayleigh range defining the distance along z for which the width w of the beam is $w = \sqrt{2}w_0$, θ_0 is the beam divergence, b is the depth of focus, λ is the wavelength of the beam and z is the position along the propagating z-axis. Generally, the beam quality factor M^2 is considered to be ≥ 1. It is a parameter used to quantify the quality of a laser beam's spatial profile and how closely it resembles the fundamental Gaussian beam mode. It provides information about divergence as it limits the degree to which the laser beam can be focused for a given beam divergence angle. Also, it indicats the focusing characteristics of the beam as it propagates. In this work, the laser beams exhibit a quality factor $M^2 \sim 1$.

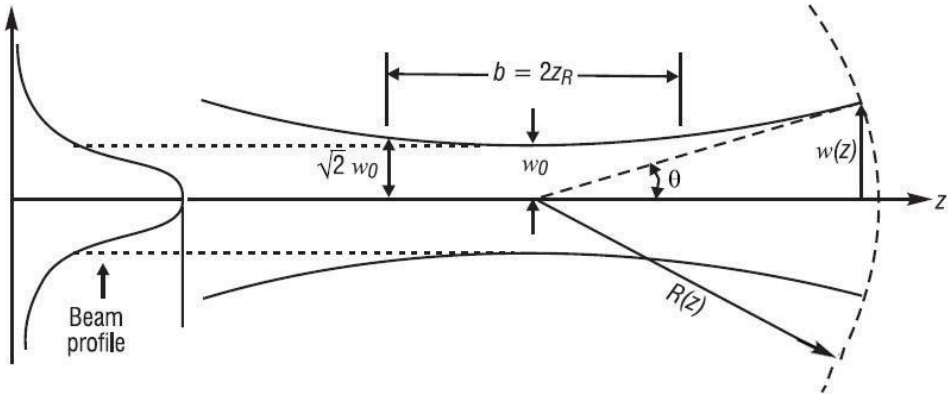

Figure I-13 : Schematic presentation depicting the divergence of the Gaussian Beam as it moves away from the waist. Taken from [www.s-laser.com]

- Strong laser-beam focusing with an objective lens

When a Gaussian beam is focused using a microscope objective with a given numerical aperture (NA), it is therefore possible to determine its size at the focus plane and the area of the irradiated zone. The Rayleigh criterion allows to measure its dimension.

For a NA <0.7, the beam waist at the focus plane is given by:

$$w_0 = 0.581\frac{\lambda_0}{NA} \qquad \text{I-16}$$

While for higher NA>0.7, it is given by:

$$w_0 = 0.61\frac{\lambda_0}{NA} \qquad \text{I-17}$$

where λ_0 is the wavelength in the free space and NA the numerical aperture of the focusing objective [50].

Focusing using a high numerical aperture for achieving dimensions on the order of lambda poses technological and optical complexities. Consequently, Equation I-17 serves as an approximate representation. Additionally, optical objectives are fine-tuned to minimize aberrations under particular conditions, typically at a specified distance from the surface

(often around 170 µm) with a specific refractive index for the sample and a given wavelength. Beyond these manufacturer specifications, the beam size considerably diverges from the standard Equation I-17. Finally, having a numerical aperture greater than 0.7 restricts the Rayleigh zone, reducing the cumulative impact of spatial nonlinear phenomena like auto-focusing and Kerr effects. This strong focusing thus simplifies the interaction.
When using a microscope objective with high NA, a higher angle of light is captured which means that it is possible to obtain better optical resolution. So, one can conclude that using a higher NA objective *i.e.*, focusing the beam tighter, leads to the creation of smaller structures and vice versa.

I.4.4.b.Focused Gaussian-Bessel Beam

The Gaussian beam, when strongly focused, encounters a limitation with its notably short Rayleigh length. Nevertheless, there is a category of beams called Gaussian-Bessel beams that can maintain strong focus while extending the Rayleigh region. Bessel beams, initially introduced by Durnin *et al.* in 1987 [51], belong to a unique category of laser beams and have been widely employed in applications related to both optics [52], [53] and acoustics [54], [55]. These beams are characterized by a slight and brilliantly illuminated central core, which is encircled by a sequence of concentric rings (see Figure I-14(a-c)). In an ideal scenario, these rings would extend over an infinitely long distance which is why they are often referred to as "diffraction-free". Gaussian-Bessel beam modes are characterized by an integer n, known as the order of the beam. The propagation of a Bessel beam along the *z*-direction can be understood as the combination of infinite plane waves. These plane waves have wave vectors that are distributed in a cone-like pattern centered around the z-axis. The angle that characterizes the spread of these wave vectors, often referred to as the conical half-angle θ, as shown in Figure I-14(b), can be mathematically expressed as follows:

$$\theta = tan^{-1}(\frac{k_r}{k_z}) \qquad \text{I-18}$$

where k_r and k_z are transverse and longitudinal wave vectors related to k through $k = \sqrt{k_r^2 + k_z^2}$ and they are expressed as follows: $k_r = k\ \sin\theta$ and $k_z = k\cos\theta$ with $k = \frac{2\pi}{\lambda}$.

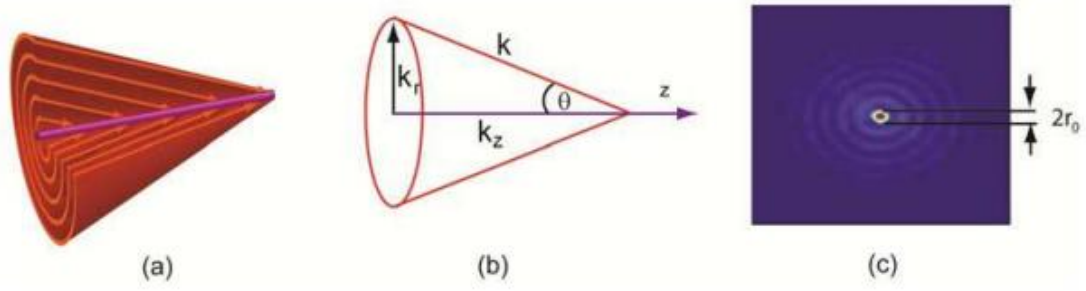

Figure I-14: Schematic representation showing Gaussian-Bessel beam characteristics. (a) The conical flow of energy inwards towards the central lobe of the beam. (b) Demonstration of the relationship between the wave vectors that form a non-diffracting Bessel beam. (c) The

transverse intensity profile of the Bessel beam revealing the central core size of the Bessel beam, represented as $2r_0$. Taken from [56].

When employing a finite energy approximation, researchers have successfully generated Bessel beams over finite distances in experimental settings. The pioneering work by Durnin *et al*.[51] marked the first demonstration of Gaussian-Bessel beam generation through experiments. Their method involved placing an annular slit at the back focal plane of a converging lens and illuminating it with a plane wave. While this technique is very simple, it does have some limitations and drawbacks. Numerous alternative methods for generating Bessel beams have also been successfully demonstrated. For instance, Bessel beams have been generated utilizing axicon lenses [57], [58], spatial light modulators [59], [60], diffractive optical elements [61], [62], [63], and optical fibers [64],[65]. The shaping technique consists in applying a spatial phase onto a Gaussian beam, creating what is called a Gaussian-Bessel beam [66].

Usually, laser beams have a Gaussian-shaped profile. However, when one focuses a Gaussian beam through an optical lens, the beam undergoes a transformation forming an ellipsoidal three-dimensional focus with a depth of focus $Z_g = 2 \times z_R$, and a beam diameter $2w_g$ at e^{-2} of the maximal intensity, as seen in Figure I-15(a). This transformation occurs by changing the initially flat plane waves into a curved wavefront. The focus of a Gaussian beam is characterized by its lateral spot size and confocal length. On the other hand, the perfect Bessel beam is created by a converging conical wavefront that extends infinitely, using an axicon lens, which is the context in this work. When this conical wavefront converges precisely onto the axis of symmetry and interacts with itself, it generates the distinctive shape of a Gaussian-Bessel beam, as depicted in Figure I-15(b). As the wavefronts converge at the conical intersection while passing through the axicon lens, they give rise to an interference pattern. The axicon consists of a conical wavefront, and its interaction with the laser beam leads to the creation of a focus that resembles a line shape. This focus, characteristic of a Gaussian-Bessel beam, includes a high intensity central lobe surrounded by a series of low intensity concentric lobes. The thickness of the inner ring remains constant and is comparable to the radius of the incident beam. The Gaussian-Bessel beam is defined by its half-conical angle θ, its depth of focus (Bessel length) Z_b, and the diameter of the central core $2w_b$ at e^{-2} of the maximal intensity. In contrast to the conventional Gaussian beam produced by a focusing lens, the Gaussian-Bessel beam provides a notably longer depth of focus. Typically, this depth of focus is approximately one order of magnitude greater than that of the Gaussian counterpart, even when the beam diameter is similar (approximately $2\omega_g \sim 2\omega_b$). A deeper detailed explanation of the generation of a Gaussian-Bessel beam using an axicon lens will be presented later in Chapter IV (Section IV.5.2 and IV.7.2).

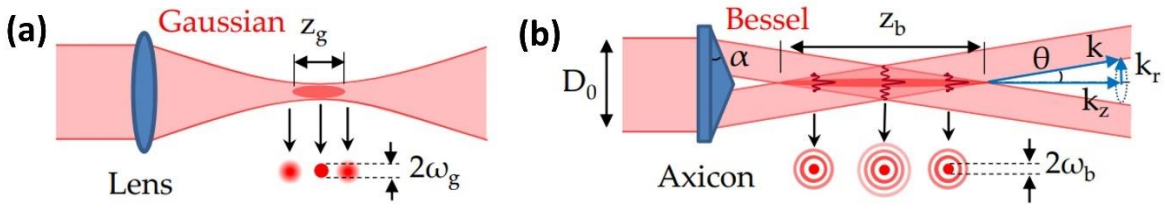

Figure I-15: Schematic illustration of (a) the Gaussian beam focused by a converging lens and (b) the non-diffractive Bessel beam generated by an axicon. Taken from [67].

In a Gaussian beam setup, achieving an extended depth of focus would require the use of lenses with long focal lengths and incident beams with small beam diameters. This traditional setup has inherent limitations and results in an undesired consequence: the focused beam ends up having a large beam diameter. Consequently, this limitation restricts its applicability when working with objects that have small features. In contrast, the Gaussian-Bessel beam configuration offers an ideal solution. It provides a beam with a long depth of focus while simultaneously maintaining a small beam diameter. This characteristic makes it well suited for applications that require precise processing of objects with small-scale features.

I.5.Conclusion

Laser-matter interaction is a broad and versatile field with applications spanning from materials processing to cutting-edge scientific research and technology development. It continues to drive innovations in various industries and scientific disciplines. This chapter places its focus on underlying the concepts of the phenomena that arise in laser-matter interactions.

The initial part of the chapter provides a definition of glass, along with an explanation of the glass transition phenomenon and the process leading to its formation. In addition, the two techniques used for producing glasses used in this manuscript are discussed. Also, the optical window transparency of glasses in different wavelengths and its refractive index change are some of the optical properties highlighted in this chapter. The second part focuses on the ultrafast laser-glass interaction processes. The nonlinear absorption mechanism phenomena are presented in detail as well as the different timeline of physical processes following such interaction. It was also shown that laser parameters play an important role on the glass responses and presents two inscription regimes based on the heat accumulation process that were classified as athermal and thermal regimes. Consequently, femtosecond laser interaction enables material modifications which will be discussed in the next chapter. The final part of this chapter presents a short focus on the basic notions related to femtosecond beam engineering and delivering for the Gaussian and Gaussian-Bessel beam, which are

important for understanding Chapter IV.

II Direct Laser Writing in glasses

This chapter will delve into the processes involved in Direct Laser Writing (DLW) of glasses using a femtosecond laser source, and especially in silver-containing phosphate glasses.

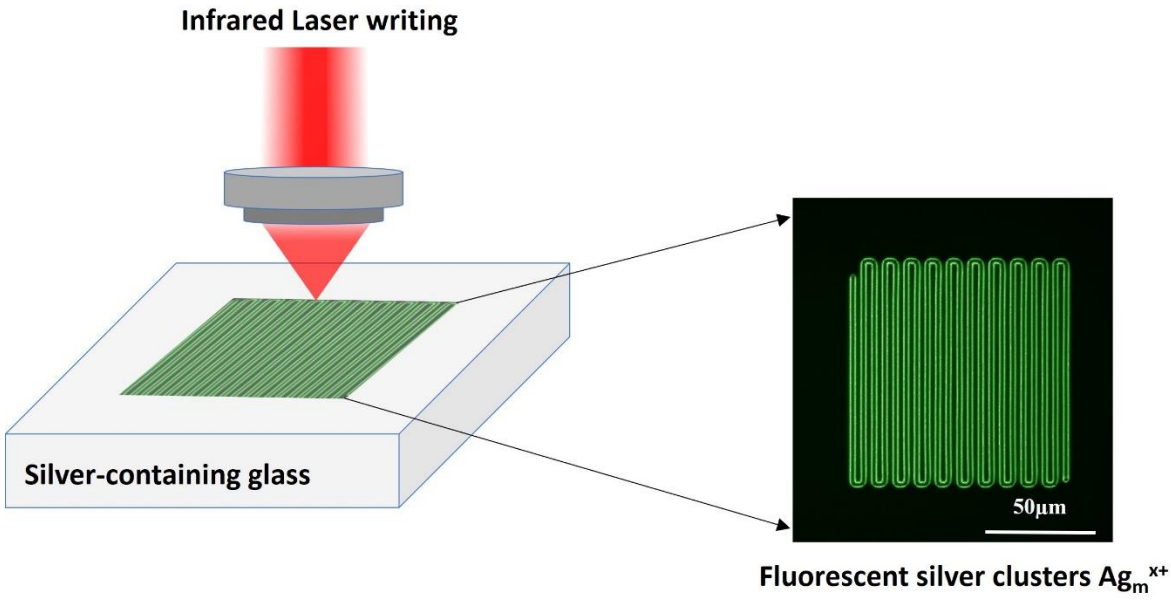

II.1.Introduction

Ultrafast lasers, characterized by their incredibly short pulse durations, have revolutionized various fields of science and technology over the past few decades. One of the most significant areas where ultrafast lasers have made a profound impact is in materials processing. Direct Laser Writing is a versatile and precise micro-fabrication technique that uses a focused laser beam to create three-dimensional multi-scale structures or patterns with high spatial resolution. The key feature that sets ultrafast lasers apart is their ability to deposit energy in extremely short time frames, enabling localized and controlled material transformations with minimal thermal damage to the surrounding regions. This technique is commonly used in various fields, including microelectronics, photonics, or microfluidics, and it bears an intrinsic high potential for industrial transfer and advanced all-optical manufacturing.

The first part of this chapter provides an overview of the direct laser writing technique and discusses the three distinct types of refractive index change that can result in materials. The second part delves into silver-containing phosphate glasses, initially focusing on the optical properties of pristine glasses. The third part explores the unique response of silver-containing glasses to femtosecond laser pulses. This section covers the complex processes involving multi-physics and multi-scale phenomena during the interaction of femtosecond lasers with these glasses. Notably, this interaction leads to the photo-activation of silver-based chemistry at the root of the generation of new molecular species such as fluorescent silver clusters near the interaction voxel, resulting in a novel refractive index change referred to as Type-A, after *Argentum*. This section also presents key properties of the photo-induced silver clusters and showcases various integrated photonic devices in silver-containing glasses, based on Type-A modifications. These devices include waveguides, couplers, splitters, refractive index sensors or integrated Bragg gratings, etc.

II.2.General background on Direct Laser Writing

This section provides an introductory overview of the direct laser writing technique and delves into the distinct types of refractive index changes Δn it can induce.

II.2.1.Principle of DLW

Focused femtosecond laser pulses and carrying energies in the range of a few hundred nanojoules, have emerged as a pivotal tool for locally altering the physical characteristics of glass in a three-dimensional (3D) manner. This effective and resilient method, well known as direct laser writing, has experienced significant growth over the past two decades. Due to the

nonlinear interaction, the energy delivered by a focused femtosecond pulse is restricted to the focal volume, leading to sub-micrometer spatial resolution for localized structuring. This breakthrough has opened new possibilities for developing integrated and compact optical micro-systems directly within transparent materials, whether they are in bulk form or fiber-based [68], [69]. DLW consists of simply moving the sample, placed on a 3D translation stage, through the focus of the femtosecond laser beam using a microscope objective Figure II-1.The material surrounding the focal volume experiences minimal impact from the passing writing beam, enabling structures to be created at various depths and in a three-dimensional manner. As demonstrated by Davis *et al*. in 1996, focused fs IR laser-matter enables the creation of permanent and localized modifications inside glass materials [60].

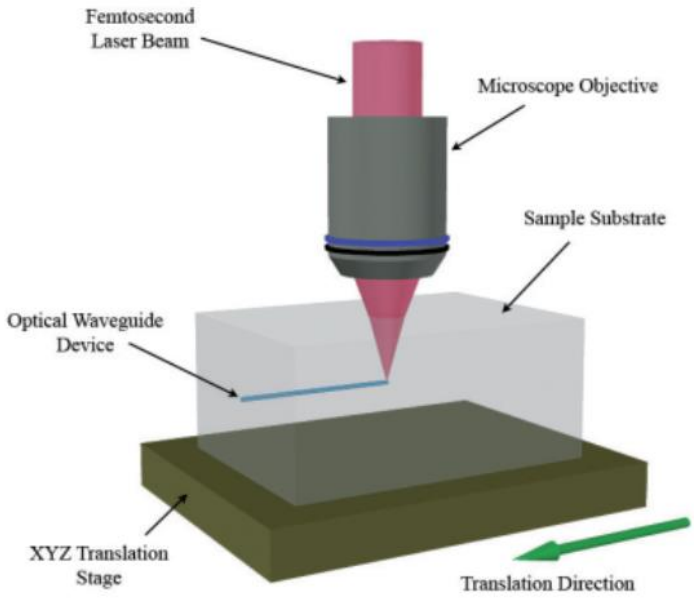

Figure II-1: Schematic presentation of the femtosecond laser writing process in a transparent glass medium. Taken from [71].

The micro-lithography processes consisting of layer-by-layer depositions often involve multiple steps and encounter challenges when producing complex structures. In contrast to it, the direct laser writing method enables the integration of desired functionalities into the material in a single step, and allows for inscribing free-form buried optical structures in transparent dielectric materials [72], showcasing distinct benefits in cost effectiveness, versatility and repeatability within the industrial context. In addition, this technique has been a growing research due to its simplicity and flexibility to directly address 3D material structuring and associated optical properties in a wide range of materials, such as crystals [73], [74], polymers [75], [76] and mostly glasses [30], [77]–[81]. Femtosecond laser-induced photochemistry was reported in a large variety of glass matrices, including silicates [82], [83], aluminosilicates [84], [85], aluminoborates [86], borates [87], fluorides [88],

chalcogenides [89], phosphates [90], and germanates [91], as well as composite plasmonic metal/dielectric media [92], [93]. The creation of 3D integrated photonic structures within a transparent glass substrate offers distinct opportunities for applications across various fields: opto-fluidic [94], sensing [95], [96], optical communication [71], astro-photonics [97], quantum photonics [98], and optical data storage [99], [100]. Indeed, this technique has already been used to fabricate waveguides [60], [101], [102], power splitters [103], couplers [104], [105], gratings [106], [107], computer-generated holograms [108] and optical storage devices [109], [110].

This remarkable feature positions DLW as a promising candidate for potential adoption in advanced industrial manufacturing processes, in addition to its capabilities to be expanded from 3D [30] to five-dimensional (5D) applications [100], [111], [112].

II.2.2.Photo-induced modifications

As already mentioned, the initial report on the induced local modifications in silica glass by focusing a femtosecond Ti-Sapphire laser operating at 810 nm was made by Davis *et al*. in 1996 [60]. Normally, the refractive index change results from the nonlinear absorption of the femtosecond laser pulses as previously explained in chapter I (section I.4.1).

The morphological changes observed can typically be categorized into three main types of structural alterations: a smooth refractive index change [86], a birefringent refractive index modification [113], [114], and the formation of micro-explosions resulting in empty voids [115]. The specific modification regime and resultant morphological changes depend on a multitude of exposure parameters, including energy, pulse duration, repetition rate, wavelength, polarization, focal length, scan speed, and others. Material properties such as band gap and thermal conductivity also play a crucial role in determining these outcomes.

- **Type-I.** Generally, Type-I modifications are smooth, uniform and isotropic changes of the material density and thus of its refractive index allowing the formation of waveguides for optical circuit applications [90], [116]–[118]. Such change is associated to the formation of color centers [119]–[121] and/or the change in the glass density [122]–[124]. In this case, numerous parameters are influential in determining both the sign (positive or negative) and the magnitude of the refractive index modification in the glass. These parameters range from laser inscription parameters to the composition of the glass itself.
- **Type-II.** Sudrie *et al.* were the first to report that when higher pulse energies are used, birefringent refractive index changes can be observed within the bulk of fused silica glass, associated to Type-II modifications [125]. Such type of modifications is related to the formation of birefringent periodic nanostructures [126] and to self-organized nano-gratings due to the production of local moderate plasma [113], [127], [128]. This effect can be exploited to fabricate

buried micro-channels for micro-fluidic applications [129]–[131], or to enhance chemical etching selectivity for substrative manufacturing [131].

- **Type-III.** When the pulse energy is further increased, it results in Type-III modifications that manifest as voids or disorganized damage features within the glass matrix. This occurs due to excessive plasma production and the subsequent Coulomb explosion. These effects are generally exploited to the fabrication of photonic devices, for 3D memory storage [132] or photonic band gap materials [133], but are not suitable for optical waveguides.

Figure II-2 presents a chart illustrating the evolution of various refractive index changes in direct laser writing for a silica glass. The modification process is presented in four different regions, depending on two main factors: the pulse energy and the numerical aperture of the microscope objective used to focus the femtosecond laser. This classification can potentially be applied to all types of glasses, with adjustments made to the modification thresholds and the energy range for each region (region I, II, III, or IV) based on the specific glass's band gap and photosensitivity characteristics. The red horizontal line marks the self-focusing threshold specific to silica, which signifies the critical optical power level that can result in damage. Additionally, it's worth noting that the magnitude of the induced refractive index change diminishes as the writing speed, or the sample's translation speed, increases. Conversely, it increases with higher pulse energy. This is presented in reference [111].

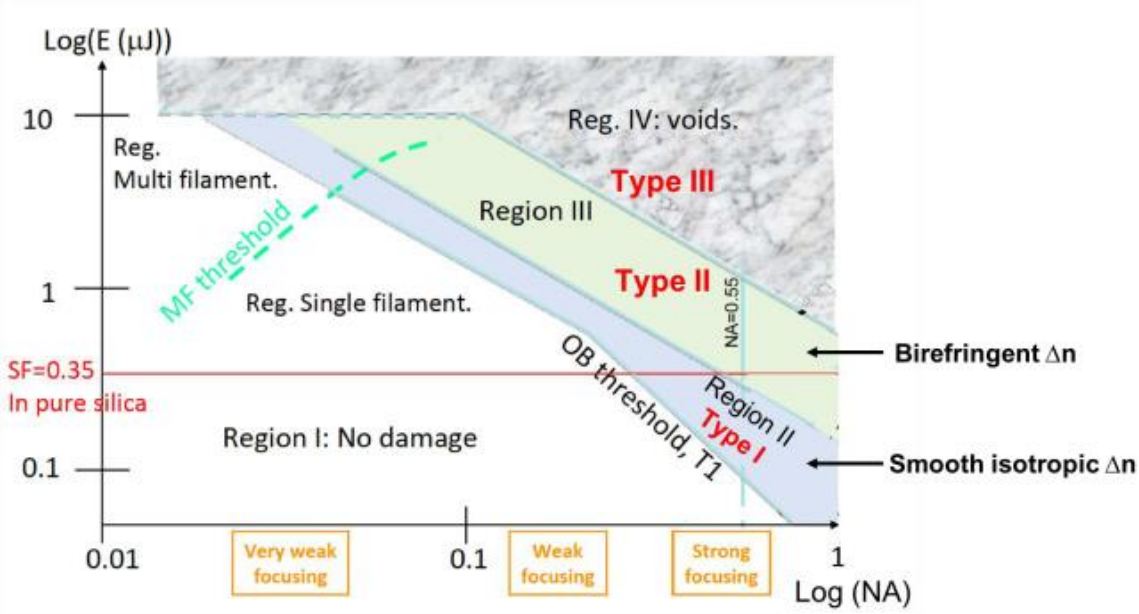

Figure II-2: Illustration of the evolution for the different types of refractive index modifications in fused silica, depending on the pulse energy and the numerical aperture of the microscope objective. Adapted from [134]. Such an illustration shall partially differ with respect to the laser repetition rate.

II.3.DLW in silver-containing glasses

DLW has been conducted in different types of glasses during the past decades. This section focuses on the advantages of choosing photosensitized glasses, namely silver-containing glasses, both for their initial optical properties and the induced optical characteristics. The selection of such material is made due to its numerous advantages over other types of glasses, which will be elaborated in the next section.

II.3.1.Choice of material

Phosphate glasses offer numerous advantages over other types of glasses, as discussed in references [41], [135]. Notably, the glass matrix can effectively accommodate significant quantities of rare earth elements and metals, which in turn helps reduce photo-darkening [136]. However, it's important to note that phosphate glasses have a relatively low resistance to water corrosion, primarily due to the pentavalent nature of the phosphorus atom. To mitigate this vulnerability, an oxide modifier can be introduced to enhance their resistance to water corrosion. The addition of modifiers, such as SiO_2, TiO_2, Nb_2O_5, Al_2O_3, Fe_2O_3, PbO, ZnO, improves the chemical durability by limiting the influence of water. Nevertheless, most of these elements are also photosensitive with individual spectral ranges that overlap those of silver. The choice was therefore made to select zinc oxide, whose photosensitivity is low, to simplify the understanding of laser-glass interactions by limiting the interacting elements. Furthermore, the addition of oxides like Al_2O_3 or Ga_2O_3 significantly enhances the chemical durability of these glass networks, particularly in terms of their resistance to water etching and solubility. Moreover, the phosphate glass family possesses a wide range of attractive properties. Depending on their specific composition, they exhibit excellent chemical durability, outstanding optical characteristics, ion exchange capability, and the ability to be drawn into optical fibers [136], [137]. Additionally, they are well known for their capacity to hold relatively high concentrations of photosensitive agents like silver. The incorporation of silver oxide (Ag_2O) in the phosphate glass matrix serves as a photosensitive support for direct laser writing. Silver, along with copper and gold, possesses an electronic structure characterized by a d^{10} valence layer. This unique electronic configuration makes their luminescent properties highly dependent on their surrounding environment and pairing. Therefore, gold, copper, and silver are considered promising candidates for photosensitization. However, incorporating gold into glasses at high concentrations is challenging as it easily precipitates, which prevents the formation of well dispersed gold elements and highly homogeneous glasses. Besides, copper tends to dismutate from Cu^+ into Cu^0 and Cu^{2+}. When introduced into glass, such instability prevents preparing the glass with a well-defined degree of oxidation. Indeed, only Cu^+ exhibits luminescence while Cu^{2+} has a broad absorption band covering the visible spectrum, leading to self-absorption phenomena.

Given these considerations, silver has been selected as the preferred photosensitive agent. A phosphate type glass material has been chosen, as opposed to silicate glasses, because phosphate glasses are known for their ability to harbor high concentrations of silver ions [138].

Concerning the matrix and taking again the classification explained above, the phosphate oxide (P_2O_5) are the formative oxides. They are oxides whose unit is the tetrahedron $(PO_4)^{3-}$. They form the vitreous network by forming more or fewer bonds with other phosphate tetrahedra. Depending on the [O]/[P], Oxygen-to-Phosphorus ratio, the phosphate chain length can be described as a sequence of phosphorus tetrahedra of four different kinds [139]. Therefore, different families of phosphate glasses can be categorized depending on the [O]/[P] ratio, as the following:

- **Ultra-phosphates:** long phosphate chains and a glass matrix having a reticular structure (three-dimensional highly polymerized structure), for which [O]/[P] < 3.
- **Poly-phosphates**: long one-dimensional chains without interconnections, for which [O]/[P] > 3.
- **Meta-phosphates:** a specific class of polyphosphates where the theoretical chain length is infinite ([O]/[P] = 3).
- **Pyro-phosphates:** these glasses are primarily composed of dimeric phosphate entities (3.25 < [O]/[P] < 3.75).
- **Ortho-phosphates:** a majority of monomeric phosphate entities interacting through the mediation of another network-forming entity [140] ([O]/[P] > 3.75).

To define them, the phosphate tetrahedron is expressed as a Q^n unit [139], [140] where *n* denotes the number of bridging oxygen between phosphorus elements and Q the PO_4 tetrahedron. The poly-phosphate glass exhibits long chains of Q^2 entities ending with a minor amount of Q^1 structures while pyro- and ortho-phosphate exhibit a majority of Q^1 paired and Q^0 isolated PO^4 tetrahedra, respectively.

The experiments detailed in this manuscript primarily employ two types of phosphate glasses:

- Zinc-phosphate glasses, where a small percentage of Ga_2O_3 oxide is added to the PZn glass matrix to enhance its chemical durability [13], [141], [142].
- Sodium-gallium phosphate glasses, where the glass matrix belongs to the ternary diagram of gallium, sodium and phosphorous elements, which is composed of sodium metaphosphate ($NaPO_3$) with Ga_2O_3 oxide added in higher percentages compared to those used in zinc-phosphate glasses [13].

II.3.2.Optical properties of pristine silver-containing glasses

Silver-containing phosphate glasses exhibit a transparency window from the UV range to the Mid-Infrared (MIR) being typically limited by hydroxyl groups around the 2.9 µm range. Indeed, phosphate glasses exhibit a characteristic absorption spectrum, as illustrated in Figure II-3 for both the zinc-phosphate glass (PZG) and sodium-gallium-phosphate (GPN) glass families. In particular, in Figure II-3(a), the absorption spectra of the PZG samples are compared with and without the addition of silver, for composition $40P_2O_5$-55ZnO-(5-x)Ag_2O-xGa_2O_3 (% molar oxides) where x = 0, 1, 2, 3, 4, 5 [141].

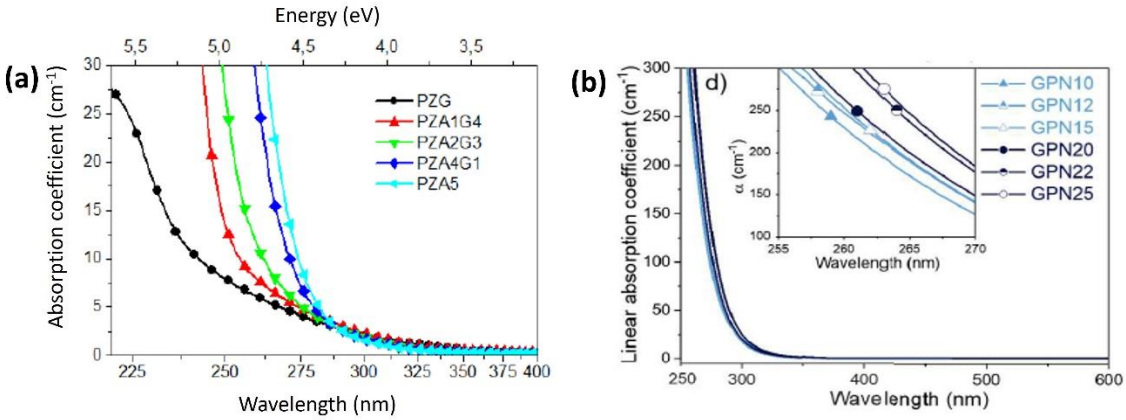

Figure II-3: Absorption spectra in UV-Visible range of (a) zinc-phosphate glasses (PZG) containing and non-containing silver ions (Image from [141]), and of (b) silver-containing sodium-gallium phosphate glasses (GPN) (Image from [13]).

Figure II-3(a) for the PZG glass, the spectrum exhibits two distinct bands: one at approximately 225 nm and another around 250 nm. These absorption features are associated with the existence of defects and impurities within the glass. The 225 nm band might be attributed to the presence of electron centers, such as electrons trapped within phosphate groups, which form during the glass tempering process [143]. The 250 nm band exhibits a similar behavior and, in this instance, is likely due to the presence of Fe^{3+} ions [144].

However, when silver ions are introduced in the phosphate matrix, substantial absorption bands emerge in the UV) range, shifting the UV cut-off of the silver-containing material towards longer wavelengths. As the concentration of silver increases, this UV transmission threshold gradually keeps on shifting towards lower energies, corresponding to longer wavelengths. Such silver-induced shift of the material band gap to lower energy levels further contributes to allowing for the laser-activation photochemistry of silver species under IR femtosecond laser exposure [141].

In PZG glasses without silver, no luminescence is detected whatever the excitation conditions. Therefore, it is reasonable to attribute any detected emission in glasses that contain silver oxides exclusively to the presence of silver. Two broadband luminescence

emissions have been identified within the glass matrix following the insertion of Ag_2O in the glass composition [141]:

- The first one is at high energy (excitation centered around 220 nm, emission at 290 nm) with a relatively short lifetime (τ = 14 µs), observed for the lowest silver concentrations, corresponding to the isolated Ag^+ ions.
- The second one is at lower energy (excitation at 260 nm, emission at 380 nm) exhibiting a longer lifetime (τ = 35 µs) as the silver concentration increases, associated with the transition $4d^{10} \leftrightarrow 4d^9\ 5s^1$ of the Ag^+ ion.

Thus, this second band can be shifted by changing the molar percentage of silver, or by adding different substitution oxides such as SiO_2 or Al_2O_3 [145]. This band is linked to the existence of Ag^+-Ag^+ pairs in glasses for a high-enough concentration of silver. These pairs consist of closely positioned Ag^+ ions that exhibit electrostatic interactions but do not form a molecular dimer. Silver environments, whether they belong to isolated Ag^+ ions or to Ag^+-Ag^+ pairs, have been distinctly identified and labeled as site A for low insertion of silver oxide (below 1.5%) and site B for an increasing insertion of silver oxide (above 1.5% up to 8%), respectively, as described in [135]. Figure II-4 reports on the emission and excitation spectra in silver-containing phosphate glasses with different molar percentages of silver and highlights the evolution of the intensity of the site A versus site B. For λ_{exc} = 230 nm, two emission bands can be distinguished with the maxima centered at 290 nm and 370 nm (Figure II-4(b)). By increasing the Ag^+ concentration, the relative intensity of the 290 nm band vanishes compared to the emission at 370 nm. When the excitation wavelength is raised up to 280 nm typically, the emission band near 370 nm is favored, which indicates the presence of different emitting centers (site B) (Figure II-4(D)). This differentiation in pristine silver-containing glasses is significant because it notably influences photosensitivity under femtosecond laser irradiation as it involves different orders on nonlinearity for multiphoton energy deposition, on the one hand, and because the concentration of silver elements as well as the involved sites/environments shall play a role on the laser-activated photochemistry of silver elements under fs laser irradiation.

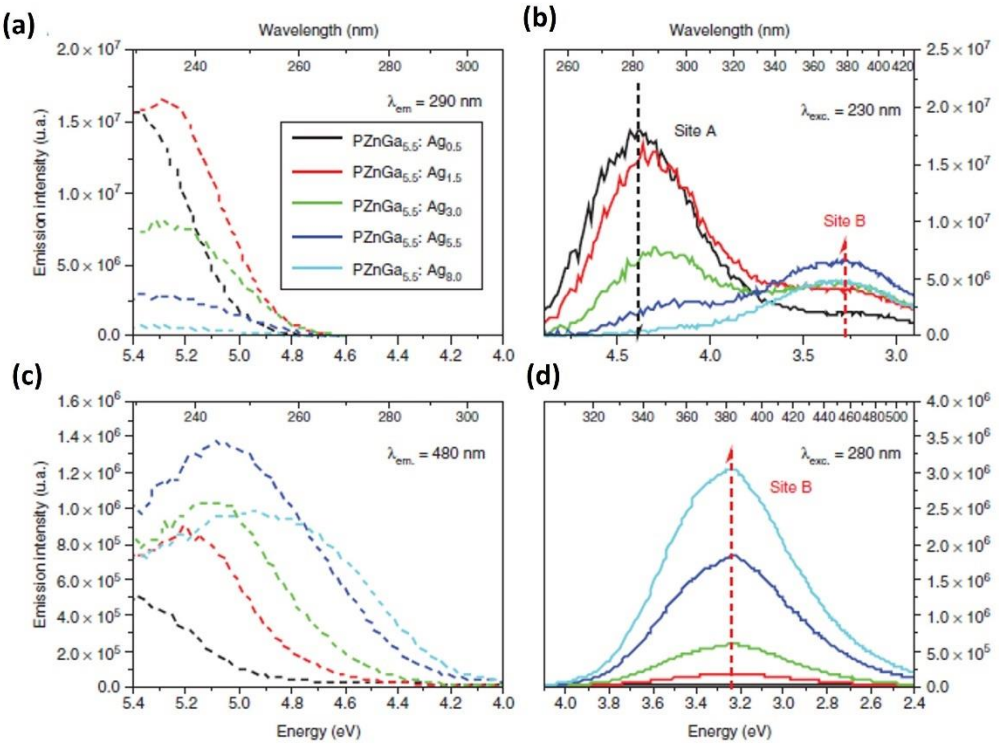

Figure II-4: Photoluminescent characteristics in silver-containing phosphate glasses: (a) excitation graph (for emission=290 nm), (b) emission graph (for excitation=230 nm), (c) excitation graph (for emission=480 nm) and (d) emission graph (for excitation=280 nm. Taken from [135].

It is important to note that the ratio between the concentration of silver ions and silver pairs is influenced by the structure of the glass matrix. As we progress from polyphosphates to pyrophosphates and finally to orthophosphates, the concentration of silver pairs gradually rises relative to the concentration of silver ions [146]. The absorption band between the three glass structures shifts which is significantly due to changes in that ratio: when moving from poly- to pyro-phosphate to ortho-phosphate glasses, a red-shifted absorption band is observed (Figure II-5(a)), which in turn leads to a red-shifted luminescence excitation band compared to that of isolated silver ions (Figure II-5(b)). Therefore, there is a clear correlation between the presence of silver pairing and photosensitivity: orthophosphate glass compositions contain the highest proportion of silver pairing, as well as they exhibit the highest photosensitivity to femtosecond laser writing. It's possible to propose that the four-photon absorption process is favored in this case, thanks to the presence of silver pairing that absorbs between 250 nm and 280 nm [139]. This demonstrates that both the concentration of silver and the structure of the glass matrix are crucial factors in generating silver pairs and, consequently, in customizing material photosensitivity.

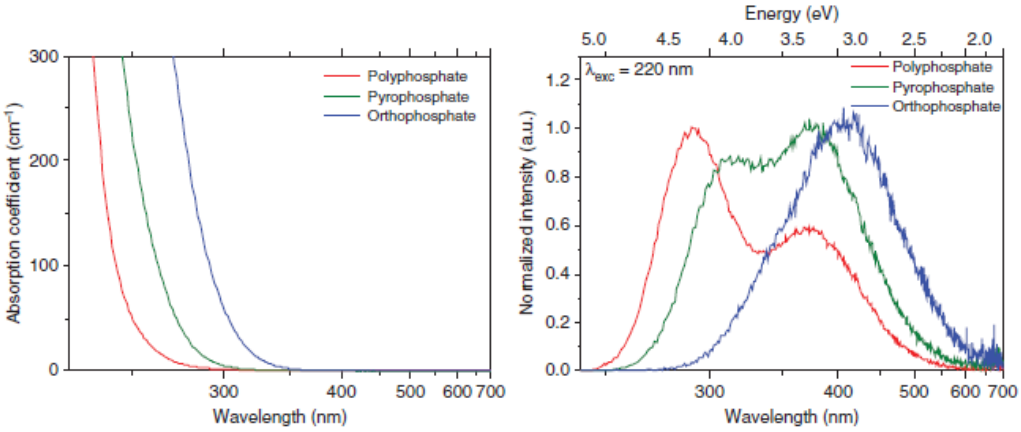

Figure II-5: (a) Absorption and (b) emission spectrum for excitation at 220 nm for the three glass matrices of a silver-containing sodium-gallium-phosphate glasses. Taken from [146].

II.3.3.Laser-silver-containing glasses interaction

This section focuses on the multi-physics response resulting from laser inscription in silver-containing glasses, leading to the formation of silver-based species.

II.3.3.a.Physical mechanism of silver clusters formation

During the laser pulse, a reservoir of free electrons is generated thanks to multiphoton absorption. Figure II-6 illustrates this reservoir corresponding to the radial distribution of these free electrons, depicted as the pink disk when irradiation takes place. These electrons originate from the silver ions (Ag^+) and from the phosphate chains within the glass matrix.

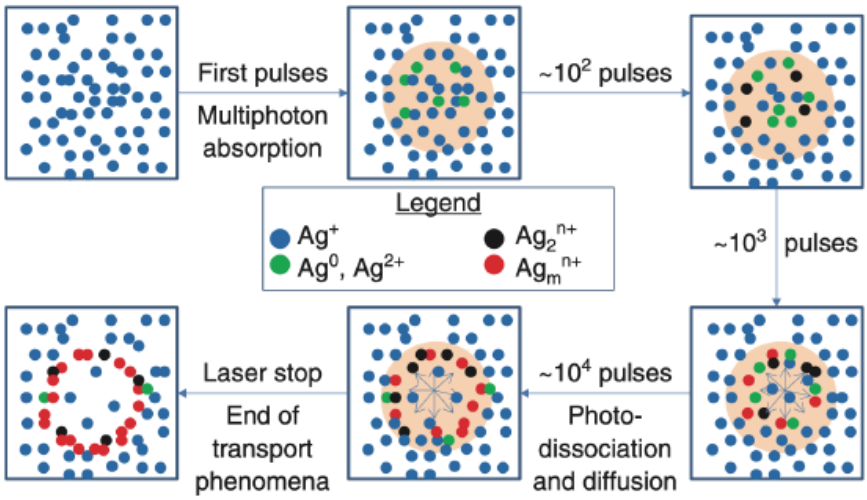

Figure II-6: Schematic representation of the mechanism leading to the formation of silver clusters following a series of fs pulses. Taken from [42].

The formation of silver atoms (Ag^0) starts to occur when the concentration of free electrons reaches its maximum level, as the following:

$$Ag^+ + e^- \rightarrow Ag^0 \qquad \text{II-1}$$

Positively charged holes are produced either directly from the ionization of silver ions (Ag^+) or from the glass matrix itself, such holes getting trapped then by these ions during the Ag^0 formation process. The kinetic reaction is presented as follows:

$$h^+ + Ag^+ \rightarrow Ag^{2+} \qquad \text{II-2}$$

It's important to note that these traps are considered immobile. Ag^{2+} may be seen as a hole trapped in close proximity to a silver ion Ag^+ rather than a doubly ionized silver ion. Hence, the mobility of such pairs is negligible compared to that of silver ions Ag^+, primarily due to their delocalization around the phosphate chains forming the glass network. Additional recombination processes also compete with the charge trapping associated with the formation of Ag^{2+} and Ag^0 species:

$$h^+ + Ag^0 \rightarrow Ag^+ \qquad \text{II-3}$$

$$e^- + Ag^{2+} \rightarrow Ag^+ \qquad \text{II-4}$$

The reaction II-1 ends when the concentration of free electrons diminishes. At this point, the spatial distribution of Ag^0 corresponds to the slightly diffused distribution of pre-existing free electrons, with the diffusion resulting from both the free electron diffusion itself and/or the diffusion of induced Ag^0 species. Simultaneously, the energy deposited by the laser leads to a localized temperature distribution, such distribution being generally limited to a few tens of degrees. The corresponding energy deposition in our glasses is less than 1%. The radial diffusion of Ag^0 species, driven by the temperature distribution and concentration gradient, allows these species to encounter Ag^+ ions and participate in the kinetic reaction:

$$Ag^0 + Ag^+ \rightarrow Ag_2^+ \qquad \text{II-5}$$

This thermal activation occurs even though the induced temperatures remain well below the material's melting temperature and glass transition temperature. The trapping of Ag^0 by the silver ions leads to the first stage of the formation of the clusters Ag_2^+. The reaction II-5 of the first phase of silver cluster formation stops either when the local concentration of Ag^0 precursors diminishes or when their mobility decreases, resulting in fixed Ag^0 species. For the first irradiation pulse, distribution of Ag_2^+ qualitatively corresponds to the slightly diffused distribution of the silver cluster precursors, namely the distribution of Ag^0. Alternatively, a pair of closely neighboring Ag^+ ions (Ag^+-Ag^+) may also easily trap a free electron, directly leading to the formation of Ag_2^+ species through the mechanism:

$$Ag^+ - Ag^+ + e^- \rightarrow Ag_2^+ \qquad \text{II-6}$$

Further growth of larger silver clusters follows similar photo-activated chemical pathways during a given pulse irradiation but mostly under cumulative pulse-after-pulse irradiation. By also introducing a laser-activated mobility of the Ag^+ ions, the production of silver clusters globally results from a series of reactions, corresponding generally to:

$$x\ Ag^+ + y\ Ag^0 \rightarrow Ag_m^{n+} \qquad \text{II-7}$$

with the nuclearity $m = n + y$ [148]. Finally, specific stable Ag_m^{n+} clusters with adapted nuclearities m and associated charges n^+ are created [69], [149]. It's expected that silver clusters Ag_m^{n+} do not exhibit mobility as their diffusion and site hopping are inhibited by stearic issues. Consequently, the net outcome of silver cluster formation after a single laser pulse is the balance between the photodissociation of pre-existing silver clusters and the photo-activated diffusion and chemical reactions of small silver elements (Ag^0 and Ag^+) that create silver clusters. The trapping and reaction processes are so rapid (within a few ps scale) that the concentrations of free electrons, holes, and Ag^0 diminish before the next laser pulse, even in the case of lasers with high repetition rates, typically up to 10 or 80 MHz. These processes described above repeat from pulse to pulse. In the subsequent laser pulse, silver clusters in the center undergo photodissociation where the laser pulse is most intense. The next laser pulse generates a new reservoir of free electrons, triggering kinetic reactions responsible for the formation of silver clusters. This cycle repeats itself from one pulse to another within a material. Taking into account the photodissociation of silver clusters in the high-intensity central part of the laser voxel as well as the pulse-to-pulse progressive radial redistribution of silver elements in various silver species, one observes that non-dissociated silver clusters gradually accumulate on the periphery of the laser beam, forming a ring-shaped structure [37], [150]–[153] following a series of pulses. As a result, the rapid diffusion of free electrons and subsequent stabilization disrupts the initial spatial charge neutrality of the electron-hole plasma within the focal spot, creating an intense and localized ambipolar electric field (estimated up to 10^{8-9} V/m [68]). It is not demonstrated whether such a static buried electric field does contribute or not to accelerate diffusion processes, but the final localization of silver clusters corresponds to areas of lower electrical potential in relationship with such a static electric field [154]. This process results in the formation of a static charge distribution in space and a corresponding radial static electric field [152], as reported in [155], then show a permanent stability as long as temperature remains below the glass transition temperature [68].

II.3.3.b.Characteristics of photo-induced silver clusters

As already explained, photo-induced 3D structures were created due to the nonlinear behavior of the laser writing process for a static inscription of silver-containing glasses [150]. By adjusting the laser dose (fluence, number of pulses, and repetition rate), these stabilized intense fluorescent structures, composed of silver clusters, can be achieved with a perfect control of the luminescence intensity, the emission spectrum, and the spatial distribution at the nanometer scale. The sample's displacement during the laser inscription process thus allows the creation of three-dimensional fluorescent structures that are typically excitable between 270 and 530 nm and possess a broad emission spectrum covering almost the entire visible range. To gain a clearer understanding of the shape of these structures, Figure II-7

reveals their morphology.

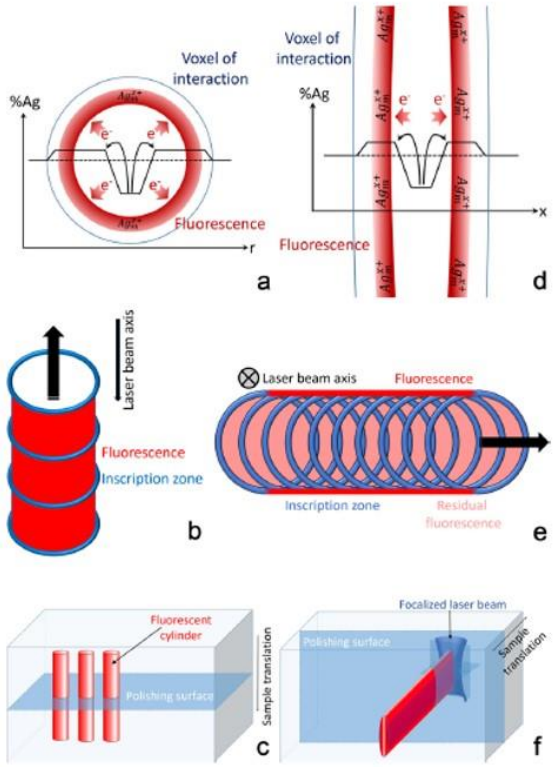

Figure II-7: Schematic representation of laser inscription of silver-based photochemistry and created silver cluster distributions : (a) top view of the diameter, (d) lateral view of the confocal parameter trace of the interaction voxel, along with the localization of fluorescence from molecular silver clusters. Illustration of superposition of inscription zones in the voxel, pulse by pulse, during (b) longitudinal and (e) transverse linear displacements relative to the laser propagation axis, respectively. A diagram of the DLW process for movements (c) along and (f) perpendicular to the laser beam axis, respectively, along with the corresponding induced fluorescent structures brought to the surface after polishing for subsequent studies. Taken from [154].

Figure II-7(a) shows a top view representation of the voxel and illustrates the principle of spatially stabilized fluorescent silver clusters Ag_m^{x+} in a ring shape. This configuration is attributed to the distribution of silver clusters around the interaction voxel and results from the photodissociation of the silver clusters formed at the center, influenced by the transverse Gaussian profile of the laser beam. Figure II-7(d) displays the cross-section of the voxel in a plane parallel to the axis of the laser beam, thus exhibiting two fluorescent lines arranged into a pipe shape along the propagation axis with a length corresponding to the Rayleigh range (Figure II-7(c)). The sample motion during the laser writing process gives access to the formation of 3D fluorescent structures within the glass volume. However, it is necessary to study two distinct motion cases, namely linear displacement parallel to the axis and linear displacement in a direction perpendicular to the axis. Figure II-7(b) illustrates the principle of the superposition of laser pulses deposited successively in the case of parallel displacement. The initial cylindrical surface is translated in the *z*-direction, leading to the inscription of a luminescent tube whose length corresponds to the translation distance of the sample. The

result of three inscribed luminescent tubes is represented in Figure II-7(c). Figure II-7(e) illustrates the superposition of laser pulses for a perpendicular type of displacement. The deposition of fluorescence occurs only along two external walls indicated in red lines in the figure. As a result of this type of translation, double planes are inscribed, as depicted in Figure II-7(f). This photo-induced structuring is dependent on the irradiance, the number of pulses, the laser repetition rate, and the velocity of the glassy sample's movement, as demonstrated by Bellec *et al.* [150]. Consequently, the diameter of the structures increases with irradiance and the locally accumulated number of pulses. Globally speaking, whatever the direction of motion of the sample, the laser inscription process imprints silver cluster distributions around the focus of the nonlinear voxel. As the nonlinear voxel is generally more elongated in the longitudinal direction, the number of cumulate pulses is larger for longitudinal motion than for later motion, as far as the sample's velocity is kept constant.

The photo-induced silver clusters are characterized by two main absorption bands in the UV range, typically centered around 290 nm and 340 nm, and by a broad fluorescence emission in the whole visible range, as shown by Figure II-8. Such absorption bands are associated to the creation of distinct types of silver clusters, labeled $Ag_{\alpha}(1)$ and $Ag_{\alpha}(2)$ clusters respectively depending on their ability to grow into metallic nanoparticles showing surface plasmon resonance under subsequent thermal treatment around the glass transition temperature, as discussed in detail in [149].

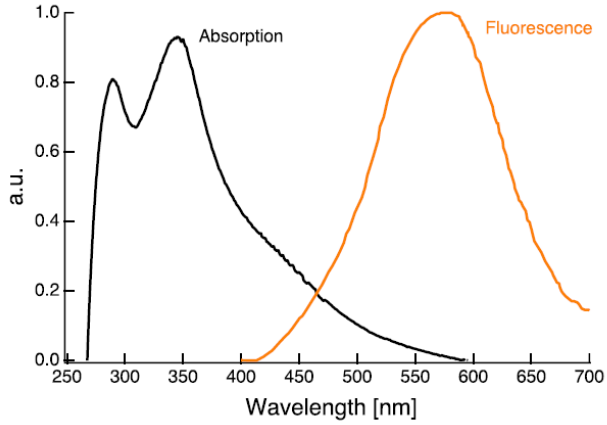

Figure II-8: Absorption (black) of the photo-induced silver clusters following laser irradiation exhibiting two main absorption bands around 290 and 340 nm. Fluorescence emission (orange) under blue light excitation at 405 nm. Taken from [147].

Indeed, different types of silver species are generated through DLW, as identified by Marquestaut *et al*. [149]et Bourhis *et al*. [141] and outlined in Table II-1.

Table II-1: Different silver species identified following DLW in silver-containing glasses [141].

Ag specie	Absorption position(nm)	Emission position (nm)
Ag_m^{x+}	290 350	Visible range
Ag^0	345 365 387 405	460 470
Ag_n	442	0.049
Ag^{2+}	280 320 380	660

For a static fs laser irradiation, a ring shape structure was created, as already explained, on the plan perpendicular to the laser beam propagation. High Resolution Scanning Electron Microscopy (HRSEM) photos were investigated by polishing and etching the glass sample using acid to reveal the structures to the surface. Significantly, the backscattered HRSEM image in Figure II-9(a) reveals that the silver-induced structure (which corresponds to an excess of concentration of elements with high atomic number) exhibit radial features. In fact, the profile acquired through HRSEM imaging of the structure depicted in Figure II-9(b), along the red line, reveals that this structure has a wall thickness of ~ 80 nm, falling within the sub-micron range.

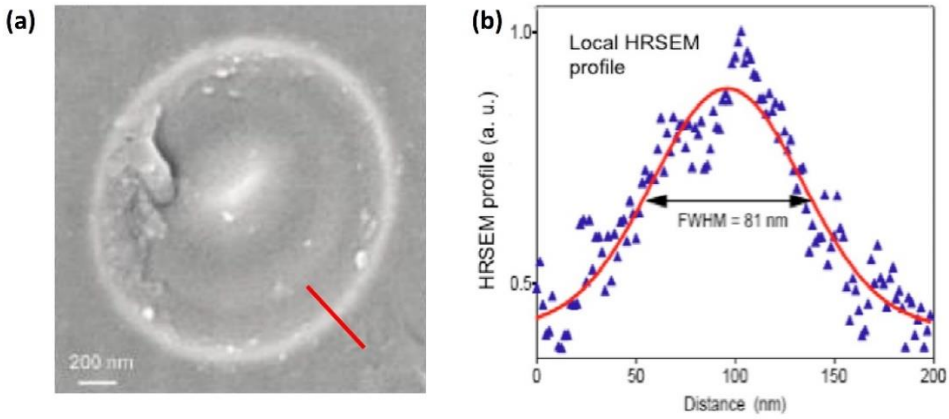

Figure II-9: (a) HRSEM image (in the direction perpendicular to the beam propagation) of a static spot irradiated by a focused femtosecond laser. The transversal profile of the HRSEM image along the red line, demonstrating a ~80 nm wide structure. Taken from [151].

Moreover, Bellec *et al*. had also investigated the dependence of the fluorescence intensity of the photo-induced silver clusters on the laser irradiance and the number of pulses applied for different repetition rates. This evolution is reported in Figure II-10. The highest fluorescence intensity was observed at the highest irradiance possible at 11 TW.cm^{-2} below the explosion threshold and for a number of pulses of 10^7, for a 10 MHz repetition rate. It was shown that reducing the laser's repetition rate leads to a decrease in fluorescence intensity despite the

cumulated number of pulses was kept the same, *i.e.*, so that the formation of silver clusters dropped when dropping by decades the irradiation repetition rate. Even though it's reduced for lower repetition rate, fluorescence intensity remains detectable at a repetition rate of 100 kHz for a total of 10^7 pulses and for 10 kHz for the highest irradiance. Thus, it should be noted that the fluorescence intensity depends linearly on the irradiance roughly while depending logarithmically on the number of pulses [150]. To generate silver clusters, a significant number of pulses and the appropriate laser irradiance are both essential. The interval between two pulses needs to be shorter than the lifetime of the intermediate species Ag^0, which typically falls within the microsecond range. The existence of an adequate number of electron traps in the form of Ag^0 between successive pulses is a fundamental requirement for further allowing the formation of silver clusters.

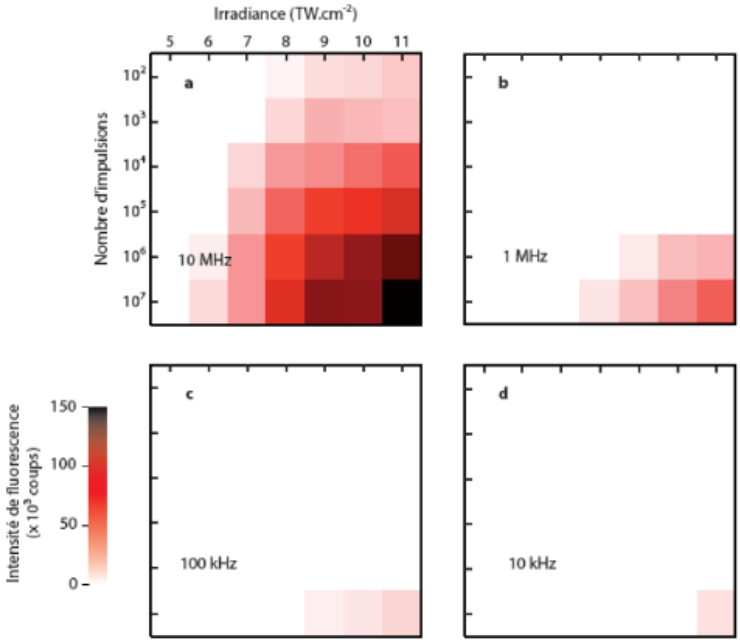

Figure II-10: Correlation of the fluorescence intensity on the laser irradiance and number of pulses for different repetition rates: (a) 10 MHz, (b) 1 MHz, (c) 100 kHz, (d) 10KHz. Taken from [141].

Beyond absorption and fluorescence properties of silver clusters, one can also wonder the relationship of absorption and refractive index properties related to such species. In this framework, Figure II-11(a) demonstrates the absorption spectrum of silver cluster distributions obtained by differential transmission microscopy. This measurement has been deduced by comparing differential transmission measurements between an irradiated area and a pristine one, while considering the filling factor of the spatial distribution of fluorescent laser tracks composed of silver clusters. As already reported by Marquestaut *et al*., the absorption characteristics of the silver clusters are dominated by two distinct absorption bands in the UV range (around 290 nm and 340 nm). This allowed to estimate the associated

refractive index change by using the Kramers-Kronig analysis performed on the differential absorption spectrum of the silver clusters (Figure II-11(b)). One can see a positive refractive index change across the entire visible-near-infrared spectrum, with a peak value of 2.5 x 10^{-3} occurring at a wavelength of 365 nm. In this context, such findings indicate that the refractive index change is a result of the laser-induced formation of a novel chemical silver species within a localized region. This species possesses an enhanced molecular electric polarizability, in direct relationship with the formation of new chemical bonds, consequently causing a localized increase in electric susceptibility, which in turn leads to the observed change in refractive index. Indeed, this Δn is independent of the modifications of the glass matrix itself due to the laser-induced modifications of the local density as it is the case for Type I modification.

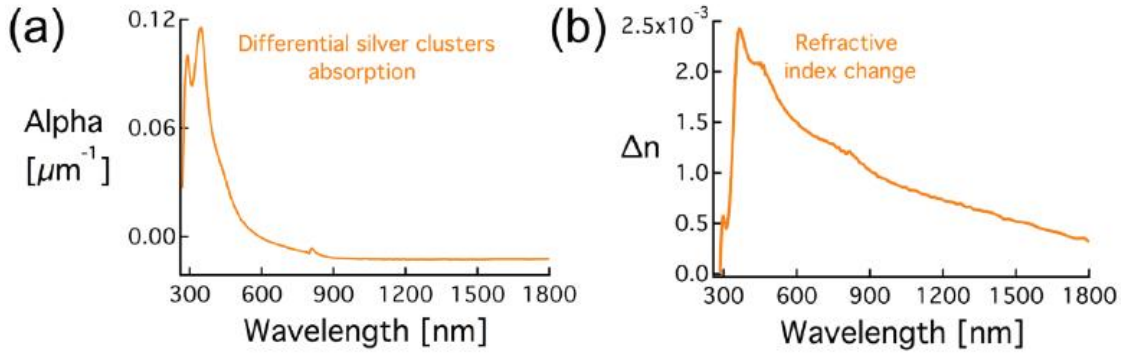

Figure II-11: (a) Differential absorption spectrum of silver clusters, illustrating their response to different wavelengths and displaying two prominent absorption bands at approximately 290 nm and 350 nm. (b) Refractive index change, extracted from the spectrum displayed in (a), determined through a Kramers-Kronig analysis. This analysis takes into account the filling factor of the spatial distribution of silver clusters. DLW parameters: 7 TW/cm² - 40 µm/s. Taken from [147].

II.4.Type-A refractive index modifications

II.4.1.Optical properties

As already explained, the refractive index change in phosphate glasses is attributed to the formation of photo-induced silver clusters and, more specifically, correlatively to their absorption bands. By locally inducing silver clusters in phosphate glasses, new chemical bonds are created with a different electronic polarizability from that of the non-irradiated material, resulting in a local change in the refractive index. In 2017, we showed the production of a novel type of positive refractive index modification Δn based on the photochemistry of silver species [156]. This distinct modification is referred to as Type-A, for *Argentum*, related to the spatial distribution of the photo-induced silver clusters in the vicinity of the laser-glass interaction voxel [156]. Type-A was demonstrated in numerous glass

matrices containing silver ions, as it appears being selectively related to the laser-activated photochemistry of silver. It allows for various local highly contrasted optical responses (luminescence or refractive index) for the fabrication of photonic components and integrated devices. The study of Type-A refractive index change was conducted in a silver-containing phosphate glass by inscribing a cartography of serpentine structures at 160 µm below the surface. Figure II-12(a) shows top view fluorescent images (under 480 nm excitation) of the inscribed structures, where the irradiance as well as the number of pulses *i.e.*, the translation speed of the stages were varied during the writing. It was depicted that the fluorescence intensity of these written structures increases with higher laser irradiance and/or an increased number of laser pulses, as already reported previously [99], [150]. A pop-up phase image of one written structure was collected using a 100× microscope objective (Zeiss) with 1.3 NA (used with a matching index oil n = 1.518) and the SID4-Bio sensor (Phasics) plugged to an Axiovert 200M Zeiss microscope. As represented in Figure II-12(b), this device allows for the construction of the phase image and the extraction of the local optical path difference (OPD) between the written lines and the pristine glass. The refractive index change associated with the inscription of the serpentine structures is obtained from the OPD extracted from the phase image and calculated using the following equation:

$$\Delta n = \frac{OPD}{e} \qquad \text{II-8}$$

where e is the thickness of the optically thin inscribed structures.

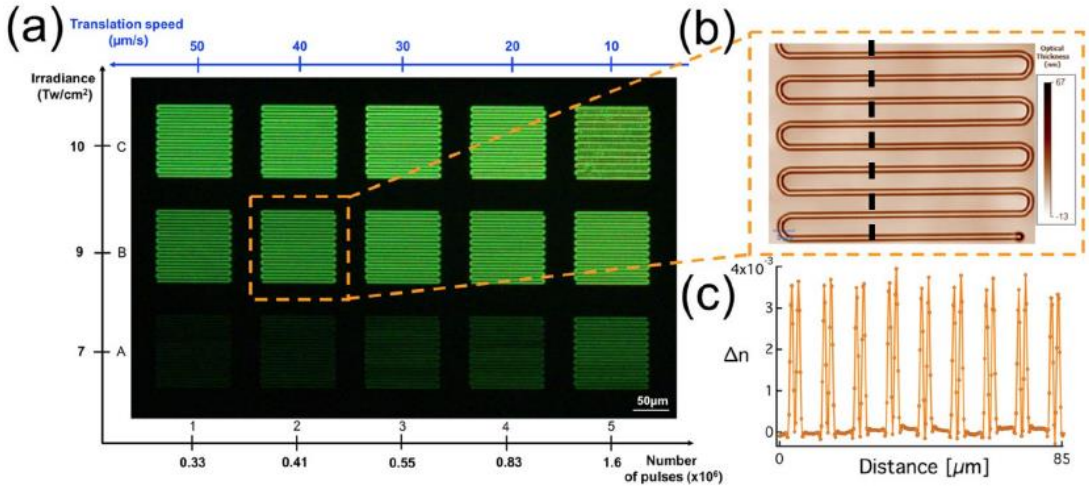

Figure II-12: (a) Fluorescence image (λ_{ex} = 480 nm, λ_{em} = 550 nm) of the inscribed cartography of the serpentine structures while varying the writing irradiance (along the vertical axis) and the number of pulses (along the horizontal axis) (b) Popup of the phase image of one of the structures, acquired through the SID4-Bio device (c) Line profile of positive refractive index change associated with the double-track Type-A structures. Such line profile is extracted from a horizontal cross-section of the structure (dashed black line in (b)). Taken from [156].

The estimation of the Δn value from the measured OPD relies on the consideration of the proper object thickness to be used. For thin structures with in-depth dimensions much

weaker than the imaging wavelength, the thickness to consider is indeed the physical thickness of the imaged object. However, for thicker objects, the situation of such interferometric phase imaging method is more complex. In this framework, Abou Khalil *et al*. recently published a complex and comprehensive approach allowing for the quantitative retrieval of the refractive index modification based on the measured OPD, especially for thick structures, by considering cylindrically shaped volume modifications with varying diameters and heights [157]. Indeed, one shall remember that the relevant effective longitudinal length to be considered can depend on the physical lateral dimension of the studied object: this originates from deep consideration of diffraction theory and its impact on such an interferometric microscopy imaging.
Figure II-12(c) reports the profile of the induced Δn, along the black dashed line in Figure II-12(b), with a considered thickness of 6 µm for the tracks of silver cluster distributions. This profile presents double line change, known as Type-A modifications, associated to the photo-induced silver clusters at the periphery of the interaction voxel for every laser passage [156]. This proves that the photo-induced silver clusters are responsible for the positive Δn peaks following DLW.

Furthermore, to enhance the femtosecond-induced refractive index change in glass samples without any pre- or post-treatment, multiscan inscriptions are employed. As implied by its name, the multiscan technique involves repeating laser passes in a localized area, sometimes with a slight translation in one of the inscription directions. This process allows for the modification of both the structure's geometry and the associated refractive index change. The method relies on the glass matrix's ability to retain a memory of the laser pulse absorption, especially when consecutive laser passes overlap with one another [158]. Multiscan structures have been created in a commercial silver-containing zinc-phosphate glass, for a different number of cumulative absorbed pulses, i.e., the total number of pulses absorbed in the N_{scan}(number of cumulative scans) and different laser irradiance. It was shown that the repetition of the inscription process multiple times leads to the induction of a higher number of silver clusters. The refractive index change for the inscribed structures has been calculated by quantifying the growing thickness associated with the increase of the number of scans.
Figure II-13 presents the dependence of the refractive index change on the cumulative number of absorbed pulses and the DLW intensity.

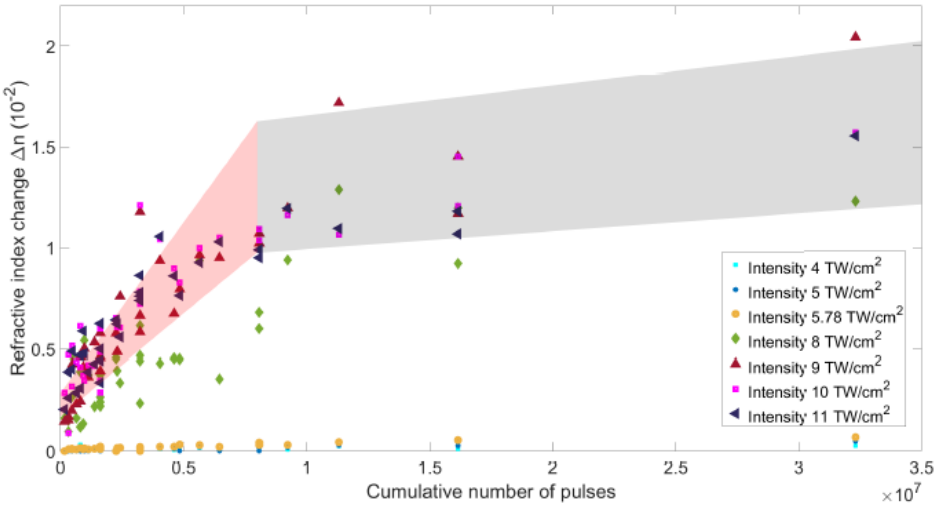

Figure II-13: Refractive index change corresponding to each inscribed multiscan structure as a function of the number of cumulative absorbed pulses, i.e., the total number of pulses absorbed in the N_{scan}, for a specific laser irradiance. Image taken from [159].

Note that some identical cumulated numbers of pulses have been obtained with distinct couples of parameters $\{N_{scan};\ v\}$ as long as the product $\frac{N_{scan}}{v}$ remains constant. At high intensity, for $I \geq 8$ TW/cm^2, the Δn associated with the multiscan structures rapidly increases to 1×10^{-2} after $N_{pulses} = 0.5\times10^7$ and it remarkably achieves 2×10^{-2} after $N_{pulses} = 3\times10^7$ at $I = 9$ TW/cm^2. These Type-A refractive index changes are very high for such oxide glasses, compared to what is generally obtained with Type I even under cumulative approach [160]. In the case of high intensity, the red area demonstrates a direct correlation between the refractive index change and the cumulative number of pulses absorbed during the N_{scan} laser inscription. This linear increase in Δn with N_{pulses} underlines that the formation of silver clusters takes place in an athermal regime, whatever the involved couples $\{N_{scan};\ v\}$ for given N_{pulses} values. This red area indicates a situation with a sufficiently filled silver reservoir of the glass matrix. Conversely, the grey area represents a saturation effect, indicating that Δn stabilizes at a constant value due to a slowdown in the process efficiency of keeping on growing silver clusters. This grey area depicts here a partially empty silver reservoir, so that free electrons production and subsequent silver species formation drop down.

In addition, it was already demonstrated that the refractive index change is influenced by both the number of laser pulses and the irradiance, as illustrated in Figure II-14. Increasing the number of deposited pulses leads to an elevation in local temperature (although it remains well below the glass transition temperature) facilitating the thermal activation of silver ion migration and chemical reactivity and promoting the creation of a larger quantity of silver clusters [151], [152]. Also, higher irradiance leads to a more substantial formation of silver clusters, as previously observed [150]. Consequently, a higher value of Δn is obtained

in both cases.

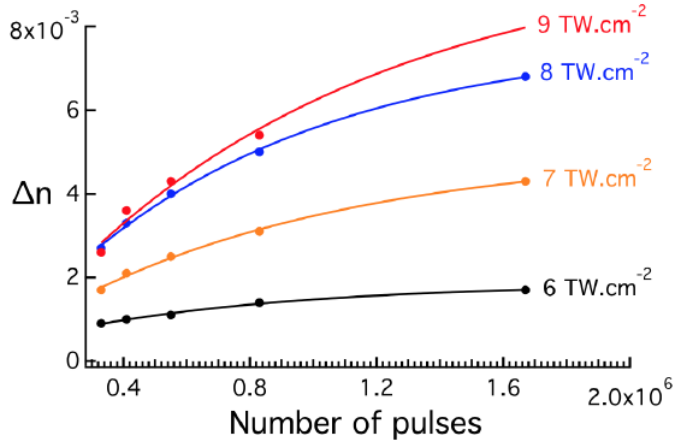

Figure II-14: Variation of Type-A refractive index change for different deposited number of pulses and laser irradiance. Taken from [156]

As already mentioned, it was shown that Type-A modification was observed in silver-containing glasses. According to Abou Khalil et *al.* [161], either Type-A or Type-I modification could be triggered in silver-containing glasses, depending on the laser parameters and the laser regime. Type-A is an extrinsic modification driven by the photochemistry of silver clusters, characterized by the presence of a double fluorescence line and a positive index variation. This regime requires high repetition rates and the cumulative behavior of many-pulse irradiation. High irradiance typically ranging on the 5-10 TW/cm^2 corresponds to moderate energy deposition and limited temperature increase (a few tens of degrees) much below the glass transition temperature. On the other hand, Type-I corresponds to the classic local densification of the vitreous matrix, with a single fluorescence line and index variation. This intrinsic modification directly affects the glass matrix itself. In this case, the laser energy heats the glass above its glass transition temperature, causing it to melt and subsequently reconfigure into a new glass structure. This newly formed glass structure can exhibit a refractive index change that may be either positive or negative. The specific sign and magnitude of Δn depend on factors such as the glass composition and the laser parameters. Considerably, higher peak energies are necessary, resulting in a much more substantial increase in temperature, even though the repetition rates are lower. Thus, Type-A modification is observed in the low pulse energy range when compared to the Type-I modification, as depicted in Figure II-15. For more details, Abou Khalil *et al*. have been reported a comparison between Type-A and Type-I modifications [161], highlighting the specificities of these two regimes of interaction that bear distinct material modifications.

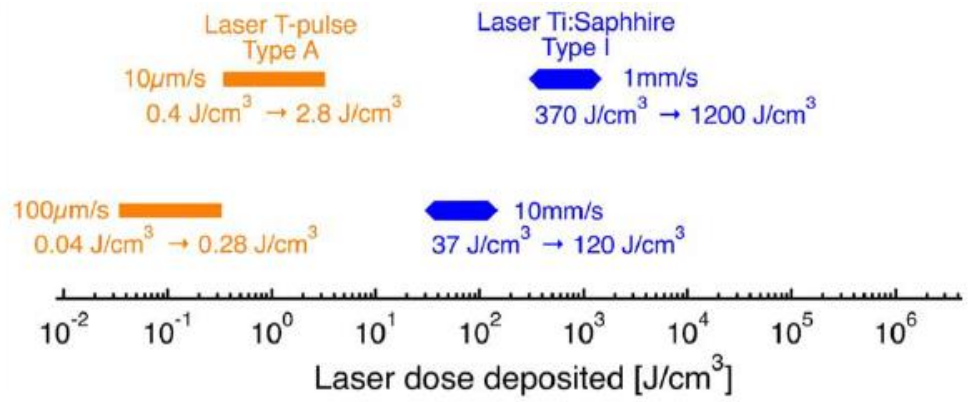

Figure II-15: Calculated laser absorbed dose as a function of the range of writing speed used for two distinct types of writing processes: the orange line corresponds to the T-pulse 200 laser used for the inscription of Type-A modification, the blue line corresponds to the Ti:Saphire laser used for the type I modification. T-pulse 200 laser has 9.8 MHz repetition laser, 1030 nm wavelength with pulse duration ~400 fs and energies in the range of 20 nJ to 120 nJ. While Ti-saphhire-Rega coherent laser operates at a low repetition rate of 250 kHz emitting at a wavelength of 800 nm with 100 fs pulse duration and pulse energies from 0.5 to 2.5 µJ. Taken from [147].

It should be noted that recently in 2022, Guérineau *et al*. have achieved the successful synthesis of silver-doped gallo-germanate oxide glasses containing both barium and potassium ions, with an extended infrared optical transmission up to 5.7 µm. For high concentration of Ba^{2+}, the induced refractive index change is primarily attributable to the presence of silver, specifically corresponding to Type-A modifications. Also, embedded periodic structures with a pitch as small as 400 nm have been effectively created. This research offers valuable insights and advantages for the fabrication of photonics devices into the MIR range. Such glass has not been used in this manuscript, therefore readers are invited to check reference [162] for more details in such heavy metal oxide glasses with extended spectral transmission in the MIR.

II.4.2.Specificities of sub-wavelength periodic structures

As already explained, laser inscription occurs at the edge of the beam through photodissociation of the center. This is because the generated clusters absorb significantly in the blue range, altering the energy deposition and threshold conditions. By intelligently manipulating the superposition of beams, it is possible to precisely control the photodissociation and diffusion process, resulting in sub-wavelength periodic structure. Precise control over inscription thresholds, and consequently over the manipulation of the silver ion reservoir, can induce a novel aggregation process during the second laser pass. From an application point of view, this concept of fluorescence redistribution is remarkable as it can enable the production of more complex fluorescent patterns and achieve sub-micrometer dimensions. While this is not the main focus of this thesis, interested readers can find detailed information on these processes in the published works. A record of 200 nm has

been achieved within these glasses [142], [150].

II.5.Type-A applications: Review on previous work

Thanks to the induced properties of the photo-inscribed silver clusters, several integrated photonics devices have been employed in such glasses, such as waveguides [156], couplers [156], beam splitters [156], refractive index sensors [163] and first-order waveguide Bragg gratings with periods down to 240 nm [164]. In such photosensitive glasses, Type-A modifications present more localized and smooth modifications than Type-I allowing for a better preservation of the glass optical quality [161].

II.5.1.Waveguiding

As already mentioned, the positive Type-A refractive index change is suitable for waveguiding applications. Multimode waveguides and single mode waveguides have been demonstrated in silver-containing phosphate glasses using Type-A modifications [147]. The original double-trace structure supported by the laser-induced silver clusters appears to behave in a manner similar to two closely interacting waveguides [165], [166]. In addition, the promising results from the multiscan inscription of high Type-A refractive index change have been used in order to create multiscan waveguides. Multiscan waveguides have been inscribed with several number of repetitions N_{scans} = 1, 2, 3, 5, 10, 20 and 30 and have been injected at different wavelengths: 750 nm, 900 nm and 1030 nm. The near-field images of guided modes at various wavelengths are presented in FigureII-16. These waveguides exhibit either single mode or multimode operation at the same wavelength, depending on the number of laser scans [159].

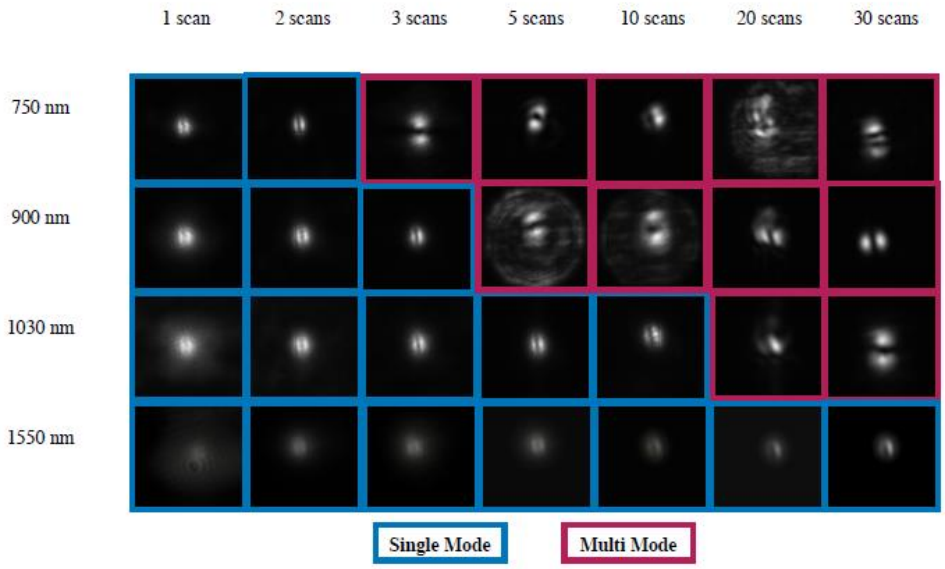

FigureII-16: Near-field images illustrating the mode profiles of each multiscan waveguide at various wavelengths. A colored edge distinguishes single-mode behavior in blue and multimode behavior in magenta. Taken from [159].

They also showcase the capacity to control the confinement of the guided mode, as a consequence of the tunable high refractive index change associated with these structures. The enhanced mode confinement achieved with multiscan waveguides has led to a reduction in propagation losses. This development holds significant promise for utilizing Type-A modifications in the creation of bent waveguides with small radii of curvature, potentially enabling the miniaturization of integrated optical circuits.

Type-A waveguides, as opposed to Type-I, are accessible at low intensities and enable the inscription of near-surface waveguides in materials without causing damage. Near-surface waveguides based on Type-A modifications were successfully inscribed without causing damage and without the need for any additional processing, which is typically required for Type-I near-surface waveguides. This characteristic has been leveraged to develop a refractive index sensor [163].

II.5.2.Y-Beam splitters

Type-A refractive index modification enables the inscription of a 50-50 Y-beam splitter typically 160 µm below the surface, towards applications such as 3D integrated circuits. This optical component divides the input light power equally through each of the two output branches [147]. Moreover, asymmetric Y-junction has been fabricated, when the upper branch was fabricated by fixing high irradiance and the lower branch by changing irradiance. Different asymmetric Y-junctions were inscribed where the split ratios are 43%-57%, 33%-67%, 27%-73%, 22%-78%, and 4%-96%. Figure II-17 depicts the output profiles and output ratios for one symmetric and four asymmetric beam splitter [167].

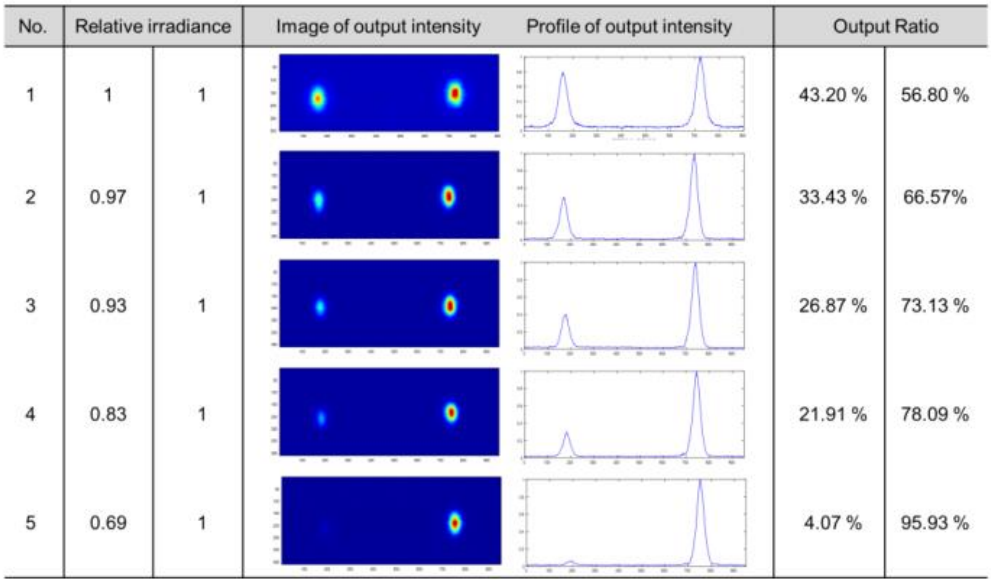

Figure II-17: Output profiles and output ratios for one symmetric and four asymmetric beam splitters, when injection position = 0. Taken from [167].

Furthermore, Le Camus et *al.* have showcased findings related to waveguides and couplers designed for the mid-infrared spectrum, which have been inscribed in a BGG glass (barium, gallium, germanium). These devices enable signal transfer between the two branches of the coupler using evanescent wave coupling [168].

II.5.3.Waveguide Bragg grating

As already mentioned, the re-inscription property of Type-A fluorescent silver clusters opens the route for the creation of sub-diffraction periodic refractive index structures, such as Waveguide Bragg grating (WBG).

The first method to fabricate Waveguide Bragg grating is using a two-step process: the first step starts by the line-by-line successive inscription of the Bragg grating with the selected period, and followed by the inscription of the waveguide thanks to a single laser pass perpendicular to the grating, as illustrated in Figure II-18(a). In order to investigate this approach to produce sub-wavelength periodic refractive index structures, various structures with different periodic structures (Λ = 240, 260 and 280 nm) with a length of 500 µm have been inscribed in GPN glass sample followed by another laser pass achieved perpendicularly to the periodic structures, with the same irradiance. Figure II-18(b) shows an example of a high resolution confocal fluorescence image of periodic Bragg Grating (Λ = 500 and 250 nm) with crossing waveguide [151].

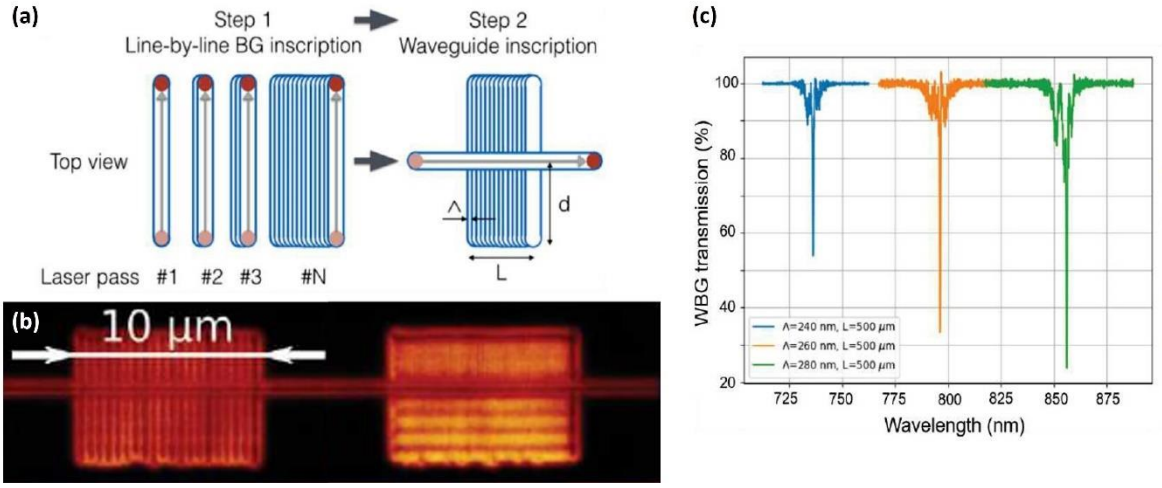

Figure II-18: (a) Schematic representation of the two-step writing process of the waveguide Bragg grating. (b) High resolution confocal fluorescence image of sub-diffraction periodic structures (Λ= 500 and 250 nm) with a crossing waveguide. (c) First-order transmission in the red and near-infrared visible range of the three 500 µm Type-A waveguide Bragg grating with the three different periodicities (Λ = 240, 260, 28 nm). Taken from [151].

Figure II-18(c) depicts the transmission spectra of the three different WBG, showing first order resonance at 736.4, 796.3 and 856.1 nm. The transmission drops demonstrate reflectivity of 46.2%, 66.7% and 76.3% for periods Λ = 240, 260 and 280 nm, respectively, for a short WBG length of 500 µm. In this case, the backward coupling coefficients κ are respectively estimated to 1.66, 2.29 and 2.69 mm^{-1}, such values being significantly higher than those reported elsewhere, especially in the visible/near-IR spectral range reported elsewhere with Type-I modifications [170].

Another method has been implemented to enhance the effective strength of the WBG, so as to improve the quality of WBG periodicity as well as the modal overlap of the guided mode with the WBG structure. This method relies on using the two-step process described above, but instead of inscribing the structure using the line-by-line technique, a squeezed single helix with an elliptical basis and a waveguide (located at the center of such a helix) have been inscribed. This method demonstrates a transmission drop of more than 99% remarkably achieved at λ_{Bragg} = 1.007 µm for a helicoidal WBG with period Λ_{helix} = 630 nm and length L = 500 µm for a periodicity of grating equal to $\Lambda_{VBG} = \Lambda_{helix}/2$. Such periodicity ($\Lambda_{helix}/2$) results from the modulation of the refractive index of the waveguide when inscribing the top and the bottom of the helicoidal gratings. Readers can get more details from the PhD manuscript of Laura Loi (University of Bordeaux, 2022) [169].

II.6.Conclusion

The interaction of an ultrafast laser pulse with a material can induce a rich diversity of multi-physics multi-scale phenomena whose final modification can be difficult to predict in some

cases. This chapter has discussed the processes involved in Direct Laser Writing of glasses using a femtosecond laser source.

The initial part of this chapter has provided a comprehensive overview of the DLW technique. Consequently, this results in three distinct modifications of the refractive index. The second part of the chapter focuses on silver-containing phosphate glasses and presents their optical properties. The introduction of silver ions into such glasses offers distinctive and intriguing properties prior to laser irradiation. This incorporation leads to the emergence of novel silver-based species at the periphery of the interaction voxel. Thus, the mechanisms underlying the formation of silver clusters have been explored, highlighting the appearance of novel spatially-resolved properties and optical contrast, which includes a novel type of refractive index change. Such a new type of refractive index modification presents several interesting optical properties and has already demonstrated its utility across various applications, as detailed in this chapter.

In the framework of this PhD manuscript, the main advantages of laser-inscribed silver-based structures are the 3D versatile access to highly stable and highly contrasted optical contrast, both in fluorescence and in refractive index change with very small sub-diffraction features possibly down to 80 nm. These remarkable abilities will be further addressed in the core of the present PhD manuscript.

III Laser inscription of silver clusters for X-ray spatially-resolved dosimetry

In this chapter, we investigate a pioneering method for X-ray spatially resolved dosimetry, which involves the use of laser-induced silver clusters embedded in high-silver-concentration glasses.

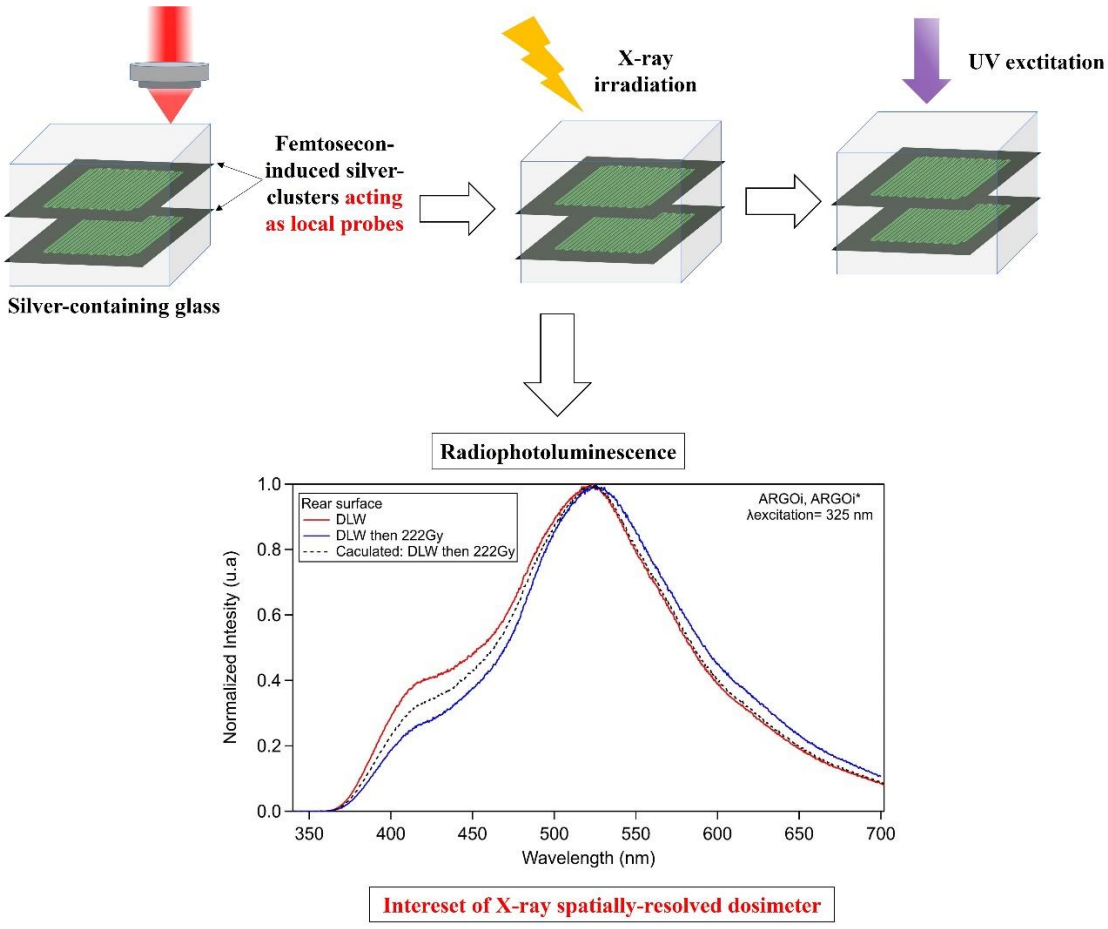

III.1.Introduction

Radiation serves as the fundamental building block of our universe, covering high-energy photons like γ-rays or X-rays, as well as various particles such as neutrons, protons, electrons, and even heavy ions. In recent years, the employment of ionizing radiation has gained significant prominence across a wide range of applications, spanning from industrial and food processing to medical treatment and diagnosis. Within radiation-rich environments like space, high-energy physics, nuclear industry, or medicine, optical materials such as bulk glasses or optical fibers offer numerous advantages.

To ensure the effective and consistent delivery of ionizing radiation, it is crucial to focus on radiation monitoring and dosimetry, which holds great importance and is an area of active research. Also, ionizing radiation has been recognized to induce a diverse range of biological effects, including cell destruction, mutation, chromosomal abnormalities, and the development of cancer. This radiation exposure commonly occurs among patients undergoing medical diagnosis or therapy, workers in nuclear environments, and even astronauts. In order to mitigate the risk of overexposure to radiation for both individuals and specific equipment, the adoption of accurate, high-performance, and resilient analysis tools has become imperative. These tools play a crucial role in ensuring precise measurement and monitoring of radiation levels, assessing potential risks, and implementing necessary safety measures. Dose limits are established to mitigate the potential biological risks associated with radiation exposure during the regular activities of workers and the public. The International Commission on Radiological Protection (ICRP) sets specific dose limits for both workers and the public [171]. Continuous research and development efforts in the field of radiation analysis tools aim to enhance their precision, reliability, and overall performance. This ongoing innovation is driven by the urgent need to enhance safety measures, ensure accurate monitoring and assessment in various radiation-related fields. The areas of improvement focus on increasing sensitivity, enabling real-time measurements, and reducing costs, all of which contribute to the development of optimal radiation dosimeters. Different approaches to radiation dosimetry have been explored, both passive and active methods. In general, three significant physical effects have been identified as a result of radiation on optical materials: radiation-induced attenuation (RIA) primarily caused by the creation of point defects, leading to the emergence of absorption bands; radiation-induced emission (RIE) that occurs due to Cherenkov emission, as well as luminescence from excited color centers and radiation-induced refractive index change (RIRIC) occurring due to the compaction phenomenon and the appearance of defect-related absorption bands, as described by the Kramers-Kronig relations [172], [173]. Indeed, among the three macroscopic effects, radiation-induced attenuation is often considered the most significant impacting phenomenon in a majority of practical cases and applications [174]. In addition, several aspects have been studied in the regard of radiation-induced emission, which relies

on the luminescent properties of materials, including radioluminescence (RL), optically stimulated luminescence (OSL), thermoluminescence (TL), and radiophotoluminescence (RPL) [175]. Radioprotection and radiation impact remains a central focus of research activities within the field of civilian protection and for the development of both sensitive or hardened material.

III.2.Scientific objectives and description of the chapter

On one hand, radiophotoluminescence has been a prominent technique in radiation dosimetry thanks to various employed methods, especially in silver-doped phosphate glasses since the pioneering work of Schulman *et al.*[176] RPL is recognized for its reliability in passive radiation dosimetry, particularly for gamma rays and X-rays. The use of silver-doped phosphate glasses (commercialized RPL dosimeters (Ag-doped phosphate glasses with 0.17% Ag (w.c.))) in RPL dosimetry has gained significant attention due to their unique properties. These glasses exhibit luminescence when exposed to ionizing radiation, and the intensity of the emitted light is directly proportional to the radiation dose rates received. This property enables accurate measurement and assessment of radiation levels. Extensive studies have confirmed their reliability and sensitivity, making them widely adopted in radiation dosimetry.
On the other hand, our group has demonstrated recently the generation of silver species in highly photosensitive silver-containing sodo-gallophosphate glasses exposed to X-rays [177]. Notably, our glasses contain two orders-of-magnitude more silver ions than the commercialized RPL dosimeters. We reported that the phosphate glass network had a decisive influence on the X-ray photosensitivity and the formation of luminescent silver species, namely Ag^{2+} hole trap silver ions and Ag_m^{x+} silver clusters. In addition, fs laser-inscribed molecular species such as fluorescent silver clusters show subsistence under X-ray irradiation.
To our knowledge, no research combining RPL and fs DLW has yet been conducted on our glasses. For these reasons, we present in this chapter the potential of silver clusters for X-ray spatially-resolved dosimetry. The targeted objective is to evaluate the performances of a spatially-resolved dosimeter exploiting the properties of the 3D laser writing of silver clusters. Those clusters are generated in phosphate glasses containing a high concentration of silver oxide (typically around 5% oxide molar fraction) by femtosecond direct laser writing technique. Thus, RPL and fs DLW have been combined to estimate the potential of those laser-inscribed structures as local probes of the deposited doses [178].

The first section of this chapter will give a general overview of the radiative environment, types of radiation, photon-matter interaction processes, the main physical and dosimetry quantities used in radiation protection and dosimetry. In addition, a summary of properties of dosimeters is presented. Moreover, the radiation-induced effects on optical materials were

detailed, such as the radiation-induced absorption, the radiation-induced emission and the radiation induced refractive index change. The several mechanisms of radiation-induced emission are detailed as well. In particular, a state-of-the-art review on the radiophotoluminescence dosimeter will be provided.

The second section of the chapter shows the post X-ray irradiation study: three phosphate glasses of different composition were investigated. First, the spectroscopic properties of the pristine glasses were studied after X-ray irradiation at different doses to assess their dosimetry potential. Second, the impact of X-rays on the three-dimensional inscribed silver clusters has been analyzed using several spectroscopy methods. Such spectroscopic properties of the 3D structures are evaluated before/after X-ray irradiation to study the resilience of the irradiated silver clusters. The depth-dependent deposited dose within the glass thickness was evaluated using a Monte Carlo Geant4 simulation. Finally, the optical and spectroscopic properties were handled to demonstrate the acheivement of a sensitive and reliable dosimeter.

The third section of this chapter delves into a real-time investigation of laser-inscribed structures when exposed to X-ray radiation. This involved the preliminary laser inscription of a waveguide along the entire length of the sample, connecting it to two radiation-resistant fibers on either lateral side. This configuration was established to enable in-situ measurement of the waveguide's luminescence and attenuation signals during X-ray exposure. Subsequently, the experimental procedures for the fabricated device, as well as the details of radioluminescence and radiation-induced attenuation, are comprehensively explained. These findings are then compared to those of a bulk sample (without fs inscription) to draw conclusions about the impact of X-ray irradiation on the fs-written silver clusters in real-time.

III.3.Basics of radiative environment and dosimetry

III.3.1.Types of radiation

Radiation is the phenomenon in which energy and momentum are emitted or propagated through waves or particles. The detection and characterization of radiation rely on its interactions with the surrounding material. As radiation propagates through a medium, it interacts with and modifies the absorbing material. Radiation can be classified into two categories based on its nature and its interaction with matter: ionizing and non-ionizing radiation. Figure III-1 provides a summary of the various types of radiation.

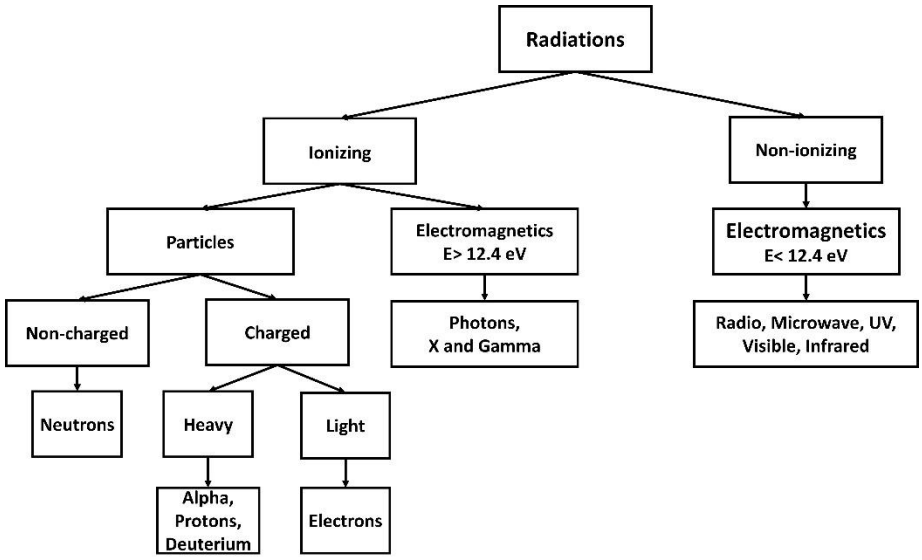

Figure III-1: Classification of radiation.

Non-ionizing radiations are electromagnetic waves whose corresponding fundamental particles – namely the related photons – do not bear individually enough energy to ionize atoms. On the other hand, ionizing radiation possesses enough energy to remove electrons from atoms of the absorbing material, resulting in the formation of positive ions. The binding energy of the lowest bonded electrons in living matter is typically around 12.4 eV. Therefore, radiation with a wavelength shorter than 100 nm can be classified as ionizing radiation.
Ionizing radiation can further be classified into two categories based on their nature: directly ionizing and indirectly ionizing radiation.

- Directly ionizing radiation comprises charged particles, including electrons (e^-), positrons (e^+), protons (p^+), alpha particles (helium nuclei), deuterium (d) or other heavy ions. These particles possess sufficient energy to directly ionize the medium. During direct ionization, the energy is transferred to the absorbing material through Coulomb interactions between the charged particle and the valence orbital electrons of the atoms. The energy transfer in direct ionization depends on the masses of the particles involved.
- Indirect ionization involves neutral particles such as electromagnetic radiation (photons, X-rays, and gamma rays) or neutrons. Indirect ionization occurs through a two-step process: In the first step, the neutral particles transfer a fraction or all of their energy to charged particles during a single interaction. It is these secondary charged particles that then ionize the absorbing medium.

In this chapter, we will concentrate on the X-ray radiation. They result from the transition of electrons between the energy levels of atoms, with wavelengths shorter than those of UV rays and longer than those of gamma rays (ranging from 10 nanometers to 10 picometers corresponding to energies in the range 100 eV to 100 keV, respectively). They can be produced naturally (astrophysical sources) or artificially (X-ray tubes, X-ray lasers

synchrotrons and cyclotrons).

An X-ray tube is a simple device comprising two electrodes: the cathode and the anode (or target). When a high voltage, typically ranging from a few kilovolts to several hundred kilovolts, is applied between these electrodes, an electrical current flows from the cathode to the anode. At the anode, the electrons lose energy and generate X-rays along with heat. The production of X-rays in an X-ray tube can be attributed to two phenomena:

- Bremsstrahlung: this type of radiation emission occurs when a charged particle, such as an electron, approaches and decelerates near the atomic nucleus of another charged particle. In the case of an X-ray tube, electrons experience deceleration near the nucleus of the target material. The result is a broad spectrum of X-rays with energies ranging from 0 electron volts (eV) to the charge of an electron multiplied by the applied voltage.
- Auger Effect: it involves the transition of an outer electron of an atom to an inner shell that has a vacancy. Subsequently, electrons from higher energy states move to fill these vacant inner shells, resulting in the emission of X-ray photons with precise energies dictated by the electron energy levels. The emission of characteristic X-rays are narrow emissions specific to the atoms composing the target material. It is important to note that the average energy of the emitted X-ray photons depends on the applied voltage, while the dose rate is influenced by the current and inversely proportional to the square of the distance from the X-ray tube.

Therefore, the emission spectrum of an X-ray tube comprises both bremsstrahlung radiation and characteristic X-ray emission. This spectrum is illustrated in Figure III-2.

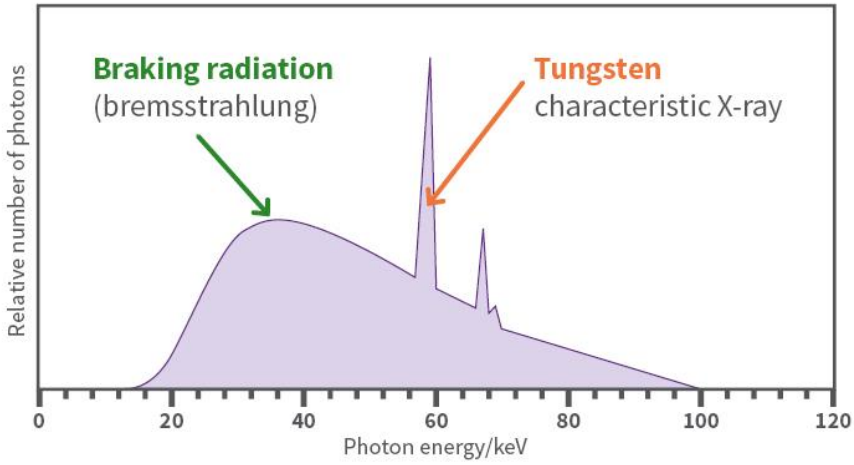

Figure III-2: The emission spectrum of an X-ray tube for a tungsten target. Taken from [179].

III.3.2.Interactions of photons with matter

When a photon traverses a material medium, its interaction with the medium depends on the nature of the interaction, either with electrons or with nuclei, as well as the specific properties of the interactions. These properties can be categorized as follows and described in Figure III-3:

1. transmitted: in this case, the photon passes through the medium without any interaction or modification.
2. deflected or refracted: some photons may experience deflection, refraction, or diffusion as they interact with the medium. However, during these interactions, no energy is transferred from the photon to the medium.
3. deviated with energy transfer: in certain interactions, the photon's path may be deviated or scattered, and energy is transferred to the medium. This can occur when the photon interacts with particles in the medium, resulting in a change in direction and a partial transfer of energy.
4. absorbed: in this scenario, the photon is absorbed by the medium, sacrificing all of its energy. The absorbed energy may contribute to various processes within the medium, such as exciting electrons or promoting chemical reactions.

These properties help to describe how photons interact with a material medium, providing insights into their behavior and the effects they have on the medium itself.

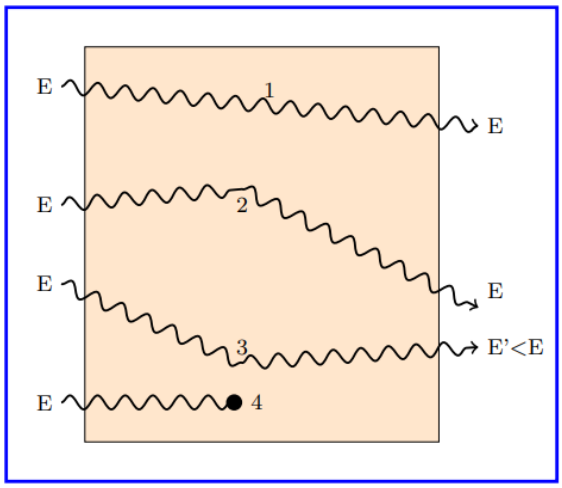

Figure III-3: Illustration of different kinds of interactions of photons with matter.

Photons have the capability to interact with matter in four distinct interaction modes, which are explained as follows.

III.3.2.a.Compton effect

The Compton effect is an interaction between an incident photon and an electron weakly bounded to its atom. For the Compton effect to occur, the energy of the incident photon $h\nu_0$ must be significantly higher than the binding energy of the electron. During this interaction, the incident photon undergoes a collision with the electron, resulting in a deflection from its original direction by an angle θ. In the process, the photon transfers some of its energy and momentum to the electron. As a result of the interaction, the electron is ejected from the atom with a kinetic energy T and at an angle ϕ with respect to the incident direction. Simultaneously, the photon is scattered with a residual energy of $h\nu = h\nu_0 - T$, where h is Planck's constant and ν_0 is the initial frequency of the incident photon (see Figure III-4). This phenomenon corresponds to the third case of photon-matter interactions described earlier in Figure III-3.

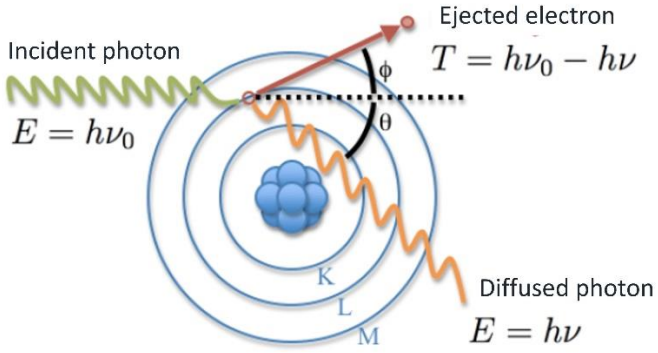

Figure III-4: Representative scheme of the Compton diffusion. Taken from [180].

III.3.2.b.Photoelectric effect

This process corresponds to the total energy transfer from an incident photon to an electron in an inner layer (K or L) of the electron cloud. The photoelectric effect corresponds to the fourth case of Figure III-3. In this case, the energy of the photon ($E = h\nu_0$) exceeds the binding energy of the electron E_l. The incident photon is completely absorbed by the electron, which is then ejected from the electron cloud as a photoelectron. The kinetic energy of the photoelectron ($E_c = E - E_l$) depends on the energy of the incident photon and the binding energy of the electron. The kinetic energy of the photoelectron can lead to further ionization and excitation of other atoms or molecules. When the ejected electron is from an inner layer, it creates a vacancy that can be filled by another electron from an upper layer or by an external electron. This exchange is accompanied by the release of energy E_R, which leads to the emission of a fluorescence photon. Alternatively, the energy E_R can be transferred to another electron with a binding energy E_P lower than E_R, resulting in the ejection of an Auger electron (such a secondary emitted electron) with a kinetic energy equal to $\mathrm{E}_R - \mathrm{E}_P$. The

photoelectric effect is predominant for ionizing photons with energies ranging from about 1 to 100 keV and primarily affects heavy materials (consisting of atoms with high atomic number, bearing thus a large electronic cloud) such as lead or aluminum.

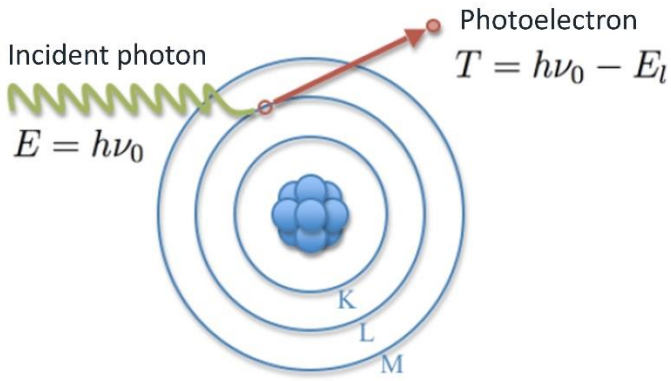

Figure III-5: Representative scheme of photoelectric effect. Taken from [180].

III.3.2.c.Pair or triplets' creation

This phenomenon occurs when highly energetic photons pass near the atomic nucleus or an electron of the electronic cortege, resulting in the formation of electron-positron pairs or triplets. The generation of pairs requires a high threshold energy, namely for energies verifying $E > 2\mathrm{E}_0$, where E_0 is the energy at rest of the electron that is equal to 511 keV, while generation of triplets is associated to a threshold of $4\mathrm{E}_0$. This triplet creation process involves the conversion of the photon's energy into a pair of particles: a positron e^+, and an electron e^- under the influence of the strong Coulombic field surrounding the atomic nucleus. Each of the two particles from a pair creation has the same mass m_0 and kinetic energy E_e. The positron emitted interacts along its trajectory with an electron and undergoes annihilation, resulting in the production of two photons with an energy of 511 keV each. These photons are emitted in opposite directions.

The law of conservation of energy is as follows:

$$E = 2\mathrm{E}_0 + \mathrm{E}_e \qquad \text{III-1}$$

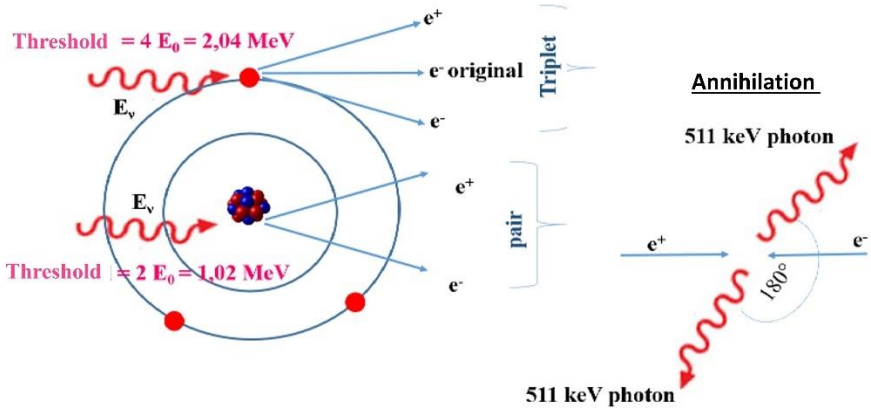

Figure III-6: Representative scheme of pairs and triplets' creation follow-up of the annihilation. Taken from [181].

III.3.2.d.Rayleigh diffusion

The Rayleigh diffusion is an interaction of a photon with a bound orbital electron, where there is no energy transfer from the photons to the atom. It is referred to as elastic scattering. During this interaction, the photon is deflected from its original trajectory by a very small angle. Rayleigh scattering does not contribute significantly to the energy transfer coefficient, but it does contribute to the attenuation coefficient. Rayleigh scattering corresponds to the second case mentioned earlier in Figure II-3, where the photon is deflected without transferring energy to the medium.

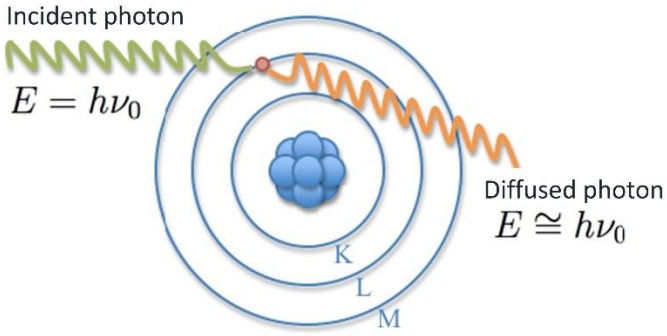

Figure III-7: Representative scheme of Rayleigh diffusion. Taken from [180].

III.3.3.Effective sections of interactions

III.3.3.a.The photoelectric process

The effective cross-section for the photoelectric effect is written as follows [182]:

$$\sigma_{PE=}\frac{8\pi r_0^2}{3}Z^5\alpha^4 4\sqrt{2}\left(\frac{1}{\varepsilon}\right)^{7/2} \qquad \text{III-2}$$

If $\varepsilon \gg 1$,formula (III-2) becomes:

$$\sigma_{PE=}\frac{8\pi r_0^2}{3}Z^5\alpha^4\left(\frac{1}{\varepsilon}\right) \quad \text{III-3}$$

Where r_0 = 2.818 fm is the classical radius of the electron; and α is the fine-structure constant ~ 1/137 and $\varepsilon = \frac{E_\nu}{E_0}$

III.3.3.b.The Compton process

The effective cross-section is given by [181]:

$$\sigma_c = 2\pi r_0^2 Z^2\left\{\frac{1+\varepsilon}{\varepsilon^2}\left[\frac{2(1+\varepsilon)}{1+2\varepsilon}-\frac{1}{\varepsilon}ln(1+2\varepsilon)\right]+\frac{1}{2\varepsilon}\ln(1+2\varepsilon)-\frac{1+3\varepsilon}{(1+2\varepsilon)^2}\right. \quad \text{IIIIII-4}$$

Where $\varepsilon = \frac{E_\nu}{E_0}$, E_0 is the energy of the electron at rest and E_ν is the energy of the incident photon.

Such effective cross-section is approached in two ways depending on the photon's energy [182]:

$$\sigma_C = \frac{8\pi r_0^2 Z^2}{3}\ if\ \varepsilon \ll 1 \quad \text{III-5}$$

$$\sigma_C = \pi r_0^2\frac{Z^2}{\varepsilon}\left(ln(2\varepsilon)+\frac{1}{2}\right)\ if\varepsilon \gg 1 \quad \text{III-6}$$

III.3.3.c.The pair production

The effective section for the pair creation is zero if $E < 2E_0$. When $E > 2E_0$, two cases should be considered [181]:

$$\sigma_{Pair} = \begin{cases}\alpha r_0^2 Z^2\left[\frac{28}{9}\log\left(\frac{2E}{E_0}\right)-\frac{218}{27}\right] & si\ 2E_0 \leq 2E_0 \leq \frac{E_0}{\alpha}Z^{\frac{1}{3}} \\ \alpha r_0^2 Z^2\left[\frac{28}{9}\log\left(183Z^{\frac{1}{3}}\right)-\frac{2}{27}\right] & si\ E \geq \frac{E_0}{\alpha}Z^{\frac{1}{3}}\end{cases} \quad \text{III-7}$$

III.3.4.Relative dominance of effects

The effective cross section associated with each type of interaction between incident photons and matter is influenced by both the energy of the incident photons and the atomic number of the material. Therefore, the total effective cross-section for all interaction types is the sum of the individual effective cross sections of the various possible processes. It can be represented as:

$$\sigma_{Total} = \sigma_{Pair} + \sigma_{PE} + \sigma_C \quad \text{III-8}$$

The importance and dominance of the different photon-matter interaction types vary depending on the energy of the photons and the atomic number of the material, as resumed in Figure III-8.

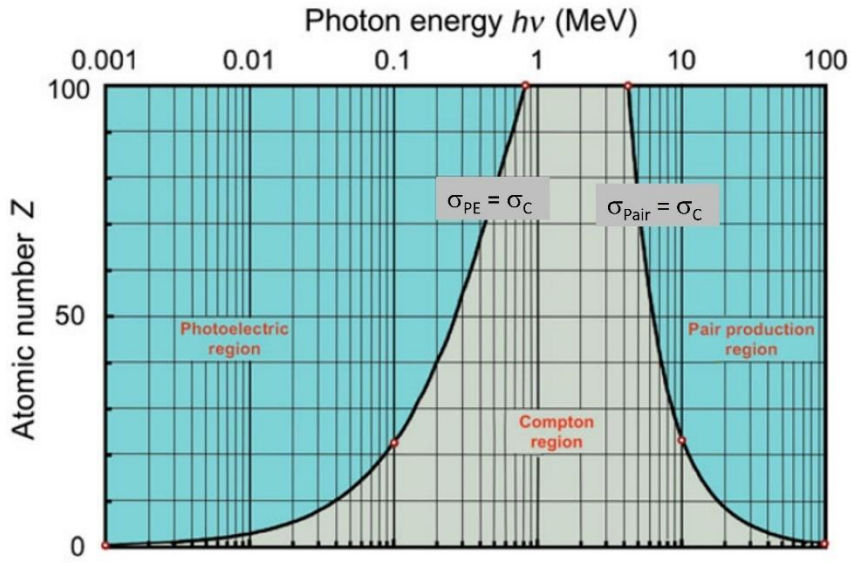

Figure III-8: Representation of the relative predominance of the three main processes of photon interaction with absorber atom in a (hv, Z) diagram where $h\upsilon$ is photon energy and Z is the absorber atomic number. Photoelectric and Compton cross sections are equal ($\sigma_{PE} = \sigma_C$) shown by the curve on the left and Compton and pair production cross sections are equal ($\sigma_{Pair} = \sigma_C$)) shown by the curve on the right. Attach points for the two curves are: $h\upsilon$ = 0.001 MeV, $Z \approx 0$; $h\upsilon$ = 0.1 MeV, $Z = 22$; $h\upsilon$ =0.8 MeV, Z = 100; $h\upsilon$ = 4 MeV, Z = 100; $h\upsilon$ = 10 MeV, $Z = 22$; and $h\upsilon$ =100 MeV, Z =0. Taken from [183]

The behavior of photon-matter interactions can be observed as follows:

- the photoelectric effect is dominant at low photon energies and for materials with high atomic numbers.
- the compton effect becomes more significant at intermediate photon energies and for materials with lower atomic numbers.
- pair creation becomes dominant at higher photon energies, typically above a few million electron volts (MeV), and for heavy materials.

III.3.5.Attenuation of the photon beam

A mono-energetic and collimated beam is attenuated by passing through a homogeneous medium, according to the following Lambert-Beer law:

$$I(x) = I_0 e^{-\alpha(h\nu,Z)x} \qquad \text{III-9}$$

Where I_0 is the initial intensity of the incident beam, x is the thickness of the crossed medium, $\alpha(h\nu,\mathrm{Z})$ is the linear absorption/attenuation coefficient that depends on the photon's energy as well as on atomic number Z. It equals to:

$$\alpha = n\sigma_{Total} = n(\sigma_{Pair} + \sigma_{PE} + \sigma_C) \qquad \text{III-10}$$

where n is the number of atoms per cm^3 in the medium and σ_{Total} is the total effective cross-section. The unit of α is cm^{-1}.

The mass attenuation coefficient takes into account the density of the material, which is equal to:

$$\alpha_m = \frac{\alpha}{\rho} \qquad \text{III-11}$$

whose unit is cm^2/g.

Figure III-9 shows an example of the evolution of the global and the partial absorption coefficients according to the energy of photons in lead, where $\mu = \frac{\alpha}{n}$.

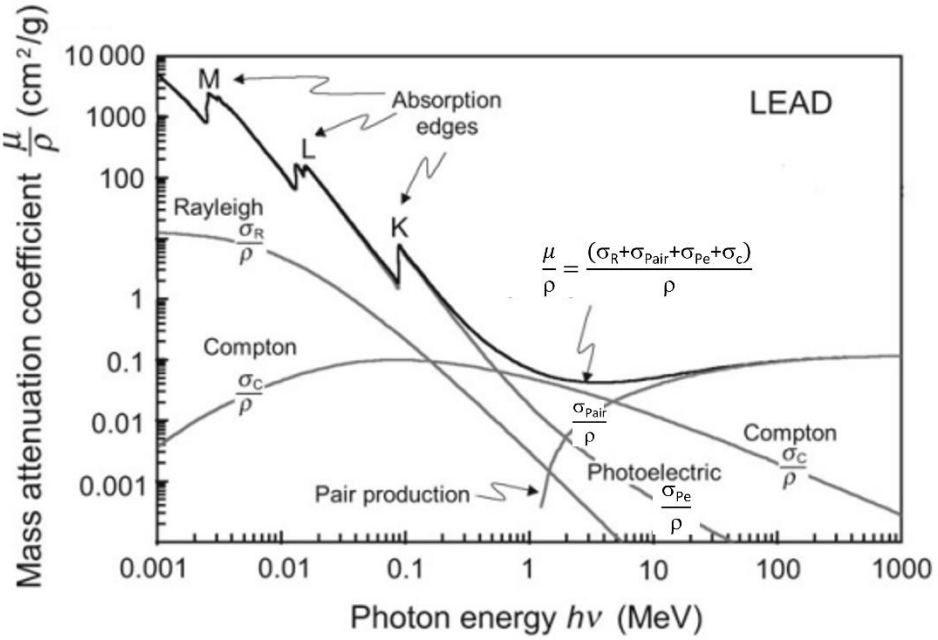

Figure III-9: Evolution of the absorption coefficient according to the energy in lead (Z=82). Adapted from [183].

III.3.6.Physical quantities of dosimetry

There are several physical quantities of dosimetry, we will resume here the most needed one in our context. For more information, readers are invited to check reference [181].

III.3.6.a.Absorbed dose

The absorbed dose, denoted as D, is defined as the ratio of the mean energy being absorbed into a volume of material $\mathrm{d}\bar{\mathrm{E}}$ to the mass of that material dm. It can be expressed as:

$$D = \frac{\mathrm{d}\bar{\mathrm{E}}}{dm} \qquad \text{III-12}$$

In this equation, $\mathrm{d}\bar{\mathrm{E}}$ represents the incident energy minus the outgoing energy. The absorbed dose is measured in units of joules per kilogram (J/kg) or Gray (Gy), where 1 Gy is equivalent to 1 J/kg. It's important to note that the absorbed dose only quantifies the amount of energy deposited in the material and does not consider the biological effects of radiation on living tissue.

III.3.6.b.Effective atomic number

The effective atomic number Z_{eff} is a parameter used to compare the radiological characteristics of various materials to one another or to water, which makes up the majority of living tissues. The following equation provides an approximation for calculating Z_{eff} for a compound material [184]:

$$Z_{eff} = \sqrt[m]{\sum f_i Z_i^m} \qquad \text{III-13}$$

In this equation, Z_i represents the atomic number of element i, $f_i = \frac{Z_i}{\sum_j Z_j}$ represents the fraction of electrons of element i relative to the sum of the atomic electrons in the material, and m is a value derived from the principles of photon-matter interactions. The specific value of m is still a matter of debate, as it depends on the involved Z_i in presence in the material and on the photons' energy. For this approximation, a value of m = 2.94 recommended by Mayneord [185] is used. For example, the effective atomic number of water is approximately 7.42.

The atomic number of an object directly affects the amount of energy it can absorb. As Z_{eff} increases and energy decreases, the absorption of radiation increases. Therefore, lower-energy photons (keV) are more strongly absorbed by matter compared to higher-energy photons (MeV). This is why the impact of Z_{eff} on the interaction between radiation and matter is crucial at low energies, namely in the regime of predominance of the photoelectric effect where the effective absorption cross-section varies like Z^2.

To accurately measure the dose in a specific medium of interest, it is desirable for the Z_{eff} value of the dosimeter to be as similar as possible to that of the target medium. For example, in microelectronics, a dosimeter with an effective atomic number equivalent to silicon (Z_{eff} = 14) is preferred in general, while dedicated medical dosimetry is required for human tissue (such tissues showing Z_{eff} = 7.42).

III.3.7.Properties of dosimeters

In the field of science known as dosimetry, a dosimeter is an essential device used to measure the level of ionizing radiation. This device plays a critical role for individuals working in environments where radiation exposure is a concern. The primary purpose of a dosimeter is to ensure that an individual does not receive a dangerous dose of radiation over a specific period. Various governing bodies establish standards for managing and protecting against occupational radiation. By adhering to these standards, dosimeters help to maintain occupational dosage levels that are as low as reasonably achievable (ALARA). Indeed, dosimeters can directly or indirectly measure and evaluate quantities such as deposited dose, KERMA (Kinetic Energy Released per unit Mass), dose rate, or equivalent dose. Humans are particularly vulnerable to the dangers of radiation, and excessive doses of radiation can be

deadly. Dosimeters serve the crucial function of informing and alerting individuals when radiation levels become too high, thus helping to prevent radiation poisoning. By using dosimeters, workers can monitor their radiation exposure levels and take appropriate measures to minimize risks, ensuring their safety and well-being in radiation-exposed environments.

A radiation dosimeter must possess specific physical features that depend on the quantity being measured (dose or dose rate), the type of particles, and their energy. The following qualities are most required:

- accuracy, precision, and reproducibility: accuracy refers to the closeness of the measured value to the true value, while precision relates to the consistency and reproducibility of measurements under similar conditions. Repeated measurements can be used to estimate precision.
- linearity: a dosimeter's response should demonstrate linearity as a function of the dose or dose rate. Nonlinearity occurs when the response exceeds a certain range and typically manifests as saturation. Nonlinearity can decline the dosimeter's sensitivity, leading to inaccurate measurements.
- spatial resolution: in situations with significant dose gradients, such as stereotactic radiotherapy or brachytherapy, dosimeters with high spatial resolution are necessary to determine the dose distribution accurately.
- energy independence: dosimeters should exhibit energy independence, enabling their universal use across various radiation energies.
- directional dependence: dosimeters may exhibit variation in response based on the angle of incidence of radiation, which is referred to as directional or angular dependence. Dosimeters often have some angular dependence due to construction details, physical size, and incident radiation energy. This dependence can affect the repeatability of measurements and consequently their reliability. However, in specific applications like in vivo dosimetry using semiconductor dosimeters, directional dependence can be important. Therapy dosimeters are generally used in the same geometry in which they are calibrated.

III.3.8.Radiation-induced effects on optical materials

Radiation-matter interaction gives rise to three primary macroscopic phenomena: radiation-induced attenuation (RIA), radiation-induced emission (RIE), and radiation-induced refractive index change (RIRIC) [186]. While these processes are well understood today [187], their outcomes are challenging due to their dependence on various parameters. Key factors influencing the amplitudes and kinetics of these phenomena include:

- Characteristics of the optical material under test, such as its composition and presence of impurities, as well as its manufacturing process and history. This includes factors like pre-treatments involving thermal treatments, gas loading,

and pre-irradiation conditions.

- Irradiation parameters, including the dose, dose rate, and temperature applied during the interaction.
- The material's specific usage profile, such as the injected power level and the wavelength of the signal.

III.3.8.a.Radiation-induced attenuation

Radiation-induced attenuation (RIA) is the phenomenon that has been extensively studied, which significantly limits the applicability of many materials [186]. When a material is exposed to irradiation, the deposited energy causes structural modifications. RIA results in a decrease in the material's transmission properties across most of its entire band gap. Consequently, absorption bands emerge within the material's transmission window, corresponding to the formation of microscopic point defects, also known as color centers. The concentration of these radiation-induced defects progressively increases with the accumulated dose. This process is easily observable and becomes predominant for doses exceeding the kGy level (in SiO_2 for exemple). The RIA can be quantified using the formula, given in dB/km:

$$\alpha_{RIA} = -\frac{10}{L}\log\left(\frac{I}{I_0}\right) \qquad \text{III-14}$$

where L is the length expressed in km, I and I_0 represent the intensities of the transmitted signal after a given duration of irradiation and before the beginning of the irradiation, respectively.

The wavelength or energy range of the signals is a significant factor that influences the properties of radiation-induced attenuation. Different defects exhibit absorption bands with distinct peak positions and widths, mostly within the UV and visible range [188]. As a result, RIA tends to increase with shorter wavelengths. However, the specific characteristics of RIA depend on the material and irradiation conditions. Generally, increasing the total ionizing dose leads to a higher level of RIA. Initially, RIA rapidly increases up to a certain dose level, typically in the kGy range, as defects are generated from pre-existing weak precursor sites. Afterward, the rate of defect generation slows down or saturates as regular bonds become less efficient at producing point defects. After the end of irradiation, the RIA can remain stable if the defects are thermally stable or exhibit a decrease with varying kinetics if thermal bleaching occurs. This phase is referred to as RIA recovery. In dosimetry applications, it is desirable to have minimal healing or recovery since a more efficient recovery leads to the loss of information about the deposited dose, which is reflected in the amplitude of the RIA. The injected light power, which can vary from a few watts to tens of watts, is an important factor to consider in RIA measurements. It can activate two opposing phenomena in the material. Firstly, at high power levels, the photobleaching effect occurs. This means that the recombination or transformation of defects is facilitated, leading to the decrease of the RIA

levels and to an acceleration of RIA recovery kinetics. On the other hand, there is also a phenomenon known as photo-darkening. This occurs when the probe light itself generates defects in the irradiated material, leading to an increase in attenuation. The high-power light can stimulate the creation of additional defects, thereby enhancing the absorption of the material. Therefore, the choice of injected light power is crucial in accurately assessing and interpreting RIA measurements.

III.3.8.b.Radiation-induced emission

Radiation-induced emission (RIE) occurs when radiation contributes to the generation of light in a material [186]. This emission can be induced through various forms of stimulation, including radiative, thermal, optical, or mechanical means. Each form of stimulation applies energy to the material, resulting in electronic transitions between the valence and conduction bands. One can distinguish different types of stimulation, named as suggested by the induced emission form: radioluminescence (RL) [189], photoluminescence (PL) [190], thermoluminescence (TSL) [191], optically stimulated luminescence (OSL) [192] and finally triboluminescence [193]. Each form of stimulation has its unique characteristics and mechanisms, which will be further discussed in this section. It is important to note that triboluminescence, which involves the production of light due to the recombination of charges at a crystal fracture, is not specifically addressed in this manuscript.
High-energy radiation can induce a specific type of radiative emission known as Cerenkov emission. This phenomenon occurs when a charged particle travels through a medium at a speed greater than the speed of light in that material (which is determined by the material's refractive index). As a result, the charged particle emits photons in a cone-shaped pattern along its direction of propagation. This emission is only observed during the irradiation process and has a continuous spectrum. The intensity of Cerenkov emission is inversely proportional to the squared wavelength of the emitted light and is also dependent on the particle flux [194]. However, it should be noted that the manuscript does not delve further into the details of Cerenkov emission, as it is not directly relevant to the context of the research being discussed.

- Radiation-induced luminescence

There are two types of stimulation that can induce luminescence: photoluminescence and radioluminescence. Photoluminescence occurs when the material is exposed to a source of UV photons with sufficient energetic photons to activate it. On the other hand, radioluminescence occurs when the interaction is with high-energy particles or X-ray/Gamma photons, where the energy transmitted during the interaction is much larger than the ionization energy of the material. Both types of luminescence involve the emission of light from pre-existing or radiation-induced point defects that are excited by the radiation. In this section, the RL will

be more detailed since our material will be exposed to X-ray irradiation. Figure III-10 depicts the radioluminescence readout mode. RL refers to the spontaneous and continuous emission of light that occurs upon radiation exposure, allowing real-time information about the irradiation to be obtained. It is produced by the transition of an electron trapped in a metastable level within the material's band gap. During irradiation, electrons are excited from the valence band to the conduction band and can become trapped in pre-existing or radiation-induced centers upon returning to the valence band. Initially, the RL signal increases as direct recombination competes with electron trapping. However, once all the electron traps are filled, trapping probability is diminished, and more electrons are available for recombination. At this point, the RL signal reaches a stable level known as a plateau, whose intensity increases with the dose rate [195]. The RL signal is generally proportional to the dose rate [196]. When the irradiation ceases, the signal decreases but does not immediately return to the background level. This afterglow, known as phosphorescence, occurs as some charges are released at a slow rate from shallow traps [195]. It is important to note that the RL behavior depends primarily on the material itself. To enhance the emission, scintillating elements such as copper, cerium, and gadolinium are often added to the matrix, especially in silica-based or plastic optical fibers.

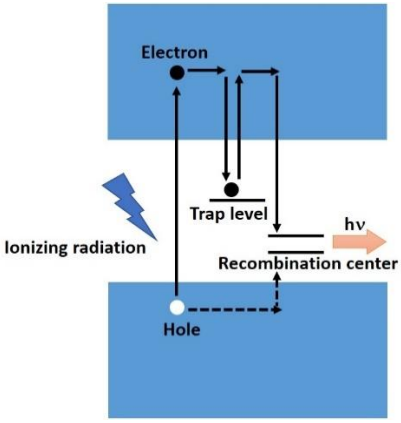

Figure III-10: Process of radioluminescence readout mode. Adapted from [197].

- Thermoluminescence and optically stimulated luminescence

Thermoluminescence is a process in which the activation energy for radiative transitions is provided by heat transfer from the surrounding thermal bath. The presence of defects or impurities in the material's band structure creates additional energy levels capable of trapping charges. When the material is exposed to radiation, charges are trapped in metastable levels. Subsequently, when the material is heated, the trapped charges undergo radiative transitions, releasing energy in the form of photons. To utilize thermoluminescence, a material must first be exposed to a radiation source. The energy deposited during the radiation exposure results in the trapping of charges in the metastable levels. By subsequently heating the material, the trapped charges are depopulated, leading to the

production of photons. The quantity of charges trapped is directly related to the dose of radiation deposited in the material. Therefore, the intensity response of thermoluminescent materials generally increases with the dose of radiation up to a saturation level [198]. Optically stimulated luminescence is a phenomenon that occurs after or during irradiation, where light from a laser is used to release trapped energy in the form of luminescence emission. OSL offers a promising technique for in vivo dosimetry in radiotherapy. The integrated dose measured during irradiation can be evaluated using OSL directly afterward [199]. To generate the OSL signal, the previously irradiated material is stimulated with light, enabling the released carriers to recombine. The principles of OSL and TL can be understood through the energy band model of electron-hole production following irradiation, as illustrated in Figure III-11. The process begins with irradiation, which leads to the ionization of valence electrons and the creation of electron-hole pairs. Pre-existing defects within the material localize the free electrons and holes through non-radiative transitions. By applying thermal luminescence or optical stimulation, or by using ultraviolet radiation (known as radiophotoluminescence or RPL, discussed later in detail), electrons gain sufficient energy to escape from the traps and recombine with holes in recombination centers. Recombination of the free electrons with the localized holes results in radiative emission and luminescence, where the stored energy is released in the form of visible light. Therefore, the TL or OSL signal is directly proportional to the dose. Under optical stimulation, the emitted light signal initially has a high value, which gradually decreases over time. This decrease indicates that the supply of electrons from the OSL traps is becoming exhausted. The OSL signal is influenced by various factors, including the number of traps, their capacity to release a charge carrier upon stimulation, the number of electrons remaining in the traps after the end of the exposure, and the wavelength of the stimulation, which determines the energy imparted to the trapped electrons. It's important to note that the OSL signal also depends on the time delay between the end of irradiation and the laser stimulation, as some electrons may get thermally detrapped before optical stimulation, a phenomenon referred to as fading [186].

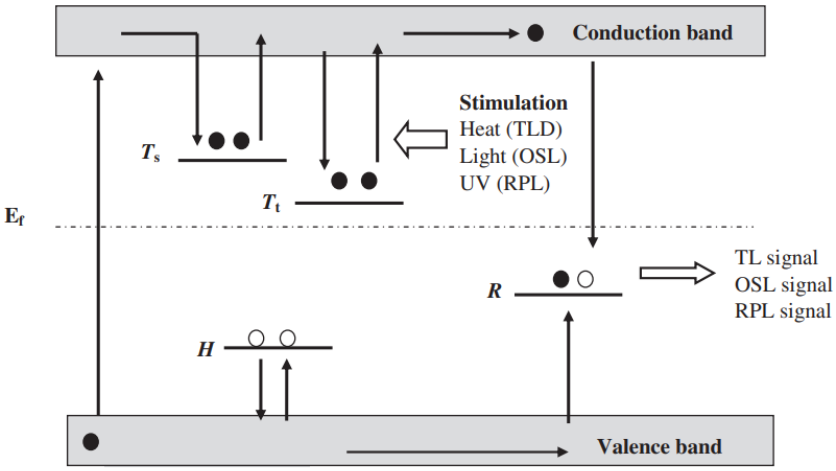

Figure III-11: Principles of TL, OSL and RPL process. Ionizing radiation creates electron-hole pairs. These electrons and holes become trapped at defects T and H. The trap T_s represents an unstable trap, from where the probability of escaping is large. T_t is a trap for storing electrons where the probability of escaping (without external stimulation) is negligible. By stimulating the sample either thermally (TL), optically (OSL) or by UV (RPL), electrons gain sufficient energy to escape from the traps and to recombine with holes in recombination centers (R). The recombination is followed by the emission of light. E_f is the Fermi level. Taken from [200].

However, a major drawback of OSL is the occurrence of fading, which is a spontaneous depletion and recombination of trapped carriers over time. Fading can be induced by ambient temperature (thermal fading) or ambient light (optical fading), and it gradually reduces the population of trapped carriers and consequently decreases the OSL signal level. The extent of fading depends on the delay between irradiation and optical stimulation. This phenomenon poses a challenge as it leads to a degradation of the collected information [181]. Therefore, the use of dedicated reading devices becomes necessary to accurately measure and interpret OSL signals [201].

- Radiophotoluminescence

The radiophotoluminescence technique, first studied by Schulman et al. [176], [202], has been extensively investigated in silver-doped phosphate glasses [203], [204]. These glasses are now considered a reliable passive radiation dosimetry method for ionizing radiation such as gamma rays and X-rays [205]–[208]. The silver atoms inserted in the phosphate glass exist uniformly and stably in the form of Ag^+ ions. After exposure to ionizing radiation, these glasses exhibit intense luminescence when excited with ultraviolet light, which is known as the RPL phenomenon. In Japan, the RPL dosimeter is commonly referred to as the "Glass Badge" and has gained widespread use through the individual dose monitoring service provided by Chiyoda Technol Corporation (CTC). The cationic weight composition of the Ag^+-doped phosphate glass was 31.55% P, 51.16% O, 6.12% Al, 11.00% Na, and 0.17% Ag.
To facilitate the diffusion of holes and accelerate the accumulation of Ag^{2+}, a preheating step is applied to the irradiated samples. Typically, the samples are preheated at 100°C for 30

minutes in a practical RPL dosimetry system, promoting the faster accumulation of Ag^{2+} species within the glass [206].

The basic mechanism responsible for luminescence in such glasses can be summarized as follows [209]–[213]-[214].

It is generally agreed that Ag^{+} ions are reduced by the capture of free electrons during irradiation to create Ag^{0} centers.

$$Ag^{+} + e^{-} = Ag^{0}(electron\ trap) \qquad \text{III-15}$$

Additionally, holes are captured by PO_4^{3-} centers to form PO_4^{2-} centers, also known as phosphorous-oxygen-hole centers (POHC).

$$h^{+} + PO_4^{3-} \leftrightarrow POHC \qquad \text{III-16}$$

Equation III-16 is reversible depending on the balance between hole trapping during irradiation and thermal release of holes at a given temperature. At room temperature and during the build-up after the irradiation period, the thermal release of holes from POHC sites is strong and leads to the subsequent capture of holes by Ag^{+} and the growth of Ag^{2+} :

$$Ag^{+} + h^{+} = Ag^{2+}(hole\ trap) \qquad \text{III-17}$$

This same defect can be brought back to its original state by releasing a hole through thermal relaxation, which will then be captured by an Ag^{+} ion.

$$Ag^{+} + POHC = PO_4^{3-} + Ag^{2+} \qquad \text{III-18}$$

There is also evidence in the literature for the formation of Ag-clusters and Ag-nanoparticles via diffusion of Ag^{+} ions. Ag^{+} may react with Ag^{0} to form Ag_2^{+} dimers, thus:

$$Ag^{+} + Ag^{0} = Ag_2^{+} \qquad \text{III-19}$$

Further reactions may occur to form Ag_3^{2+} trimers and, generally, Ag_m^{n+1} particles, with m = n+1.

Ag^{0} and Ag^{2+} become stable centers under the condition of room temperature. Additionally, RPL is a radiative transition induced by the photoexcitation of RPL centers and does not recombine the electron–hole pairs formed by ionizing radiation. Hence, information on the cumulative dose is not erased when the RPL dosimeter is read [215]. As the glass dosimeter always measures the integrated dose over time, it is necessary to subtract the cumulative dose recorded until the previous day from the total dose currently observed to determine the exposure dose for a specific period of exposure. This distinction is a significant difference compared to TL and OSL dosimetry methods. This difference has been clarified through various experimental analyses [206].

After the formation of Ag^{0} and Ag^{2+} species in RPL glasses, the migration of these species can lead to a clustering process, resulting in the formation of Ag_m^{x+} type silver clusters [216], [217]. However, the precise identification of the specific emitting centers, including their nuclearities and population concentrations, as well as their detailed generation mechanisms and optical characteristics, remains challenging. This topic is still an active field of research and debate [213]. Several species such as Ag^{2+}, Ag^{0}, Ag_2^{+}, and Ag_3^{2+} have been reported as the main RPL centers under post-irradiation UV light excitation [216]–[221]. Although several

articles have been published, no overall agreement has yet been achieved. Mainly, this phenomenon was observed by Miyamoto *et al*. (2010) and Kurobori *et al.* (2010) [211], [218]. An absorption band clearly exists around the UV region as shown in Figure III-12(a) in bleu curve and the emission spectrum from the glass excited by UV light after X-ray irradiation is also shown in black curve. It is seen that the spectrum mainly consists of two regions. It is generally agreed that the main RPL emission was ascribed to the orange emission peaking around 630 nm with a weaker blue emission peaking around 450 nm. Hence, the orange RPL was attributed to the hole-trapped Ag^{2+} centers, while the blue emission was associated to silver ion reduction [211], [212], [214], [222]. It's worth noting that the lifetime of the blue RPL emission, which corresponds to the decay time of the luminescent signal, is approximately 2-10 ns. In contrast, the orange RPL emission has a longer lifetime of about 2-4 µs [209]. This lifetime difference between the blue and orange RPL emissions is around three orders of magnitude, indicating significantly different decay characteristics for these two types of luminescence. Based on the obtained results, Figure III-12(b) displays the energy band diagram for RPL process in Ag^+-doped phosphate glass, as already explained in this section. The photoluminescence (PL) could be excitedat the wavelength of about 5.34 eV (232 nm) is observed from Ag^+-doped phosphate glass before X-ray irradiation when the glass is exposed to UV light. This emission might mainly be due to the excitation and relaxation process between the energy levels of the initial Ag^+ dopants.

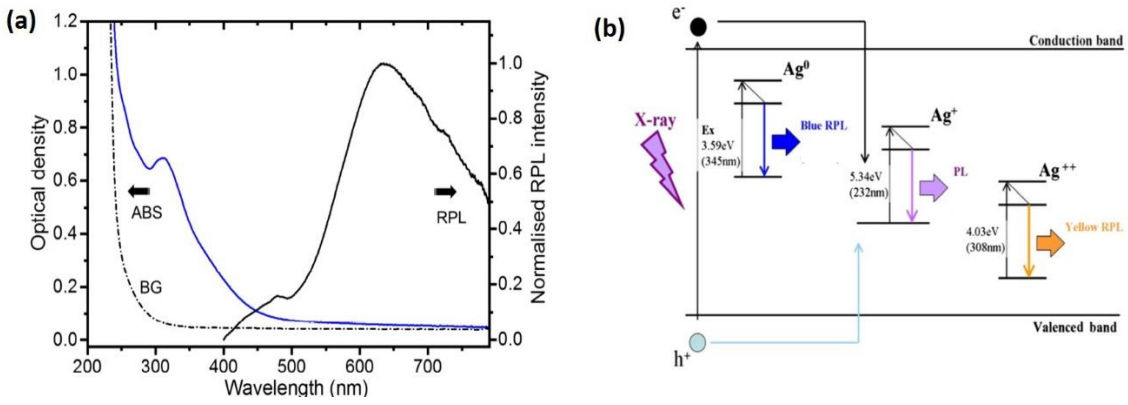

Figure III-12: (a) Optical absorption spectra (left axis) as well as typical RPL emission spectra (right axis) of Ag^+-doped phosphate glass after X-ray irradiation. Taken from [223]. (b) Energy band diagram of RPL centers as well as PL centers in Ag^+-doped phosphate glass. Taken from [224].

As RPL is known to be an established method for the determination of the absorbed doses [203], [205]–[207], this technique can be applied to the individual monitoring of ionizing radiation as well as to the monitoring of the natural environmental and/or man-made-emitting radiations in the dose range from tens of µGy up to several hundred of Gy [209]. An observed limitation is that the RPL signal continues to increase both during and after irradiation. This signal grows following a saturating, exponential-type model, reaching a

steady-state level after some hours. This well-known mechanism is called the "build-up" effect. The RPL signal is stabilized by the use of post-irradiation annealing procedures [208], [214]. The build-up effect, which is the increase in the RPL intensity with time or heating, was simulated based on the assumption that the formation of Ag_2^+, which occurs due to Ag^+ diffusion, and the hole transfer from hPO_4^2 to Ag^+ is thermally activated.

RPL glass dosimeters exhibit many good characteristics such as good reproducibility of the readout value, low energy dependence for photon energies within ±10% in the 0.03–1.3 MeV range, good dose linearity from 0.01 to 500 mGy [225]. Moreover, the luminescence centers are very stable unless the glass dosimeter is annealed at about 400 ºC. This allows repeatable measurements to be achieved with little dispersion among samples and long-term stability against the fading effect (less than 1% fading after 30 days) [209], [226]. Therefore, RPL glass dosimeters have been widely used as one of the accumulation-type dosimeters, among other types [227].

To provide a more comprehensive understanding of the current state of the RPL process and its significance in relation to our experimental work, a dedicated section will be devoted to this topic in the upcoming section III.3.9). This section will investigate the latest advancements, theories, and research findings related to the RPL process.

III.3.8.c.Radiation-induced refractive index change

The change of the glass density and the RIA are the two mechanisms responsible for the observed radiation-induced refractive-index change (RIRIC).

The Lorentz-Lorenz formula can explain how the density ρ modification affects the refractive index n, as follows:

$$\frac{n^2-1}{n^2+1} = K\rho \qquad \text{III-20}$$

where the proportionality constant K depends on the glass polarizability.

The part of the RIRIC caused by point defects is described through the Kramers–Kronig relations, which defines the relation between the refractive index and the absorption band variation [228]:

$$\Delta n(\lambda) = \frac{\lambda^2}{2\pi^2}\int_0^\infty \frac{\Delta\alpha(\lambda')}{\lambda^2-\lambda'^2}d\lambda' \qquad \text{III-21}$$

Primark has observed for the first time a refractive index increase for amorphous silica from 1.46 to 1.4670 and a refractive index decrease for quartz from 1.555 to 1.4680, in the case of the amorphous or crystalline silicon dioxides, under irradiation with a neutron fluence of 10^{20} n.cm^{-2} [229]. The RIRIC also affects the optical fiber waveguide structure, as discussed in reference [230].

III.3.9.State of art of RPL dosimeter

In this section, we will examine some of the recent progress and research findings related to the RPL process. This section will serve as a needed platform to present our results, enabling us to contribute to the field of RPL research.

The development of RPL dosimeters has led to significant progress in radiation dose measurement and has exhibited promising characteristics such as stable sensitivity, negligible fading, and reliable repeatability. Initially discovered by Schulman *et al.* in 1951 [176], RPL dosimeters have applied in measuring radiation doses ranging from 0.1 to 1 Gy. Over time, the performance of RPL dosimeters and their readout systems has significantly improved. Notably, Yokota *et al.* [217] made substantial progress by adjusting the glass composition, extending the measurable dynamic range from 0.1 mGy to 10 Gy. Despite this progress, practical limitations persisted, such as inherent photoluminescence from the glass itself and PL caused by surface dirt, which introduced noise in the measurement of true RPL. Piesch *et al.* [204] successfully addressed this issue by employing a pulsed laser beam as the excitation UV light, effectively eliminating the PL noise. This breakthrough pushed RPL dosimeters to become a practical dosimetry system. Moreover, Perry [205] has provided an extensive review of RPL studies. Currently, RPL dosimeters have made remarkable progress alongside improvements in electronics, finding wide adoption as practical dosimeters ranging from 10 μGy to 10 Gy. The application of Ag-doped phosphate glasses in RPL dosimetry systems has expanded to various fields, including personal monitoring [231], environmental monitoring [227], [232], [233], medical dosimetry [234], [235], and dose imaging [222]. Recent research has reported novel applications of Ag-doped phosphate glasses in RPL dosimeters, such as different shapes [234], [236], [237], real-time monitoring [214], [238], and high-temperature-resistant dosimeters. For instance, researchers have developed glass dosimeters in bead and sheet forms to adapt to different environments in radioactively contaminated areas. The sheet-type dosimeter, coupled with a two-dimensional RPL reader, enables the visualization of the radiation dose distribution. Moreover, RPL material hand phantoms have been fabricated to understand extremity dosimetry for the hands of radiation workers. These progress have proven to be useful in the context of radiotherapy and radiodiagnosis, where technicians often receive significant exposure at their hands [234], [237]. Furthermore, 3D dosimeters using RPL materials have been created through fused deposition modeling 3D printing technology. The RPL intensity of these dosimeters showed good linearity with respect to absorbed doses above 30 mGy. Prototype dosimeters, such as ear and ring shapes, have been developed to improve dose estimation accuracy and determine the irradiation position for radiation therapy. The ring-shaped dosimeter's function was to measure the local exposure dose to the fingers in the manner of a ring badge. The ear-shaped dosimeter helps to increase the accuracy of the dose estimation and radiation irradiation position of an ear for radiation therapy. In addition to these developments, new

RPL glass dosimeters, such as Ca-Na phosphate glass, have been designed for high-temperature conditions, showcasing superior temperature dependence compared to traditional Al-Na phosphate glass. These dosimeters have demonstrated satisfactory RPL intensity sustainability at 573 K for 3 hours [239]. Recent studies have explored the use of RPL glasses as in-situ, subsurface environmental radiation monitors, demonstrating sufficient sensitivity for measuring environmental doses of approximately 100 µGy [208]. Real-time dosimetry technology has also been developed by coupling RPL glasses with fiber systems to continuously excite the glass and collect its RPL signal [238]. However, real-time RPL dosimetry remains challenging due to the build-up effect, which involves the formation of RPL centers over time.

Overall, the continuous progress and diverse applications of RPL dosimeters have significantly contributed to the field of radiation dosimetry, expanding their utility in various sectors and pushing the boundaries of dose measurement capabilities.

III.4.Spectroscopy of fs-inscribed silver clusters under X-ray irradiation

As previously described in section IIII.2, the combination of RPL and fs DLW has been utilized to assess the potential of laser-inscribed structures as localized probes for measuring deposited doses. For this reason, the first section below will present a post-X-ray irradiation study on fs-inscribed glasses, which will be compared to pristine glasses.

III.4.1.Post-X-ray irradiation study

III.4.1.a.Experimental methods

i. Glass samples

Three glass compositions are used in this study. The first one is a commercial silver-containing zinc phosphate glass manufactured by Argolight Company (referred to as ARGO elsewhere). This glass is similar in composition to the one detailed elsewhere [240]. The second one is also a commercial glass from the same company, which is a silver-containing magnesium-phosphate glass (referred to as ARGO3 elsewhere). The third one is an academic silver-containing gallo-sodo-phosphate glass (referred to as GPN elsewhere), synthesized using a classical melting-quenching method [177]. The GPN glass is a pyro-phosphate glass with a strongly depolymerized phosphate network, mainly composed of dimeric phosphate tetrahedra. It was shown that this glass exhibits high photosensitivity to fs DLW, leading to highly fluorescent structures, which result both from its glass network and the presence of co-mobile sodium ions [146]. The refractive index of the GPN and ARGO glasses is measured at 589 nm using an Abbe refractometer enabling a precision of ±0.002. The chemical

composition, the refractive index, and the glass transition temperature of the two glass samples are reported in Table III-1. The composition of the ARGO3 glass sample is not provided by the company as it is confidential, and we didn't measure it.

Table III-1: The different properties of the three glass samples.

Acronym	**Nominal cationic composition (mol %)**	**n_{589}(±0.002)**	**Temperature of glass transition T_g (°C)**
ARGO	$39.4P_2O_5$-53.8ZnO-$5.8Ag_2O$-$1Ga_2O_3$*	1.611	375
GPN	$56.0P_2O_5$-$28.0Ga_2O_3$-$14.0Na_2O$-$2.0Ag_2O$	1.566	497

**For the ARGO glass sample, the company doesn't provide the glass composition. Indeed, we have measured this composition and our finding is similar within the measurement error bar to reference [240] with a small addition of Al_2O_3 replacing Ga_2O_3 and with the same volumetric silver oxide concentration.*

Unlike currently commercialized RPL dosimeters (Ag-doped phosphate glasses with 0.17% Ag (w.c.)), our glasses contains one order-of-magnitude more silver ions (2.87% for the ARGO composition and 0.7% for the GPN composition). Due to the high concentration of silver oxide incorporated in our two glasses, silver ions are weakly involved in isolated Ag^+ sites emitting at 290 nm for an excitation centered around 220 nm (labeled environment or site A) and dominantly involved in Ag^+-Ag^+ pair sites showing an emission band near 380 nm for an excitation near 260 nm (labeled environment or site B) [42], [146]. Silver-containing phosphate glasses exhibit a transparency window from the visible range to the MIR (typically limited around 2.9 µm due to hydroxyl groups), as already seen in Figure II-3.

ii. Infrared femtosecond DLW of pristine glasses

DLW was performed using a Yb:KGW fs oscillator (T-pulse 200, 9.8 MHz repetition rate, 412 fs pulse duration (FWHM) and emitting at 1030 nm wavelength, Amplitude system) combined with an acousto-optic modulator in order to control the pulse energy and the deposited number of pulses. The sample displacement and positioning were carried out using a high-precision 3D translation stage (XMS-50 stages, Newport). A spatial light modulator is used to compensate for both the different focal planes and the spherical aberrations. The microscope objective used for this experiment is adapted for laser focalization under a microscope cover slide of ~170 µm with a refractive index (RI) of ~1.518. Given that our glasses exhibit higher refractive indices, the corresponding refractive index mismatch leads to a focused beam diameter slightly larger than that obtained under ideal diffraction-limited focusing conditions. At the top, a CCD camera is placed in order to visualize the glass surface and the writing process. Bottom white and blue illuminations at 405 nm are applied. White light is used to visualize and find the surface of the glass while the blue illumination serves to monitor and visualize the fluorescence of the silver cluster created during DLW. A 405 nm high pass filter

is placed before the CCD in order to cut the blue diode at 405 nm allowing the observation of the fluorescence of silver clusters. The setup is presented in Figure III-13.

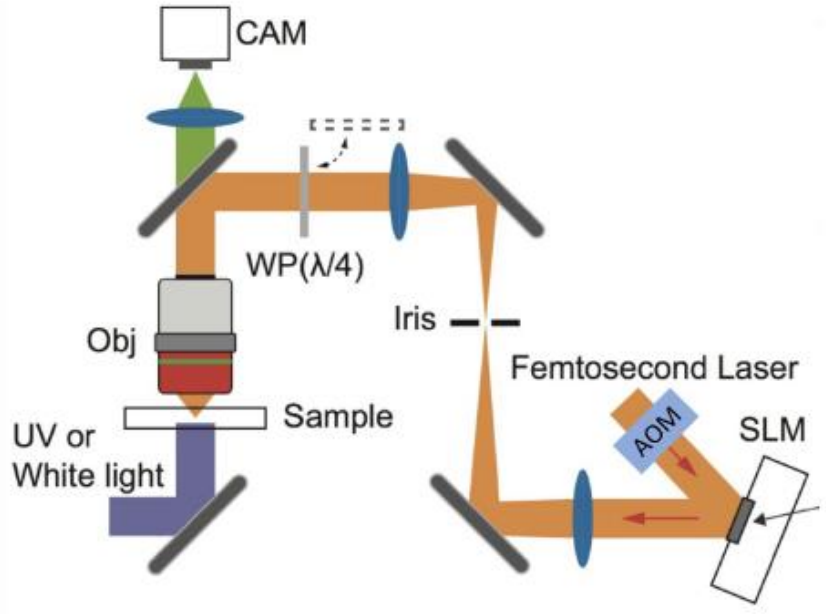

Figure III-13: Schematic of the laser setup used for direct laser writing.

In this study, two glass samples were utilized for the GPN composition. The first glass sample, referred to as GPN in the manuscript, was inscribed and irradiated as described in reference [177]. On the other hand, the second glass sample was inscribed and irradiated following the same procedures as the ARGO and ARGO3 samples. Throughout the manuscript, this second sample will be referred to as GPN2. The detailed inscription and irradiation conditions for all samples will be provided in the subsequent sections.

For the inscribed ARGO, ARGO3 and GPN2 glass samples, the fs-inscribed glasses will be referred respectively to as ARGOi, ARGO3i and GPN2i elsewhere in the manuscript, the letter *i* standing for the fs laser inscription. A cartography of square linear structures of 100 µm x 100 µm with an interline spacing of 5 µm was inscribed inside the glass typically 150 µm below the surface (adapted depth for the objective) using a microscope objective (Carl Zeiss, 20x - 0.75 NA). The irradiance I was changed during the writing for each sample while the writing speed was fixed at 70 µm/s. Therefore, the following irradiance ranges were applied: for ARGOi I = 7.5 - 11 TW/cm^2, for ARGO3i I = 11 - 14.2 TW/cm^2 , for GPN2i I= 12.7 - 14.2 TW/cm^2. To have the same laser parameters at the focus spot and thus to create identical silver clusters in two different planes, the samples were flipped by 180° to inscribe the same structures at 150 µm below each of the two glass surfaces. In this way, the same DLW structures were successively written at 150 µm and 550 µm below the glass front surface, knowing that the glass thickness is 700 µm. Similar luminescent patterns were obtained on the three samples. Figure III-14 shows the laser-inscribed silver clusters in the ARGOi glass sample.

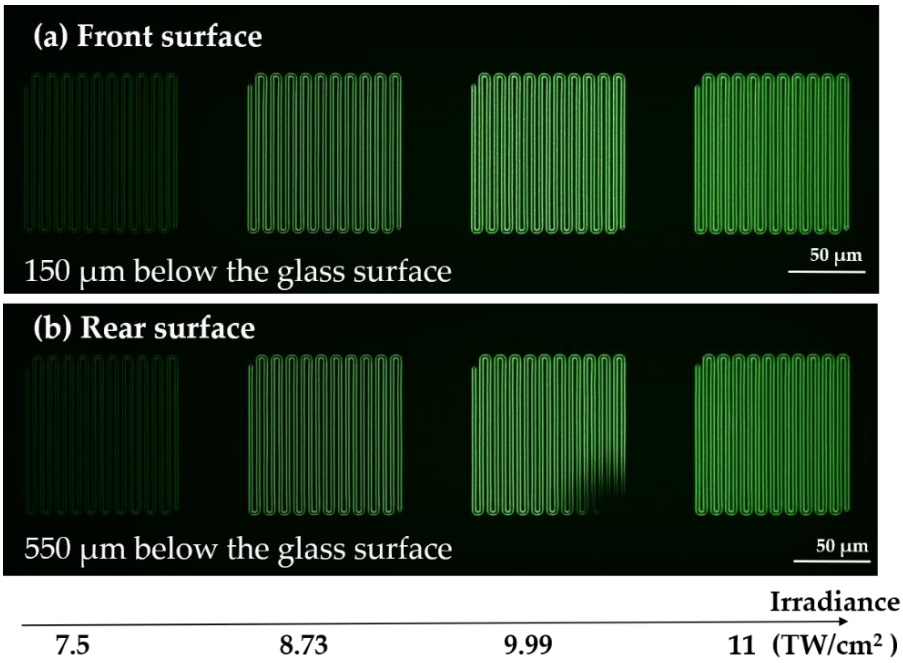

Figure III-14: Microscopy fluorescence image of ARGOi glass sample (excitation at 365 nm) of laser inscribed structures for the different writing irradiance at two different depths: (a) structures at 150 μm below the glass front surface, (b) structures at 550 μm below the glass front surface and at 150 μm from the glass rear surface.

Regarding the GPN glass, DLW was performed on a 1 mm thick sample. The inscribed glass will be referred to as GPNi elsewhere in the manuscript. The same experimental setup described above was used to create a 3×3 mm^2 square inscribed at 160 μm below the glass surface (adapted depth for the objective) for an irradiance of 13.4 TW/cm^2 and a writing speed of 100 μm/s [177].

iii. X-ray irradiations of pristine and laser-inscribed glasses

ARGO, ARGOi, ARGO3, ARGO3i, GPN2, GPN2i glasses were irradiated (referred to as ARGO*, ARGOi*, ARGO3*, ARGO3i*, GPN2*, GPN2i* elsewhere in the manuscript) using the MOPERIX X-ray irradiator of Laboratory Hubert Curien of University Jean Monnet (Saint-Etienne, France), in collaboration with the team MOPERE (Materials for Optics and Photonics in Extreme Radiation Environments, Team leader Sylvain Girard, with the involved colleagues Adriana Morana. Youcef Ouerdane and Aziz Boukenter). The X-ray tube of the irradiator, with a tungsten anode, was operated at 100 kV and a current of 13.7 mA, providing X-rays with 40 keV mean-energy fluence. X-ray irradiation measurements were taken at ambient temperature. The dosimetry was done with a PTW 23344 ionization chamber connected to a PTW UNIDOS E unit allowing to measure the deposited dose at the sample surface with respect to water. ARGO, ARGOi, ARGO3 and ARGO3i samples were irradiated with the same dose rate of 50 mGy(H_2O)/s while changing the exposure time to accumulate three different doses of 2, 22, and 222 Gy(H_2O). On the other hand, GPN2 and GPN2i followed a similar irradiation protocol but accumulated only 2 and 22 Gy(H_2O).

X-ray irradiated glasses were colored in yellow after 222 Gy as shown in Figure III-15.

Figure III-15: (a) Transparent color before irradiation (ARGO glass sample), (b) Yellow color after X-ray irradiation with 222 Gy (ARGO glass sample).*

X-ray irradiations on GPN glass (referred to as GPN* as the irradiated GPN elsewhere in the manuscript) were conducted using a Philips PW2274 X-ray tube with tungsten anode, operated at 20 kV and 32 kV for micro-luminescence and RPL experiments respectively, at the Department of Materials Science of the University of Milano-Bicocca. The dose values were obtained by comparison with a calibrated ^{90}Sr-^{90}Y beta radioactive source and using optically stimulated luminescence emission from quartz crystalline powder (100-200 µm). For the radiation-induced absorption spectra, the GPN glass sample was irradiated with a Machlett OEG50 X-ray tube with a tungsten anode, operating at 32 kV. Dose evaluation was performed using a PTW Duplex calibrated ionization chamber. Two X-ray irradiation series were conducted, from 5 mGy to 5 kGy and from 2 to 365 Gy [177].

iv. Absorption spectroscopy

The transmission spectra for the ARGO, ARGO*, ARGO3, ARGO3*, GPN2, GPN2* glass samples were recorded with a Cary 5000 (Agilent Technologies) spectrophotometer in double beam configuration between 260-800 nm with a step of 1 nm and an integration time of 0.5 second.

UV-Visible transmission spectra of the GPN and GPN* were recorded with a Cary 5000 (Varian) spectrometer in the range 200-800 nm with a step of 1 nm and an integration time of 0.1 second [177]. Note that both transmission spectroscopy spectra were collected over the entire glass thickness.

v. Radiophotoluminescence micro-spectroscopy

Distinct radiophotoluminescence measurements were carried out with two distinct equipment corresponding to a confocal LabRam Aramis (Jobin-Yvon) micro-spectrophotometer with a cooled CCD camera. One system (used for ARGO samples) was equipped with a HeCd laser (CW excitation at 325 nm), a UV microscope objective (40×, 0.5 NA) (Hubert Curien laboratory (LabHC), St Etienne, France). The other system (used for GPN samples) was equipped with a CW laser diode (excitation at 405 nm), an Olympus microscope objective (100×, 0.9 NA) (ICMCB, Bordeaux, France).

For the first system, emission spectra were dispersed by a diffraction grating of 150 lines/mm

and were recorded with a step of 5 µm during linear cartography for a spectral regions 450-800 nm. The excitation source was perpendicular to the front surface; the emission spectra were epi-recorded from the same facet. Those measurements were made for the ARGO, ARGOi, ARGO3, ARGO3i, GPN2, GPN2i, before and after irradiation. All the spectra in this experiment are not corrected by the spectral response of the instrumental chain of detection.
For the GPN* glass, the micro-luminescence measurements have been performed from the lateral facet of the glass, perpendicularly to the front X-rays irradiated face. The spectral emissions were identically collected and then recorded for different lateral positions, corresponding to different X-ray irradiation depths, with position steps every 50 µm [177].

vi. Micro-absorption spectroscopy

A homemade micro-absorption experiment was recently mounted to measure the differential absorption coefficient for the different inscribed patterns compared to a non-inscribed zone in the ARGOi*and ARGO3i* glass samples.
A tunable Ti-Sapphire laser (Chameleon Vision-S, tuning range 690-1050 nm, 80 MHz repetition rate, 75 fs pulse duration at 800 nm, average power at peak > 2.5W), was used as a broadband tunable excitation. The measurement was achieved using a BBO crystal (6×6×0.5, θ =29.2, φ= 90, SHG at 800 nm, type 1) to obtain a tunable frequency-doubled beam emission in the UV-visible range. The wavelength sampling (356-514 nm) is adjusted to have constant photon energy variation steps. The transmission spectra were collected with symmetrical scanning between a structured and a non-structured zone using a galvanometer scanning system (GSI Lumonics scan controller). A CCD camera is placed in order to visualize the structures and the scanning process. A blue diode at 380 nm was used as blue illumination to visualize the fluorescence of the structures on the CCD. A 435 nm long-pass filter is placed before the CCD to cut the blue diode, allowing the observation of the fluorescence of silver clusters.
The scanning signal is collected using a photodiode connected to an oscilloscope. A modulated current signal of a scan between an inscribed zone and a non-inscribed zone was compared to that in a fully non-inscribed zone. The difference between the two signals allows extracting the value related to the inscribed structures. The local differential linear absorption coefficient was then calculated considering the transverse filling rate of the inscribed structure.

vii. Phase imaging microscopy and local refractive index change

Refractive index variation Δn between the unmodified glass and the silver clusters was measured for all the samples, except GPN sample, using a phase-contrast microscopy method with the commercial SID4Bio wavefront sensor (PHASICS company). A 100× – 1.3 NA oil immersion objective was used to image the structures using white light illumination.

The final output of the wavefront sensor gives an intensity image and a phase image showing the optical path difference (OPD) experienced by light while passing through the laser-induced modified areas of the samples. Given the OPD, the real value of Δn could be estimated by dividing the OPD by the thickness of the structures [147].

viii. Fluorescence Lifetime Imaging Microscopy (FLIM)

The fluorescence lifetime imaging microscopy (FLIM) analysis was performed for all the samples, except GPN sample, with a Picoquant MT200 microscope equipped with two MPD single photon avalanche diodes (SPADs) and a PicoHarp300 timing board for time-correlated single photon counting (TCSPC) operation in epi-collection mode. This measurement was conducted at the ISM Laboratory (Institut des Sciences Moléculaires) with Guillaume Rafy.
The pulsed laser source was a PicoQuant picosecond laser diode (fibered) at 375 nm. The laser was injected by a 100×,1.40 NA oil objective (UPLSAPO100XO, Olympus, Tokyo, Japan) by an 80%T-20%R spectrally flat beam splitter. The fluorescence was collected by the same objective and transmitted by the same beam splitter to the confocal optics and detectors. The backscattered excitation light was rejected from the fluorescence signal through a 405 nm long-pass filter. Then, the signal was split by a 50/50 non-polarizing beam splitter cube to the two SPADs and filtered by two bandpass filters ((a) HQ510/80 with a 470–550 nm transmitted spectral window; (b) HQ425/50 with a 400-450 nm transmitted spectral window), both from Chroma Technologies, Rockingham, VT, USA. The laser was scanned by means of a piezoelectric stage in a grid pattern of 40x40 µm, 80 nm pixel and 0.6 ms/pixel. For the FLIM images, a reference time was defined at the onset of the global image decay curve. The reported lifetime in each pixel was calculated as the first statistical momentum of the histogram distribution of the single photon arrival times, minus this reference time, pixel by pixel. This method is referred to as FAST-FLIM. For quantitative analyses, decay curves corresponding to full images were fitted by a multi-exponential model using a "tail-fitting" method i.e. without considering the convolution by the impulse response function of the instrument.

III.4.1.b.Results

i. Study of non-inscribed samples exposed to X-rays

- GPN

Figure III-16(a) presents the absorption spectra for the GPN and GPN* glass samples obtained after subjecting the sample to a series of X-ray irradiation ranging from 5 mGy to 3 kGy. New absorption band contributions appear in the GPN* glass sample, showing an increase with the irradiation and having a maximum at about 320 nm (Figure III-16(a)). Moreover, the difference absorption coefficient spectra between different conditions of

irradiations are presented in Figure III-16(b) for the GPN and GPN* glass samples. At higher doses, the cut-off of the glass increases as shown in the 50 Gy vs. 5 Gy dose difference spectrum with additional bands at 320 at 390 nm (3.87 eV and 3.19 eV, respectively). A complementary contribution at 280 nm appears from the 500 mGy vs. 50 Gy dose difference spectrum and above with the growth of both absorption bands.

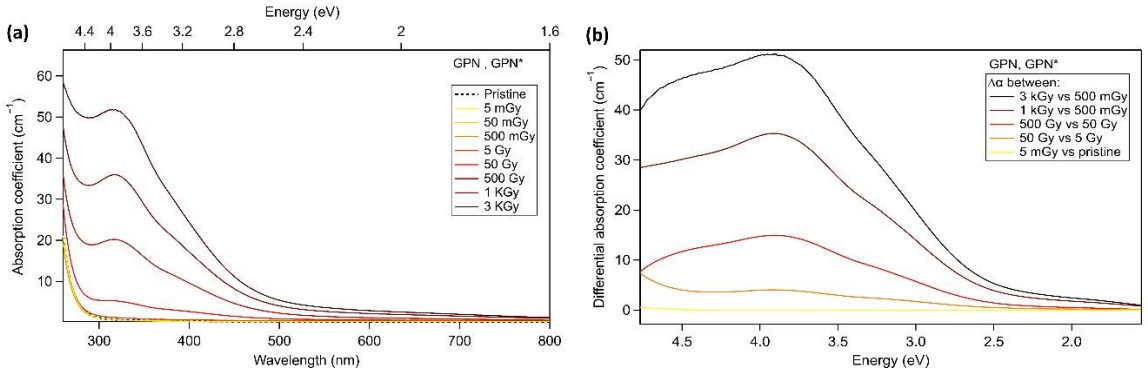

Figure III-16: (a) Absorption spectra for the GPN and GPN glasses for X-ray doses from 5 mGy to 3 kGy. (b) The difference absorption coefficient spectra between different doses conditions for GPN and GPN*. Taken from [177].*

Moreover, the emission spectra of the micro-luminescence measurements in the GPN* glass are presented in Figure III-17. These measurements were recorded from the lateral side of the GPN* glass sample so that excitation and collection conditions were kept the same, whatever the probed depth over 1 mm distance from one side to the other. The evolution of the integrated spectra measured at each depth is reported in Figure III-17(a). This integrated fluorescence signal, excited at 405 nm, increases with X-ray dose. The decrease of the emission intensity with depth results from the X-ray depth attenuation. Figure III-17(b) shows the spectral evolution for a 500 Gy dose at different depths changing from 1 mm depth up to the surface. The nearest signal collected from the surface presents a wide emission band from 440 nm to 760 nm centered at about 520 nm corresponding to silver clusters Ag_m^{x+}. The signal collected deeper below the glass surface exhibits a peak at 620 nm. According to the absorption coefficients and the emission spectra, the 620 nm emission band is related to the presence of Ag^{2+} hole traps silver ions. Thus, dose-dependent defects are generated: the lower doses generate a reservoir of luminescent Ag^{2+} hole traps silver ions while for higher irradiation doses silver luminescent clusters Ag_m^{x+} become dominant.

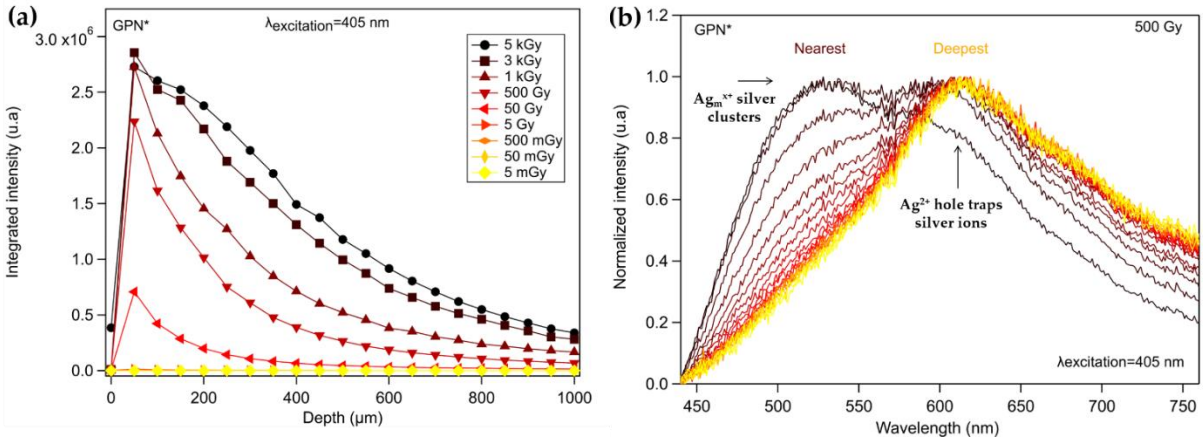

Figure III-17: Micro-luminescence of GPN glass performed on the glass optically polished side: (a) integrated fluorescence intensity at different depths, (b) normalized spectrum evolution with depth for the 500 Gy doses. Taken from [177].*

Figure III-17(a) helped us to scale in absolute values and to estimate the depth-dependent profiles of the linear absorption coefficient at 405 nm, for different incident X-ray doses (Figure III-18). The underlying hypothesis is that the depth-dependent integrated fluorescence emission amplitude (shown in Figure III-17(a)) is locally proportional to the depth-dependent linear absorption coefficients at 405 nm of the defects created by X-rays. Indeed, such depth-dependent linear absorption coefficients at 405 nm are considered to be proportional to the local X-ray dose deposition, thus to the local density of depth-dependent defects generated by X-rays (see Appendix B) [181].

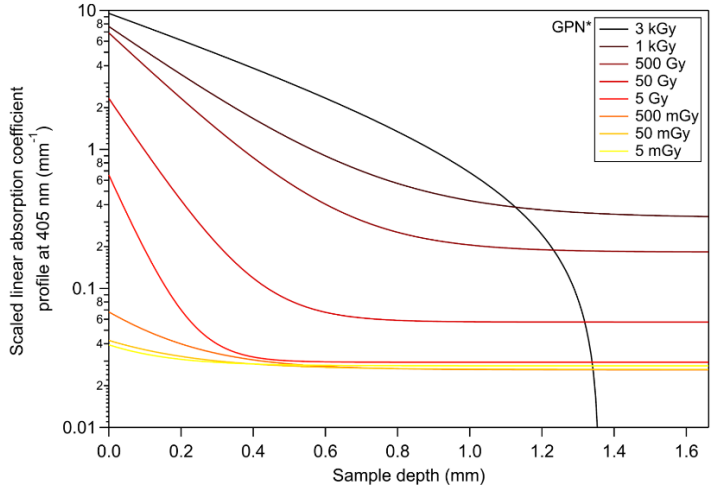

Figure III-18: Estimated depth-dependent profiles in absolute values of the linear absorption coefficient at 405 nm. Note that the asymptotic black curve (3 kGy) appears to be non-consistent with other doses, resulting from an estimated negative asymptotic value.

As represented in Figure III-18, linear absorption coefficient profiles at 405 nm are approximately constant as a function of the sample depth (> 500 µm) between 5 mGy and 5 Gy doses. This behavior is not homothetic for depths inferior to 500 µm for the same dose range. Both depth and dose-dependency are present for doses larger than 5 Gy. The slope of

the linear absorption coefficient profiles changes while increasing X-ray dose assuming the idea of the generation of distinct populations of silver species versus depth. The depth dependence of X-ray-induced glass modification depends on the local X-ray intensity (local depth-dependent deposited dose). In addition, X-ray photon energy is not absorbed in the same way through the glass sample. The process by which photons are absorbed into matter depends on their energies as well as the effective atomic number of the absorbing materials. Thus, the attenuation of the intensity with depth depends on the interaction modes of photons with matter such as the Compton effect, the photoelectric effect, Rayleigh scattering, and the production of pairs [181], [182]. Probably, the damage of the material after 3 kGy X-ray dose (radiation-induced darkening) affects the results shown in this graph, which should be taken with a precaution as the management of the baseline appears non consistent with the behavior of other lower doses.

- ARGO

The refractive index of the ARGO glass was measured before/after X-ray irradiation with an Abbe refractometer. It decreases slightly in the two surfaces after 222 Gy dose (see Table III-2)

Table III-2: Refractive index of the ARGO glass before and after irradiation with 222 Gy.

λ (nm)	**Refractive index**		
	Before irradiation	Front irradiated surface	Rear irradiated surface
589	1.611±0.002	1.608±0.002	1.608±0.002

The absorption spectra for ARGO and ARGO* glass is depicted in Figure III-19 (a) after X-ray irradiation series from 2 Gy to 222 Gy(H_2O).

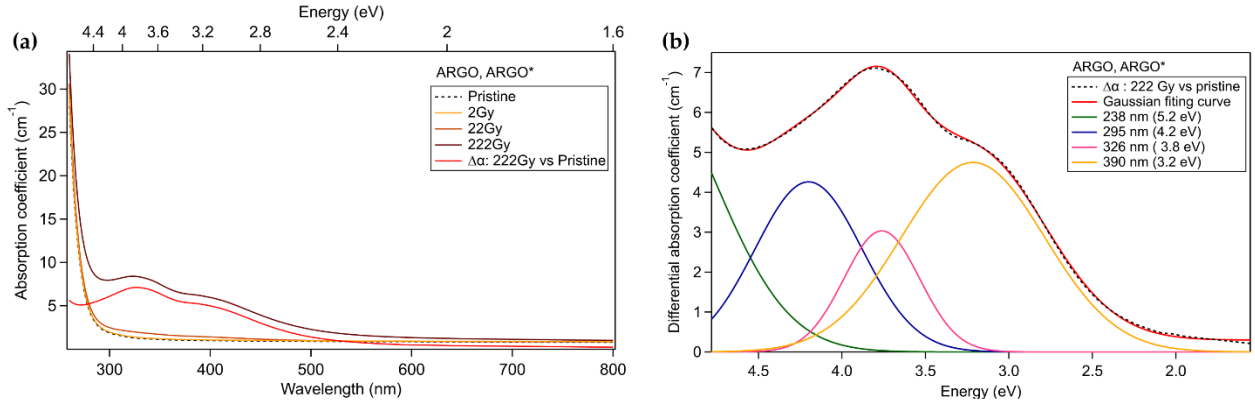

Figure III-19:(a) Absorption spectra of the ARGO and ARGO glass sample after various X-ray doses and the difference absorption coefficient spectrum for 222 Gy vs. pristine. (b) Fit of the radiation-induced spectrum (difference between 222 Gy vs. pristine) considering Gaussian energy contributions for ARGO and ARGO*.*

The radio-induced absorption bands appear in the spectral domain between 300 nm and 500 nm while increasing X-ray doses up 222 Gy (Figure III-19(a)). Two shoulders are visible in

the radiation-induced absorption (RIA) spectrum at the maximum dose. Same bands appear to the irradiated sample at 22 Gy. To better identify and track changes in the band contributions for such glass, the difference absorption coefficient spectrum (222 Gy vs. pristine) of the ARGO* glass was fitted considering Gaussian energy contributions for the photo-induced species, as shown in Figure III-19(b). It was found from the peak fitting that the absorption spectrum consists of three absorption bands peaking around 295 nm (4.2 eV), 326 nm (3.8 eV) and 390 nm (3.2 eV). Some of those absorption bands are related to different centers making the analysis not trivial. The additional band around 238 nm (5.2 eV) was assigned to the isolated Ag^{+} site in the pristine glass [135]. According to the literature, the three absorption bands respectively at around 295 nm, 326 nm and 390 nm with the maximum being 326 nm could be assigned to Ag^{2+} hole traps silver ions [69], [177], [210]. The absorption band at 295 nm and 326 nm may also be ascribed to Ag_m^{x+} silver clusters [69], [210] and the band around 390 nm may finally be also related to the presence of Ag^{0} electron traps [149], [210]. One should notice that the absorption coefficient spectra for 222 Gy of the ARGO* glass is approximately similar to the 50 Gy spectra of the GPN* glass sample (see Figure III-16(a)).

In addition, the normalized photoluminescence spectra, on each pristine and irradiated glass (222 Gy), have been performed for excitation at 325 nm, as presented in Figure III-20 for a depth around 150 µm below the surface. This approach doesn't give access to spatial sampling in depth.

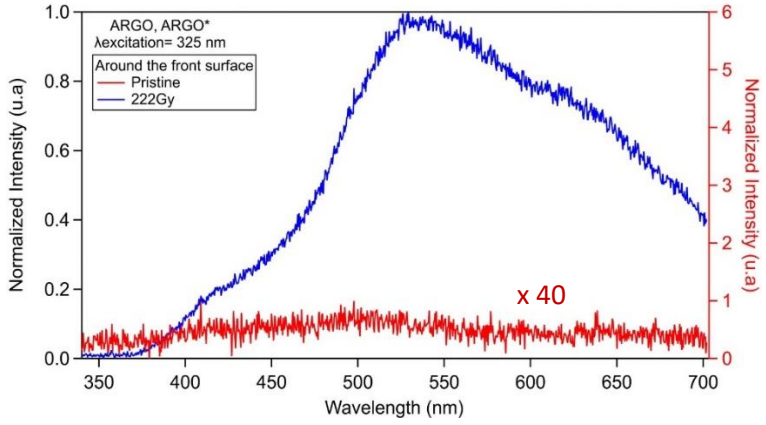

Figure III-20: Normalized RPL spectra excited at 325 nm for the ARGO (pristine – right axis) and ARGO (X-ray irradiation at 222 Gy - left axis) glasses collected around 150 µm below the surface.*

The pristine glass presents no fluorescence signal in comparison to the one irradiated at 222 Gy under excitation at 325 nm. The emission intensity profile after 222 Gy exhibits an emission band with a maximum at 525 nm with shoulders at about 420 nm and 620 nm. According to the absorption bands and the emission spectra of the X-ray irradiated glass, the 620 nm emission band is related to the main absorption band at 326 nm of Ag^{2+} hole trap silver species. The 420 nm and 525 nm emissions are attributed to Ag_m^{x+} silver clusters

[177], [210]. Those bands were also observed here above in the GPN* glass, in Figure III-17, without the band at 420 nm.

- ARGO3

Figure III-21(a) presents the absorption spectra of the ARGO3 and ARGO3* glass samples. These spectra were acquired as a result of a series of X-ray irradiation experiments in which the samples were subjected to doses ranging from 2 Gy to 222 Gy(H_2O). It can be observed that these spectra exhibit similar behavior to those of the ARGO and ARGO* glass samples. At the maximum dose of 222 Gy, the RIA spectrum reveals the presence of two distinct shoulders. As depicted in Figure III-21(b), the difference absorption coefficient spectrum of the ARGO3* glass (222 Gy vs. pristine) was analyzed by fitting Gaussian energy contributions for the photo-induced species. The analysis of the peak fitting in the spectrum also revealed the presence of three absorption bands. These peaks were assigned to the same species as observed in the ARGO* glass (see section III.4.1.b.i(ARGO)) with the presence of a band assigned to the isolated Ag^+ site in the pristine glass.

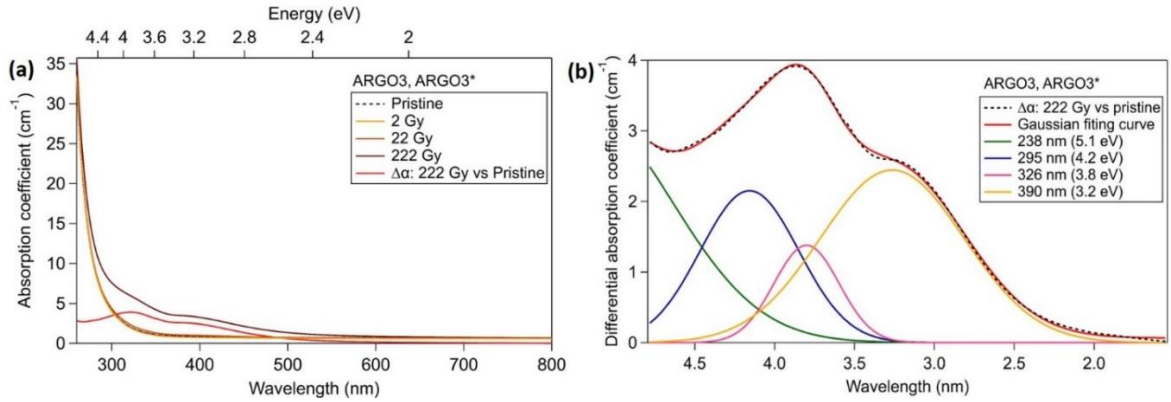

Figure III-21: (a) Absorption spectra of the ARGO3 and ARGO3 glass sample after various X-ray doses and the difference absorption coefficient spectrum for 222 Gy vs. pristine. (b) Fit of the radiation-induced spectrum (difference between 222 Gy vs. pristine) considering Gaussian energy contributions for ARGO3 and ARGO3*.*

Furthermore, Figure III-22 illustrates the RPL spectra, excited at 325 nm, for the ARGO3 and ARGO3* glasses irradiated with 222 Gy.

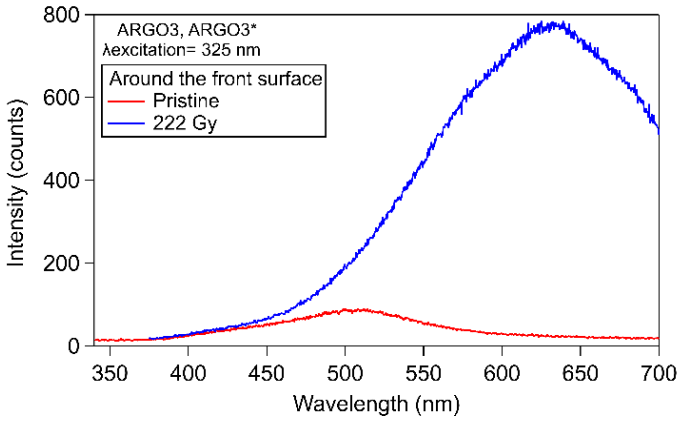

Figure III-22: RPL spectra excited at 325 nm for the ARGO3 (pristine) and ARGO3 (X-ray irradiation at 222 Gy) glasses collected around 150 µm below the surface.*

In the pristine glass, a slight fluorescence signal is observed, peaking at around 500 nm. However, the emission intensity profile of the glass after 222 Gy irradiation shows a distinct and main emission band with an intense peak at 630 nm. The correlation between the absorption bands and emission spectra indicates that this emission band can be attributed to the primary absorption band observed at 326 nm, which is associated with the presence of Ag^{2+} hole trap silver species. If we compare the non-normalized spectra, the generation of color centers in the ARGO3* glass is significantly higher, approximately 3.5 times, compared to the color centers generated in the ARGO* glass irradiated with the same X-ray dose. Furthermore, X-ray irradiation at 222 Gy in the ARGO3* glass does not lead to the generation of silver clusters, in contrast to what occurs in the ARGO* glass (see Figure III-20).

- GPN2

Figure III-23(a) illustrates the absorption spectra of the GPN2 and GPN2* glass samples, obtained through a series of X-ray irradiation experiments for doses of 2 Gy and 22 Gy(H_2O). At the highest dose of 22 Gy, the RIA spectrum does not exhibit distinct shoulders. Figure III-23(b) depicts the RPL spectra, excited at 325 nm, for the GPN2 and GPN2* glass irradiated by 22 Gy. In the pristine glass, a slight fluorescence signal, reaching its maximum around 500 nm, with a shoulder around 420 nm. However, the emission intensity profile of the glass after 22 Gy irradiation shows a distinct and main emission band with an intense peak at 630 nm, with shoulders at about 420 nm and 525 nm. The 630 nm emission band is characteristic of Ag^{2+} hole trap silver species, while the emissions at 420 nm and 525 nm are attributed to Ag_m^{x+} silver clusters.

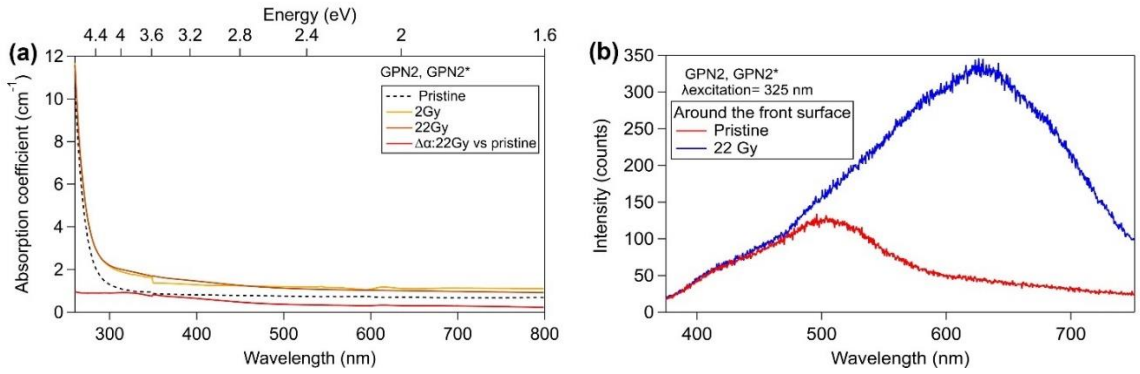

Figure III-23: (a) Absorption spectra of the GPN2 and GPN2 glass sample after various X-ray doses and the difference absorption coefficient spectrum for 22 Gy vs. pristine. (b) RPL spectra excited at 325 nm for the GPN2 (pristine) and GPN2* (X-ray irradiation at 22 Gy) glasses collected around 150 µm below the surface.*

ii. Simulation model for energy spectrum and depth-deposited dose

A simulation model has been conducted using SpekPy and Geant4 toolkits in order to simulate the dose deposited by X-rays on ARGOi*, GPNi* and GPN2i* glasses. Such simulation was made by Arnaud Meyer, a doctoral student in Hubert Curien Laboratory.

The SpekPy simulation toolkit (v2.0.6) [241]-[242] was used in order to simulate the X-ray spectrum corresponding to each facility, by providing the anode material (tungsten (W) in both cases) and supply voltage (100 kV for ARGOi* and GPN2i* sample, 32 kV for GPN1i* sample), along with a filtering of 4 mm beryllium (Be) and 10 mm air to take into account, at a first approximation, the drop in lower energies due to inherent filtering of the facilities. The resulting energy spectra are given in Figure III-24(a).

Then, the Monte-Carlo Geant4 toolkit [243] (Geant4 v11.0.0 using G4EmPenelopePhysics) was used to perform the actual simulation of dose deposition. Each sample was modeled as a box of a homogeneous material, with the composition according to Table III-1, and irradiated with photons according to the energy spectra simulated by SpekPy as described above. Each sample was cut in respectively 140 and 100 layers along their thickness, enabling a spatial resolution of respectively 5 µm and 10 µm for ARGOi*, GPNi* and GPN2i* samples. Simulation of dose in the depth of each sample, relative to the dose measured at the surface, is shown in Figure III-24(b).

Similar simulations were performed by changing the box material to water or quartz, which could be combined with the in-situ dosimetry measurements to obtain the absolute value of the deposited dose inside each sample. Calculated dose data relevant to the structures inscribed inside glass samples are reported in Table III-3.

Table III-3: Conversion factors and deposited doses for each considered silver clusters.

Glass sample	Maximum dose at surface	Silver clusters depth [µm]	Maximum dose in silver clusters [Gy(material)]
ARGOi*	222 Gy(H_2O)	150 (Front)	71.38
		550 (Rear)	23.32
GPNi*	357 Gy(quartz)	160 (Front)	74.33
GPN2i*	22 Gy(H_2O)	150 (Front)	11.29
		550 (Rear)	3.67

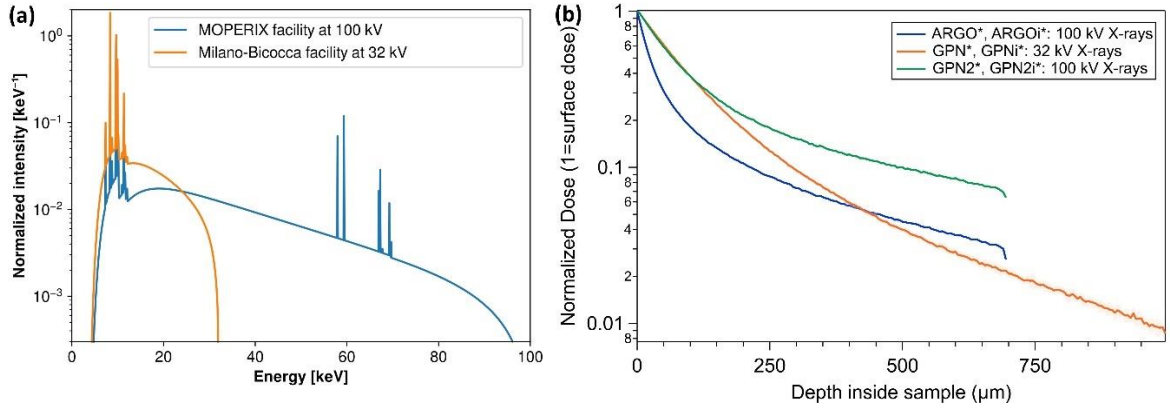

Figure III-24: (a) X-ray energy spectra simulated by SpekPy for each irradiation facility, normalized by integral. (b) Geant4 simulated depth-dependent dose inside each sample, normalized by the surface doses.

According to the simulation, both materials absorb X-rays resulting in a decreasing local deposited dose with the depth inside the material. In ARGOi* glass sample, the dose reaching the silver clusters is much lower than the one deposited at the sample surface. It is also noticeable that the rear-surface inscribed silver clusters receive an attenuated dose three times smaller than that of the front-surface inscribed silver clusters. The GPN2i* glass sample exhibits a distinct absorption characteristic, characterized by a slower decline in dose. Both the GPN2i* and ARGOi* curves share a similar trend, with the same ratio of attenuation between the rear-surface and front-surface structures. GPNi* glass sample also shows a different absorption characteristic, with a slower but steadier decrease of the dose. Knowing that the two irradiators have different energy spectra, the doses are not directly comparable.

iii. Study of silver clusters inscribed by DLW exposed to X-ray irradiation

- Silver-containing Sodo-Gallophosphate Glass (GPNi*)

All-in-one epi-collected radio-photoluminescence experiment (combining X-rays irradiation and *in situ* UV excitation at 355 nm) was realized on the GPNi* glass sample. Fluorescence collection integrates all the glass thickness and has been carried out at the fs laser inscribed structure for an irradiance of 13.4 TW/cm^2 at 160 µm below the glass surface. As shown in Figure III-25, the spectra present a broadband luminescence centered at 460 nm attributed

to silver clusters Ag_m^{X+} inscribed by DLW, with a shoulder at around 620 nm attributed to hole trap defects corresponding to silver ions Ag^{2+} generated by X-ray irradiation. The spectra represent a spectrum balance as a function of the dose. A significant increase of the Ag^{2+} luminescence with X-ray doses overlays the DLW silver clusters luminescence, that decreases indirectly due to the absorption at 355 nm of the defects generated by X-ray in the 160 µm thickness from the glass surface down to the localization of the laser-inscribed silver clusters [177]. Silver clusters are thus less emitting because they are less excited due to a lower UV intensity at their depth while X-ray irradiation goes on and produces defect centers such as the hole trap Ag^{2+} centers.

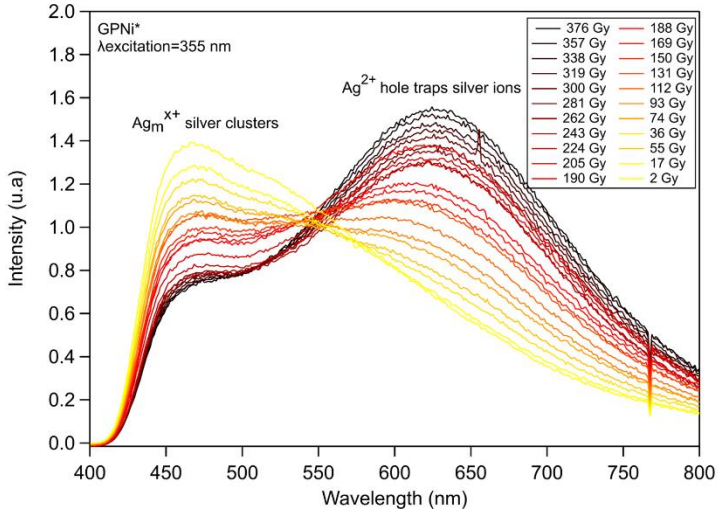

Figure III-25: Radio-photoluminescence spectra of the GPNi glass for the laser inscribed structure versus the X-ray dose. Taken from [177].*

- Commercial Argolight Glass (ARGOi)

Detailed experiments were conducted on the ARGOi and ARGOi* glass samples containing two inscribed surfaces of silver clusters. These experiments have been carried out on the fs laser inscribed structures at the highest irradiance (11 TW/cm^2) before and after 222 Gy of X-ray irradiation for the two planes (Figure III-26(a-b)). In this case, the spatial resolution is related to the inscribed silver clusters. None of the spectra in this experiment have been corrected by the spectral response of the instrumental chain of detection.

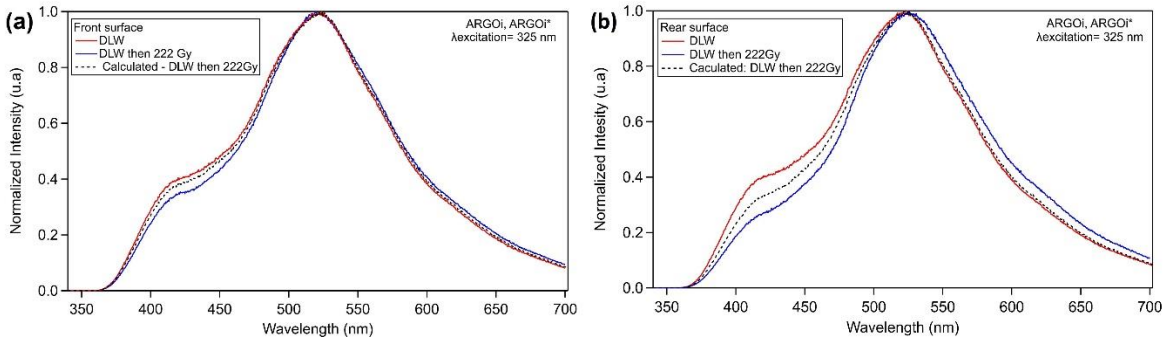

Figure III-26. Normalized RPL spectra excited at 325 nm for the highest DLW irradiance structure for ARGOi and ARGOi in the (a) front and the (b) rear inscribed surface, respectively.*

Figure III-26(a-b), conducted at the DLW structures, presents that the main contribution is centered around 525 nm with its lowest peak around 420 nm for the two planes. When irradiating with 222 Gy X-ray dose, one observes that both planes act differently in terms of emission profiles. For the front surface, the 420 nm luminescence band decreases relatively by 13% due to the subsequent partial absorption of fluorescence emission in the blue range because of the absorption of the generated silver species after X-ray irradiation. It is noticeable that for the rear surface, this band presents a greater relative decrease (about half of its original intensity) due to a larger glass thickness propagating through before collection. The collected fluorescence in the region from 525 nm to 700 nm gradually increases in the front and the rear surfaces after 222 Gy X-ray dose. It corresponds to the additionally collected fluorescence emitted from the color centers Ag^{2+} in the sample thickness from the depth localization of the laser-inscribed silver clusters up to the surface. The photoluminescence of the pristine irradiated sample at 222 Gy, as shown in Figure III-20, demonstrates well that the red region (525-700 nm) corresponds to the generation of color centers in the irradiated glass sample. The spectrum of the ARGOi* glass sample is several orders of magnitudes larger (×40) than that in the ARGO* glass sample (see blue curves from Figure III-26(a-b) compared to that of Figure III-20).

In order to quantify the difference between the fluorescence emission profiles from the rear-surface and front-surface laser-induced clusters after a 222 Gy irradiation, a calculated spectrum (black curves Figure III-26(a) and Figure III-26(b)) is obtained by estimating the attenuation of the DLW spectra (red curves in Figure III-26(a) and Figure III-26(b)) due to absorption from defects created by the 222 Gy exposure. This attenuation estimation (black dashed curve in Figure III-26(a,b)) was calculated by:

$$\tilde{I}_{ARGOi^*}(\lambda) = I_{ARGOi}(\lambda) e^{-\alpha_{222Gy}(\lambda) L} \qquad \text{III-22}$$

where L is the glass thickness from to front surface to the plane of localization of the silver clusters, namely 150 µm for the front surface and 550 µm for the rear surface; $\alpha_{222Gy}(\lambda)$ is the measured linear absorption spectrum after a 222 Gy X-ray dose from Figure III-19(a).

The difference in the 350-500 nm band between the experimental and calculated curves could be explained as follows. It was supposed that the linear absorption coefficient is averaged over the entire thickness of the two planes. As shown before, the linear absorption coefficient is depth-dependent which means that the values measured over the 700 µm thickness (Figure III-19(a)) cannot be the same in both planes at 150 µm or 550 µm depth. Note also that the emission of fluorescence of the generated defects (blue curve in Figure III-26(a)) was not taken into account in this calculated spectrum because the fluorescence cannot be quantified. This clarifies the difference in the red region (525-700 nm).

In addition, micro-absorption measurements were performed in the two planes of the ARGOi* glass sample between a non-structured and a structured zone over a 100 × 100 μm^2 surface, compared to a non-structured area. The local differential linear absorption coefficient of the

laser-induced structures is reported in Figure III-27(a) for the highest DLW irradiance structure for the two planes after 222 Gy X-ray irradiation. Other DLW irradiance structures were also investigated after 222 Gy (not shown here). The method of calculation is described in detail in AppendixC.

As from the measurements of Figure III-27(a) (in the case of one single laser-induced structure created at 11 TW/cm^2), the experimental spectra of the differential linear absorption coefficient are integrated over the optical frequency for all the DLW irradiance (Figure III-27(b)). The proposed average differential transmission $< T >$ for all these specific spectra is calculated with the equation below:

$$< T >= \frac{\int_{\omega_1}^{\omega_2} e^{-\alpha(\omega)H} d\omega}{\int_{\omega_1}^{\omega_2} d\omega} \qquad \text{III-23}$$

where α is the measured local differential linear absorption coefficient for all the spectra (as from Figure III-27(a)), H is the thickness of the laser-modified area that contains the silver clusters (6 µm estimation for the ARGOi glass), ω is the optical frequency corresponding to the experimental wavelength sampling. The associated average differential absorption $< A >$ is defined as $< A >= 1 - < T >$, as shown in Figure III-27(b).

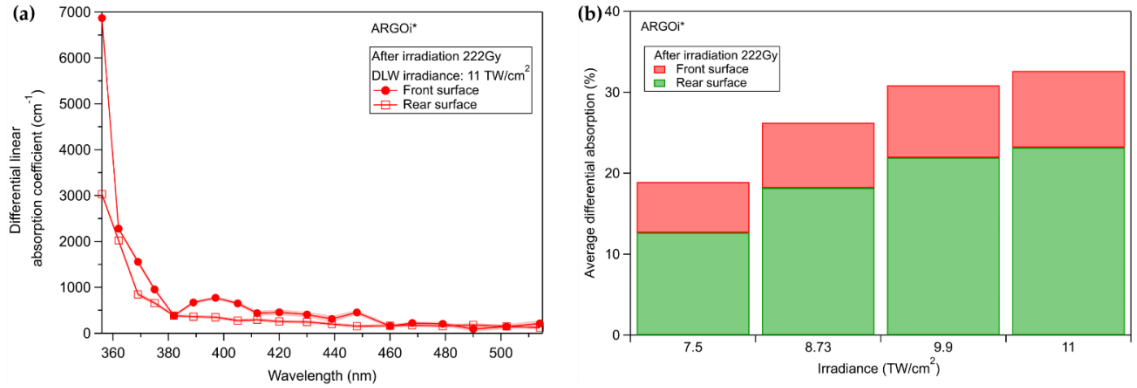

Figure III-27: (a) Differential linear absorption coefficient of the laser-inscribed structures (11 TW/cm^2) for the two planes after irradiation at 222 Gy X-ray dose in the ARGOi glass sample. (b) Average differential absorption of the inscribed structures for each DLW irradiance (as from Figure III-27(a)).*

One can observe the increase by approximately 30% of the estimated average differential absorption of the clusters being inscribed close to the front surface compared to those inscribed close to the rear surface. Such a 30% increase between the two silver cluster planes is approximately independent of the DLW irradiance. Due to the dose profile with depth (see Figure III-24(b)), the deposited dose is locally larger in the plane of front-surface clusters compared to that in the plane of rear-surface clusters. Thus, the average absorption increase of the front-surface clusters is directly related to the larger deposited dose than that deposited at the depth of the rear-surface clusters. Further interpretation of such a 30% increase of the local absorption of the silver clusters front-surface plane compared to that at the rear-surface plane will come here after, with the Lorentz-Lorenz and Clausius-Mossotti

interpretation, which requires first knowing the local refractive index properties.

In this framework, the refractive index variation Δn between the pristine glass and the written structures was estimated using the wavefront sensor (see Experimental methods section) before and after X-ray irradiation for the two surfaces. Square structures of 50 µm x 50 µm with an interline spacing of 10 µm were inscribed with the same laser parameters in order to measure the refractive index modification. One example of a top view phase contrast image of the written structure at 11 TW/cm^2 is shown in Figure III-28(a). Based on it, the OPD profile is plotted and correlated to the spatial distribution of the silver clusters showing two positive peaks for every laser passage (Figure III-28(b)). Knowing the structures' thickness (6 µm estimation for the ARGOi glass), the refractive index modification is calculated for the different laser-inscribed structures before and after X-rays for the two different planes (Figure III-28(c)).

Our study shows that Δn increases as a function of laser irradiance, the higher the irradiance the greater the formation of silver clusters, as previously mentioned in chapter II. The local refractive index modification slightly decreases quite similarly in the two irradiated planes after the 222 Gy X-ray dose.

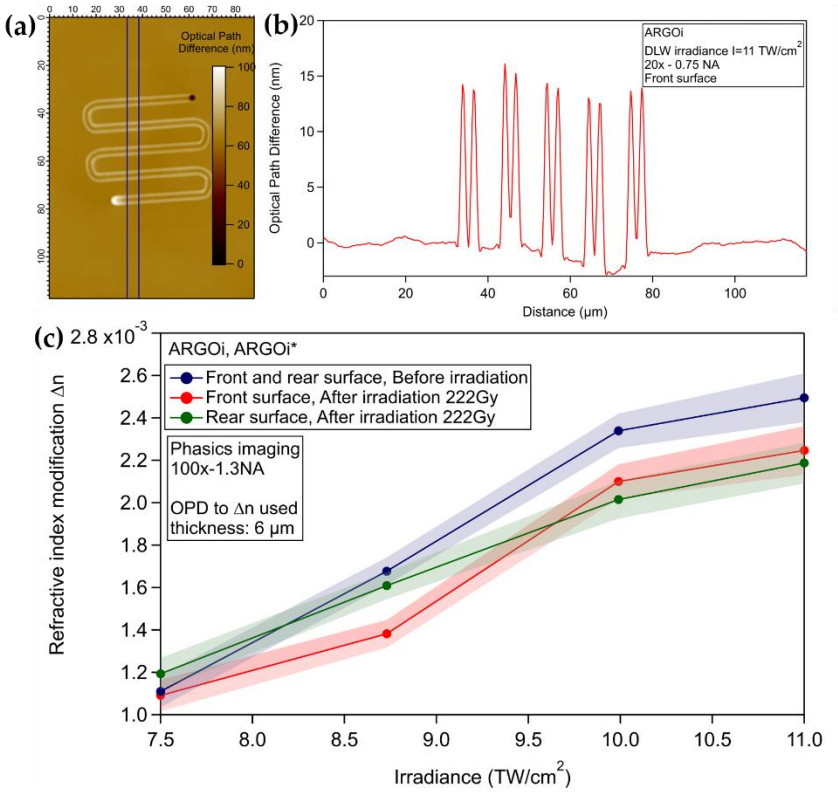

Figure III-28:(a) Phase image under white light illumination of the laser inscribed structure (11 TW/cm^2) before irradiation. (b) Optical path difference determined from the phase image. (c) Refractive index modification Δn as a function of laser irradiance before/after 222 Gy-dose for the two planes in ARGOi, ARGOi glass sample.*

In order to understand the phenomenon that happened after X-ray irradiation and to explain

our results, the Clausius-Mossotti equation has been considered, defined as:

$$\frac{\hat{n}^2 - 1}{\hat{n}^2 + 2} = \frac{N\alpha}{3} \qquad \text{III-24}$$

where N is the number of molecules per unit volume, α is here the mean molecular polarizability of the silver clusters. The local refractive index of the laser-modified glass stands for $\hat{n} = n_g + \Delta\hat{n}$, where n_g is the refractive index of the glass, $\Delta\hat{n}$ is the laser-induced complex index modification written as $\Delta\hat{n} = \Delta n + i\,\Delta\kappa$, with Δn and $\Delta\kappa$ its real and imaginary parts, respectively.

Since the pristine glass shows a slight refractive index decrease (Table III-2) and additional absorption and emission bands (Figure III-19(a) and Figure III-20) after X-ray irradiation of 222 Gy, the environment of silver clusters is modified under X-ray irradiation. Equation III-24 allows recognizing the effect of the environment on the clusters' refractive index modification $\Delta\hat{n}$. Note that the measured Δn corresponds to the measured quantity from the phase imaging technique, as shown in Figure III-28(c). The measured $\Delta\kappa$ is calculated using the average differential transmission from the micro-absorption experiment (Figure III-27(b)) as follow: $\Delta\kappa = \frac{-\lambda}{4\pi H}\ln(< T >)$ where $< T >$ is the average differential transmission, H is the thickness of the laser-modified area that contains the silver clusters (6 µm estimation), λ is the wavelength (589 nm). Both measured values will be compared to calculated values using Equation III-24: Measured values from Figure III-28(c) and Figure III-27(b) have been compared to calculated values using Equation III-24.

First, the Clausius-Mossotti equation allows for calculating $\frac{N\alpha}{3}$ before irradiation. Since the micro-absorption experiment wasn't made before irradiation, the average differential absorption before irradiation was approximated to be 10% less than that in the rear surface. Since the variation after irradiation between the two planes is 30%, the value before irradiation was considered to be 10% less than the founded value of 30% after irradiation. Then, the calculation of both parts of $\Delta\hat{n}$ after irradiation takes into account the refractive index of the irradiated glass (Table III-2). We applied a decrease of 0.48% in the value of $\frac{N\alpha}{3}$ after irradiation compared to its initial (before irradiation) value, in order to adjust the calculated and measured values. It was interpreted that the polarizability α of the silver clusters has not changed (less than 1%) after irradiation. The comparison between the calculated and measured $\Delta\hat{n}$ is depicted in Figure III-29 for the two planes.

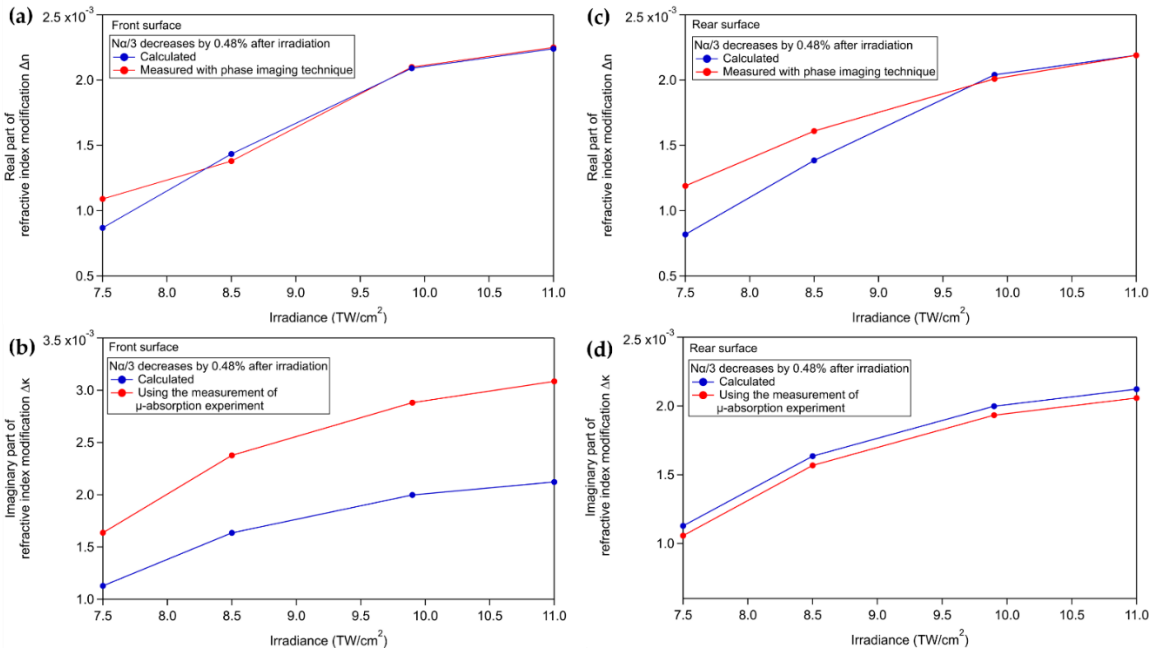

Figure III-29: Comparison between calculated and measured $\Delta\hat{n}$ after irradiation for a decrease of $\frac{N\alpha}{3}$ by 0.48%: (a, c) real part Δn for the front and rear surfaces, respectively; (b, d) associated imaginary counterparts $\Delta\kappa$ for the front and rear surfaces, respectively.

In the front surface (Figure III-29(a)), the calculated real part of the local refractive index modification superposed well with the measured one when $\frac{N\alpha}{3}$ weakly decreases by only 0.48%. A difference is observed in Figure III-29(b) as the imaginary part $\Delta\kappa$ measured is higher than the calculated one in the front surface. In the rear surface (Figure III-29(c-d)), the calculated real and imaginary parts of the local refractive index modifications closely match with the measured one. This underlines that the Δn decrease after irradiation seen in the phase imaging technique is attributed to the modification of the cluster's environment due to the creation of colored centers *i.e.*, the variation of the ambient polarizability of the irradiated matrix. The two curves comparing the imaginary parts of the front surface in Figure III-29(b) show a significant difference: achieving their matching would require a much larger increase of $\frac{N\alpha}{3}$, by approximately 10% (instead of a decrease of 0.48%). This suggests additional absorption in the front-surface structures during the 222 Gy irradiation, resulting from the creation of additional silver clusters in the front surface.

The integrated measure of the fluorescence amplitude was performed for the different structures of the two surfaces before and after 222 Gy X-ray dose for an excitation at 365 nm (Figure III-30). Fluorescence images were obtained using an Olympus fluorescence microscope BX53 with a LUCPlanFLN objective of 60× - 0.70 NA. The excitation light passes through the glass sample to reach the silver clusters of each surface, the emitted light is epi-collected from the same facet. The rear surface was measured by turning the glass in order to have the same excitation reaching the structures, after propagating over the same depth of 150 µm. It shows that the fluorescence intensity of the two planes before irradiation is

approximately the same, within the measurement error bars.

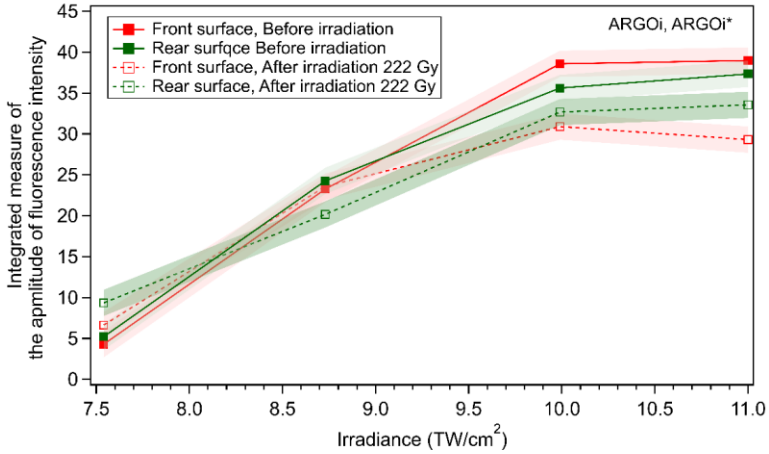

Figure III-30: Integrated measure of the fluorescence amplitude for the different laser irradiances before and after the 222 Gy dose for the two planes in ARGOi and ARGOi glass sample, under 365 nm excitation.*

The fluorescence intensity of the clusters decreases weakly after X-ray irradiation in the two planes. After irradiation, the front surface presents a weakly less fluorescence emission than the rear one due to less excitation available for the clusters of the front surface compared to those in the rear one: indeed, the front surface has been submitted to a larger X-ray dose deposition than that at the rear one. The creation of a large number of color centers in the front surface attenuates the excitation light at 365 nm as well as the emitted light while passing through the same thickness to reach the surface. Oppositely, greater fluorescence excitation appears to be available for the irradiated clusters of the rear surface, because such a 365 nm excitation is less absorbed thanks to the smaller number of color centers generated by the X-rays. Moreover, the emitted light of those clusters is even less absorbed while passing through the same thickness. Note that these generated color centers are stable at room temperature. As demonstrated before, it is possible that additional silver clusters were generated in the front surface by X-rays (from Figure III-29(b)). Note that the additional fluorescence of X-ray induced silver clusters is dominated by the X-ray additional losses (both reduction of excitation due to a larger pump absorption by th X-ray induced color centers, and also partial absorption of silver cluster fluorescence by these color centers).

Fluorescence lifetime imaging microscopy results using the Fast-FLIM algorithm are shown in Figure III-31 in order to evaluate the effect of the X-rays on the cluster emission. Such an experiment does not allow collecting longer lifetimes, namely those attributed to silver hole centers in the microsecond range.

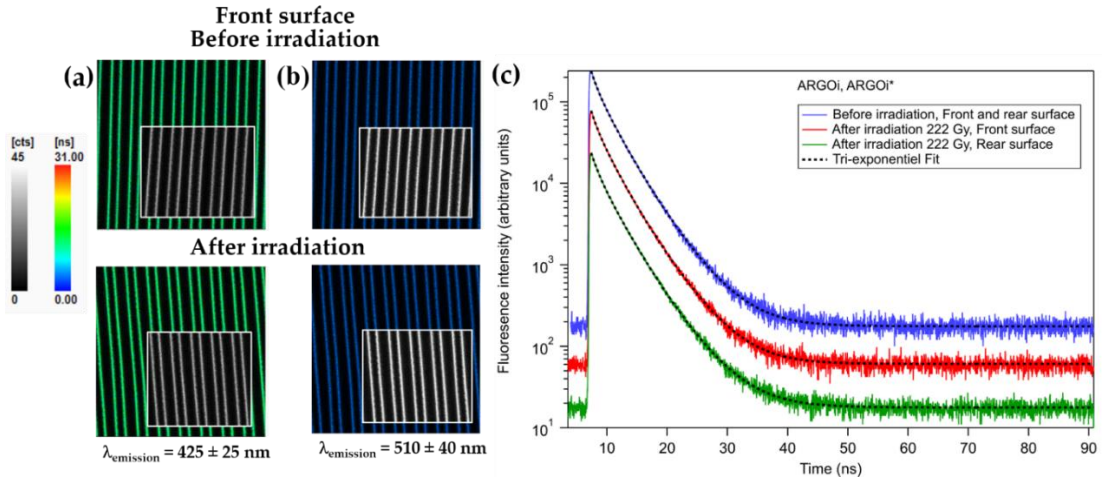

Figure III-31: (a) Composite FLIM and fluorescence intensity microscopy images of the laser-induced structure (11 TW/cm²) in the ARGOi glass before (top) and after (bottom) irradiation for an emission at 425 nm from the front surface; the color-code represents the mean lifetime obtained by FAST-FLIM algorithm (color scale from 0 to 31 ns); inset: luminescence intensity only (grey-scale from 0 to 45 counts). (b) Same composite FLIM and luminescence intensity images for an emission at 510 nm. (c) Luminescence decays in arbitrary units for the emission at 425 nm of the same structure before and after irradiation for the two surfaces, and fitting curves using an arbitrary three-exponential decay function.

As shown in Figure III-31(c), the fluorescence lifetime was evaluated with a triple exponential decay model in the ns range. The luminescence decays were normalized and shifted in axis for better vision. Note that it is not attempted thereby to attribute each component to a precise population of emitters. Based on the fittings, the three fluorescence lifetimes for all the laser-inscribed structures don't change before and after irradiation for the two planes for an emission at 425 nm, as well as for an emission at 510 nm. The variation remains well below the accuracy of the measurement. The associated amplitudes of each of the three lifetimes of the fitting model are also stable when comparing before and after X-rays. From the analysis of the fluorescence decays for all DLW irradiances, before and after irradiation, lifetimes and associated amplitudes average values with their standard deviations were derived and reported in Table III-4. The peak intensities were between 6.6 x 10^3 and 1.5 x 10^4; the average chi² was 1.05 with a standard deviation of 0.05, corroborating the good quality and relevance of the three-exponential fitting model.

Table III-4: Fitting parameters and associated statistical numerical error with a three-exponential decay time model for all DLW irradiances.

		Fluorescence decay $\bar{\tau}_i ; \sigma_{\tau_i}$ **(ns)**			**Associated amplitude** $\overline{A_i} ; \sigma_{Ai}$ **(%)**		
λemission	**ARGOi**	$\bar{\tau}_1 ; \sigma_{\tau_1}$	$\bar{\tau}_2 ; \sigma_{\tau_2}$	$\bar{\tau}_3 ; \sigma_{\tau_3}$	$\overline{A_1} ; \sigma_{A_1}$	$\overline{A_2} ; \sigma_{A_2}$	$\overline{A_3} ; \sigma_{A_3}$
425 ± 25 nm	**Before irradiation***	0.9 ; 0.1	2.9 ; 0. 2	5.1 ; 0. 5	28 ; 2	56 ; 4	16 ; 3
	After irradiation, Front surface*	0.9; 0.1	2.8 ; 0.2	5.2 ; 0.5	32 ; 4	52 ; 12	16 ; 8

	After irradiation, Rear surface*	0.9 ; 0.1	2.8 ; 0.2	5.0 ; 0.6	34 ; 3	51 ; 3	15 ; 7
510 ± 40 nm	**Before irradiation***	1.8 ; 0.2	4.3 ; 0.2	7.5 ; 0.5	28 ; 3	57 ; 3	15 ; 3
	After irradiation, Front surface*	1.9 ; 0.2	4.5 ; 0.2	7.7 ; 0.4	29 ; 3	56 ; 3	15 ; 3
	After irradiation, Rear surface*	1.9 ; 0.3	4.4 ; 0.3	7.4 ; 0.5	30 ; 5	53 ; 5	17 ; 5

**Average statistical error over all measurements*

It was clearly observed that the fluorescence lifetime was not correlated to irradiation with 222 Gy X-ray dose, independently of the penetration depth and DLW irradiance; their distribution is approximately constant also. It demonstrates that the nature of silver clusters is invariable, resilient to X-ray irradiation at the investigated dose levels. The absence of substantial change in both the decays and associated weights indicates that neither conversion of silver clusters into a species of a different lifetime, nor generation of acceptors for energy transfer from the excited silver clusters occurred upon irradiation.

- Commercial Argolight Glass (ARG03i)

Normalized photoluminescence spectra were acquired for both pristine and irradiated glass samples (222 Gy) with excitation at 325 nm. These measurements were performed on the femtosecond laser-inscribed structures, employing the highest irradiance of 14.2 TW/cm^2, for both the front and rear planes, as shown in Figure III-32(a-b).

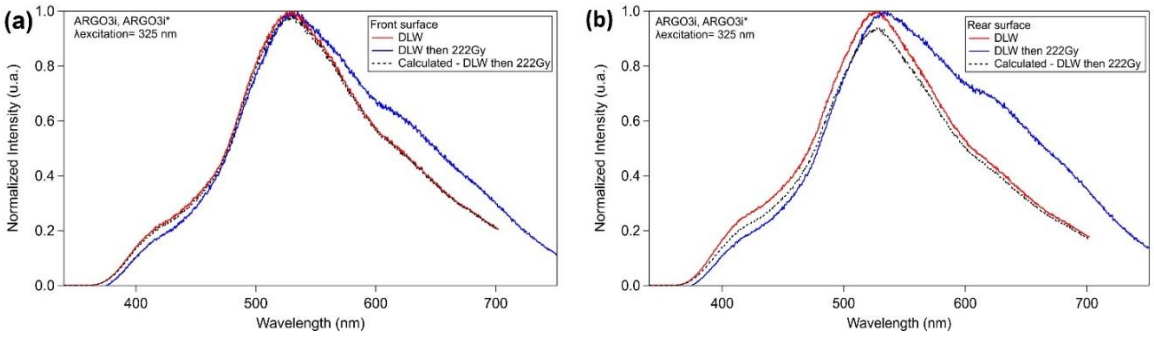

Figure III-32: Normalized RPL spectra excited at 325 nm for the highest DLW irradiance structure for ARGO3i and ARGO3i in the (a) front and the (b) rear inscribed surface, respectively. The black dashed curve has been calculated using Equation III-22.*

Figure III-32(a-b) carried out on the DLW structures, illustrates that the primary contribution is focused at approximately 525 nm, with its lowest peak occurring around 420 nm for both planes. When exposed to a 222 Gy X-ray dose, it becomes evident that both planes exhibit

distinct emission profiles. This behavior was previously observed in the RPL spectra conducted on the DLW structure in the ARGOi* glass (see section iii.). The black dashed curves present the calculated spectra obtained by estimating the attenuation of the DLW spectra (red curves in Figure III-22Figure III-32(a) and Figure III-22Figure III-26(b)) due to absorption from defects created by the 222 Gy exposure (Figure III-21). This attenuation estimation was calculated using the Equation III-22. and behaves in the same manner as the case of the ARGOi* glass (see section iii.).

Micro-absorption measurements were also performed in the two planes of the ARGO3i* glass sample, following the same steps as described above for the ARGOi* glass sample. In Figure III-33, one can observe the increase of the estimated average differential absorption of the clusters inscribed close to the front surface compared to that corresponding to the ones close to the rear surface. Such an increase between the two silver cluster planes is slightly dependent on the DLW irradiance. As previously mentioned, the significant increase in absorption observed in the front-surface clusters is mainly due to the higher dose deposition in that region, as compared to the dose received at the depth where the rear-surface clusters are situated.

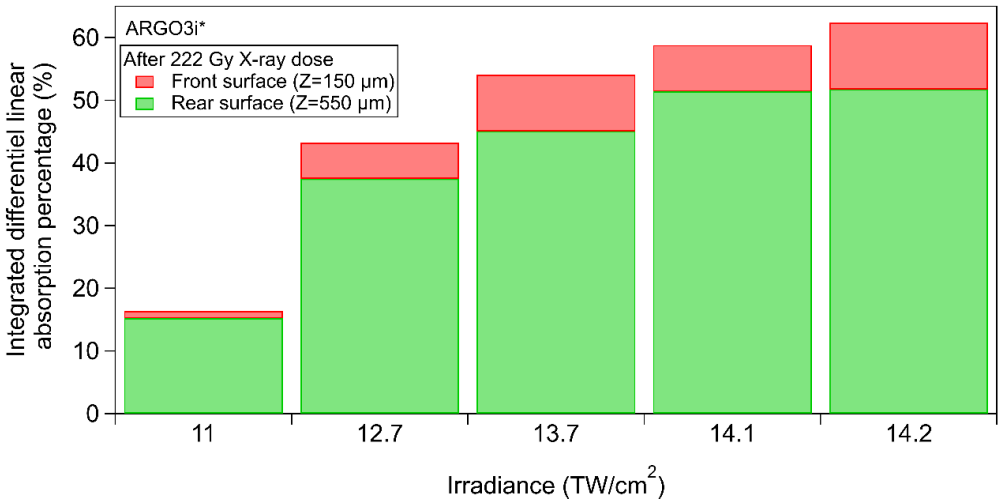

Figure III-33: Average differential absorption of the inscribed structures for all DLW irradiance for the front- and rear-surface silver clusters in the ARGO3i sample.*

Moreover, the refractive index can be calculated for the different laser-inscribed structures before and after X-ray irradiation for both planes (for an estimation of 6 µm thickness for the ARGO3i glass). As presented in Figure III-34, the local refractive index modification demonstrates a decrease in the front irradiated plane following the 222 Gy X-ray dose, whereas the rear irradiated plane maintains a relatively stable refractive index modification compared to the pre-irradiation state. At this stage, we assume that the local environment of the rear-surface silver clusters is not affected after irradiation thereby their refractive index change is maintained as it is before irradiation. While, for the front-surface the Δn decreases after irradiation which is attributed to the modification of the cluster's environment *i.e.*, the

variation of the ambient polarizability of the irradiated matrix.

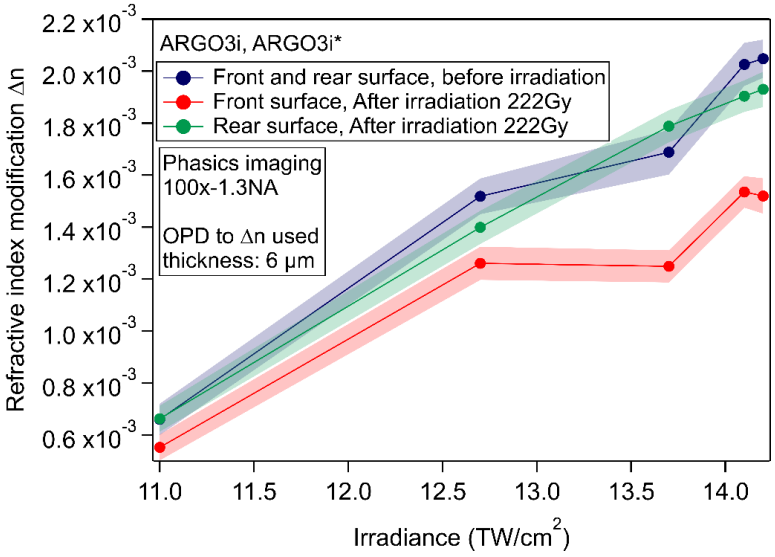

Figure III-34: The refractive index modification Δn as a function of laser irradiance before/after 222 Gy-dose for the two planes in ARGO3i, ARGO3i glass samples.*

The fluorescence lifetime was evaluated using the fluorescence lifetime imaging microscopy (FLIM) results employing the Fast FLIM algorithm. The result was fitted with a triple exponential decay model in the ns range. From the analysis of the fluorescence decays for all DLW irradiances, before and after irradiation, lifetimes and associated amplitudes average values with their standard deviations were derived and reported in Table III-5.

Table III-5: Fitting parameters with a three-exponential decay time model for all DLW irradiance for the AG03i and AGO3i glass samples.*

		Fluorescence decay $\bar{\tau}_i ; \sigma_{\tau_i}$ (ns)			**Associated amplitude $\overline{A_i} ; \sigma_{Ai}$ (%)**		
λemission	**ARGO3i**	$\bar{\tau}_1 ; \sigma_{\tau_1}$	$\bar{\tau}_2 ; \sigma_{\tau_2}$	$\bar{\tau}_3 ; \sigma_{\tau_3}$	$\overline{A_1} ; \sigma_{A_1}$	$\overline{A_2} ; \sigma_{A_2}$	$\overline{A_3} ; \sigma_{A_3}$
425 ± 25 nm	**Before irradiation***	0.7 ; 0.1	2.6 ; 0. 4	5.7 ; 0. 5	5 ; 1	70 ; 1	25 ; 1
	After irradiation, Front surface*	0.7 ; 0.1	2.4 ; 0.3	5.3 ; 0.3	32 ; 5	52 ; 7	16 ; 3
	After irradiation, Rear surface*	0.7 ; 0.1	2.9 ; 0.1	5.5 ; 0.5	29 ; 5	56 ; 5	15 ; 4
510 ± 40 nm	**Before irradiation***	1.3 ; 0.2	4.6 ; 0.2	8.3 ; 0.5	21 ; 10	68 ; 8	11; 4
	After irradiation, Front surface*	1.5 ; 0.3	4.7 ; 0.8	7.8 ; 0.7	38 ; 12	49 ; 12	13 ; 3
	After irradiation, Rear surface*	1.9 ; 0.9	4.3 ; 0.6	9 ; 0.7	27 ; 4	59 ; 5	14 ; 3

**Average statistical error over all measurements*

The fluorescence lifetime remained mostly unaltered regardless of exposure to a 222 Gy X-ray dose, regardless of the penetration depth and DLW irradiance when exciting at 425 nm. While the amplitude weights evolve more strongly, but a related physical interpretation is not obvious since (i) the three-exponential decay model is not strictly associated to identified independent populations of given silver species, and (ii) one cannot fully exclude multiple possible numerical fitting solutions with distinct ratios.

The integrated measure of the fluorescence amplitude was performed for the different structures of the two surfaces before and after 222 Gy X-ray dose for an excitation at 365 nm (Figure III-35). Fluorescence images were obtained using the same method mentioned for the measurement of the ARGOi, ARGOi* glass sample.

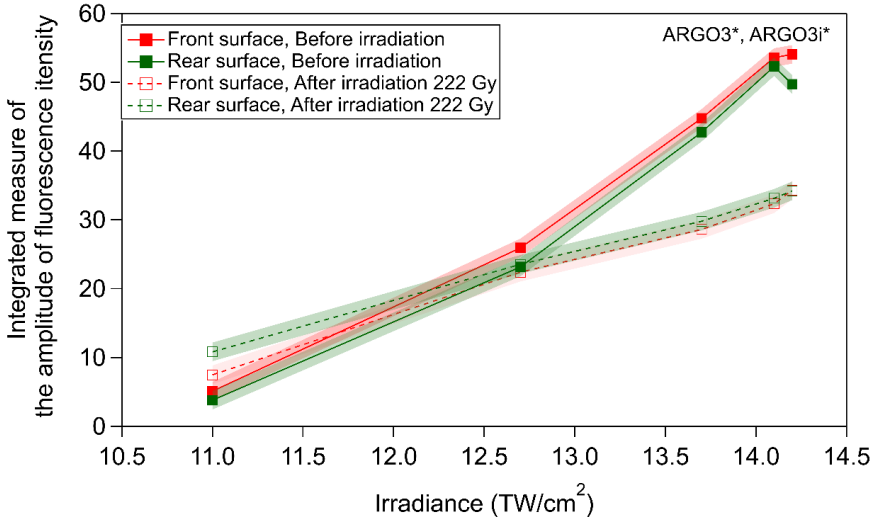

Figure III-35: Integrated measure of the fluorescence amplitude under 365 nm excitation, for the different laser irradiance before and after 222 Gy-dose for the two planes in ARGO3i and ARG3Oi glass sample.*

After X-ray irradiation with 222 Gy, it can be observed that the fluorescence intensity of the clusters decreases in both planes for the two highest irradiances. This reduction in fluorescence can be attributed to the limited excitation available for the clusters on the irradiated surface compared to before irradiation. This is due to the formation of color centers following irradiation contributing to the attenuation of the excitation light at 365 nm reaching the clusters. Additionally, the emitted light from these clusters is further absorbed as it passes through the same thickness. The observed result for the two planes after irradiation differs from the one observed in the ARGO* glass sample. First, the fluorescence amplitude of the front surface is roughly equivalent to, and not greater than, that of the rear surface. If the absorption (of the excitation and emission light) was the only phenomenon in this case, the fluorescence of the rear-surface silver clusters should be higher than that of the front-surface structures, as already explained in the case of the ARGOi* glass. Second, the difference in attenuation in the ARGO3i* sample between the fluorescence amplitudes is greater than the level of attenuation observed in the ARGOi* glass. Thus, the absorption of

the excitation and collected light may not account alone for this significant attenuation. As shown from Table III-5, the weights of the emission amplitudes have been altered following irradiation. Hence, this alteration could result in a decrease in the fluorescence emission of the silver clusters, contributing to an additional attenuation to the absorption of both excitation and collection light. In addition, Figure III-33 shows additional absorption prior X-ray irradiation of the front-surface. Thus, the front-surface clusters exhibit fluorescence levels equivalent to those of the rear-surface clusters.

In addition, one can see that X-ray irradiation could lead to the generation of additional silver clusters, in the case of low irradiance (11 TW/cm^2). It is visible that the fluorescence of the generated clusters increases in both of the two planes after X-ray irradiation. This was already observed for low laser irradiance when subjected to thermal treatment [244].

- Silver-containing sodo-gallophosphate - Glass 2

The normalized photoluminescence spectra for the GPN2i and GPN2i* were obtained for both pristine and irradiated glass samples (22 Gy), with excitation at 325 nm. These measurements were conducted on the femtosecond laser-inscribed structures at the highest irradiance of 14.2 TW/cm^2, for both the front and rear planes (as depicted in Figure III-36(a-b)).

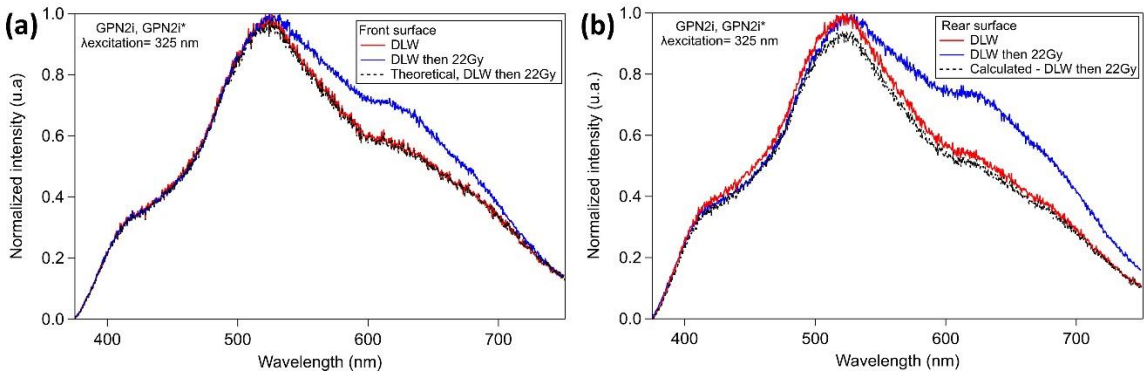

Figure III-36: Normalized RPL spectra excited at 325 nm for the highest DLW irradiance structure for GPN2i and GPN2 in the (a) front and (b) rear inscribed surfaces, respectively. The black dashed curve has been calculated using Equation III-22.*

Figure III-36 (a-b) presents that the main contribution is centered around 525 nm with its lowest peaks at around 420 nm and 625 nm for the two planes. Contrary to the case of ARGO anf ARGO3 glasses, the 420 nm luminescence band doesn't decrease after irradiation because the absorption spectrum of the glass doesn't change after 22 Gy due to the absence of absorption bands after such an irradiation (see Figure III-23). The collected fluorescence in the region from 525 nm to 700 nm gradually increases in the front and the rear surfaces after 22 Gy X-ray dose due to the same reason explained before for the cases of ARGOi* and ARGO3i*. The dashed curve is computed as elaborated in the preceding section, confirming

that there is no alteration in the UV range, as previously mentioned.

The refractive index variation Δn between the pristine glass and the written structures was estimated before and after X-ray irradiation for the two surfaces. One example of a top view phase contrast image of the written structure at 14.2 TW/cm^2 is shown in Figure III-37(a). Based on it, the refractive index profile (for 6 µm estimation of the structure's thickness) is plotted and correlated to the spatial distribution of the silver clusters, showing two positive peaks for every laser passage (Figure III-37). The depletion in the center corresponds to the displacement of the sodium reservoir with radial diffusion out of the central zone of laser inscription. The negative and positive peaks of the refractive index change were plotted in Figure III-37(c) and (d), respectively. The local refractive index modification is maintained the same in the two irradiated planes after the 22 Gy X-ray dose.

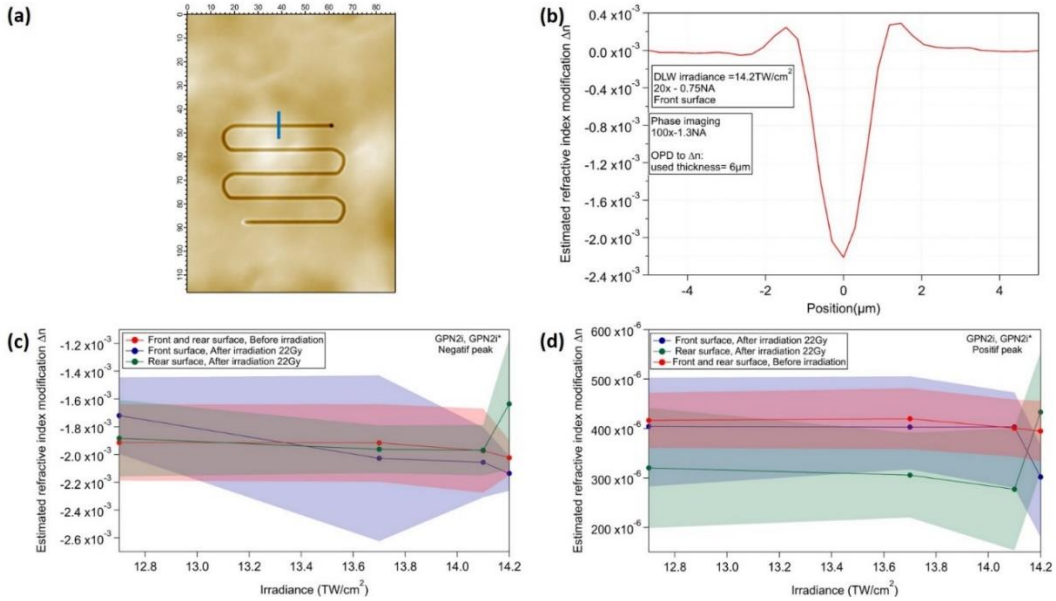

Figure III-37: (a) Phase image under white light illumination of the laser inscribed structure (14.2 TW/cm^2) of the front surface after irradiation. (b) Estimated refractive index modification determined from the phase image. (c,d) The negative and positive peak, respectively, of the refractive index modification Δn as a function of laser irradiance before/after 22 Gy-dose for the two planes in GPN2i, GPN2i glass sample.*

The integrated measure of the amplitude of fluorescence intensity was performed for the different structures of the two surfaces before and after 22 Gy X-ray dose for an excitation at 365 nm (Figure III-38). These images are obtained using the same method described for Figure III-30. Following X-ray irradiation, it becomes apparent that the overall fluorescence intensity of the clusters increases in both planes, indicating the appearance of additional silver clusters resulting from X-ray irradiation. This reveals a very sensitive behavior of the GPN glass to create silver clusters under irradiation, compared to the ARGO and ARGO3 commercial glasses.

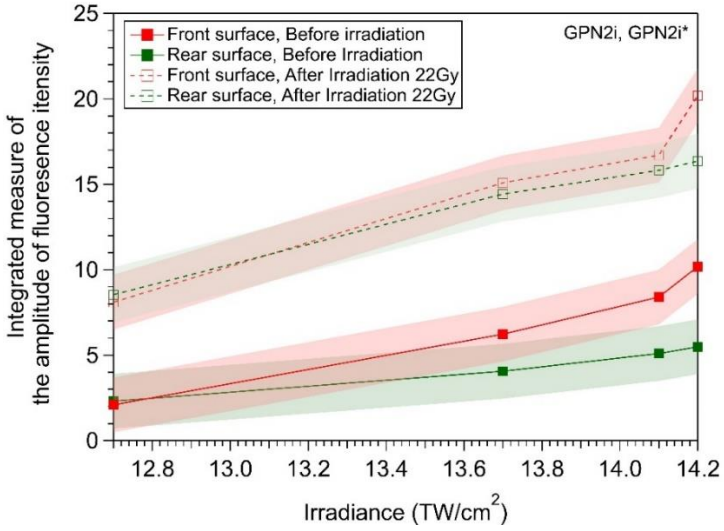

Figure III-38: Integrated measure of the amplitude of fluorescence intensity under 365 nm excitation, for the different laser irradiances before and after 22 Gy-dose for the two planes in GPN2i and GPN2i glass sample.*

The Fast FLIM algorithm was used to obtain Fluorescence lifetime imaging microscopy (FLIM) results in order to assess the impact of X-ray exposure on cluster emission. The fluorescence lifetime was fitted using a triple exponential decay model within the nanosecond range. Table III-6 reports the lifetimes and associated amplitudes average values with their standard deviations, before and after irradiation.

Table III-6: Fitting parameters with a three exponential decay time model for all DLW irradiance for the GPN2i sample.

		Fluorescence decay $\bar{\tau}_i ; \sigma_{\tau_i}$ (ns)			**Associated amplitude $\overline{A_i} ; \sigma_{Ai}$ (%)**		
λemission	**GPN2i**	$\bar{\tau}_1 ; \sigma_{\tau_1}$	$\bar{\tau}_2 ; \sigma_{\tau_2}$	$\bar{\tau}_3 ; \sigma_{\tau_3}$	$\overline{A_1} ; \sigma_{A_1}$	$\overline{A_2} ; \sigma_{A_2}$	$\overline{A_3} ; \sigma_{A_3}$
425 ± 25 nm	**Before irradiation***	0.7 ; 0.1	2.8 ; 0.3	5.1 ; 0.3	15 ; 1	55 ; 7	30; 6
	After irradiation, Front surface*	1.2; 0.1	3.7; 0.2	6.2 ; 0.4	13 ; 2	63 ; 5	24 ; 3
	After irradiation, Rear surface*	0.9 ; 0.1	2.9 ; 0.4	5.3 ; 0.3	17 ; 3	49 ; 8	34 ; 8
510 ± 40 nm	**Before irradiation***	1.5 ; 0.1	4.9 ; 0.2	9.1; 0.5	16 ; 3	63 ; 2	21 ; 1
	After irradiation, Front surface*	1.4 ; 0.2	4.7 ; 0.2	8.8 ; 0.3	17 ; 3	64 ; 3	19 ; 3
	After irradiation, Rear surface*	1.6; 0.2	4.9 ; 0.2	9.2 ; 0.5	20 ; 4	63 ; 2	17 ; 3

**Average statistical error over all measurements*

Table III-6 demonstrates a significant increase in fluorescence lifetime in both planes after exposure to a 22 Gy X-ray dose, their associated amplitudes distribution is approximately constant. In addition, Figure III-38 shows a significant increase in the fluorescence amplitude after irradiation. To consider these two observations (longer lifetimes and more intense fluorescence emission, we propose the hypothesis that X-ray irradiation has impacted the non-radiative lifetime transition, leading to fewer photons undergoing non-radiative de-excitation. Indeed, fluorescence lifetime can be expressed as follows:

$$\frac{1}{\tau_{measured\ *}} = \frac{1}{\tau_{radiatif*}} + \frac{1}{\tau_{non\ radiatif*}} \qquad \text{III-25}$$

Consequently, excited silver clusters appear to be more likely to deexcite radiatively, namely with photon emission, which corroborates both the observed increase in $\tau_{measured\ *}$ and the concurrent increase in fluorescence amplitude after irradiation.

iv. Inscribed glasses with silver clusters for application to X-ray dosimetry

Working on the luminescence spectra for excitation at 355 or 325 nm of distinct species (namely the inscribed-silver clusters and/or the color centers created after irradiation), an amplitude ratio of emission bands for GPNi* and ARGOi* glasses (Figure III-39(c) and (d)), respectively) can provide information regarding the dosimetry performances of those glasses. The RPL spectra of the GPNi* glass sample (see Figure III-25 for DLW irradiance of 13.4 TW/cm^2 at 160 µm below the glass surface) could systematically be decomposed in three Gaussian emission bands with fixed widths and positions while the related amplitudes (associated to silver clusters Ag_m^{x+} at 460 nm and hole traps Ag^{2+} at 620 nm) were evolving with the dose, as seen in (Figure III-39(a)). ARGOi and ARGOi* glass samples were also studied (Figure III-39(b)). For these two glasses, a deconvolution only with two Lorentzian bands (not three bands, contrarily to what was previously needed for the GPN glass) was realized for the non-normalized RPL spectra in the rear surface (see Figure III-26(b) for DLW irradiance of 11 TW/cm^2 at 550 µm below the glass surface).

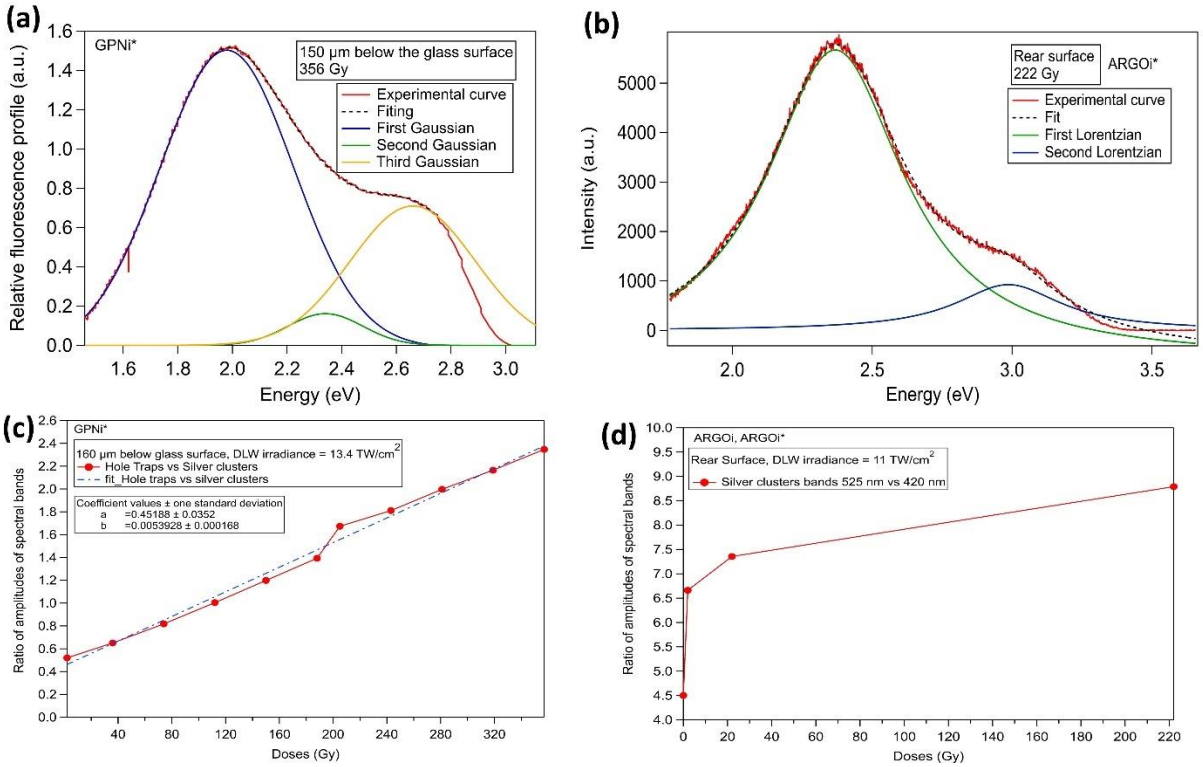

Figure III-39: (a) Fit of the RPL spectra of the GPNi glass for the laser inscribed structure at 150 µm below the glass surface at 356 Gy X-ray dose. (b) Fit of the RPL spectra of the ARGOi* glass for the highest DLW irradiance structure of the rear surface at 222 Gy X-ray dose. (c) Dose-dependent evolution of the amplitude ratios of extracted spectral bands of the hole trap center Ag^{2+} at 620 nm over the silver clusters Ag_m^{x+} band at 460 nm for the GPNi* glass sample for DLW irradiance of 13.4 TW/cm² at 160 µm below the glass surface. (d) Case of the ARGOi and ARGOi* glass sample for DLW irradiance of 11 TW/cm² at 550 µm below the glass surface (rear surface) for ratio of the two silver cluster bands (namely, the 525 nm band over the 420 nm band).*

By evaluating the dose-dependent evolution of the amplitude ratio of hole traps (band at 620 nm) versus that of silver clusters (band at 460 nm) in the GPNi* glass sample (Figure III-39(a)), a linear response is obtained, exhibiting a slope of sensibility ~ 0.005/Gy over the 2-357 Gy range. The precision of the dose sensitivity in this glass was estimated at 7% error for 1 mm sample thickness in the dose range of 2 to 357 Gy. This precision can change depending on the depth of the silver cluster and thus on the material thickness crossed by X-ray irradiation. Concerning the ARGOi and ARGOi* glass sample, the dose-dependent evolution of the amplitude ratio of the two silver clusters bands (525 nm over 420 nm) presents a highly nonlinear response in the dose range 0-222 Gy. A saturation starts to occur from the 2 Gy X-ray dose (Figure III-39(b)). Thus, it is not obvious to have a dosimetry behavior with a linear response in this dose range (2 to 222 Gy) using this glass sample. Oppositely, a highly-varying evolution could be achieved with X-ray doses lower than 2 Gy for this glass sample in the rear surface. Therefore, ARGOi* glass sample presents a very strong dynamic for X-ray doses lower than 2 Gy, having a slope sensibility ~ 1/Gy over 0-2 Gy, which is much larger than what is measured for the GPNi* sample : this glass could thus be of interest for high-sensitivity dosimeter in this range [238].

Regarding the ARGO3i* glass sample, insights into its dosimetry behavior can be extracted by analyzing the fluorescence lifetime measurement's emission amplitude.

Therefore, it is evident that various methods can be employed to assess dosimetry behavior. In the case of ARGO and GPN glass samples, emphasis has been placed on utilizing the fluorescence bands of the silver species. Conversely, for the ARGO3 glass sample, consideration could be given to employing the amplitude fluorescence lifetime. Although not explored in this study, an established technique in the literature involves investigating Bragg gratings for dosimeters. This approach, involving the distribution of multiple gratings within fibers or bulks, could be a valuable means of understanding the response of the deposited dose on the gratings distributed along the length.

III.4.1.c.Partial discussion on the post-X-ray study

The generation of silver species has been investigated in the present section, in three types of silver-containing phosphate glasses exposed to X-ray irradiation, which includes the formation of hole trap Ag^{2+} silver ions and molecular Ag_m^{x+} silver clusters (except for the ARGO3*). These silver species have shown a depth dependence in direct relation with the local X-ray deposited dose. Subsequently, several optical properties of the glass matrix are affected, such as the creation of radiation-induced absorption and emission bands, as well as the small decrease in the glass refractive index. Moreover, laser-inscribed fluorescent silver clusters had been validated previously to be thermally stable in silver-containing phosphate glasses [150], [151], [240], [245] and resilient to X-ray irradiation in the GPNi* glass sample [177]. This gives an opportunity for the laser-inscribed silver-based structures to be considered as local in-depth probes of the deposited X-ray dose. In this framework, identical silver cluster distributions inscribed at two different depths have been investigated in the three glass samples before/after X-ray exposure. The generation of color centers in the irradiated matrix has several effects on the spectroscopic properties of the laser-inscribed silver clusters. In fact, these color centers modify the glass environment of the silver clusters, which impacts in turn the observation of the silver clusters optical properties.
First, concerning the ARGO glass sample, the indirect changes in the fluorescence spectra, the fluorescence intensity, the modification of the refractive index of the silver clusters after X-rays are interpreted as resulting from the glass environment modifications more than the direct modification of the silver clusters themselves. Furthermore, the stability of the fluorescence lifetime of the irradiated laser-inscribed silver clusters, as well as their associated amplitudes, show their resilience to X-rays in both depths at the considered doses. However, additional X-ray-induced silver clusters may occur depending on the dose deposition, as shown with the micro-absorption measurements at the front surface laser-inscribed clusters, depending on the glass sensitivity under ionization radiation. This ensemble of experiments highlights the resilience of laser-induced silver clusters, these

species acting as local probes of the depth-dependent deposited doses and potentially behaving as in-depth local probes of the X-ray energy deposition.
In the case of the ARGO3 glass sample, femtosecond-written silver clusters at the front surface exhibit additional absorption due to the deposited-dose. Also, they may present less fluorescence emission as the weights of the amplitudes of the fluorescence lifetime have been altered following irradiation, being slightly influenced by the deposited dose at this specific level. Concerning the rear-surface silver clusters, the result of the refractive index change demonstrates no modification to the local environment of the silver clusters.
Regarding the GPN2i* glass sample, X-ray irradiation did not have an impact on the optical path difference i.e., the resulting refractive index change. However, it is evident that the fluorescence of the silver clusters has increased in both planes. This increase could be attributed to the effect of X-ray irradiation, which reduces the non-radiative lifetime, consequently resulting in a slight improvement in the measured fluorescence lifetime.
Consequently, the silver clusters inscribed in the GPN2i* and ARGO3i* glass composition do not demonstrate the same level of resilience as those formed in the ARGOi* glass sample.
Finally, the optical and spectroscopic properties were handled to demonstrate the realization of a dosimeter with detailed sensitivity. While GPNi* showed nice linearity of its sensing behavior over the 2-357 Gy range, ARGOi* glass sample tends to have a higher sensitivity for lower X-ray doses (especially for doses ranging below 2 Gy).

III.4.2.Real-time X-ray irradiation study

The silver clusters inscribed in the ARGO glass exhibit remarkable stability in their characteristics when subjected to X-rays, showing no significant signs of deterioration. These confined structures demonstrate impressive durability and could be considered as highly sensitive probes suitable for real-time fluorescence or absorption dosimetry within the material. The following section delves deeper into this concept, which we explored using an integrated optical device. The objective of this section is to examine, in real time, how fs-written silver clusters respond when exposed to X-ray irradiation to facilitate real-time monitoring of dose rates and doses. To achieve this, a waveguide was inscribed along the length of the ARGO glass sample. The waveguide will be connected to radiation-resistant fibers on both ends to transmit the emitted signals from the silver clusters during X-ray exposure. This device was chosen since the measurement equipment cannot be installed inside the radiation chamber. Therefore, we require transport fibers to connect the waveguide to them.

III.4.2.a.Experimental methods

i. Laser inscription of waveguides

The waveguides inscriptions were carried out using a prototype femtosecond fiber laser operating at a wavelength of 1030 nm. The laser had a repetition rate of 9.25 MHz, a pulse duration of 400 fs (FWHM), and an average output power of 5 W. During the laser inscription process, the precise positioning of the samples was maintained with an accuracy of 30 nm, thanks to the utilization of motorized 3-axis stages from Newport (XMS100 - VP5ZA). The inscription was performed on the same commercial silver-containing phosphate glass ARGO from Argolight company used in the section III.4.1.a.i. A waveguide of 50 µm of diameter was written along the length of the sample (~ 1 cm) using a 40x microscope objective with N.A. 0.75. To prevent aberrations, the center of the waveguide was chosen to be inscribed at a depth of 160 µm below the sample's surface. The 50 µm diameter was created for the purpose of connecting it to the super RadHard GI multimode optical fiber, which also features a core diameter of 50 µm. This dimension was selected to enhance the precision and reliability of the connection. A larger diameter could potentially lead to issues with the irradiance of the inscription process as a function of the depth, primarily due to spherical aberrations.

The waveguide is constructed according to a set of points, such that the produced structures have an approximately circular cross-section. This point distribution is the projection of lines inscribed along the *x*-axis onto the *yz*-plane. When using a microscope objective with 0.75 NA, the inter-distance dimension of the double line structure generated by one laser pass is ~ 1.5 µm (depending on the laser irradiance) along the *y*-axis while its thickness is 6 µm along the *z*-axis. Therefore, 20 planes (along the *y*-axis) with a separation of 1.5 µm between each laser pass was inscribed to form the 50 µm diameter in the lateral section. This signifies that one of the tracks of the double fluorescent lines aligns approximately with the previously inscribed track of the previously inscribed double lines. Along the *z*-axis, a separation between the depth planes of 2 µm (movement of the stages) was taken, achieving ~ 47% depth overlap. When moving the stages, it's important to consider that the actual depth of the focal point is the mechanical depth (movement of the stages) multiplied by the refractive index of the glass (1.59 for ARGO glass), so that successive laser-inscribed planes were physically separated by 3.2 µm. This method was employed to create the 1-pass waveguide, as shown in Figure III-40.

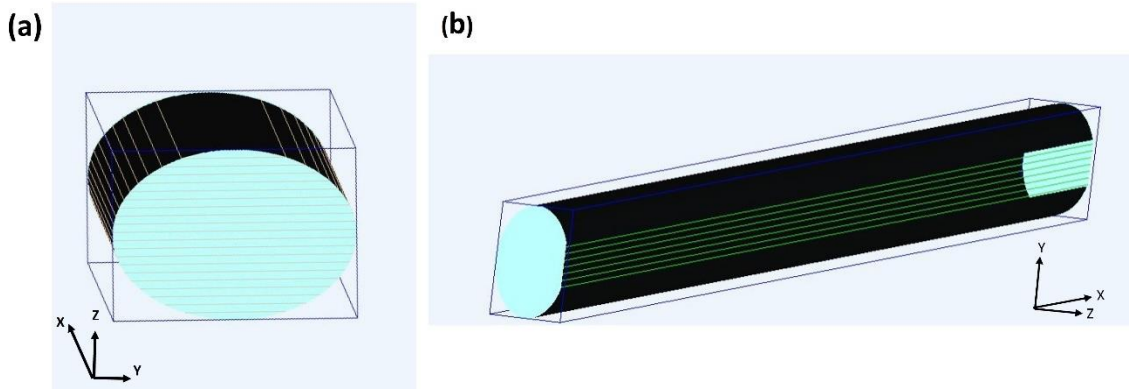

Figure III-40: Schematic representation of the inscribed waveguide: (a) showing the 20 planes along the y-axis, (b) showing one of the projected lines along the x-axis and stacked along the y-axis.

Additionally, a 5-pass waveguide was inscribed with the goal of achieving a significant refractive index change, thereby improving light transmission. The inscription process for the 5-pass waveguide closely follows that of the 1-pass waveguide. However, there is a variation in the depth overlap: in this case, a 3 µm movement of the stages is considered, resulting in a 4.8 µm physical step between successive planes which corresponds to 20% overlap of adjacent planes. This adjustment is implemented to prevent saturating the refractive index change and to mitigate any potential issues during the inscription process, such as reaching the inscription threshold and causing the material to explode. The 1-pass waveguide was created using an irradiance of 4.95 TW/cm² and a sample translation speed of 100 µm/s, whereas the 5-pass waveguide was inscribed with a slightly lower irradiance of 4.63 TW/cm², maintaining the same translation speed. An example of a top view and cross-sectional view observed under an optical microscope is shown in Figure III-41(a-b) and (c-d) for the 1-pass and 5-pass waveguides, respectively.

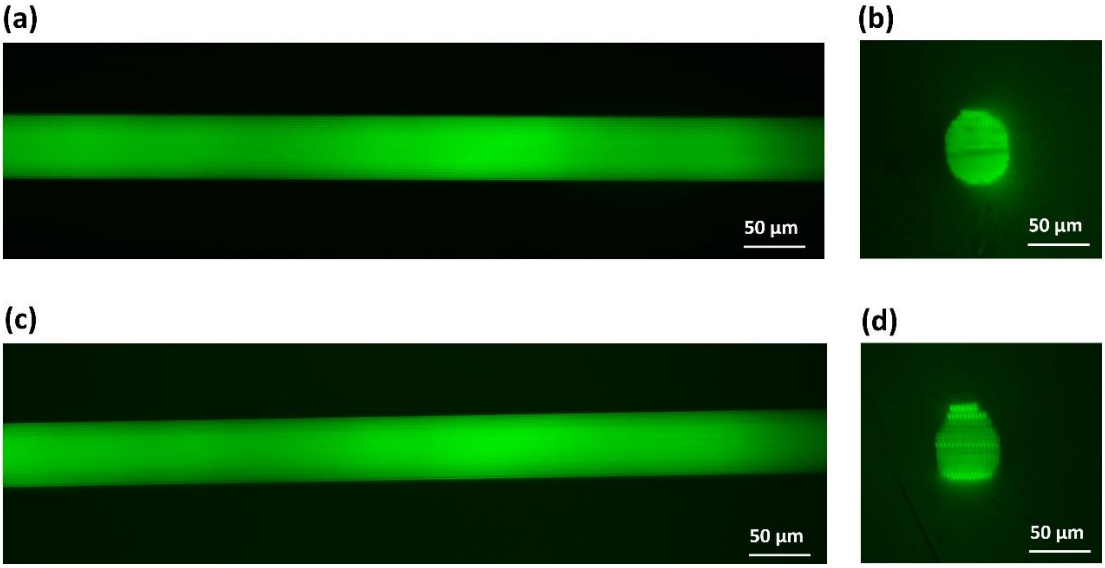

Figure III-41: Microscopy fluorescence image (excitation at 365 nm) of the: (a-c) top view and (c-d) side view after polishing the lateral surface, of the waveguide inscribed using one and five scans, respectively.

ii. Waveguides characteristics

• Numerical aperture

The numerical aperture of the waveguide was measured and compared to the one of the radiation-resistant fiber (0.2 NA) to assess how the injected light interacts with the waveguide.

To determine the numerical aperture of the waveguide, they were injected at 1030 nm using a tunable Ti:Sapphire laser provided by Coherent, which operated at a repetition rate of 80 MHz and delivered an output power exceeding 2.9 W at 800 nm. The injection process was performed in free space, employing a 20x microscope objective with NA 0.28. Subsequently, the near-field mode profiles of the waveguide were captured using a 12-bit camera beam profiler from Thorlabs. To facilitate the numerical aperture calculation, a distance of 5.21 mm was maintained between the facet of the sample and the camera's sensitive CCD matrix. Figure III-42 illustrates the mode profile at the 5-pass waveguide exit facet, demonstrating a multimode operation.

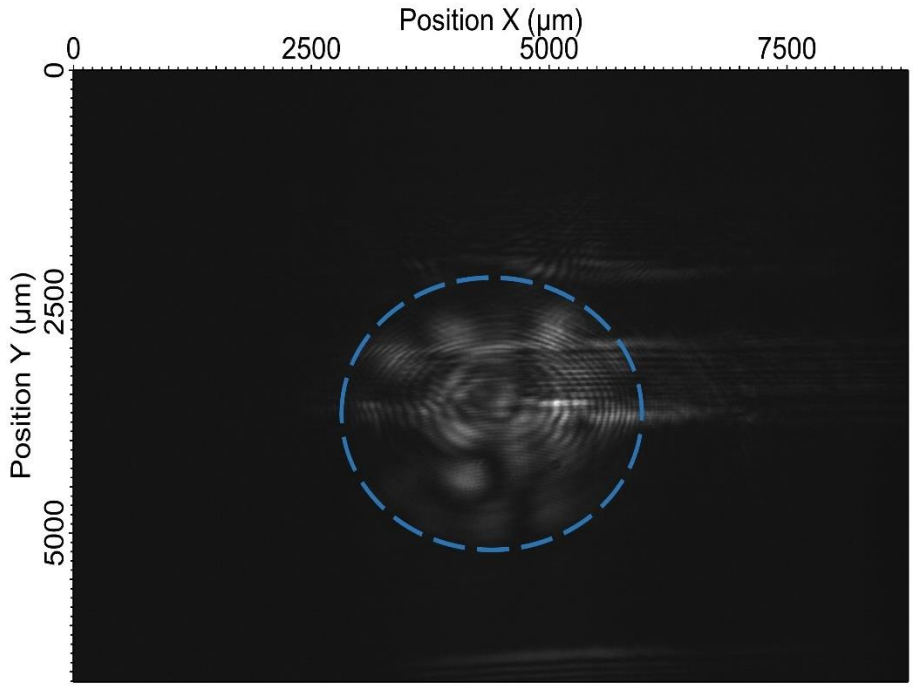

Figure III-42: Near-field image of the multimode guided profile (in blue circle) of the 5-pass waveguide at 1030 nm at the exit facet.

Hence, the numerical aperture is determined through the following equation:

$$NA = \sin(\theta_a) \qquad \text{III-26}$$

where θ_a represents the acceptance angle necessary for guiding the light, which can be calculated as follows:

$$\theta_a = tan^{-1}(\frac{w_0}{d}) \quad \text{III-27}$$

Here, w_0 denotes the mode's width obtained from the Gaussian fit of the horizontal and vertical line profiles of the near-field mode image, while d represents the distance between the exit of the waveguide and the camera beam profiler.

Therefore, the calculation results indicate that the numerical aperture of the waveguides with five passes is approximately ~ 0.28 ±0.02. The numerical aperture of the one-pass waveguide was not measured, but we suspect it is slightly lower than that of the 5-pass waveguide. Thus, the fiber used to connect the waveguide has a smaller numerical aperture than the waveguide itself. It means that, when injecting light into the waveguide to connect it to the fiber, the fiber can collect a narrower angle of incident light compared to what the waveguide can accept. In other words, the fiber provides less light (namely a slightly narrower angular distribution, NA =0.2) than what the waveguide can potentially carry. This can lead to a loss of efficiency in the light injection process, as some of the incident light will not be effectively injected into the waveguide. Conversely, it can also impact the collection of emitted light from the waveguide when trying to connect the waveguide to the second fiber. Note that the steps of the manufactured device will be explained later in this section.

- Transmission and fluorescence of the waveguides

The transmission characteristics of the waveguides were assessed across various wavelengths by injecting them and recording the transmitted power relative to the injected power. This experiment was conducted to study the transmission of such multimode waveguide in the visible range (the emitted range of luminescence after X-ray exposure).

Specifically, injections were performed at 600 nm, 650 nm, 700 nm, and 750 nm using a broadband supercontinuum white light laser source (Sambda-450, Leukos). To select the desired wavelengths for this measurement, a passband filter was employed. Additionally, in order to compare those results, the waveguides were illuminated at 700 nm and 1030 nm using a tunable Ti:Sapphire laser from Coherent. The injection of light was conducted in free space, employing a 20× microscope objective with NA 0.28. To collect the output from the waveguides, a 100× microscope objective with NA 0.7 was used. Table III-7 displays the calculated transmission values at the exit of the 1 cm long waveguides across various wavelengths, accounting for the transmission of the injecting and collecting objectives as well as the Fresnel reflection at the input and output interfaces of the sample.

Table III-7: Transmission data for the two waveguide geometries at various injected wavelengths.

	Transmission of the waveguides (%)			
λ (nm)	**5 laser pass**		**1 laser pass**	
	Ti:saphire	**Leukos**	**Ti:saphire**	**Leukos**

600	-	0.50		1.8
650	-	1.3		4.5
700	28.0	22.9		11.2
750	-	42.1		18.8
1030	89.5	-	65.0	-

It's important to mention that the waveguide's transmission is quite low until 700 nm. The transmission then begins to increase, reaching 89.5% and 65.0% for the 5-pass and 1-pass waveguides, respectively, at 1030 nm. Even though our aim was to measure if such multimode waveguides present transmission characteristics in the visible range, these results clearly emphasize that these silver-based waveguides exhibit significant absorption properties up to the range of 600-650 nm, as previously discussed in Chapter II. Figure III-43 illustrates the transmission characteristics of the 5-pass waveguide when injected by the white light source, emphasizing its transmission in the red range while absorbing light in the UV-blue range.

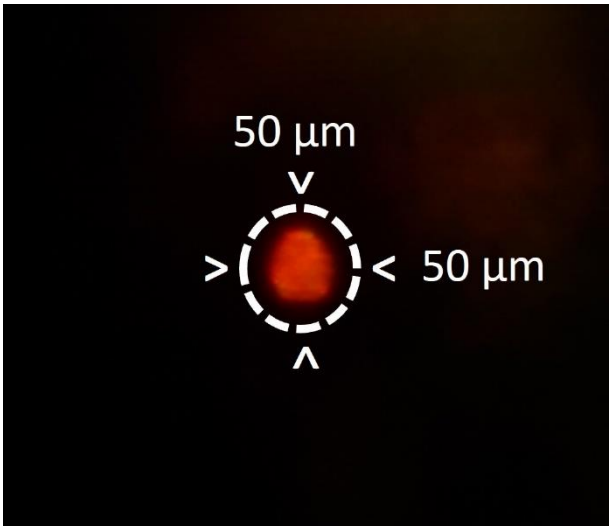

Figure III-43: The transmission of the 5-pass waveguide using the white light Leukos source.

From Table III-7, we can calculate the propagation loss coefficient at 1030 nm which is 0.5 dB/cm for the 5-pass waveguide, while it was found to be 1.87 dB/cm for the waveguide with only 1 laser pass. In addition, it is important to estimate the absorption coefficient in the visible range for this waveguide. To do so, we first assume that at 1030 nm the waveguide's transmission is 100% (full transparency of the glass and no additional absorption bands of silver clusters) so that the coupling coefficient is 89.5% (ideally corresponding to the measured experimental transmission of Table III-7). Second, we suppose that the coupling coefficient at 600 nm is similar to that at 1030 nm, namely 89.5%. In this context, we can

estimate that the absorption coefficient at 600 nm is approximately 5 cm^{-1}. If we assume a 90% absorption rate, we can calculate a length of 0.46 cm. This indicates that beyond this thickness, 90% of the light at 600 nm is indeed absorbed.

Moreover, the fluorescence spectra were recorded before subjecting the 1-laser pass waveguide to X-ray irradiation. The waveguide was excited with a 405 nm UV diode (OBIS, Coherent, 50 mW). The waveguide was excited from the lateral side of the sample using a Mitutoyo microscope objective with a 10x - 0.28 N.A. Fluorescence collection was executed with a Mitutoyo microscope objective with a 20x 0.5-N.A. A 435 nm long-pass filter was employed before the objective to block the UV diode's emission, enabling the observation of the fluorescence emitted by silver clusters. Subsequently, a Mitutoyo microscope objective 20x - 0.5 NA is employed to focus the output mode into an optical fiber (P400-1-SR) which was connected to a spectrometer (USB2000, Ocean optics) for the measurement of the fluorescence spectra.

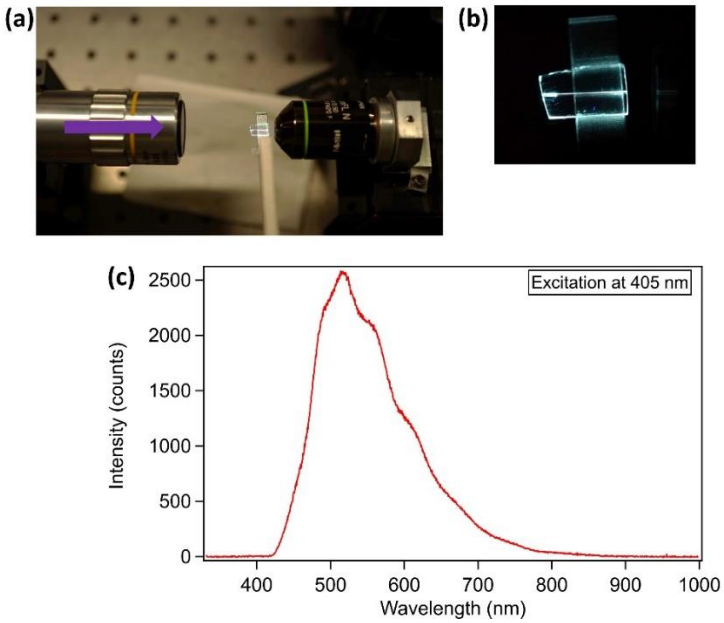

Figure III-44: (a) Setup of UV laser diode injecting at 405 nm from the lateral side of the sample. (b) Fluorescence image of the inscribed waveguide inside the glass. (c) Fluorescence spectra of the inscribed waveguide.

iii. Device manufacturing

The purpose of the device is to establish a connection, using transport fibers, between the two ends of the waveguide, in order to collect the luminescence and the induced absorption of the silver clusters while exposed to X-ray irradiation or to enable the injection of light from one side and collect the emission response from the opposite side of the connected fibers.
For this purpose, a custom-made piece was constructed in our laboratory workshop, comprising a rectangular aluminum plate. Within the center of the plate, a small rectangular

platform is used to maintain the sample, while two V-grooves (HFV002 from Thorlabs) will be fixed to the right and left sides of the sample's input and output surfaces. The different steps for preparing the device are reported in Figure III-45.

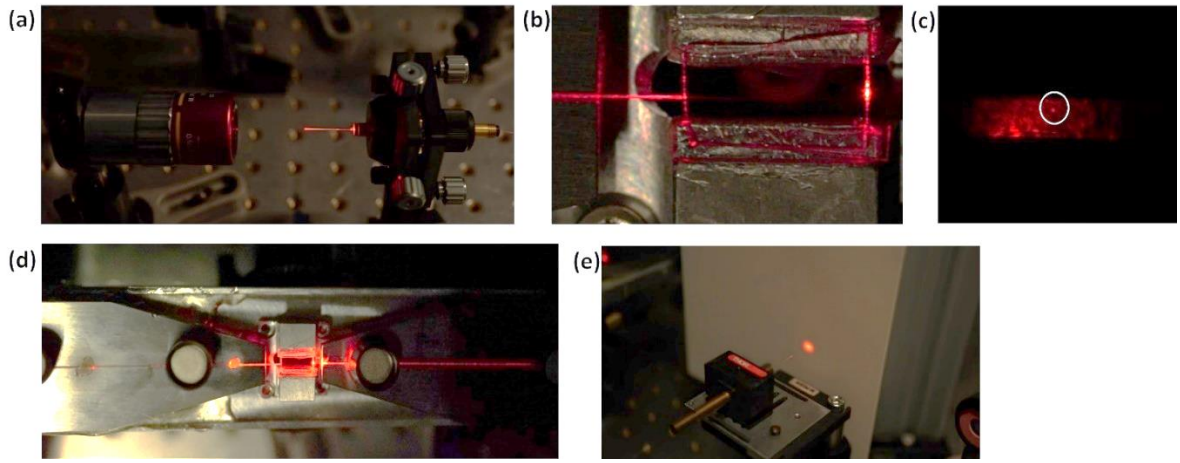

Figure III-45: Connectorization process of the laser-inscribed waveguides showing steps of the injection and connection of the waveguides to the radiation hardened fibers at both the entrance and exit facets.

The initial phase involves injecting the fiber by employing a 630 nm He-Ne laser source. This specific wavelength was selected because it offers better visibility. We used a Super RadHard GI-multimode fiber, sourced from DrakaEliteTM. This fiber is highly resilient to X-ray exposure and features a core diameter of 50 µm, a cladding diameter of 125 µm and a numerical aperture of 0.2. The input side of the fiber is precisely positioned using a 6-axis Newport stage and is injected using a Mitutoyo microscope objective with a 10x - 0.2 NA (Figure III-45(a)). The output side of the fiber is secured in the V-groove, mounted on a 3-axis translation stage. The aluminum plate, containing the sample at its center, is fixed on a 3-axis rotating stage. To inject the waveguide inscribed into the sample, the 3-axis translation and rotation stages are adjusted to bring the fiber on the V-groove close to the input facet of the sample and inject the waveguide (Figure III-45(b)). A top view of the injection process is visualized using a Sony Camera, while the injected mode is collected using a 20x microscope objective with a 0.4 NA. Figure III-45(c)) reports the injected mode of the waveguide on a white screen. Once the injection at the input surface of the sample is optimized using both translation and rotation stages, the V-groove is permanently glued to the rectangular aluminum plate. After the adhesive has dried, the microscope objective used for mode collection is removed. Subsequently, a second fiber, also held on a V-groove, is placed on another translation stage to collect the injected mode at the output surface of the sample (Figure III-45(d)). Hence, the light injected through the initial fiber is gathered at the output of the second fiber, due to the silver-based waveguide inscribed within the glass (Figure III-45(e)). Figure III-46 depicts the final outcome of the manufactured device. Consequently, the transmission for the device at 630 nm with the waveguide inscribed in a

single laser pass is 0.52%, whereas for the one with five laser passes, is 0.38%. However, it becomes challenging to directly compare the transmission of both waveguides due to the presence of multiple factors influencing these outcomes. Indeed, several factors contribute to the difficulty of comparing the transmission of both waveguides. Firstly, the inherent weakness of transmission at this wavelength plays a role. Additionally, factors like the coupling coefficient, the quality of the fiber and sample surfaces come into play. It's worth noting that the lateral surfaces of the sample were polished using polishing paper to bring the waveguides to the surface.

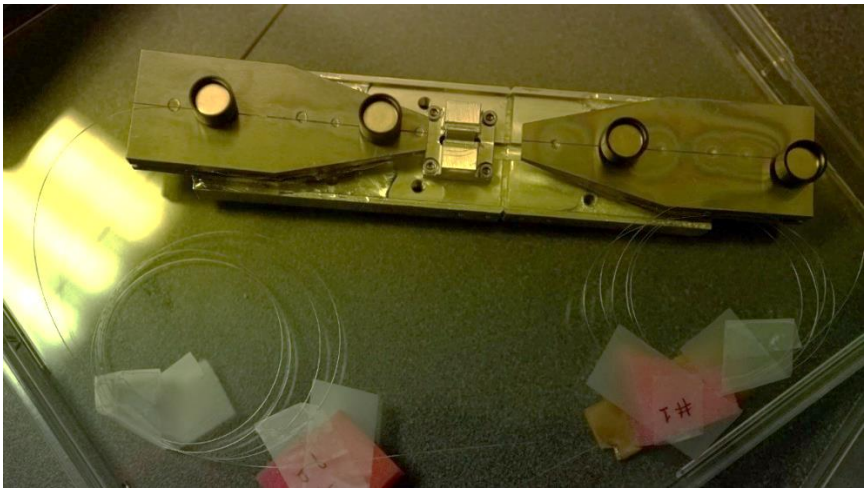

Figure III-46: The ultimate result of the manufactured device for the 5-pass waveguide after connectorization with radiation hardened fibers for the perspective of in-situ radiophotoluminescence and radiation-induced attenuation.

iv. X-ray irradiation setup

X-ray irradiation was carried out using the LabHX X-ray machine located at the Laboratory Hubert Curien (University Jean Monnet, Saint-Etienne, France) in collaboration with the group MOPERE (Team leader Sylvain Girard, with the involved colleagues Adriana Morana, Youcef Ouerdane and Aziz Boukenter). This X-ray device provides an irradiation area of 10 x 10 cm^2 featuring a tungsten anode, operating at 100 kV and producing X-rays with a mean energy fluence of 40 keV. The current had the capability to be increased to 30 mA. The irradiation chamber was sufficiently large, to cover a wide range of dose rates, spanning from 400 µGy(H2O)/s to ~60 Gy(H_2O)/s, encompassing the entire accessible height from the bottom of the enclosure to the tube contact point. However, for a specific height setting, the range of attainable dose rates was constrained by the photon flux that could interact at that height under the maximum tube operating current. The sample was positioned at a distance of 18 cm from the tube, enabling dose rates to vary between 5.81 mGy(H_2O)/s and 1.74 Gy(H_2O)/s by adjusting the current. In the rest of this part, all reported dose rates are in H_2O. We expect a 10% accuracy on the dose rate.

Three devices (the 5-pass and 1-pass waveguide devices as well as the bulk sample) are

placed separately in the LabHX machine. The device was connected from both sides by two detectors via transport fibers which are the same as the one connected to the device. Both fibers are fusion-spliced to other fibers at the exit of the radiation source to be connected to the measurement equipment but were not exposed to radiation. The initial detector used is a spectrometer (QE PRO- Ocean insight), enabling the capture of the spectral characteristics of the luminescence band. The second detector is a photomultiplier tube (PMT) (Hamamatsu photon counting head) which integrates all the light within its spectral range. The PMT setup provides information only about the intensity value of radiation-induced luminescence, but it allows measuring extremely low signal intensities. Preliminary results showed that this super RadHard optical fiber produces a nonnull RL signal when exposed to X-rays [246]. Thus, this was shielded using 3 mm thick lead (Pb) plates, covering most of their length inside the irradiation chamber until the connecting point with the sample under test.

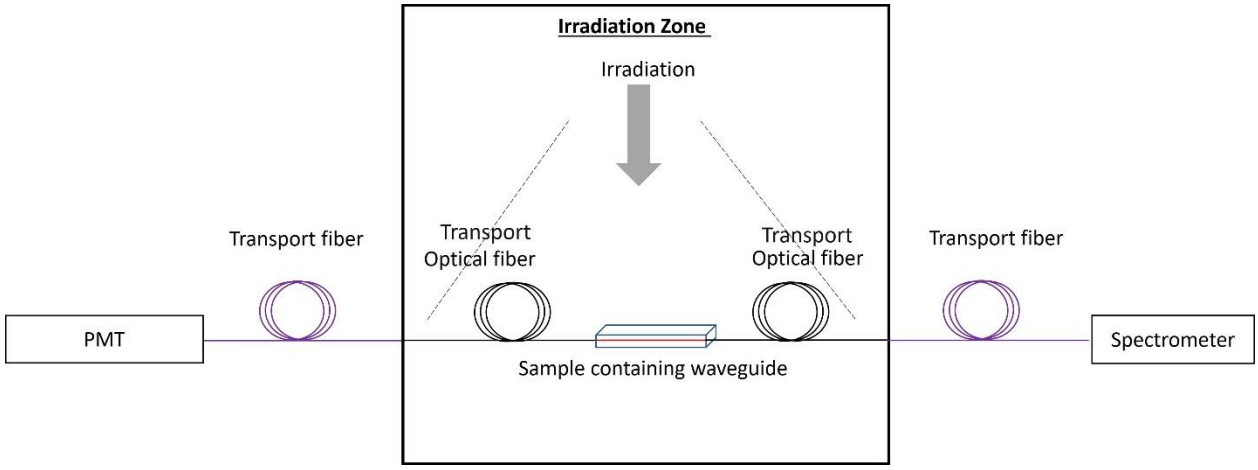

Figure III-47: Schematic representation of the experimental setup implemented at Hubert Curien laboratory, for radioluminescence and radiation-induced attenuation measurements.

v. Radiation-induced luminescence measurement

Radiation-induced luminescence measurements do not require an external light source, as the signal being detected is generated by the radiation itself. For this measurement, the PMT and spectrometer are both employed, with each connected to the transport fibers on one side. To perform a calibration of the radioluminescence measurement emitted by the waveguides and the bulk sample, a stepwise progression in dose rates was conducted to collect the radioluminescence amplitude associated with each dose rate. Each step corresponds to an irradiation duration of 1 minute, followed by a recovery phase lasting 3 minutes, allowing the radioluminescence to fade away. This approach subjected the sample to 12 values of dose rates from 5.81 mGy(H_2O)/s to 1.743 Gy(H_2O)/s, as shown in Figure III-48. The X-ray tube filament current was set from 0.1 to 30 mA to reach these dose rate values. This experiment was carried out on both samples containing the waveguide with 1 and 5 passes as well as the bulk sample, as further detailed after. Prior to the first run, the 5-

pass waveguide, the 1-pass waveguide, and the bulk sample have already been exposed to 10 Gy, 2 Gy, 100 Gy, respectively for testing purposes. Total dose deposited on the sample is accumulated because of subsequent runs at different dose rates and reaches 404 Gy at the end of the sequence. The radiation-induced luminescence signal is acquired by the PMT, and each acquisition is performed with an acquisition time of 0.5 seconds.

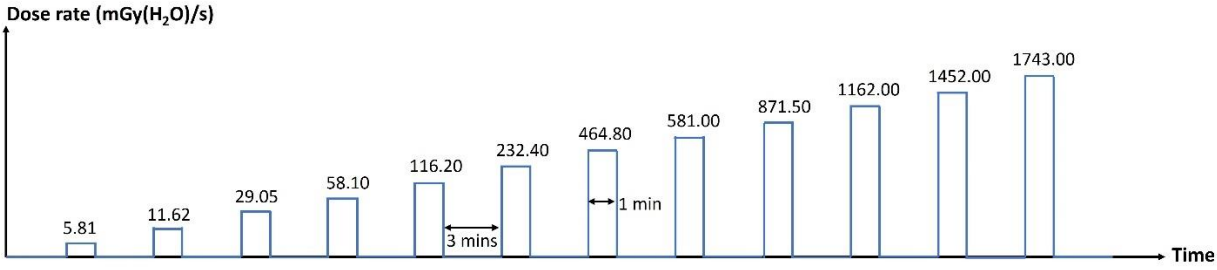

Figure III-48: Sequence of dose rates applied for irradiating each sample during RL measurements.

vi. Radiation-induced attenuation measurement for the connectorized device

In the post-Xray irradiation study, we have presented postmortem radiation-induced attenuation measurements allowing to observe stable defects.

In this section, real-time radiation-induced attenuation spectra are obtained by acquiring the transmission spectra of a sample as a function of time both before irradiation and during exposure to the radiation beam along with a recovery time. In this context, the resulting RIA depends on either the elapsed time or the dosage received during irradiation. Subsequently, RIA is defined as follows:

$$RIA(\lambda,t) = -\frac{10}{L} log_{10}\left(\frac{I(\lambda,t) - I_{noise}(\lambda)}{I(\lambda,t_0) - I_{noise}(\lambda)}\right) \quad \text{III-28}$$

where L is the length of the tested waveguide, $I(\lambda,t)$ represents the transmitted spectrum obtained at time t, $I(\lambda,t_0)$ serves as the reference spectrum recorded immediately prior to irradiation initiation, t_0 is the start of irradiation and $I_{noise}(\lambda)$ corresponds to the noise spectrum, acquired when no signal is transmitted in the waveguide.

In situ RIA measurements for the connectorized device were performed with the setup illustrated in Figure III-49, by acquiring the transmitted spectra with a deuterium/halogen source and a UV-Vis spectrometer (with an integration time of 10 sec). When investigating the RIA of glass materials at a radiation facility, it is not feasible to place the light source and spectrometer inside the irradiation room. Instead, the light source situated in the instrumentation area is connected to the sample exposed to radiation via radiation-resistant multimode optical fibers. Additionally, a connection extends from the sample to the spectrometer positioned outside the radiation room. In our case, measurements can be

performed by placing the investigated device under a homogeneous radiation beam and simply splicing the connected fiber to the waveguide to radiation-resistant transport fibers. Both the transport fibers and the one connected to the waveguide are shielded to avoid any impact on the RIA response of the waveguides.

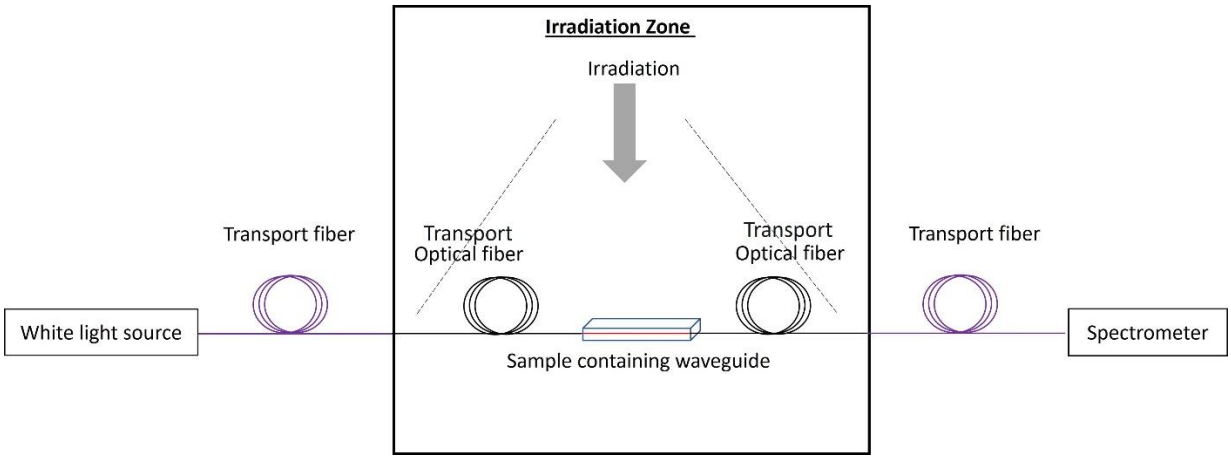

Figure III-49: Setup for in-situ RIA measurements using a white light source.

Furthermore, in-situ RIA measurements were performed by employing a UV diode operating at 405 nm (OBIS, coherent, 50 mW) during the exposure of the waveguide to X-ray irradiation. This approach quantifies the losses acquired during irradiation by exciting the waveguide at 405 nm and utilizing the emitted signal in the visible spectrum to assess these losses. The RIA spectral dependence is determined by irradiating the 5-pass waveguide and measuring its transmitted spectra at different time points, both before the irradiation begins and while the waveguide is exposed to the radiation beam, followed by a recovery time. A new setup was implemented, as illustrated in Figure III-50. This measurement was conducted on the pre-irradiated 5-pass waveguide (1.225 kGy). The UV source, positioned outside the irradiation chamber, is focused into an optical fiber using an objective. The fiber's output is directed to a cylindrical lens (focal length of 7.5 cm), creating a focused beam of light that illuminates the whole length of the waveguide inscribed within the glass sample.

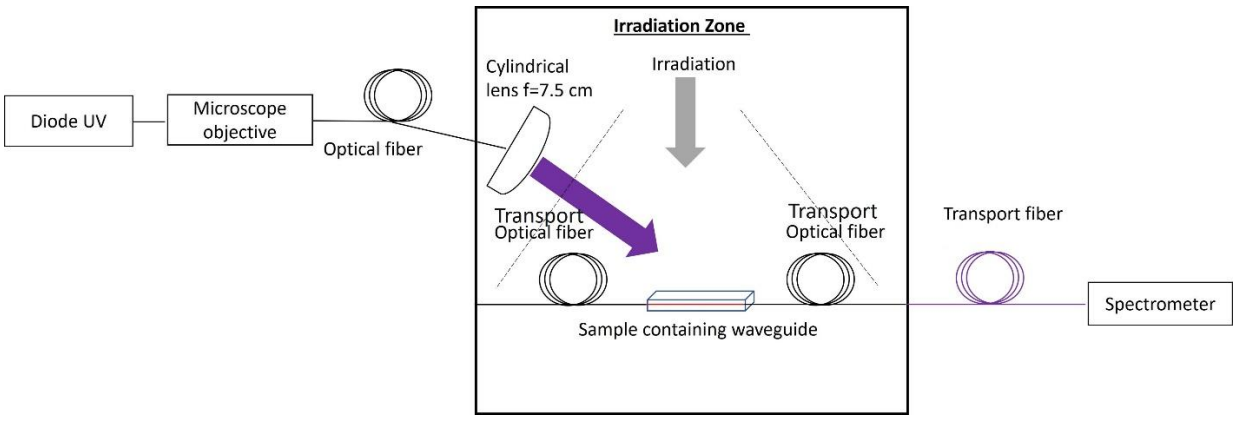

Figure III-50: Setup for RIA measurement using a UV diode at 405 nm.

vii. Radiation-induced attenuation measurement for a bulk sample

In order to measure the RIA of the bulk sample, a different setup was employed for online measurement compared to the one used for the connectorized device. This particular setup was developed specifically by our colleagues at the Huber Curien laboratory [247], to conduct online RIA measurements during and after X-ray exposures on bulk glasses. In this setup, a the light of a deuterium-halogen source is introduced into a multimode fiber (Draka MM SuperRadHard) pigtail. This fiber is connected to a UV-Enhanced Aluminum Reflective Collimator (Thorlabs RC02SMA-F01), which is designed to efficiently capture the input light signal and produce a parallel light beam with a diameter of 2 mm. Using a parabolic mirror, the distance between the fiber and the mirror can be adjusted in order to reduce the spot size. However, to assure a small light spot on the sample a circular slit with a diameter of 1 mm was placed between the parabolic mirror with the incoming light and the sample. The incident beam is directed onto the test sample. It travels through the air for a significant distance, typically spanning tens of centimeters, before reaching the top surface of the glass sample. This surface, situated just below the area exposed to X-rays from the tube positioned above it, is where the beam interacts with the sample. Upon traversing the sample, which can range from less than 1 mm to over a centimeter in thickness, the emerging beam is collected by another Thorlabs RC02SMA-F01 component. Subsequently, it is coupled into a multimode transport fiber that connects to a spectrometer (QE6500 from ocean optics) designed to operate within the wavelength range of UV/Visible. In addition, the RIA of the bulk sample was compared to that of the fs-inscribed structure. To do so, a serpentine square of 2 x 2 mm^2 was inscribed in another bulk glass with the same laser parameters as the one used for the 1-pass waveguide. Both samples were irradiated with the same dose rates at 0.58 Gy(H_2O)/s for 1 hour, followed by a recovery time of few hours. RIA in then calculated using Equation III-28 described above. Figure III-51 depicts a schematic illustration of the used setup.

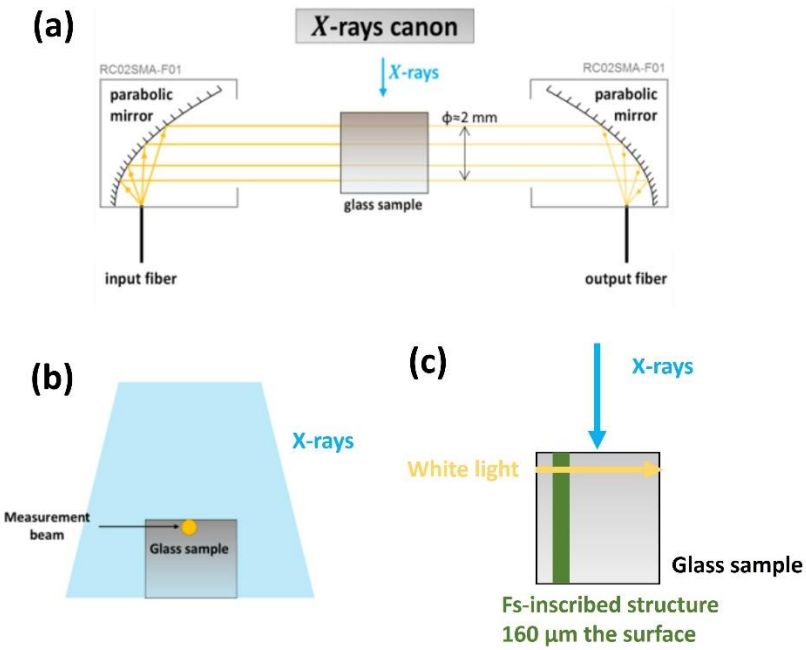

Figure III-51: Illustration of the irradiation setup, from(a) the front view and (b) the side view, (c) the front view in the case the fs-inscribed glass.

III.4.2.b.Results

i. Radiation-induced luminescence measurement

Before the initial run, the 5-pass waveguide had already received an irradiation dose of approximately 10 Gy, performing some tests to optimize the acquisition parameters. Figure III-52(a) depicts the signal on the PMT of the 12 experimental steps conducted on the 5-pass waveguide as a function of irradiation time. An example of time traces of measured RL signal of the 5-pass waveguide is shown in this figure. As previously explained, each RL signal step on the graph is measured for a different dose rate subjected on the 5-pass waveguide for 1 minute of irradiation. For each irradiation, a RL profile is obtained, which serves as a direct signature of the interaction between the waveguide and the X-ray beam. We observe that all tested samples show a significantly measurable RL signal down to the lowest investigated dose rate of 5.81 mGy/s. This graph effectively demonstrates that as the dose rate increases, so does the intensity of the recorded RL signal. The signal emitted by the waveguide follows the same growth pattern as the dose rate, as evidenced by each step increase in intensity. Once the dose rate stabilizes, the radioluminescence remains at an average value throughout the irradiation period. Notably, the radiation-induced luminescence levels from the sixth dose rate to the twelfth dose rate (particularly at higher dose rates) exhibit a decrease with irradiation during the initial run, as shown in Figure III-52(a).

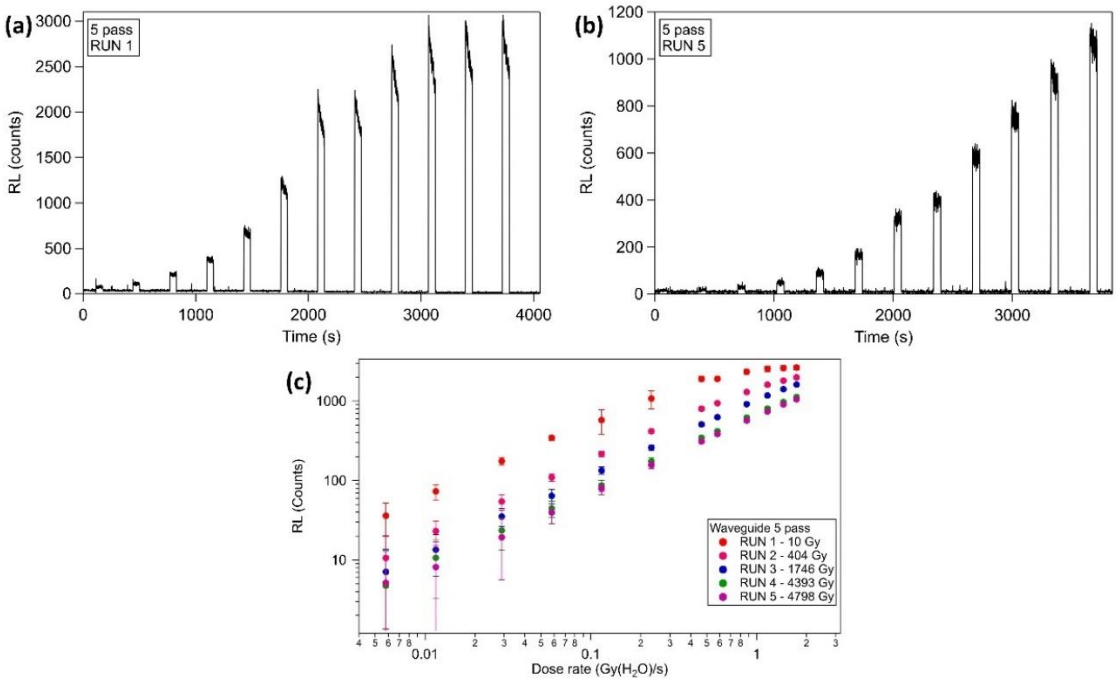

Figure III-52: Radioluminescence signal recorded for the 5-pass waveguide during 12 consecutive sequences at dose rates ranging from 5.81 mGy(SiO_2)/s to 1743 mGy(SiO_2)/s, maintaining a 1 minute irradiation period followed by a 3 minutes healing phases: (a) initial run, (b) fifth run. (c) Radioluminescence signal under X-ray irradiation as a function of dose rates for five repeated runs for the 5-pass waveguide. Note that the dose recalled in the legend of Figure (c) depicts the dose already deposited before each run. The deposited dose before the second and third runs are not linear as we conducted another test between those runs on that sample.

To establish a calibration with the dose rate, the amplitude of each interval is extracted and then averaged over the period of irradiation. A standard deviation of the signal over this period is also calculated to serve as an error for this average. The noise is also extracted by averaging the signal before the start of each irradiation. The average RL amplitude, after noise subtraction, with the corresponding standard deviations are depicted in Figure III-52(c) for the 5-pass waveguide, as a function of dose rate. One can see that the RL level is saturated in the first run at higher dose rates (red markers), the amount of RL signal appears to be decreasing compared to an expected linear extrapolation. This can be explained by two phenomena: the occurrence of RIA at the fluorescence emission wavelengths along the fluorescent waveguide which may reduce the amount of collected light, or/and the decrease during irradiation of the silver clusters population which would correspond to a reduction of the fluorescent efficiency of the waveguide under X-ray irradiation.

To mitigate the observed effects of RIA on the linearity of RL response on radiosensitive samples, an identical series of measurements were performed on pre-irradiated samples, obtained by repeating additional four times the irradiation sequence described in Figure III-48. The results shown in Figure III-52(b) were obtained during the fifth run, therefore, on samples pre-irradiated with a total ionizing dose (TID) of 4789 Gy. In the case of the fifth run, the reduction of the RL signal over the 1 min irradiation period is less pronounced at

high dose rates. This can be attributed to the activation of precursor centers during the preceding exposures. In the initial run, we initiated the activation of all centers that are easily activated, resulting in the decline of the radioluminescence amplitude, as observed by the sharp decreases in the measured signal. Consequently, we achieve a consistent RL response by the end of the fifth run because we have effectively stabilized the matrix in terms of radiation-induced attenuation. Indeed, RIA stabilizes as TID increases, and therefore the linearity of the RL signal improves. Indeed, an ideal dosimeter would exhibit a signal that is directly proportional to the dose rate. Figure III-52(c) reveals that this criterion is obtained after 3 successive runs. The RL signal measured on pre-irradiated samples exhibits a more linear response for the fourth and fifth run in Figure III-52(c), making these pre-irradiated samples more benefiting for dosimetry applications. In other words, pre-irradiation needs to be included in the calibration process of such sensors for future dosimetry applications, for doses higher than a few tens of Gy [248]. The afterglow *i.e.,* remaining RL signal after irradiation appears to be absent or too low. It is such a positive point since the post-irradiation luminescence tail can overlap with the luminescence produced during the subsequent irradiation. The luminescence amplitude during this new irradiation may be influenced by the kinetics of the tail distribution and the plateau when the dose rate stabilizes. This effect is expected to be more pronounced when the time between two irradiations is getting short, and when the dose rates are high. Consequently, this overlap can lead to an overestimation of the amplitude corresponding to the used dose rate, thereby degrading the dosimeter's performance. However, since we have a weak RL signal (compared to other materials), it is easier to avoid such afterglow. Because of the low RL signal delivered by the waveguides, our setup was unable to measure a significant RL spectrum for these samples. Since our experimental setup employs low-energy X-rays (≤100 keV), the Cherenkov effect, which is typically associated with higher-energy radiation, does not take place [201]. As a result, we did not assess its impact on the RL signal within the scope of our study.

In order to compare with the RL induced from the 5-pass waveguide, the same experiment was conducted on the 1-pass waveguide and on a pristine glass sample that had not undergone femtosecond inscription. This unmodified glass sample was likewise linked to a fiber with the intention of subsequently splicing it to the transport fibers for connection to the PMT. The bulk sample had been pre-irradiated, before the runs at different dose rates, to approximately 100 Gy and the 1-pass waveguide has been exposed to 3.8 kGy. Figure III-53(a-b) presents a comparison of the RL signal under X-ray irradiation as a function of dose rates with repeated five runs for the 5-pass waveguide versus the bulk sample and for the 1-pass waveguide versus the bulk sample, respectively. In Figure III-53(a), between the second and third exposition of the bulk sample, we subjected it to an additional 4 kGy irradiation to facilitate comparisons: the third run (bulk) with the fourth run (waveguide) and the fourth run (bulk) with the fifth run (waveguide).

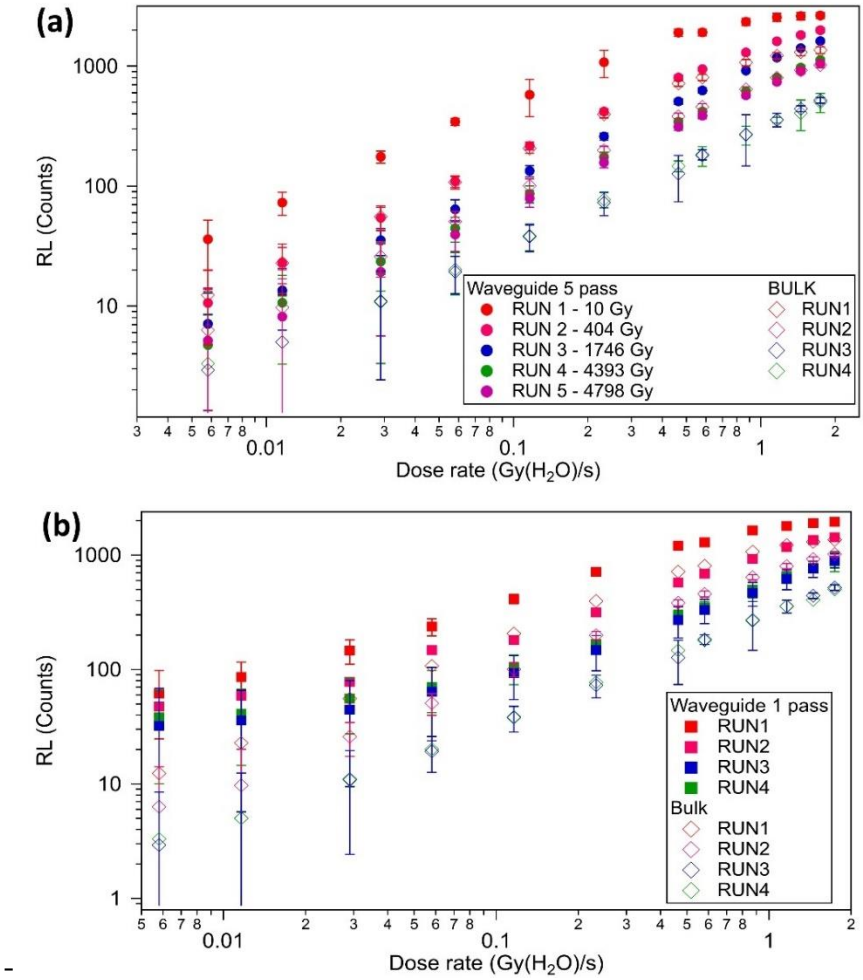

Figure III-53: Comparison of the RL signal under X-ray irradiation as a function of dose rates with repeated five runs for (a) 5-pass waveguide vs. bulk sample, (b) 1-pass waveguide vs. bulk sample.

The RL signal of the bulk sample is slightly lower than that of the 5-pass and 1-pass waveguides. A bit more luminescence is guided by the waveguides composed of the inscribed clusters than in the bulk glass. Therefore, we cannot be certain that the difference is solely due to the luminescence of the inscribed structure under X-ray irradiation; it may also be related to the collection efficiency of luminescence. Still, it should be noted that photo-induced silver clusters indirectly demonstrate resistance to X-ray irradiation, as evidenced by the resilience of the waveguides (which are supported by the distribution of silver clusters) to X-ray exposure. However, silver clusters did not show any X-ray activated fluorescence emission, even under laser inscription with multiple passes.

ii. Radiation-induced attenuation measurement of the connectorized sample

To understand the impact of RIA effects on the RL, it is important to know the magnitude and the spectral distribution of this phenomenon. Two experiments of RIA were conducted. In the

first one, transmitted spectra for the 5 and 1-pass waveguides were obtained using a halogen source (Ocean optics- DH2000 - UV-VIS-NIR light source) and a UV/Vis spectrometer. Figure III-54 depicts the progression of the transmitted spectra for the 5-pass waveguide throughout the end and the start of irradiation. Transmitted spectra are captured before, during, and after irradiation. The experiment involving the 5-pass waveguide was conducted at a constant dose rate of 0.58 Gy/s with an irradiation duration of 3900 seconds followed by a recovery phase of ~ 1 hour. By the end of this experiment, the waveguide has accumulated a total dose of 2.24 kGy. It's worth noting that this waveguide had already been exposed to a dose of 1.75 kGy prior to this experiment, which was conducted between the third and the fourth run of RL measurement. This visualization highlights a reduction in transmission intensity during irradiation, explaining the decrease in amplitude of RL as observed in Figure III-52(a) for high dose rates.

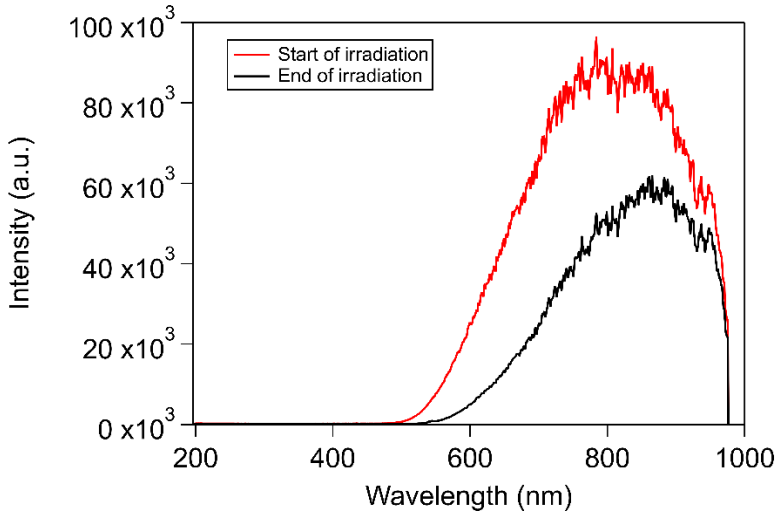

Figure III-54: Evolution of the transmitted spectrum of a white light source through the 5-pass waveguide at the beginning and the end of irradiation for a TID of 2.24 kGy at the end of the depicted sequence.

Regarding the 1-pass waveguide, we maintained the same dose rate for approximately 6300 seconds, followed by a recovery phase of 10 minutes. This waveguide was already pre-irradiated by less total ionizing dose than the 5-pass waveguide (2 Gy).
By using lead shielding, the lead covered a portion of the 1-pass waveguide sample, leaving only 0.7 cm exposed to irradiation, whereas the whole 1 cm length was irradiated for the 5-pass waveguide. By employing Equation III-28 and considering the specified length for each waveguide, the RIA spectra are obtained from the transmitted recorded spectra. This constitutes a differential measurement that excludes the losses of the pristine glass. It resembles two consecutive measurements in which the dose is accumulated, allowing us to observe the changes in absorption over time and for different wavelengths.

The spectral RIA for each waveguide is illustrated in Figure III-55(a), at the same total ionizing dose of ~ 2.3 kGy. It was shown that, even if both waveguides are previously

irradiated with different total doses and even if the 1-pass waveguide has been exposed to irradiation for a longer time, the RIA curve follows the same slope, as shown in Figure III-55(a). This suggests that the RIA is not influenced by the inscribed number of silver clusters.

By analyzing all the transmitted recorded spectra, it is possible to also examine the growth and decay kinetics of RIA. Typical results from the same dataset at wavelengths of 500, 550, 600, 650, 700, and 750 nm are presented in Figure III-55(b) for both waveguides. It is evident that as the wavelength decreases, RIA increases. Under irradiation, we produced a considerable number of absorbing centers, whose bands are mainly centered at wavelengths shorter than 500 nm, as seen in Figure III-54 and Figure III-55(a). When the irradiation stops, RIA decreases, as evidenced at times after 6300 seconds for the 1-pass waveguide and after 3900 s for the 5-pass waveguide, respectively. As already mentioned, both waveguides exhibit the same RIA levels even for different irradiations conditions (different exposition time and pre-irradiation doses).

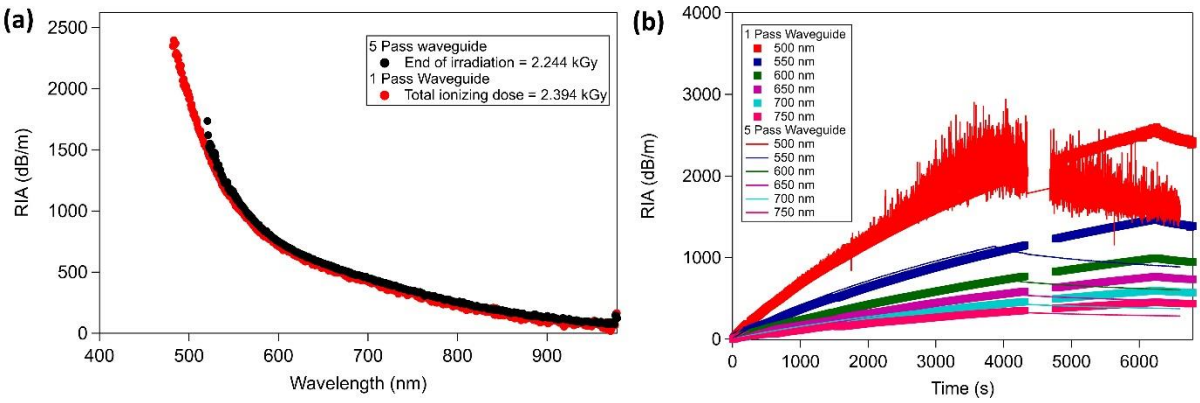

Figure III-55: (a) Spectral RIA acquired on the 5-pass and 1-pass waveguides having a 1 cm and 0.75 cm length, respectively, after a accumulated dose of ~ 2.3 kGy (b) RIA kinetics for six wavelengths covering the spectral RIA, in the case of the 5 and 1-pass waveguide. The 5-pass waveguide is subjected to 581 mGy(H_2O)/s for 3900 seconds while the 1-pass waveguide is irradiated for 6300 seconds for the same dose rate. Increase of the RIA under irradiation and subsequent slowlier decay after the stop of the irradiation.

The second experiment of RIA was conducted using a UV diode source at 405 nm, to excite the clusters' luminescence and a UV/VIS spectrometer. This experiment was carried out on the 5-pass waveguide only. Figure III-56 illustrates the evolution of transmitted spectra for the 5-pass waveguide, at the beginning and the end of irradiation for two different dose rates and two irradiation times. This experiment was repeated two times varying both the irradiation time (1 min, 3 min) and the current (30 mA, 10 mA, respectively) *i.e.,* the dose rates (1743 mGy(H_2O)/s, 581 mGy(H_2O)/s), with the aim of subjecting the waveguide to an equivalent total dose (104.58 Gy(H_2O)/s). Figure III-56 depicts a decrease of the amplitude during irradiation for the short wavelength (450-650 nm), emphasizing the occurrence of radiation-induced attenuation in this range.

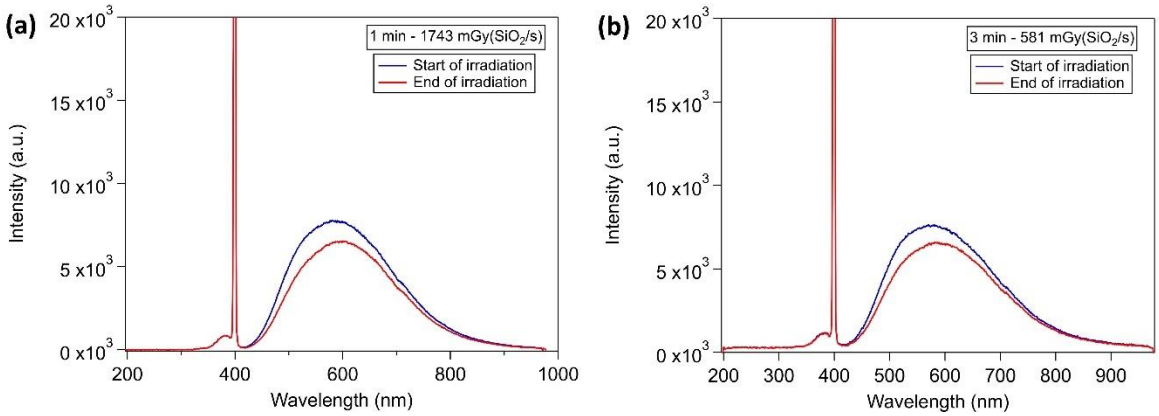

Figure III-56: Fluorescence spectra excited from the top facet and recorded at the exit facet of the 5-pass waveguide at the beginning of the irradiation (blue line) and at the end of irradiation when receiving the highest TID (red line) for : (a) a dose rate of 1743 mGy/s during a 1 minute of irradiation, (b) a dose rate of 581 mGy/s during a 3 minutes of irradiation. The peak observed at 405 nm is associated with the UV diode source.

Figure III-57(a-b) reports the kinetics over time for RIA measurements at different wavelengths when exciting the waveguide using a UV diode at 405 nm, for the two distinct conditions. All kinetics are calculated by averaging over a spectral range of 4 nm. As already found for the RIA measured by injecting a white light source, even in this case a larger RIA is observed at smaller wavelength. An absorption band centered at wavelengths shorter than 450 nm is observed.

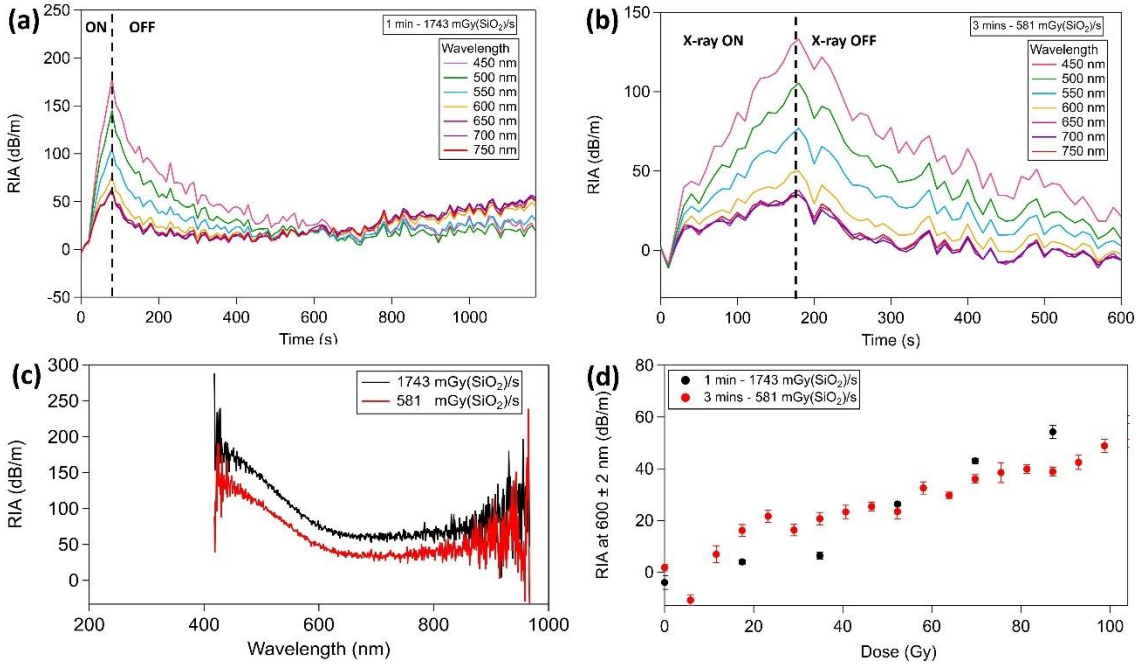

Figure III-57: Kinetics over time for RIA measurements at distinct wavelengths under two distinct conditions while maintaining the same total dose applied: (a) for 1 minute at a dose rate of 1.743 Gy/s, and (b) for 3 minutes at a dose rate of 0.581 Gy/s. The black dashed line represents the end of irradiation. (c) Spectral RIA recorded at two different dose rates shown at

the end of irradiation, corresponding to a TID of 104 Gy. (d) Evolution of RIA at 600 ± 2 nm as a function of the same applied TID, for the two different dose rates during two irradiation times.

Figure III-57(c) shows the spectral RIA measured at two different dose rates at the end of irradiation, receiving each one a total induced dose of 104.58 Gy. This indicates that the attenuation is approximately 1 dB/cm, meaning that approximately 20% of the signal is attenuated. The RL signal of the first run for the 1.743 Gy/s (the last dose rate) presents a decreasing slope of ~19% which is coherent with the RIA measurement (see Figure III-52(a)). Certainly, this measurement confirms that the RL signal's behavior is mainly due to the RIA. As previously noted, this effect stabilizes after a specific dose.
Figure III-57(d) shows the evolution of RIA at 600 ± 2 nm wavelength over TID of 104.58 Gy for the irradiation conditions. The RIA fluctuations are mainly due to fluctuations and instability of the UV diode source, that with the actual set up cannot be corrected. This highlights a slight dependence of RIA on the dose rate. RIA still increases with the doses till 104 Gy and has not arrived at a saturation yet.

iii. Radiation-induced attenuation measurement of the bulk sample

As previously noted, the comparison of RIA between the irradiated bulk glass and the fs-inscribed structure was carried out using a dedicated device. Figure III-58(a-b) depicts the RIA kinetics at 450 and 600 nm wavelengths, respectively, under a white light source for both the irradiated pristine and fs-inscribed glass. It is noticeable that the RIA for the fs-inscribed glass exhibits an 8% increase compared to the pristine glass. In fact, these curves were generated by considering the entire length of the glass sample, which is 700 µm. However, in the case of the fs-inscribed glass, the thickness of the structures is approximately 6 µm, significantly smaller than the 700 µm thickness of the overall sample, as seen in Figure III-51(c). Hence, we cannot be sure that this minor variation can be attributed solely to the X-ray modified silver clusters, since the radiation-induced absorption from the irradiated pristine glass is expected to be dominant and would obscure any contribution from the silver clusters, assuming they are present. Alternatively, this minor variation may be reasonably ascribed to the excitation of the inscribed silver clusters using the 425 - 500 nm wavelength range from the white light source, leading to the appearance of simultaneous absorption bands and a reduction in the transmission of the injected light, which was already demonstrated [147]. Otherwise, it could be a measurement error. Additional experiments conducted without the excitation light of the clusters are necessary to ensure a valid and conclusive result.

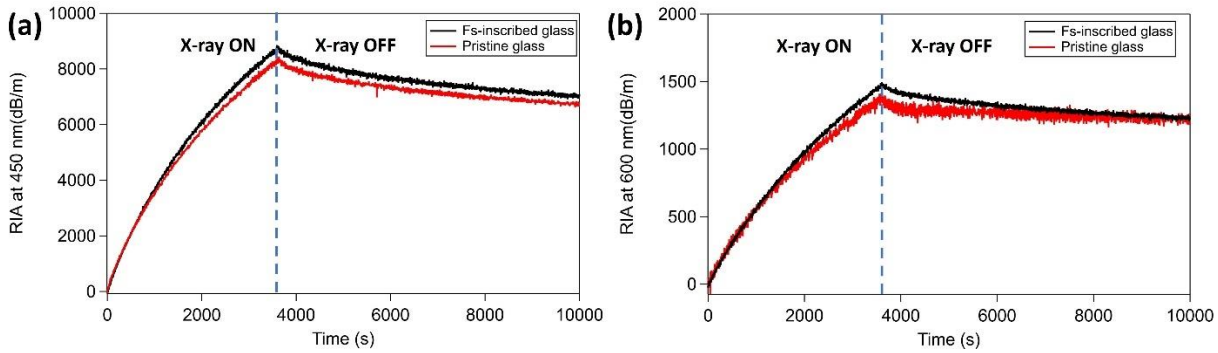

Figure III-58: Kinetics over time for RIA measurements of the fs-inscribed and pristine ARGO bulk glass at: (a) 450 and (b) 600 nm wavelengths for the same irradiation conditions. Note that these samples were not irradiated before this measurement. Both samples were irradiated with the same dose rates at 0.58 Gy(H_2O)/s for 1 hour.

III.4.2.c.Partial discussion on the real-time X-ray study

The study of the fs written silver clusters under *in-situ* X-ray irradiation has been investigated in this section. The 5-pass and 1-pass waveguide tested in this study did show a significant measurable RL signal with an increase range of dose rates from 5.81 to 1743 mGy(H_2O)/s. It was seen that RL reaches a very stable response after the fourth run, which is compatible with the fact that the RIA also becomes more stable. This strongly suggests that this stabilization could work at the long term. Surprisingly, the RL signal of the 1-pass and 5-pass waveguides was shown to be almost identical, as shown in Figure III-53. Moreover, pristine glass was also subjected to the same sequence of irradiation, showing a slightly lower RL signal than that coming from the inscribed waveguide. Consequently, it's challenging to attribute this difference exclusively to the luminescence of the inscribed structure under X-ray irradiation. This suggests that the luminescence of the matrix itself is efficiently collected due to the presence of waveguides. Therefore, it can be concluded that photo-induced silver clusters exhibit resilience to X-ray irradiation and do not emit specific fluorescence under X-ray exposure, even when subjected to a laser inscription with multiple passes. Based on those results, fs-inscribed silver clusters do not seem to have the potential to act as local emitting probes for real-time luminescent dosimetry sensor. This behavior is not unprecedented and has been observed in other materials before. Furthermore, radiation-induced attenuation measurements were carried out on both waveguides utilizing a white light source. These measurements demonstrated that, for the same total dose, the spectral RIA and the RIA kinetics remain consistent regardless of the number of inscribed scans and the pre-irradiation conditions. Note also that both waveguides have been subjected to a different doses prior irradiation before this measurement. A slight increase of the RIA was shown when comparing the pristine glass to the fs-inscribed one, which may be provided from the excitation of the inscribed silver clusters using the UV range of the white light source. This initial finding should undergo further investigation.

III.5.Conclusion

In this chapter, we explore an innovative approach to X-ray spatially distributed dosimetry using laser-induced silver clusters within high-silver-concentration phosphate glasses.

First, we have provided a concise introduction to the fundamentals of the radiative environment and dosimetry. This included an overview of radiation types, the interaction of photons with matter, and their defining characteristics. Additionally, we briefly outlined the key physical parameters involved in dosimetry and described the properties of dosimeters. Furthermore, we explored the various effects observed when optical materials are exposed to ionizing radiation. Finally, we have presented a summary of the current state of radiophotoluminescence dosimetry.

The targeted objective of the second section is to evaluate the performances of a spatially-resolved dosimeter exploiting the properties of the laser-induced silver clusters localized in purpose in silver-containing phosphate glasses. To achieve this, radiophotoluminescence and femtosecond direct laser writing techniques are combined to evaluate the potential of these laser-inscribed structures as local indicators of deposited radiation doses. The first part of the section has investigated the impact of X-rays in pristine silver-containing phosphate glasses for all the compositions. Also, we have conducted an in-depth analysis of recent findings involving silver-containing sodo-gallophosphate glass. These findings enabled us to estimate depth-dependent profiles of the linear absorption coefficient in absolute values. In the second part of the section, two-depth localizations of identical fluorescent silver clusters were inscribed using fs DLW in three different glass compositions. Moreover, the depth-dependent deposited dose within the glass thickness was evaluated using a Monte Carlo Geant4 simulation. The spectroscopic properties of the 3D structures are evaluated before/after X-ray irradiation to study the resilience of the irradiated silver clusters. Our analysis underscored the remarkable resilience of identical silver clusters inscribed in two depth localizations to X-rays at the deposited dose levels, especially in the ARGO glass sample. The rear surface seemed to have more reliable conditions to the investigated X-ray dose, taking into account the depth-dependent deposition of the dose in relationship with the X-ray energy spectrum. It's important to highlight that the photo-induced species in the ARG03 and GPN2 glass samples exhibit slightly distinct responses compared to those inscribed in the ARGO glass sample after irradiation. Information on the dosimetry performances of two glasses was achieved using the fluorescence amplitude ratio of the bands corresponding to color centers and/or inscribed-silver clusters. Indeed, laser-induced silver clusters could be used as local probes of the depth-dependent deposited doses. With these local probes, it was possible to adapt the dynamic and the linearity zone of the detector at differentiated dose ranges, giving the interest of spatially-resolved dosimeter.

The third section focused on an in-situ examination of the laser-inscribed silver clusters to

investigate their behavior when exposed to X-rays. To achieve this, 1-pass and 5-pass waveguides were precisely inscribed beneath the glass surface, spanning the entire length of the material. They were then linked on both sides using radiation-resistant fibers, allowing for the real-time collection of radioluminescence and radiation-induced attenuation data from the inscribed structures. Upon comparing this data to that of the pristine sample, we observed that the measured radioluminescence signals originated from the irradiated matrix rather than the silver clusters themselves. In addition, the cluster's density and their spectroscopy do not change when exposed to X-ray irradiation. Regrettably, these resilient local probes cannot be used for real-time luminescence dosimetry applications. Furthermore, in-situ radiation-induced attenuation measurements were performed on the 5 and 1-pass waveguides, confirming that the multipass inscription does not influence this outcome. When compared with the bulk glass, there is a slight 8% increase in the RIA of the fs-inscribed structures. However, further experiments are required to draw a definitive conclusion regarding this observation.

IV Femtosecond writing of Type-A volume Bragg gratings

In this chapter, we introduce Type-A Volume Bragg gratings inscribed using femtosecond laser writing in silver glasses. These gratings are created through various fabrication methods.

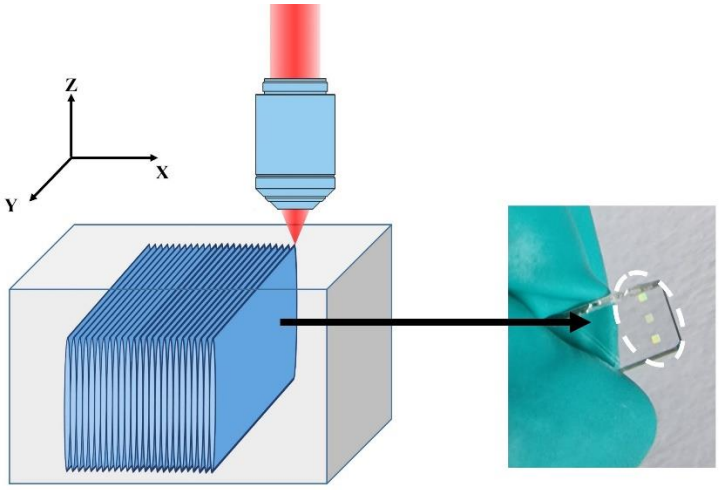

Silver-containing glass Type-A volume Bragg grating

IV.1.Introduction

Volume Bragg gratings (VBGs) are optical devices having a 1-dimensional periodic refractive index modulation (Δn) that occupies a large volume inside a transparent material. In the past decades, VBGs have been extensively used in many applications such as for spectral and coherent laser beam combining, notch filters, wavelength stabilizers in laser systems or diodes, etc. So far, they have been commonly inscribed in photo-thermo-refractive (PTR) glasses that have been shown to be an ideal photosensitive material for recording phase volume holograms. PTR glasses are homogeneous multicomponent silicate glasses that bear all the advantages of optical glasses: thermal stability, high laser damage threshold, and a wide transparency range. The standard process for creating holograms in PTR glasses involves exposing them to continuous-wave ultraviolet (UV) laser light, followed by a thermal development to achieve the correct refractive index modulation for a desired value of diffraction efficiency [249]. The glass is widely used for the fabrication of high-efficiency, low-losses, robust VBGs [250] and phase masks [251] that, in turn, find their application in laser beam control systems [252], [253]. These achievements have mostly been developed more than a decade ago at the College of Optics and Photonics/CREOL at the University of Central Florida. Nowadays, OptiGrate is a leading manufacturer of commercial VBGs-based PTR glasses. The inconvenience of such an approach is that the phase hologram recording using UV light limits the choice of the materials and thus their application. In addition, the limit of the PTR glass is their transparency around 2500 nm, which limits their use in the mid-infrared and beyond. Moreover, femtosecond (fs) laser writing has opened the avenue to obtain VBGs in other photosensitive and non-photosensitive materials supported mainly by Type-I refractive-index modification. Still, fs laser inscription also has inherent issues, such as possibly exceeding the damage threshold of the material and the self-focusing effect while using high laser intensity: inscription parameters must then be managed and controlled within the adequate range to produce high-quality VBGs in the fs laser inscription regime, without degrading the diffraction efficiency of the VBG due to the inhomogeneity in the inscription process. In fact, there is always growing interest in inscribing VBGs in more photosensitive glass matrices, using lower laser intensities, enabling the generation of stronger refractive index modifications and accelerating the recording time of the inscription process, while taking advantage of the fs laser approach. Indeed, improving the throughput of fs laser inscription is a key issue to overcome the time processing limitation when thinking about any potential industrial transfer. On the other hand, fs laser inscription allows for benefiting of multi-photon absorption, which gives a versatile access to 3D multi-scale architectures and to the ability of producing free-form VBGs.

In particular, as already detailed in the previous chapters, silver-containing phosphate glasses exhibit many attractive properties [41], [42], [137], [254], [255]. Depending on their composition, they possess good chemical durability, excellent optical properties, ion

exchangeability, and fiber drawing ability [137], [254]. As already mentioned in Chapter II, these glasses have a distinct modification type referred to as Type-A for Argentum, related to the spatial distribution of the generated silver clusters around the interaction voxel. Also, such modification shows two positive Δn peaks for every laser pass, which has recently been allowed to reach values of up to 2 x 10^{-2} using the multi-scan approach [159]. Writing Type-A structures thus requires a laser system outputting much lower pulse energy compared to that required for classical fs laser inscription. In addition, silver-based photochemistry associated with Type-A modifications can be triggered without modifying the glass matrix. Thus, Type-A inscription preserves the optical quality of the glass matrix better than the Type-I regime [161]. Moreover, the overall transparency window of these photosensitized glasses covers the visible (VIS) to the far end of the near-infrared (between 380 nm and 2700 nm), which allows for applications in this wavelength range. In addition, silver-doped gallo-germanate glasses have recently been synthesized that exhibit transmission up to the mid-infrared (MIR) range. In these glasses, the variation of Type-A refractive index modification is investigated; depending on their composition [162]. Indeed, these Type A–based periodic structures offer new insights and advantages for the fabrication of volume Bragg gratings for the VIS-MIR range. It should be noted that waveguide lasers have been fabricated using ultrafast laser inscription in phosphate glasses that uses waveguide Bragg gratings as a feedback element for laser systems [170].

For all the reasons cited above, our choice converged on inscribing volume Bragg gratings based on Type-A refractive index modification, which has not yet been demonstrated to our knowledge. Thus, this chapter deals with the femtosecond laser inscription of Type-A volume Bragg gratings in commercial silver-containing phosphate glasses. First, the state of the art about volume Bragg gratings is briefly discussed, providing an overview of their applications, the materials in which they are fabricated, and the different fabrication processes. Then, the *Type-A* Volume Bragg gratings are presented using several techniques, from multi-layer using standard Gaussian beam geometry to the phase mask approach. In addition, the transmission characterization is described for angular and spectral measurement. Moreover, the inscribed geometry and the VBGs written in different techniques are presented. The transmission spectra are analyzed using the Coupled Wave Theory to extract the effective gratings parameters. For some techniques, further optimizations are required to obtain promising diffraction efficiencies.

IV.2.Definition and applications of VBGs

Volume Bragg grating is a uniform phase grating that occupies the volume of a transparent medium. This pattern is produced by the periodic distribution of the refractive index modulation inside this medium. One can distinguish between thin and volume Bragg gratings. By increasing the thickness of the grating, each layer can be seen as a thin grating that

diffracts all the orders of the periodic pattern. By tilting this grating, there is a unique condition that puts in phase only one order diffracted by all these thin gratings while the other orders will be non-phased-matched. This condition is known as the "Bragg condition", where light is strongly diffracted in one order only. Such gratings are distinguished into two types, either transmitting or reflecting Bragg gratings depending on the diffraction angle and grating orientation in the medium as shown in Figure IV-1:

- *A transmitting Bragg grating (TBG),* if the incoming light that matches the Bragg condition is diffracted and crosses the back surface.
- *A reflecting Bragg grating (RBG)*, if the incoming light that matches the Bragg condition is diffracted and crosses back the front surface.

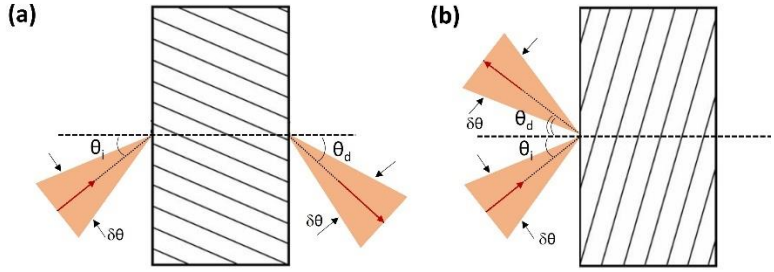

Figure IV-1: Beam geometries for (a) transmission Bragg grating and (b) reflective Bragg grating. θ_i and θ_d are the incident and diffracted angles in the air. Adapted from [28], [256].

Volume Bragg gratings are depicted by their angular and spectral selectivity. The angular selectivity at the Half Width Full Zero (HWFZ) level, $\delta\theta^{\mathrm{HWFZ}}$, is the angle between the central maximum and the first minimum of the diffraction efficiency distribution. In the same manner, the $\delta\lambda^{\mathrm{HWFZ}}$ spectral selectivity is determined as the distance between the central maximum and the first zero of the spectral distribution of the diffraction efficiency distribution. These two sorts of VBGs' features govern how they are used in various applications such as spectral beam combining for high-power lasers and wavelength stabilizers for diode lasers where they are advantageous due to their spectral filtering properties [257]–[260]. Since spectral selectivity can go down to 15-20 pm if constructed properly, RBGs are particularly well suited for use as narrow wavelength filters used in Raman spectroscopy [261], [262]. Contrary to RBGs that typically have angular acceptance values of more than 10 mrad and up to 100 mrad, TBGs can be utilized as narrow angular filters with acceptance values as low as 0.1 mrad [263]. Also, VBGs can find their application in pulse stretchers and compressors [264], [265] or in beam quality improvement as angular beam deflectors/magnifiers [266].

IV.3.Recording materials

Photosensitivity is the most important property for optical materials to be used for recording VBGs. This photosensitivity is quantified by the depth of modulation of the inscribed laser intensity used to create the corresponding refractive index modification in the material. Also, it determines the exposure duration of the inscribed VBG, which is better to be kept as short as possible. The quality of spatial resolution and periodicity is one of the key elements to achieve efficient VBG. Another factor is the dynamic range of the material, related to the maximum achieved refractive index modification. This property impacts the thickness of the VBG and the maximum number of multi-scanned gratings. Moreover, other properties are also crucial such as excellent optical quality and homogeneity of the considered glass matrix, as well as a high optical damage threshold, low losses and good chemical stability. These requirements are highly demanded in high precision and high-power laser applications [256], [263].

For inscribing VBGs, a diversity of photosensitive materials has been used [267], [268]. Dichromated gelatins, photopolymers, photo-refractive crystals, and photo-thermo-refractive glasses were the most often used recording materials. The properties of each of these materials have been thoroughly examined in literature [269]–[277]. The typical production method relies on a two-step process, with exposing PTR glasses to a periodic interference pattern from a UV continuous laser with a wavelength between 280 nm and 350 nm [249] and followed by a thermal post-processing. To do so, the UV beam is split at a beam splitter and the derived beams are overlapped with an appropriate angle to make an interference pattern at the desired grating period. In fact, the glass does not directly present a significant refractive index change after exposure to UV light. The interfering UV beams create a latent image in the glass, which is therefore converted to a real phase hologram upon thermal development [279]. Such glasses have been used due to their ability to handle high-power laser light due to their low losses, environmental durability, and high spectral selectivity in the range of 0.01 nm for UV and 0.1 nm for near-IR spectral regions [275]–[277]. More recently, infrared femtosecond laser writing has also been used to address both photosensitive and non-photosensitive glasses. Indeed, fs laser pulses have gained interest due to their broadly versatile ability to induce local modifications inside transparent materials by confining energy deposition thanks to nonlinear multi-photon absorption, as originally reported by Davis et *al.* in 1996 [280]. Using fs laser writing, VBGs have been recorded in oxide glasses (fused silica [281], [282] and borosilicate [283]) exhibiting excellent chemical and thermal stability, low absorption in the visible and near-infrared wavelength regions, and high damage threshold at high power levels. Also, fabricated gratings inside gallium lanthanum sulfide chalcogenide glass substrates have been reported using fs laser writing. Such glasses operate in the near and mid-infrared range, which could be used for remote sensing and astronomical instruments. In addition, the fabrication of volume gratings using fs lasers in polymer materials was demonstrated. It was found that the

aging issues after manufacturing affect the induced refractive index. Indeed, it was reported that gratings inscribed in polymethyl-methacrylate (PMMA) exhibit nonconstant diffraction efficiency: time-lapse measurements of the diffraction efficiency showed initial increase followed by a slow decrease [284], [285]. After that, refractive index change increased again, and recovery of grating occurred. Such recovery is known as self-regeneration [286]. In addition, VBGs have been inscribed using fs laser writing in multicomponent fluoride glasses having interest due to their large transparency window spanning from the UV to the mid-infrared range, allowing for a wide range of applications [287].

IV.4.Diffraction properties of volume Bragg gratings

Figure IV-2(a) shows the schematic representation of a transmitting Bragg grating inscribed in the volume of a photosensitive medium by sinusoidal modulation of the refractive index. The diffraction scheme represents the propagation of optical rays through the VBG, where the angle of the incident beam crosses the back surface and diffracts from θ_{i} to θ_{d}; while θ_{i}' and θ_{d}' are the incident and diffracted angles in the medium, respectively.

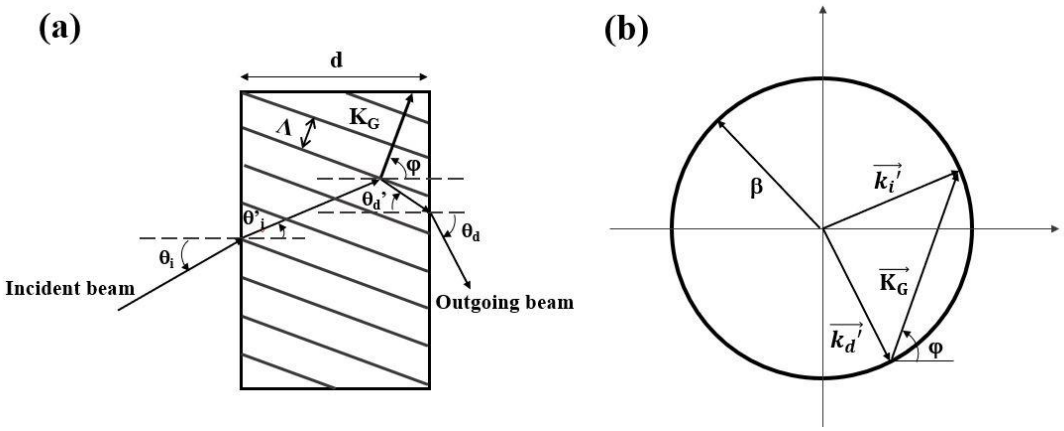

Figure IV-2: (a) Diffraction representation of a transmission VBG. (b) Vector diagram for Bragg condition.

The VBG is characterized by the following set of parameters: the amplitude of refractive index modulation Δn_{AC}, the grating period Λ, the grating thickness *d*, the inclination or slant angle φ between the normal to the surface and the grating vector K_G, which is directed perpendicularly to the planes of a constant refractive index with a module of $K_G = \frac{2\pi m}{\Lambda}$; where m is the order of the VBG refractive-index modulation. The diffraction condition is analyzed using the momentum or *K*-space diagram method. Figure IV-2(b) illustrates the wave vectors k_i' and k_d' of the incident and diffracted waves, respectively. The vector relation is connected with a circle of radius $\beta = \frac{2\pi n}{\lambda}$ where *n* is the bulk index of refraction of the material and λ the

wavelength in free space.

The Bragg condition is satisfied for the corresponding vector equation as follows:

$$\overrightarrow{k_i'} + \overrightarrow{K_G} = \overrightarrow{k_d'} \quad \text{IV-1}$$

Therefore, diffraction of a beam with a certain wavelength occurs for only one angle, according to Bragg's condition:

$$|\cos(\varphi - \theta_i')| = \frac{K_G}{2\beta} = \frac{\lambda m}{2 n \Lambda} \quad \text{IV-2}$$

The diffraction efficiency of transmitting VBGs is modeled based on Kogelnik's coupled wave analysis [288] given by:

$$\eta = \frac{\sin^2\sqrt{\xi^2 + \upsilon^2}}{1 + \frac{\xi^2}{\upsilon^2}} \quad \text{IV-3}$$

where ξ is the dephasing parameter describing the deviation from the Bragg condition and υ is the phase incursion that determines the maximum diffraction efficiency of VBG, written as:

$$\xi = \frac{d\left(K_G \cos(\varphi - \theta_i') - \frac{K_G{}^2\lambda}{4\pi n}\right)}{2\left(\cos\theta_i' - \frac{K_G}{\beta}\cos\varphi\right)} \quad \text{IV-4}$$

$$\upsilon = \frac{\pi \Delta n_{AC}\, d}{\lambda\sqrt{(\cos\theta_i')\left(\cos\theta_i' - \frac{K_G}{\beta}\cos\varphi\right)}} \quad \text{IV-5}$$

IV.5.Techniques for inscribing VBGs

In this chapter, we will concentrate on fs-written VBGs. Various methods exist, which will be detailed in this section.

IV.5.1.Gaussian beam

This technique involves creating refractive index changes achieved by tightly focused Gaussian laser beams through a microscope objective. Their depth is limited to the short confocal length of the focused beam. As seen in Figure IV-3, the sample is moved in the *y*-axis to inscribe one line whose thickness corresponds to that of one single layer. The lateral dimension is written by moving the sample along the *x*-axis. To obtain a VBG with the needed thickness, it is necessary to stack multiple layers from bottom to top of the considered material along the *z*-axis [289].

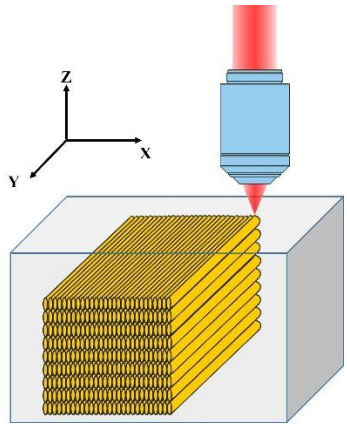

Figure IV-3: Schematic drawing of the volume Bragg gratings fabrication using the Gaussian laser beam approach.

MacLachlan *et al*. have reported on the inscription of gratings in gallium lanthanum sulfide chalcogenide glasses using fs laser inscription while focusing with a 0.4 NA lens. They have created 17, 35, 53, and 71 layers, resulting in grating thicknesses of 41, 84, 127, and 170 µm, respectively, with a lateral period of 3 µm. The thickest grating, produced using 71 layers, exhibited the highest peak efficiency of 61% at 1300 nm. The measured data were best fitted with a 150 µm thick structure and a binary refractive modulation $\Delta n_{AC} = 7.5 \times 10^{-3}$. The peak efficiency of the two thickest gratings is somewhat lower than the theoretical maximum. This could indicate manufacturing imprecision that results in a reduced diffraction efficiency, among which the difficulty of perfectly aligning the periods of the grating layers or the issue to maintain the in-depth homogeneity of the modified region's refractive index of the successive inscribed layers [290]. In addition, gratings in fused silica have also been made with a Gaussian laser beam, leading to the formation of Type II modifications with birefringence. Due to the short axial length of these Type II modifications, VBGs need a high level of multiplexing (20 layers) to attain a 90 µm thick VBG. A grating size of 1x1 mm^2 and a period of 2 µm took more than 3 hours to be written with a velocity of less than 1 mm/s, showing a diffraction efficiency at 633 nm of ~60% for p-polarization and ~29% for s-polarization [291].

IV.5.2.Gaussian-Bessel Beam

Several limitations could happen while inscribing multi-layer VBGs using a Gaussian beam, which will be detailed later in section IV.9.1. Such limitations could be overcome by using an elongated and non-diffracted beam, known as a Gaussian-Bessel beam. The formation of the Gaussian-Bessel beam is detailed hereafter.

IV.5.2.a.Properties and generation of Gaussian-Bessel Beam

As mentioned earlier in chapter I in section I.4.4.b, an axicon can be used to convert a

Gaussian laser beam into a non-diffracting Bessel beam. It is an optical device that focuses the laser beam over a length that largely exceeds the confocal Rayleigh length. Indeed, axicon optics create an interference pattern with radial symmetry to form an elongated non-diffracting voxel along the optical axis.

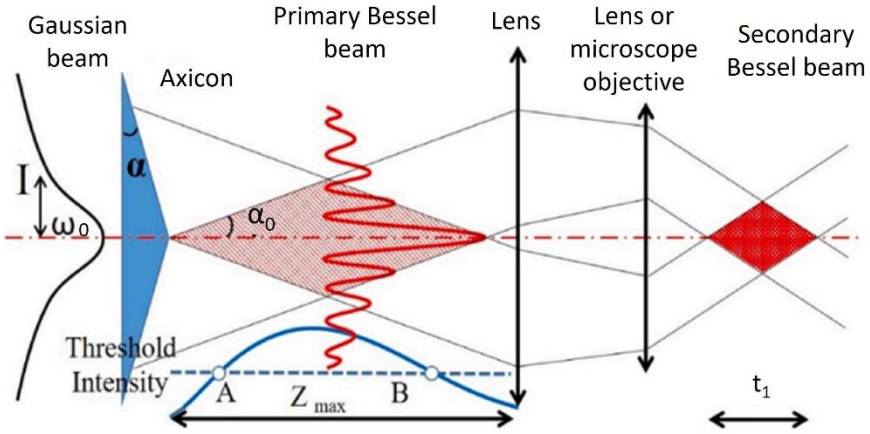

Figure IV-4: Geometric evolution of the spatial shape of the Bessel beam with ω_0 the radius of the Gaussian beam, α the base angle of the axicon lens, α_0 the Bessel inclination angle, Z_{max} the distance of the primary Bessel beam and t_1 the secondary Bessel beam length. The red and blue lines represent the spatial light intensity distribution of the Bessel beam profile and the on-axis longitudinal section, respectively. Adapted from [292].

Figure IV-4 shows the geometric evolution of the spatial shaping of the Bessel beam. When a collimated monochromatic Gaussian laser beam with a flat phase front is normally incident on an axicon lens having a base angle α, two portions of the beam deviate towards the main axis *i.e.,* along the propagation direction with an angle α_0, and overlap resulting in an interference effect. It is this interference that yields the Bessel beam characteristics, namely the longitudinal extent. The Bessel interference region (primary Bessel zone) after the axicon, represents the length of non-diffractive propagation and is expressed using the following formula:

$$Z_{max} = \frac{\omega_0 \cos(\alpha_0)}{\sin(\alpha_0)} \qquad \text{IV-6}$$

where Z_{max} represents the length of non-diffractive propagation *i.e.,* the depth of focus, α_0 is the cone half-angle and ω_0 is the incident beam radius.

The central core radius of the primary Bessel beam (defined as the radial distance between the central intensity maximum and the first intensity minima) is calculated using the following equation:

$$\rho_0 = \frac{1.2024\lambda}{\pi \sin(\alpha_0)} \qquad \text{IV-7}$$

The central spot size does not change along the interference field, hence the denomination "diffraction-free".

Bessel beam modes are characterized by an integer n, known as the order of the beam. An ideal Bessel beam of the n^{th} order can be expressed as follows [293]:

$$E(r,\phi,z) = A_0 e^{(iK_z z)} J_n(K_r r) e^{(\pm in\phi)} \quad \text{IV-8}$$

where r, ϕ, and z are the radial, azimuthal, and longitudinal coordinates, respectively. A_0 is constant amplitude, K_r and K_z are the radial and longitudinal wave vectors, respectively and J_n is the n^{th} order Bessel function of the first kind.

The evolution of the on-axis intensity as a function of the propagation distance z can be derived along the optical axis from the stationary phase approximation of the Fresnel diffraction integral. It can be expressed as follows [56], [294]:

$$I(z) = \frac{8\pi P_0 z \sin^2 \alpha_0}{\lambda \omega_0^2} e^{-2\left(\frac{z \sin \alpha_0}{\omega_0}\right)^2} \quad \text{IV-9}$$

where P_0 is the peak power of the laser beam incident on the axicon lens and the origin z=0 is taken in the plane at the output of the axicon.

Figure IV-5(a, b) depicts the axial and radial intensity distributions of the Bessel beam along the propagation direction. Correlatively to Equation IV-9, the distribution of light intensity initially increases and then decelerates as the beam propagates.

Then, a 4F system is combined with the axicon to de-magnify the generated Bessel beam and correlatively to increase the power. This system involves the combination of a lens (having a focal length F_1) and an objective lens (having a focal length F_2), leading to the focal length ratio $\frac{F_1}{F_2}$. The secondary Bessel beam length t_1 is compressed by a factor of $\left(\frac{F_1}{F_2}\right)^2$ after passing through the telescope, while the central core radius is reduced by $\frac{F_1}{F_2}$. We note that upon refraction from air to the medium, both the wavelength and the cone half-angle are corrected by the index of refraction of the medium. These corrections cancel out and do not change the value of the central spot size in the material [295]. In contrast, the length of the Bessel zone is increased by the factor of the index of refraction. This is similar to the case of a Gaussian beam where the Rayleigh length is increased while the waist remains identical [296]. The Bessel beam intensity distribution after the 4F system is shown in Figure IV-5(c,d). The primary Bessel beam is compressed to produce a secondary Bessel beam that has a higher energy density, which is advantageous for accurate multiphoton-based processing of glass materials.

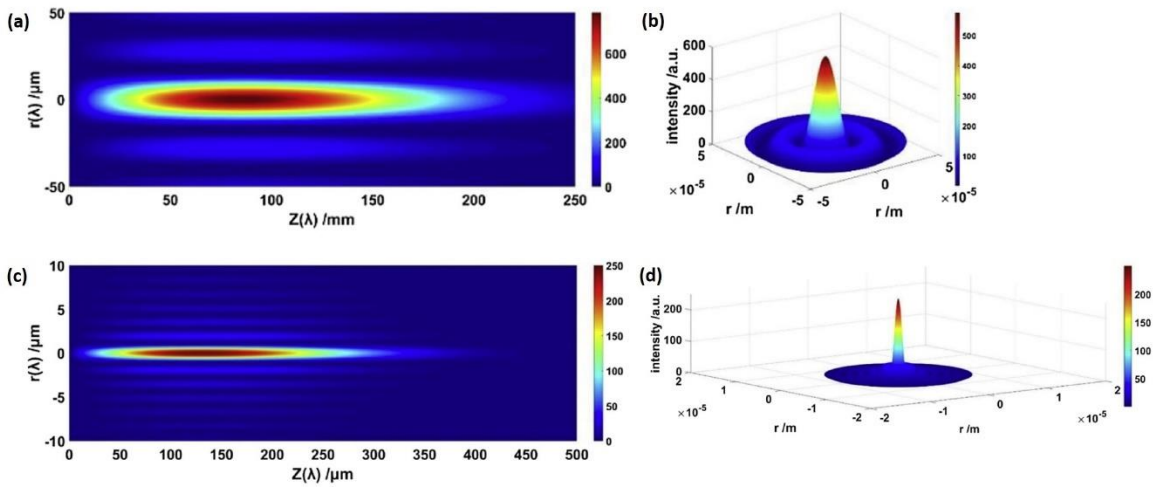

Figure IV-5: Intensity distribution of the Bessel beam based on an axicon and after the 4F system. (a,c) 2D color maps of the intensity distribution where (a) is the magnification of the on-axis area of (c), (b,d) identical intensity distributions in polar coordinate where (b) is also the magnification of the on-axis area of (d). Taken from [297].

For most of the applications, we use $n = 0$. The power contained in the Bessel beam up to radius b is then calculated from [298]:

$$P = A_0^2 \int_0^{2\pi} \int_0^{b} J_0(k_r r)^2 (r k_r) r dr d\theta = A_0^2 b^2 \pi \left(J_0(k_r b)^2 + J_1(k_r b)^2\right) \qquad \text{IV-10}$$

where b is the m^{th} zero of the zero function (for 'm' rings) and $k_r = \frac{2\pi \sin(\alpha_0)}{\lambda}$

Thus, the following section details the formation of standard Gaussian-Bessel beams, which is a second technique to inscribe volume Bragg gratings. It describes the state of art of achieved VBGs written using the Gaussian-Bessel beam geometry.

IV.5.2.b.Fabrication of VBGs using Gaussian-Bessel beams

Several groups have reported the inscription of VBGs using Gaussian-Bessel beams. Paipulas *et al.* have reported results of volumetric fused silica modifications using femtosecond Gaussian and Gaussian-Bessel laser beams [289]. For the Gaussian beam, the laser spot was focused with 0.42 NA – 50x objective in the bulk of the sample. The spot diameter and the confocal length at the focus were $2\omega_0$ = 1.7 µm and $2Z_r$ = 4.5 µm, respectively, where ω_0 is the beam waist radius and Z_r is the Rayleigh length. To create a Gaussian-Bessel-type beam, an axicon with a base angle of 0.5° was inserted before the objective. The calculated central core radius and Bessel zone length were 0.66 µm and 116 µm, respectively. Indeed, a greater layer modification depth has been achieved using the Gaussian-Bessel beam method. Therefore, it allowed to inscribe VBGs while reducing the required number of consecutive layers and thus leading to a faster recording time and better efficiency. When using Gaussian beams, many layers of gratings must be constructed on top of one another to get a sufficient grating thickness (Figure IV-6(a). However, with Gaussian-Bessel beams, a single layer

already produced gratings that are 90 µm thick in the case of Paipulas et al. (Figure IV-6(b)). In fused silica, VBGs written with a Gaussian-Bessel beam are obtained by multiplexing 4 layers leading to a 352 µm thick VBG with a ~90% diffraction efficiency at 633 nm, with a refractive index modulation Δn_{AC} of 9.5×10^{-4}. Such grating has a spectral bandwidth narrower than 10 nm. Its lateral size was 6×6 mm^2, and the periodicity was 1.5 µm, which took less than an hour to be recorded with a translation speed of 20 mm/s [299]. In comparison to the Gaussian beam, the inscription of the multi-layer VBG in fused silica is detailed in the section above (section IV.7.1).

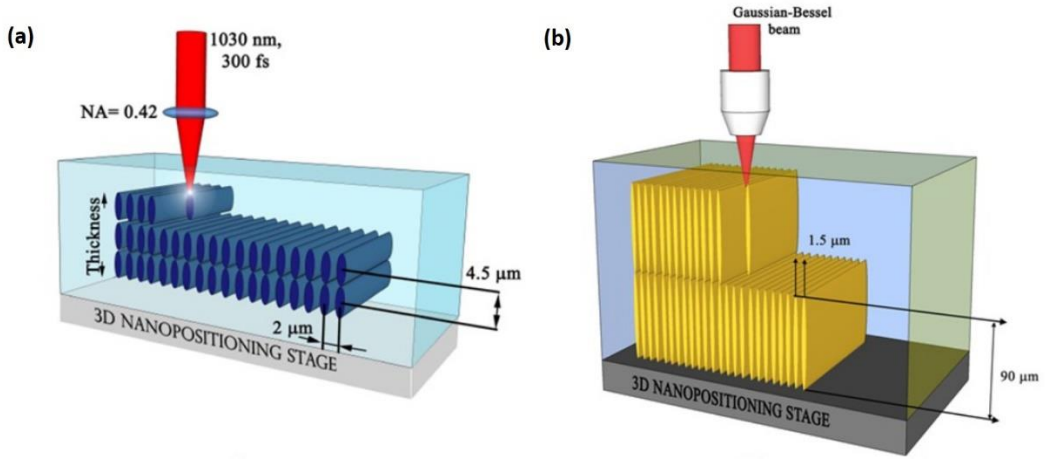

Figure IV-6: Formation of thick Bragg gratings using the DLW approach with a (a) Gaussian, (b) Gaussian-Bessel laser beam. Taken from [289].

The inscription of VBGs with fs Gaussian-Bessel laser beams has been reported in different materials, other than fused silica: a 1 mm thick VBG with a period of 5 µm in PTR glasses achieved a diffraction efficiency of ~95% at 532 nm, with a refractive index modification around 2.3×10^{-4} [300]; and a 2 mm thick VBG in PMMA obtained after three days of the fabrication reached a diffraction efficiency of ~ 96% at 633 nm, with Δn_{AC} value estimated as 1.7×10^{-4} and a periodicity of 10 µm [301].

IV.5.3.Phase mask approach

Another technique developed for inscribing Bragg gratings with femtosecond lasers is the phase mask writing method. The phase mask is a transparent substrate with a pre-designed grating pattern on its surface characterized by a series of grooves of period Λ_{PM} and depth δ, which acts as a diffraction grating. When a laser beam passes through the phase mask, the beam is diffracted by the grating pattern, resulting in a periodic intensity pattern that is projected onto the photosensitive material under processing [302]. There are two methods for fabricating the phase mask: by etching a photoresist using an electron beam [303], [304] or by interferometric lithography [305]. The

advantage of the etching method is the possibility of customizing the characteristics of the grating as desired. On the other hand, the error in the absolute positioning of an electron beam is about 5 nm, which may be significantly depending on the targeted period of the induced grating. In addition to positioning errors, variations in the uniformity of the substrate and of the resolution of the resin create fluctuations in the periodicity of the structure, a phenomenon called fitting error or stitching error. These imperfections of the phase mask are then transposed when inscribing the desired VBG [306]. The holographic method ignores most of these problems since it uses an interferometric method which ensures the regularity of the grating period. In return, obtaining long phase masks can be problematic since their manufacturing process requires optical components (lenses, mirrors, etc.) of large size and excellent quality without aberration so as to prevent destroying the interference pattern.

The principal setup for the phase mask scanning technique is shown in Figure IV-7. Using the phase mask perpendicular to the incident beam allows obtaining the diffraction orders m=0 and m=±1. The diffraction angle θ_m of the *m* order is calculated as follows:

$$\sin\theta_m = \frac{\mathrm{m}\,\lambda}{\Lambda} \qquad \text{IV-11}$$

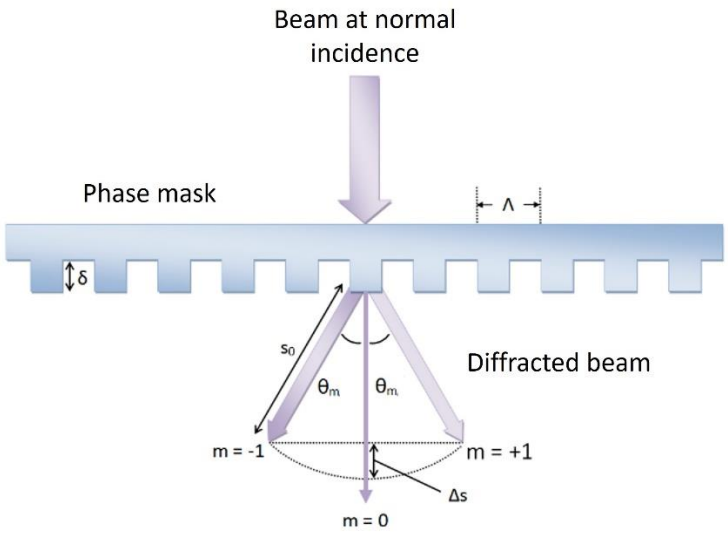

Figure IV-7: Sketch of a phase mask characterized by a series of grooves of period Λ and depth δ. Adapted from [307]

An interferogram is created when a laser beam illuminates a phase mask with normal or oblique incidence, allowing diffraction orders to overlap beneath the mask at distances before reaching far field diffraction. Figure IV-8 illustrates the various configurations that can be used to produce the interference pattern. Under normal incidence, the interference pattern is the result of the overlap of its ±1 diffraction orders with a period that is half of that of the phase mask (Figure IV-8(a)Figure IV-7). It should also be noticed that the orders m≠±1 reduce the visibility of the fringes, which is detrimental to the interference pattern as they

contribute to create a more complex and less contrasted electric field distribution. However, diffraction orders greater than m=±1 are generally much weaker in intensity than the latter, so that their contribution can be considered as minor. This is not necessarily the case for the order m=0 that can lead to a large contribution so that specific order requires to be minimized on purpose in the fabrication process. Generally, when designing the phase mask, the fraction of energy tolerated in the zeroth order of diffraction must be minimized, which limits the distortion of the interference pattern after the phase mask, as described by Dyer et al. in 1995. This has the effect of degrading the spectral response of the Bragg grating. It has been defined that the maximum value of the energy contained in the zeroth order should be less than approximately 5% to enable the generation of high-performance Bragg gratings. The implementation of vector calculations is, therefore, necessary for optimizing the periodic structure. A method based on the rigorous coupled-wave analysis (RCWA), as demonstrated by Moharam et al. in 1981, has been used for numerically modeling the diffraction efficiency of the diffractive structures [308]. Under Littrow incidence (Figure IV-8(b)), the phase mask is not perpendicular to the incident beam, which means that the incident beam has a specific incident angle with respect to the position of the phase mask. In this case, the interference pattern is produced with the same period Λ of the phase mask due to the overlap of the 0^{th} and the -1^{st} diffraction orders. In this case, the mask must be designed to increase the efficiency of 0/-1 orders in Littrow condition and to extinguish any other order [309].
The length of the interference pattern computes to:

$$L_i = 2W - 2\mathrm{d}\tan\theta_m \qquad \text{IV-12}$$

where W is the radius of the beam at the level of the mask, d denotes the distance between the phase mask and the bulk and θ_m is the diffraction angle.

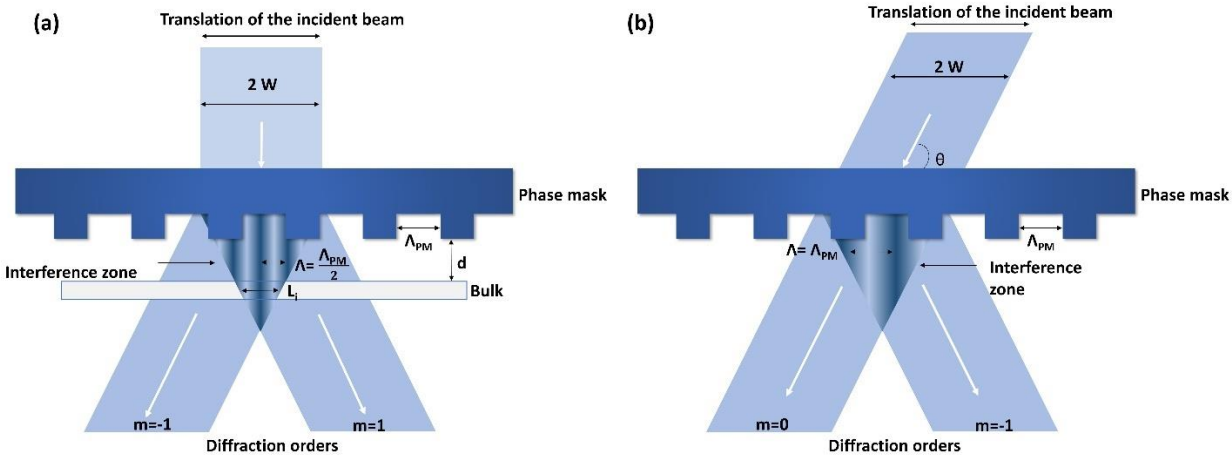

Figure IV-8: Schematic sketch of the phase mask illuminated by a Gaussian beam in (a) normal condition and (b) Littrow condition. The incoming laser beam is diffracted by the phase mask

and the transmitted diffraction orders interfere in their overlapping zone. Adapted from [307], [309].

In addition, it should be mentioned that in the Littrow condition, the diffraction of ultrashort pulses by the transmitting grating generates pulse front tilt. Pulse front tilt is a time delay across the transverse direction of the pulse since the pulse front is no longer perpendicular to the propagation direction after diffraction. Hence, the pulse front is tilted with respect to the direction of the beam/pulse propagation, while its phase front remains perpendicular to it. As depicted in Figure IV-9, the left and right sides of a laser pulse diffracted by a transmission grating at an angle θ_d will have a path length difference Δ, resulting in a tilt angle γ of the pulse front. Therefore, the orders m=0 and m=-1 no longer generate good interference pattern because of the degraded contrast caused by the spatial front pulse tilt. This phenomenon is not observed while using continuous or UV laser light [310].

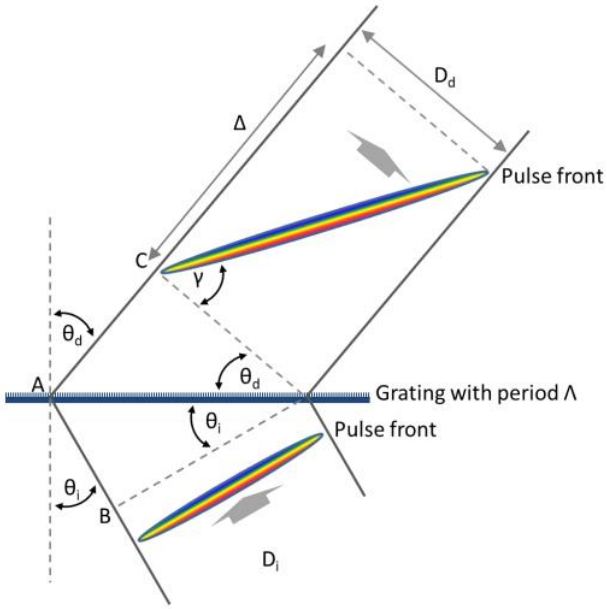

Figure IV-9: Grating-induced pulse front tilt using ultrashort pulses. Taken from [310].

It should be noted that ultrafast pulses interact differently with phase masks compared to nanosecond pulses or continuous wave sources. For ultrashort pulses, the diffracted pulse envelopes have different arrival times at a given distance *d* normal to the phase mask. The interference of two beams can be fabricated by exploiting the short pulse duration of a femtosecond laser source and the walk-off of the diffracted phase mask orders along an axis perpendicular to the phase mask. This walk-off effect can be understood based on a simple geometrical model, as seen in Figure IV-10. The different diffracted orders have different arrival times since they propagate with different angles. Thus, the diffracted order pairs (0, ±1, ±2) no longer overlap for sufficiently large distance *d*. This is not possible for longer pulse sources, as there would be much more

diffraction orders that overlap at large distances from the phase mask, leading to the reduction of the contrast of the interference distribution and thus resulting in much lower quality imprinted VBGs [311], [312]. Thus, for the phase masks used for UV inscription, the energy contained in the zeroth order must be reduced to a few percent to avoid the inscription of a parasitic periodical structure. With ultrashort pulses, it is possible to obtain pure two-beam interference without such high requirements on the phase mask design as a consequence of the order walk-off effect [313].

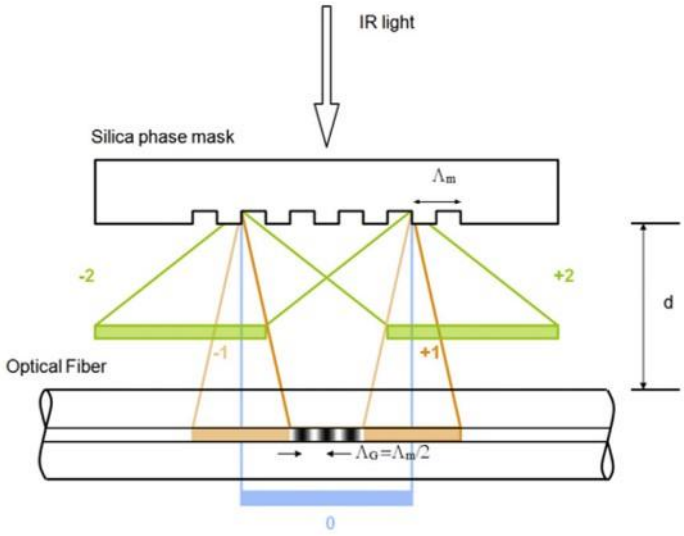

Figure IV-10: Walk-off effect for which ±1 and ±2 interference patterns take place at different depths, ensuring a highly contrasted interference pattern at the targeted periodicity while considering proper depth positioning of the sample to modify. Zeroth order contribution is filtered out by temporal delay and miss overlap with the ±1 orders. Taken from [314].

By selecting an appropriate distance between the phase mask and the sample, the 0th order won't be able to interfere with the 1st order since the time difference between them is greater than the ultrashort laser's coherence length l_{coh}. The required distance s_0 between the phase mask and the bulk for this walk-off to occur can be estimated by:

$$s_0 > \frac{l_{coh}}{1 - cos\theta} \qquad \text{IV-13}$$

This allows for the temporal separation of the zeroth from the first-order pulses which ensures that these orders cannot interfere anymore together. In such conditions, only the ±1 order pulses overlap and a pure two-beam interference pattern with high contrast is observed [314], [315].

A simple way to get rid of the zero-order effect is simply to block it with an obstacle. In return, it will be necessary to bypass the diffraction orders ±1 with the help of two mirrors so as to further superimpose to form an interference pattern inside the glass sample. This configuration is called the Talbot interferometer, as seen in Figure IV-11. The two mirrors can

be moved laterally and rotated on themselves, allowing a certain tunability of the Bragg wavelength. The advantage of moving the interference zone away from the mask is the significant reduction of the risk of damage to the mask. This method has already been applied successfully in a LiF crystal [316] or in Ti:Sa layers [317], as well as to inscribe VBGs in non-photosensitive glass material S-TIH53 [318].

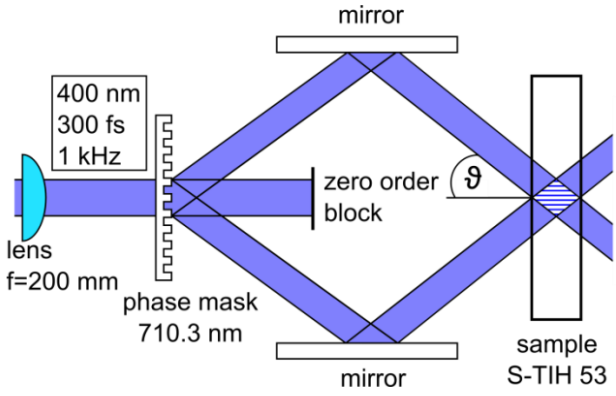

Figure IV-11: Talbot interference setup. Taken from [318].

Concerning the inscription method, translating the material with respect to the phase mask would impose high requirements on the accuracy of the positioning system. Thus, it is more reasonable to write significantly longer and more effective gratings simply by moving both the bulk and the phase mask together and translating them with respect to the laser beam or to employ both the phase mask and the bulk statically while the inscription beam sweeps across its full surface. In these cases, the interference pattern generated by the mask is not altered when the beam is translated along both the mask and the bulk. This novel method was proposed by Martin *et al*. in 1994 [319]. Using this method, it is better to make sure to keep the glass matrix and the phase mask locked together to minimize any potential minor relative movements and thus to enhance the quality of the engraved interference fringes. The joint movement of both the phase mask and glass matrix has been kept together using a variety of approaches, most notably by gluing the phase mask directly to the writing glass [320]. However, the inscription beam was substantially absorbed by the adhesive, also leading to degrading both the silica phase mask, its resulting interference pattern and the final imprinting VBG. In addition, another technique was used in PTR bulk glass. It consists in covering the glass with a layer of dichromate gelatin, in which the phase mask was first produced by the interference of two laser beams. The newly produced phase mask was then used to inscribe the VBG inside the PTR bulk [321]. In addition, it was recently reported that volume Bragg gratings (VBGs) could be femtosecond engraved directly inside phase mask substrates (fused silica and fused quartz samples) as shown in Figure IV-12 [322]. This method could enhance the robustness as the interference pattern produced by the phase mask and the writing medium is one single medium so that they are fundamentally linked

together. The phase masks were fabricated in UV-fused silica and fused-quartz substrates, having a period of 1075.9 nm and 738.5 nm, respectively. As a result, first-order peak reflectivity of 99% at Bragg wavelength of 1070.5 nm and 99.7% at Bragg wavelength of 1558 nm, in fused quartz and fused silica respectively, were obtained at the top of the gratings reaching Δn_{AC} of 5.9×10^{-4} and 3.2×10^{-4} respectively. Such gratings reach a depth of 1.5 mm.

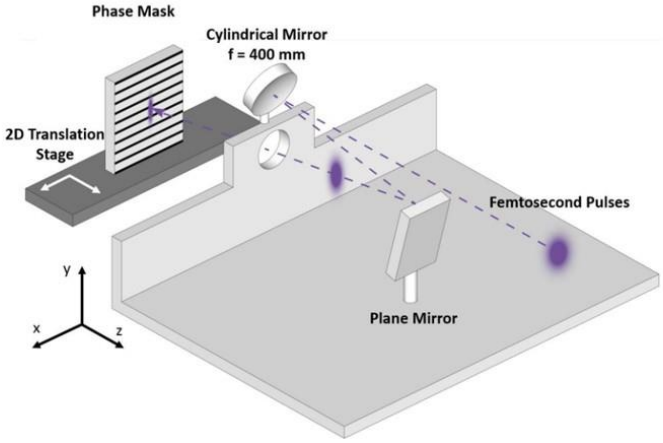

Figure IV-12: Schematic of the VBG inscription setup directly in the phase mask substrate. Taken from [322].

In general, the inscription of volume Bragg gratings (VBG) using a femtosecond laser and a phase mask has been performed in several works. Voigtländer *et al*. showed the inscription of reflective VBGs in fused silica, generating an interference pattern with half of the phase mask period (2.15 µm). The second-order reflection (Bragg wavelength = 1552.2 nm) shows an efficiency of about 74% for a 1 mm long grating with a refractive index change of about $6.4\text{x}10^{-4}$ [282]. Talbot *et al*. reported the first demonstration of VBGs inside bulk multicomponent fluoride glasses exhibiting refractive index modulations of up to 3.2×10^{-4} at the surface of the VBG with reflectivity up to 90% at a wavelength near 2.8 µm [287]. This grating exhibits a thickness of 10 mm with a period of 0.95 µm. Very recently, a chirped VBG with a depth of 2.5 mm and a 95% reflectivity at the third Bragg order has been inscribed inside fused silica using a phase mask bearing a chirp rate of 10 nm/cm [323].

IV.6.Summary of Volume Bragg gratings

Table IV-1 summarizes some of the recorded materials used to inscribe VBGs as well as the used inscription methods. The VBGs parameters are listed such as the diffraction efficiency, the period, the refractive index modification, and the effective thickness.

Table IV-1: Non-exhaustive list of reported volume Bragg gratings inscribed with different methods with their parameters such as the inscription wavelength, the period of the VBG, the experimental diffraction efficiency, the refractive index modulation, the effective thickness and the Bragg wavelength.

Material	Technique	Inscription wavelength (µm)	Diffraction efficiency (%)	Bragg period (µm)	Effective thickness (mm)	Δn_{AC} (10^{-4})	Bragg wavelength (µm)
PTR **[324]**	UV hologram	0.325	~ 90	1.6	3.1	1.65	1.090
S-TIH53 **[318]**	Talbot interferometer	0.4 (fs laser)	-	0.3551	0.1	0.25	0.6328
GLS-chalcogenide **[290]**	Gaussian beam	1.064 (fs laser)	61	3	0.15 (71 layers)	7.5	1.3
Fused silica **[299]**	Gaussian beam	1.030 (fs laser)	60 (p)/29 (s)	2	0.09 (20 layers)	20(p)/ 10.5(s)*	0.633
PTR **[300]**	Gaussian-Bessel beam	0.8 (fs laser)	95	5	1	2.3	0.532
PMMA **[301]**	Gaussian-Bessel beam	0.8 (fs laser)	96	10	2	1.7*	0.633
Fused silica **[299]**	Gaussian-Bessel beam	0.515 (fs laser)	90	1.5	0.352 (4 layers)	10	0.633
Fused silica **[323]**	Phase mask	-	95	Chirped period-0.01/cm	2.5	-	Third order
Fused silica **[282]**	Phase mask	0.8 (fs laser)	74	1.075	1	6.4	1.5522
Fused silica **[322]**	Directly inside phase mask	0.266 (fs laser)	99	0.53795	1.5	5.9	1.558
Fused quartz **[322]**	Directly inside phase mask	0.266 (fs laser)	99.7	0.36925	1.5	3.2	1.0705
Fluoride **[287]**	Phase mask	0.8 (fs laser)	90	0.95	10	3.2	2.8

**The refractive index modulation is not mentioned in those articles. Thus, we used Kogelnik's equation (Equation IV-4) to extract the simulated Δn_{AC} from the experimental data.*

IV.7.Experimental methods

VBGs were written using the various methods mentioned above and by optimizing the laser

parameters to achieve the highest diffraction efficiency and to accomplish high throughput in the inscription process. There is a non-exhaustive list of glasses producing Type-A modification [152], [156], [159], [162], [325], [326]. In the present experiments for this PhD work, we have chosen to use a commercial silver-containing zinc phosphate glass (AG01®, Argolight) as this commercially available glass offers great chemical stability, excellent homogeneity, and reproducibility. The measured composition of this sample is $39.9P_2O_5$-53.8ZnO-$5.8Ag_2O$-$1Ga_2O_3$ (nominal cationic composition in mol%).

IV.7.1.Fabrication of VBGs using the Gaussian Beam

The VBGs inscriptions using the Gaussian beam have been performed using a prototype fs fiber laser emitting at 1030 nm, 9.25 MHz repetition rate, 400 fs pulse duration, and an average output power of 5 W. The positioning of the sample during the laser inscription was assured within a precision of 30 nm by motorized 3-axis stages (XMS100 – VP5ZA, Newport). First, a single line has been inscribed using a microscope objective (Nikon, 40x 0.75 NA) using an irradiance of 16.4 TW/cm^2 and a writing velocity of 100 µm/s. By analyzing the top view fluorescence microscope image under 365 nm excitation, the diameter of the inscribed line with the chosen irradiation conditions in the regime of Type-A inscription was equal to ~2 µm (see Figure IV-13(a) (Top view)). The lateral polished side of the sample was used to measure the modifications thickness which was around ~9 µm (see Figure IV-13(c) (Side view)).

To obtain a VBG with an appropriate thickness using this approach, it is therefore necessary to stack multiple layers from bottom to top of the considered material. In this way, a multi-layer grating was achieved by stacking several single-layer gratings on top of each other with an overlap of 50% between different plans. The grating transverse area was 500×500 µm^2 with a periodicity of 2 µm. Such periodicity was chosen for proof-of-concept of VBG inscription based on Type-A modification, as it typically corresponds to the diameter of the individual photo-inscribed structures, as shown in Figure IV-13(b). However, note that periodicities are not restricted to the diameter of the inscribed structures [159], [162], [325], [326]. Figure IV-13(d) shows the schematic representation of the inscription process and the structure's geometry in the case of the 5-layers grating with a global achieved thickness of 30 µm.

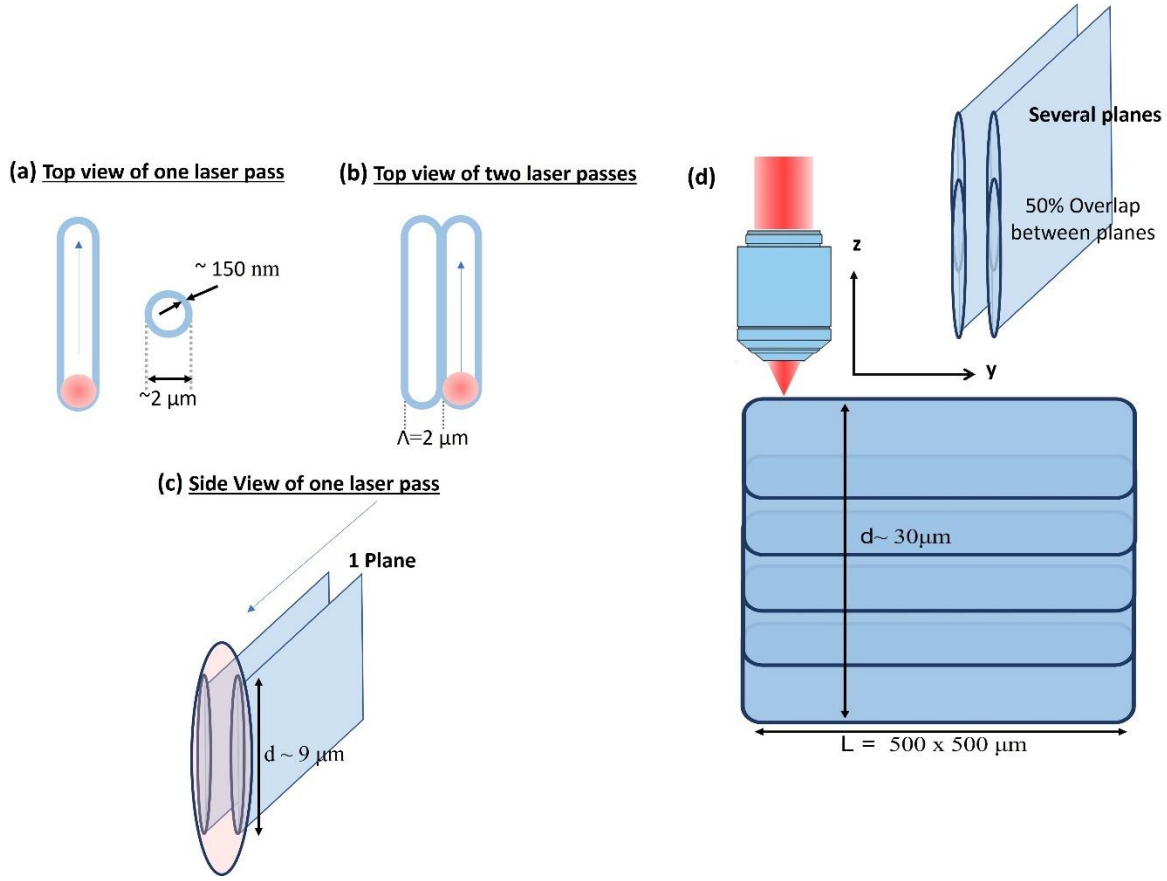

Figure IV-13: Schematic representation of the individual inscribed structures with one single laser pass, shown from (a) top and (c) side views. (b) Schematic representation of the inscribed structures with two laser passes shown from top view. (d) Inscription process for the fabrication of the multi-layers VBGs, showing here a 5-layers grating achieving a thickness of 30 µm.

Two additional multi-layers VBGs with different thicknesses were obtained by increasing the number of layers (N = 8 and 19) with the same overlap of 50% between each layer. The gratings exhibited then a thickness of 45 µm and 100 µm, respectively.

IV.7.2.Fabrication of VBGs using the Gaussian-Bessel Beam

Based on the encouraging Gaussian beam approach, VBGs were also written using Gaussian-Bessel laser beams [327]. As explained in section IV.5.2, a greater layer depth of modification can be achieved directly with a single laser pass, therefore reducing the required number of consecutive layers to inscribe, thus leading to a faster recording time and a better overall efficiency [291].

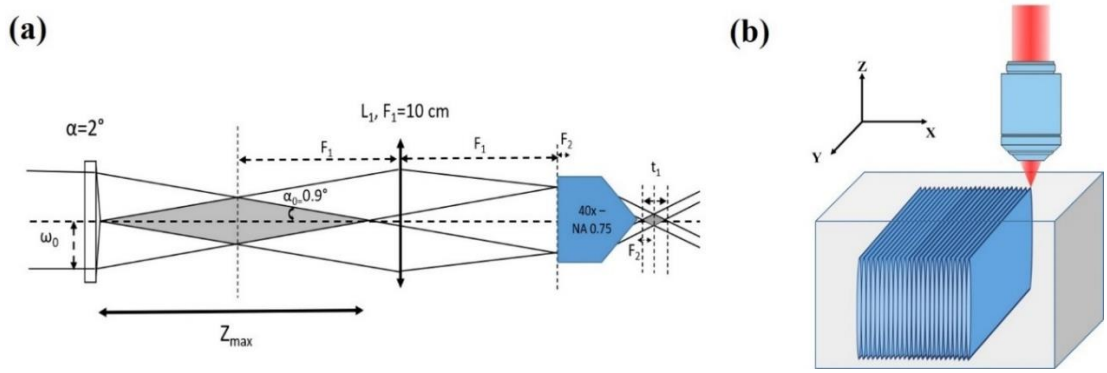

Figure IV-14: (a) Schematic drawing of the experimental setup for the generation of the Gaussian-Bessel beam using an axicon and the demagnifying 4F optical system. (b) Schematic drawing of the volume Bragg gratings fabrication using the Gaussian-Bessel laser beam approach.

The Bessel beam is formed using the technique shown in Figure IV-14(a). A UV-fused silica axicon (AX252-B, Thorlabs) having a physical angle of 2° enables the conversion of the incident Gaussian laser beam into a Gaussian-Bessel beam. The incident Gaussian beam had a radius of 2.58 mm at 13.6% of maximal intensity. Using the formulas (IV-6) and (IV-7), the dimensions of the primary Bessel beam were thus estimated to Z_{max} = 166 mm and ρ_0 = 25.3 µm. Then, a 4F system involves the combination of a lens (F_1 = 10 cm) and an objective lens (F_2 ~ 4.5 mm, Nikon CFI PLAN FLUOR 40× - 0.75NA) with the focal length ratio $\frac{F_1}{F_2}$ = 22.22. The compressed Bessel beam (secondary Bessel region) showed a length of 336.3 µm with a central core radius of 1.14 µm. With such a long non-diffractive length, it is possible to inscribe volume Bragg gratings with sufficient thickness with only a single layer instead of hav-ing to superimpose many layers like when using a Gaussian beam, as shown in Figure IV-14(b). Figure IV-15 presents the image profile of the intensity cross-section of the Gaussian-Bessel beam measured at ~10 cm after the axicon lens (near the $\frac{Z_{max}}{2}$ region). Note that the small beam at the left of the central beam is probably a parasitic Fresnel reflection. Theoretically, each ring of the Bessel beam (including the central lobe) contains the same amount of energy [298]. As the experimental measurement exhibits 40 rings, it shows that the energy in the central lobe of the beam is very weak compared to the total beam energy. By measuring the power before the axicon and using the equation (IV-10) while considering the 40 rings existing in the Bessel beam, we calculate the peak intensity (or irradiance) A_0^2 in the center of the Bessel beam after the telescope.

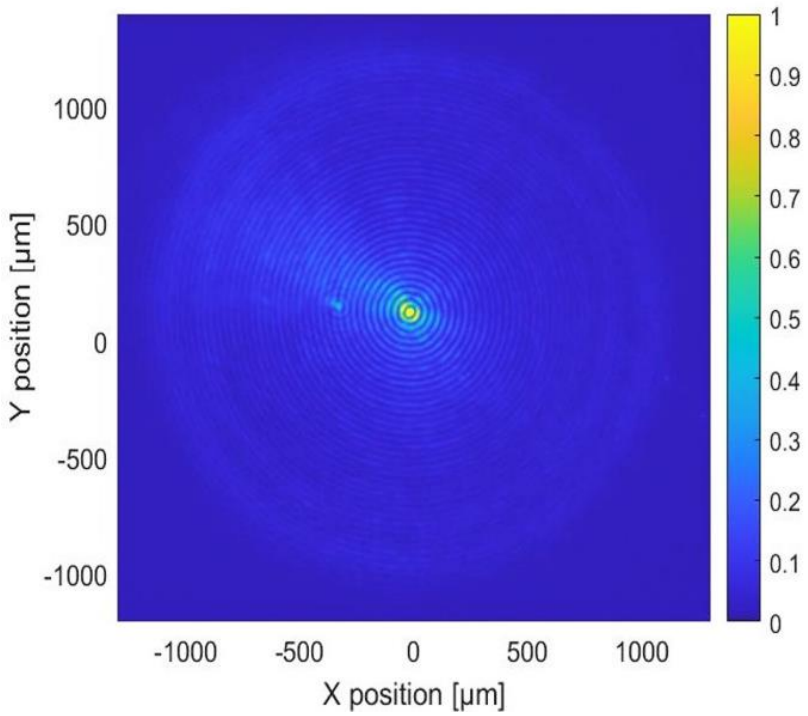

Figure IV-15: Experimental image profile of the intensity cross-section of the Gaussian-Bessel beam close to the $\frac{Z_{max}}{2}$ region.

An ytterbium laser (Yuja, Amplitude system) was used to realize the fs-writing of VBGs. The laser source operates at 1030 nm and delivers 417 fs pulses at a 1 MHz repetition rate, with a maximum average power of 10 W. While propagating from air to glass (n = 1.59), refraction extended longitudinally the secondary Bessel beam to a length of 534 µm in the glass material [297]. On the other hand, the radius of the central ring is not affected from such a propagation from air to glass. The grating transverse area was 400×400 µm^2 with a periodicity of 2 µm. The diameter of the inscribed structures here was of the same order of magnitude as in the case of the Gaussian beam. This explains the reason for the chosen periodicity of 2 µm as clarified in section IV.7.1 and as further detailed in Figure IV-22(a). VBGs were produced with their top position located at 160 µm below the surface for a series of writing velocities (20 $\mu m/s$ – 60 $\mu m/s$ – 80 $\mu m/s$). In the chosen experimental conditions, the writing processes were typically achieved from 30 minutes up to 1 hour, for velocities from 80 $\mu m/s$ down to 20 $\mu m/s$, respectively. VBGs were written with two average measured powers of 2.47 W and 2.59 W after the objective, corresponding to estimated writing irradiances of 5.05 and 5.30 TW/cm^2, respectively, using equation (IV-10), corresponding to pulse energies in the range of 2.47-2.59 µJ. Note that these irradiances are similar to the values typically used for inscribing Type-A modifications with a standard Gaussian beam. As the experimental measurement exhibits 40 rings, it shows that the energy in the central lobe of the beam is very weak compared to the total beam energy. Normally, for inscribing with a Gaussian beam, we use a 300-400 mW average power coming from a 1030 nm laser with a repetition rate of 10 MHz: modifications typically appear for irradiations of 4-5 TW/cm^2 and

pulse energies of 25-35 nJ per pulse. In the case of the Gaussian-Bessel written structures, we have used a more energetic laser with a maximum mean power of 2.47-2.59 W for the inscription and a repetition rate of 1 MHz (2.47-2.59 µJ per pulse) to reach sufficient irradiances in the beam's central lobe capable.

The important point is that we maintain the Type A inscription regime over the whole length of the Gaussian-Bessel beam. While standard Gaussian beam inscription requires ~5 TW/cm2 over 6 µm, the Gaussian-Bessel beam inscription thus requires about ~5 TW/cm2 over 160 µm with similar lateral dimensions, such that pulse energies standing in the µJ level are required.

Note that Type-A laser modifications are triggered at low laser irradiances, typically two orders of magnitude lower than the Type-I regime threshold in such photosensitive glasses [161]. Thus, the inscription beam propagation is mostly propagation in a linear regime without any influence of nonlinear effects. Indeed, each Gaussian-Bessel ring can be considered as to contribute to a typical modification depth of 5-10 µm: on the one hand, Kerr effects show no role under such a limited propagation distance at high intensity at the TW/cm^2 level; on the other hand, energy deposition for each ring is also a minor fraction of the carried energy (within the % range, similarly to what was measured by Bellec *et al.* on the Gaussian geometry [328]. Consequently, multiphoton absorption and associated energy deposition are a side product of the beam propagation. This is experimentally verified in Figure IV-22(a) since, as shown by the silver clusters' fluorescence profile in depth, the energy deposition is smooth and in agreement with the expected propagation of a Gaussian-Bessel beam in a linear regime.

IV.7.3.Fabrication of VBGs using the light-sheet method

To further progress in the versatility of laser inscription of VBGs as well as in increasing the Type A inscription throughput, a 1030 nm laser (Tangor, Amplitude System) emitting pulses of 507 fs and a maximum output power of 100 W was used to realize the fs-inscription of VBGs using the light-sheet method. This method creates a laser beam focused in one direction while being kept collimated in the other. This helps to create a sheet of light along the *x* and *z*-axis. The glass sample can be moved in the *y*-direction to inscribe another light-sheet right next to the first one and therefore obtain the VBG's transverse area with a specified periodicity. The laser was used in burst mode, *i.e.,* 10 pulses spaced 30 ns apart at a repetition rate of 200 kHz. The advantage of the burst mode is to still allow for reaching the irradiance threshold for the *Type-A* modification while shortening the VBGs' writing time by delivering the needed multi-pulse energy deposition to inscribe efficient VBGs. A cylindrical afocal system (f_1=7.5 cm and f_2=2.5 cm) was used to reduce the output beam in only one axis to produce a beam of 0.9 x 2.7 mm. Then, the beam diameter of 2.7 mm is focused into the glass sample by a cylindrical lens (*f=5 cm*) in only one direction, generating a light-sheet

of 900x24x900 μm^3, where : the 900 µm length in the *x*-direction resulted from the initial cylindrical afocal system; the 24 µm width in the y-direction was produced by the final f=5 cm cylindrical lens and the 900 µm depth dimension originated from the depth of focus (2 x Rayleigh length) in air when focusing the 24 µm diameter. The schematic representation of the cylindrical lens setup is depicted in Figure IV-16. When propagating from air to glass (n=1.59), refraction extended the beam to a length of 1.43 mm in the glass material. Thus, we inscribe a VBG with only a single layer, by translating the bulk along the *y*-axis with a periodicity of 7.5 µm. The writing process was achieved within 33 min for 500 μm of transverse length.

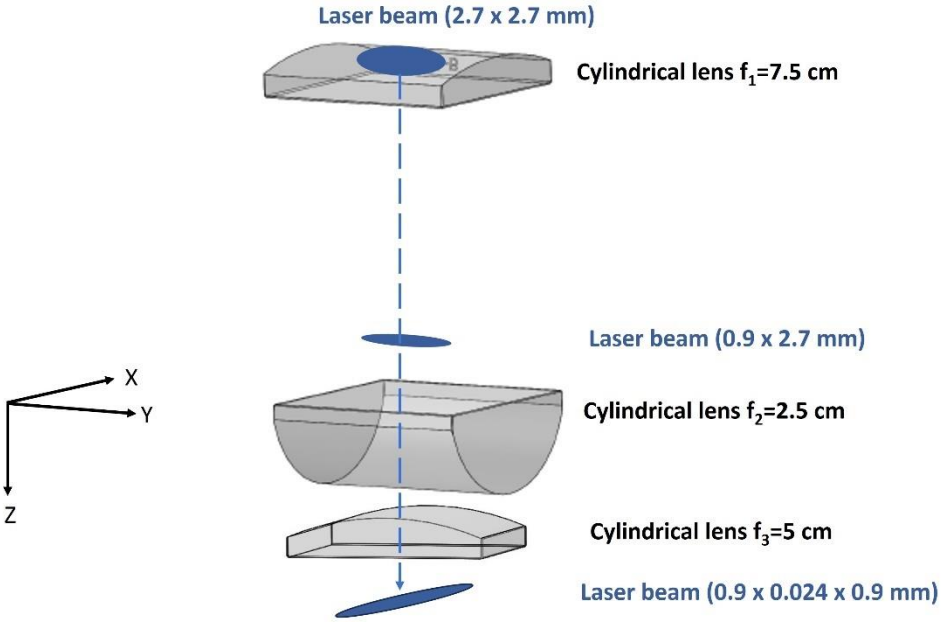

Figure IV-16: Schematic of the cylindrical lenses setup used to create the light-sheet.

IV.7.4.Fabrication of VBGs using the phase mask technique

The experiment using the phase mask inscription setup was conducted in collaboration with the COPL laboratory (Centre d'Optique, Photonique et Laser, University Laval, Québec), with Lauris Talbot and Martin Bernier. We have employed ultrashort laser pulses (30 fs) and a low repetition rate (1 kHz) of a Ti:Sapphire laser (Coherent Inc., Astrella) using the scanning phase mask technique to achieve a high period stability. An 800 nm beam with an 11 mm Gaussian diameter (at $1/e^2$) is reflected by a cylindrical mirror (*f=40 cm*). Such a long focal lens was chosen to obtain a long beam confocal parameter (~2.7 mm in air) and to limit aberrations induced by the refractive-index mismatch between air and the bulk glass. The beam was then reflected by a planar mirror and sent toward the phase mask. The inscription setup is the same as that shown in Figure IV-12, except a slight difference. In our experiment, the phase mask and the bulk material were retained in the same mount,

separated by 150 µm, to ensure the robustness of the induced fringes (as shown in Figure IV-17). Such a configuration prevents the problem of stitching errors while extending the size of the grating inside the bulk. The fs beam is focused approximately on the top position of the sample using the *z*-translation stage. The mount containing the phase mask and the glass sample was placed on a motorized 2D translation stage (Aerotech, ALS130H) to move the glass medium in the *x*-plane with respect to the focalized beam. This stage was controlled by a Labview program developed by the company PhotoNova Inc. During the inscription process, the sample was only moved in the *x*-direction to scan the focalized beam over the required VBG width. After thorough optimization testing of the phase mask periodicities, the final VBGs were fabricated with a phase mask period of 14 µm. Above a certain laser power, a filament effect begins to appear in the phase mask while the threshold of this effect is lower in the glass sample. Gratings with a transverse length of 250 µm were inscribed. The VBGs were written with different irradiances and writing speeds. Section IV.9.4 will presents more details about the laser parameters of the inscribed VBGs.

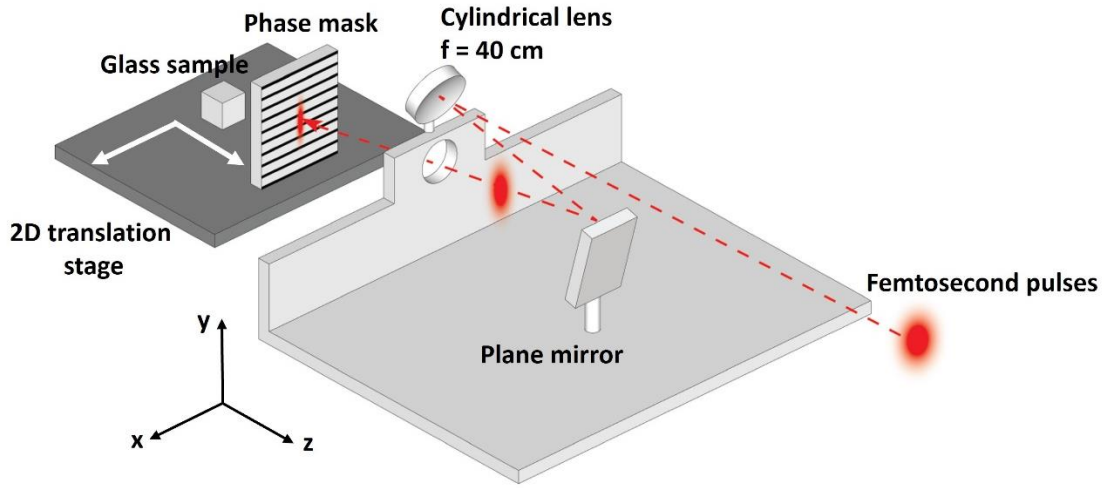

Figure IV-17: Schematic of the VBG inscription setup in a glass sample using the phase mask substrate. Adapted from [322].

IV.8.Characterization of volume Bragg gratings

Diffraction efficiencies of all the inscribed VBGs were measured in transmission at the Bragg condition. First, a TEM_{00} He-Ne laser (632.8 nm wavelength) was used. Figure IV-18 presents the experimental setup for characterization using the He-Ne laser. The analyzed sample is positioned on a motorized rotation stage with an additional manual 3D translation stage. A lens of focal length *f*= 40 cm was chosen to loosely focus the beam inside the VBG, leading to an almost collimated propagation along the sample's thickness while having a beam diameter smaller than the VBG transverse area. For each angle detuning from the Bragg angle, we estimated the first-order Bragg diffraction efficiency as the ratio of the first-order diffracted

beam power P_1 to the sum of the non-diffracted (zero order) power P_0 and the diffracted (first-order) power P_1. It should be noted that the power P_m of the diffracted orders (with m≠0,±1) are approximately zero. This relative diffraction efficiency is calculated as follows:

$$\eta_{Exp} = \frac{P_1}{P_1 + P_0} \qquad \text{IV-14}$$

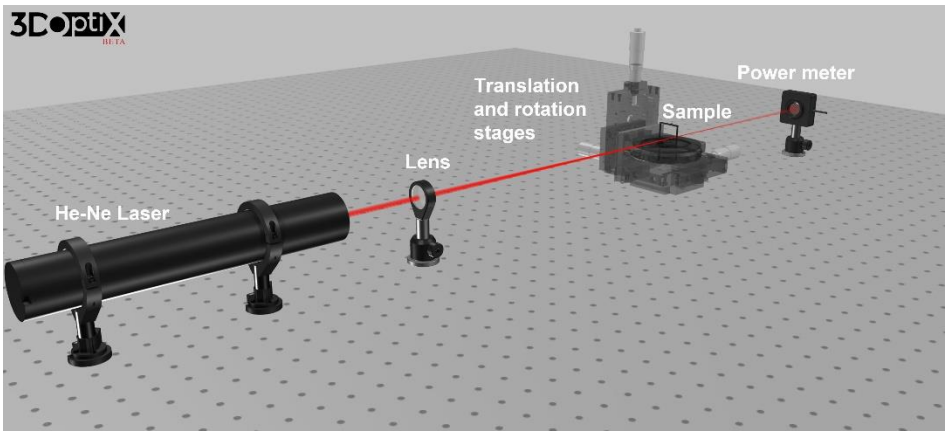

Figure IV-18: Experimental setup for characterizing transmitting VBG using a He-Ne laser.

In addition, diffraction efficiency was measured with a single-frequency fiber laser at 1.55 µm (FL-1550-SF, Changchun New Industries Optoelectronics Technology Co., Ltd.). The beam from the fiber-coupled light source was collimated and propagated through the same optical path described previously (the same setup for characterizing VBG using a He-Ne laser). Moreover, the spectral characteristics of the VBGs were analyzed using a broadband supercontinuum white light laser source (Sambda-450, Leukos). Then, light was focused inside the glass bulk using the same setup as for the He-Ne laser. The transmitted light was refocused into an optical fiber (P400-1-SR) connected to a spectrometer (USB2000, Ocean optics). We measured the successive transmission dips of the zeroth order corresponding to both the first and second diffraction orders of the grating. The transmission spectra were normalized according to a spectrum obtained at normal incidence on the glass bulk inside the VBG's area.

In addition, a theoretical diffraction efficiency has been retrieved from fitting the experimental measurements with the reported Kogelnik's model (using Equation IV-3) to extract the modulation of the refractive index and the effective thickness associated to each of these gratings.

IV.9.Results

IV.9.1.Characterization and limitations of VBGs using Gaussian beams

Figure IV-19(a-b) presents the wide field fluorescence microscope images of the top and side views, respectively, of the inscribed 5 layers of VBG with the Gaussian beam geometry. As detailed in Chapter II, such fluorescent layers are composed of photo-induced silver clusters. Figure IV-19(b) illustrates well the induced 30 µm thickness. Such fluorescent images were taken with a microscope (BX53, Olympus), using a camera (EP50, Olympus) and a 10× - 0.3 NA microscope objective (Olympus) for the top view (Figure IV-19(a)) while a 20× - 0.5 NA microscope objective (Olympus) was used for the side view image (Figure IV-19(b)).

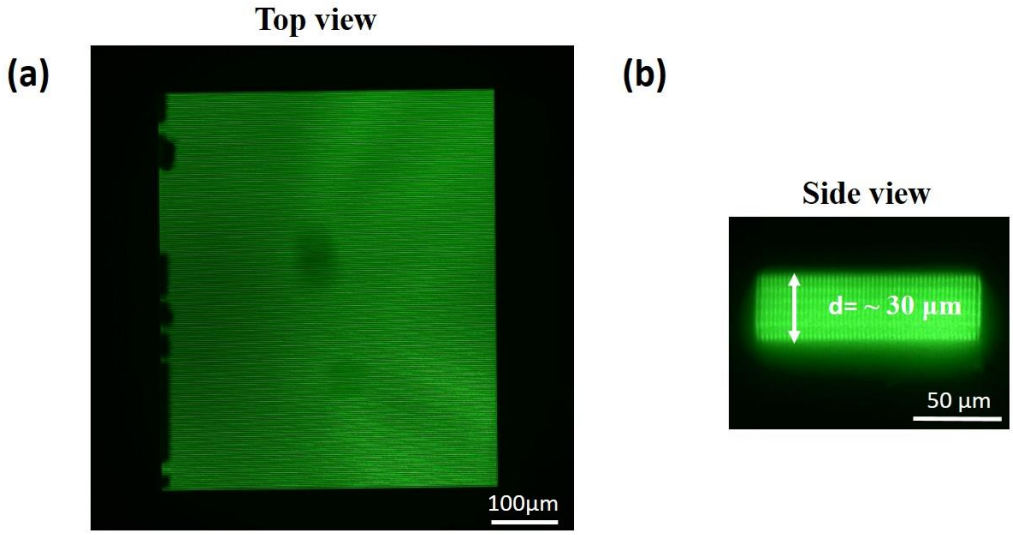

Figure IV-19: Fluorescent microscope images (excitation at 365 nm) of the 5-layer VBG. (a) Top view, and (b) Side view.

Figure IV-20 shows the good agreement between the experimental and simulated angular selectivity of the 5 multi-layers inscribed VBG. The experimental measurement demonstrates a peak transmission diffraction efficiency of ~6.8% at the Bragg condition at the wavelength of 632.8 nm. By fitting the experimental data with Kogelnik's equation (Equation IV-3), we can extract an effective thickness of 30 µm (in agreement with the fluorescence in-depth thickness of Figure IV-19(b)) and a refractive index modulation $\Delta n_{AC} = 1.72\times10^{-3}$ (such a value showing a reasonable consistency with Type-A refractive index modifications).

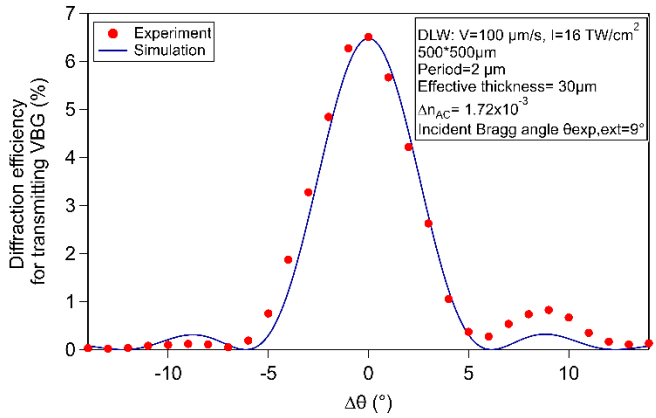

Figure IV-20: Experimental and simulated dependence of the diffraction efficiency on the deviation from the Bragg angle of the transmitting Bragg grating for λ=632.8 nm for incident Bragg angle = 9° (first order).

This result offered hope for increasing the number of layers to improve diffraction efficiency as the obtained value of the refractive index modification (for 5 layers and 30 µm thickness) is already high enough for such thickness compared to the literature. Thus, two additional multi-layer VBGs were inscribed with 8 and 19 layers using the same laser parameters as those for the 5-layer VBGs. Table IV-2 summarizes the experimental and simulated results for all the multi-layer VBGs of the angular characterization at 632.8 nm.

Table IV-2: Experimental and simulated results of the angular characterization at 632.8 nm for the several inscribed multi-layer VBGs.

VBG	Number of planes	Bragg period (µm)	Diffraction efficiency (%)	Effective thickness (µm)	Δn_{AC}	Inscription time (hour)
A	5	2	6.5	30	1.72×10^{-3}	1.7
B	8	2	14.7	45	1.75×10^{-3}	2.8
C	19	2	24.7	100	1.05×10^{-3}	6.6

The experimental measurement for the VBG "C" (19 layers) was conducted for an incident Bragg angle different than 9° (corresponding to Bragg angle at 632.8 nm for 2 µm periodicity). Moreover, the refractive index modification was lower than the one for the other VBGs. To understand this result, the diffraction efficiency for transmitting VBG was simulated versus a range of thicknesses, using Kogelnik's equation for the same case of our inscribed VBG (namely with a period of 2 µm and an effective refractive index modulation of 1.72×10^{-3} obtained from the simulation). This simulation is represented in Figure IV-21. One can see that the measured diffraction efficiency of VBG "A" and "B" (5 and 8 layers corresponding to a thickness of 30 µm and 45 µm, respectively) follow the simulated sinusoidal law, while the efficiency of VBG "C" (19 layers corresponding to a thickness of 100 µm) is lower than expected. This may happen due to the stitching of periodicity when inscribing multiple layers. Indeed, the intensity of the inscription varies with the inscription depth, affecting therefore

the inter-distance width of the structures and the induced periodicity. Thus, from the experimental diffraction efficiency of VBG "C", we can extract a lower refractive index modulation of 1.05×10^{-3}.

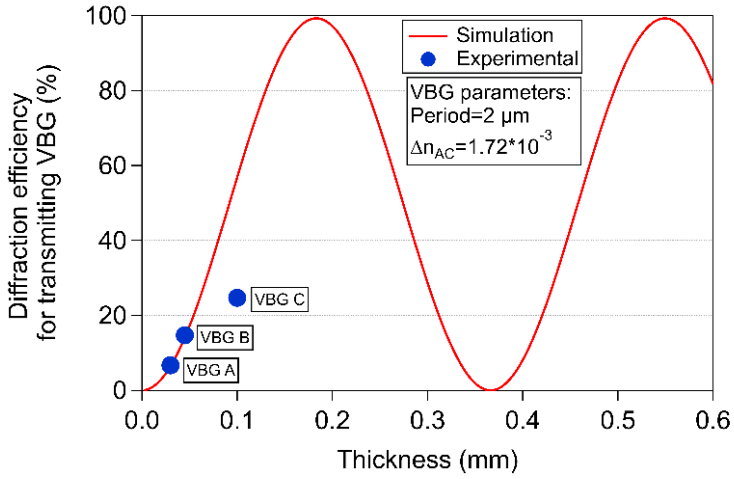

Figure IV-21: Simulated dependence of the diffraction efficiency for transmitting Bragg grating versus VBG's thickness for λ=632.8 nm, Δn_{AC} =1.72 x 10^{-3}, Λ=2 µm.

Inscribing VBGs with several layers using the Gaussian beam has significant drawbacks, such as the required level of stability and positioning accuracy that is not maintained over the whole inscription volume. Moreover, possible limitations regarding the homogeneity of the achieved periodicity when using this layer-by-layer approach alongside the line-by-line writing technique. As a result, the achieved experimental diffraction efficiencies are often lower than those expected, as well as the long inscription times that linearly scale with the targeted depth of the VBG. To overcome these limitations, VBGs have been formed using Gaussian-Bessel laser beams. Indeed, a greater layer modification depth can be achieved, therefore reducing the required number of consecutive layers to inscribe, and thus leading to a faster recording time and better efficiency.

IV.9.2. Glass modification and characterization of VBGS using the Gaussian-Bessel beam

The glass modification using the Gaussian-Bessel beam was studied by inscribing lines of 200 µm in length along the *y*-axis. Those lines were inscribed with the same laser parameters as those used to inscribe the VBGs described in Section IV.7.2. The side view fluorescence images (along the *z*-axis) have been acquired with a microscope (BX53, Olympus), using a camera (EP50, Olympus) and a 10× - 0.3 NA microscope objective (Olympus) with excitation light at 365 nm. Figure IV-22 shows the axial modification tracks produced by the Gaussian-Bessel beam, representing the traces of fluorescence composed of silver clusters. The longest depth of the modified tracks after inscribing one plane is around 300 µm when the writing

speed is set to 20 $\mu m/s$. This value is slightly lower than the theoretical one of 534 µm (see SectionIV.5.2.a), which is probably due to spherical aberrations or slight misalignment in the primary Bessel beam. Indeed, the creation of silver clusters and their associated fluorescence intensity depend strongly on the local parameters of the focused laser beam during the inscription process. Furthermore, the material change in each modified track is not fully homogeneous: the fluorescence intensity is higher in the center than on both longitudinal edges (along the *z*-axis). As recently demonstrated, Δn is dependent on the laser irradiance [156]. Thus, the refractive index modification may also be not fully homogeneous in the individual tracks. However, as explained elsewhere in the present work of this PhD, it is important to note that our glass provided only Type-A modification all along the axial depth in the achieved local intensity distribution [161]. In contrast, the presence of both types I (smooth isotropic Δn) and II (anisotropic scattering centers) in fused silica using Gaussian-Bessel beams has been reported, which is related to the large variation of intensity along the modified structure and thus presenting a limitation to the diffraction efficiency of the VBG [289].

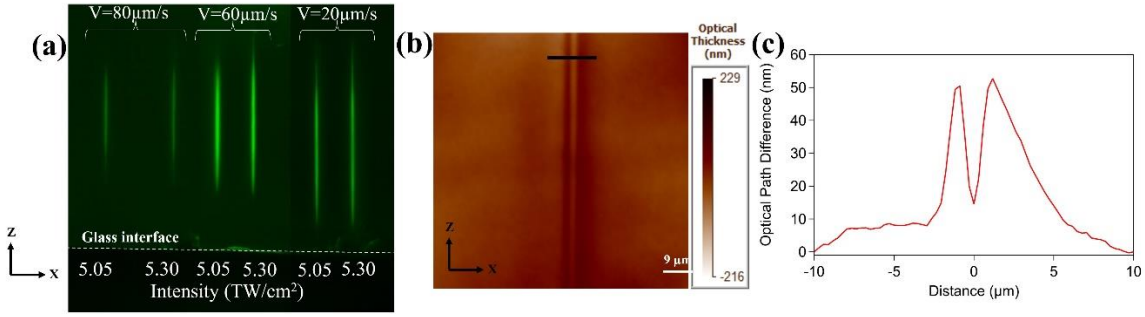

Figure IV-22: (a) Side view microscopy fluorescence image (excitation at 365 nm) of modifications induced with the Gaussian-Bessel beam for different laser intensities and writing speeds. (b) Phase image of one laser-inscribed line (DLW parameters: 20 $\mu m/s$ and 5.05 TW/cm^2) taken from the lateral side of the sample, acquired through the SID4-Bio device. (c) Line profile of the typical OPD associated with the double-track Type-A structures. Such line profile is extracted from a horizontal cross-section of the structure (black line in (b)).

The side-view image of one of these structures was collected using a 100× microscope objective (Zeiss) with 1.3 NA (used with a matching index oil n = 1.518) and the SID4-Bio sensor (Phasics) plugged into an Axiovert 200M Zeiss microscope. As represented in Figure IV-22(b), this device allows for the construction of the phase image and the extraction of the local optical path difference (OPD) between the written lines and the pristine glass. Figure IV-22(c) shows an example of the OPD line profile with two positive peaks of refractive index modification for an inscribed line at a velocity of 20 $\mu m/s$ and irradiance of 5.05 TW/cm^2. As detailed in chapter II, such double line changes are typical of Type-A modifications, associated with the photo-induced silver clusters at the periphery of the interaction voxel for every laser passage [156], [159], [161], [329]. The inter-distance between the double lines

was ~2 µm, which is approximately the size of the focalized laser beam diameter in our case. This inter-distance can be partially adjusted by tuning the peak intensity, writing speed, or the numerical aperture of the objective. This also supported the choice of our VBGs' period (2 µm) as a double pass could have a period-homogenization effect. Moreover, because these thick structures (thickness along the *y*-axis of Figure IV-22(b)) may not be perfectly orthogonal to the glass interface and to the axis of observation of the phase imaging device, this may introduce an asymmetric blurring effect, as seen in the right track in Figure IV-22(c). This is usual for quantitative phase imaging measurement with thick phase objects. Abou Khalil *et al.* recently published an approach allowing quantitative retrieval of the refractive index modification based on the measured OPD, especially for thick structures, by considering cylindrically shaped volume modifications with varying diameters and heights [330]. It has been shown that saturation behavior for the measured OPD occurs when structures become too thick (namely for thicknesses beyond those for which the Fresnel criterion spans from near field to far field distances in the rigorous diffraction theory). Such a depth dependence and saturation also depend on the confocal length of the phase imaging conditions. Therefore, due to the difference in shape (linear shapes with a diameter of 2 µm in our case), it is not possible to compare the OPD saturation level in our case with the work published in the reference [330]. Thus, the associated refractive index modification cannot be directly evaluated by phase imaging in the present case, since the thickness is much larger than the effective length that can be coherently integrated with the phase imaging. However, we can roughly estimate from Figure IV-22(c) a refractive index modification of the order of 5.8×10^{-3} for an estimated thickness of ~ 8 µm.

Figure IV-23(a-b) shows the experimental and simulated angular dependence of the VBG inscribed with a period of 2 µm at 20 $\mu m/s$ with an estimated irradiance of 5.05 TW/cm^2 in the central lobe of the secondary Gaussian-Bessel beam in the glass sample. As shown in Figure IV-23(a), the experimental measurement demonstrates a peak transmission diffraction efficiency of ~95% at Bragg condition for an external incident Bragg angle of -21.7° at the wavelength of 632.8 nm. By fitting the experimental data with IV-3, the refractive index modulation Δn_{AC} and the effective thickness of the inscribed VBG were extracted. The measured data were best fitted with an effective thickness of 150 µm and an index modulation $\Delta n_{AC} = 1.78\times10^{-3}$. In addition, this VBG was probed at the second diffraction order at an external Bragg angle of incidence of 6.17°. This second-order grating still exhibits a significant diffraction efficiency of ~65 %, resulting in an effective thickness of 165 µm and a slightly lower refractive index modulation $\Delta n_{AC} = 1.12\times10^{-3}$. This second-order diffraction is observed since the induced refractive index profile of the inscribed gratings is not a pure sinusoidal function, due to the highly nonlinear process of energy deposition during femtosecond laser inscription [331]. Note that such a second-order diffraction efficiency shall further be investigated for other VBG periods that differ from the typical diameter of the

single-pass laser inscription. The VBG angular selectivity for the opposite orders was also measured. From the fitting of the experimental data, approximately similar values were obtained for the effective thickness as well as for the refractive index modification. Note that due to the moderate values of the incident and diffracted angles at the different diffraction orders, the correction of Fresnel reflections played no role in the measurements. Typically, a transmitting VBG with an inclination of $\varphi = \pm 90°$ is known as a symmetric grating or a normal grating. The direct modeling of our inscribed VBGs showed the necessity to take into account a slant angle of ~82.5° that allowed us to fully interpret the experimental incident angles. Such a value is reasonable, considering that the sample had been put by the eye into the laser inscription setup, so that a few degrees of misalignment (~7.5° here) from the normal grating orientation are very realistic.

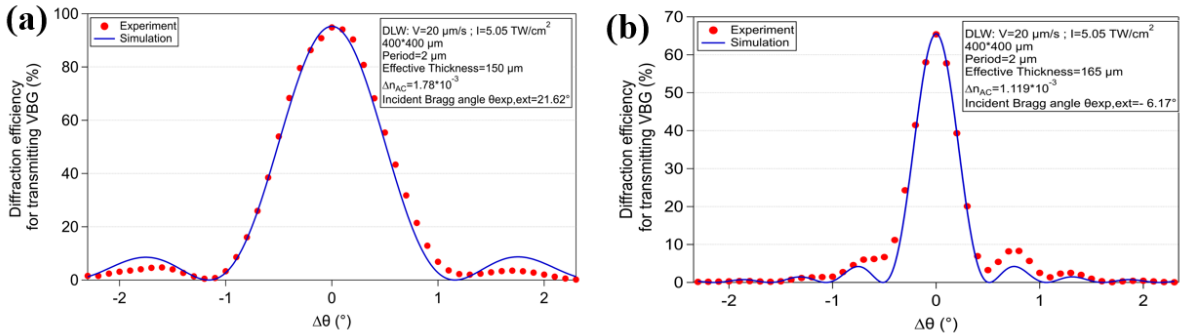

Figure IV-23: Experimental and simulated dependence of the diffraction efficiency from the Bragg angle of the transmitting Bragg grating for λ=632.8 nm. (a) Incident Bragg angle at 21.62° (first order), (b) incident Bragg angle at -6.17° (second order).

It's important to highlight that if we wanted to inscribe a volume Bragg Grating using a Gaussian beam with an effective thickness of 150 µm (such as the one inscribed with the Gaussian-Bessel beam), we will have to arrange 30 planes in a stack with a 50% overlap. The estimated time for writing this grating will be about 33 hours. For the VBG inscribed by Gaussian-Bessel beam, a 400 x 400 µm^2 grating with a period of 2 µm at 20 µm/s took ~ 1 hour.

In addition, the diffraction efficiency of all inscribed VBGs was measured for the two first Bragg orders to evaluate the influence of the different laser parameters. Their relative refractive index modification and effective thickness have been extracted from simulations. Note that VBGs inscribed with an irradiance of 5.3 $\mathrm{TW/cm^2}$ (as described in Section 2.1) were characterized, showing approximately the same diffraction efficiencies as those inscribed with 5.05 $\mathrm{TW/cm^2}$. The diffraction efficiency depended mostly on the writing velocity. Figure IV-24(a) summarizes the peak diffraction efficiency for the different writing speeds used to inscribe the VBGs. Their associated refractive index modification, extracted from the

numerical simulation is represented in Figure IV-24(b). The highest refractive index modification is obtained for the lowest writing speed (20 $\mu m/s$). This value decreases with the increase of speed during the inscription of VBGs. In addition, the second-order VBGs present lower refractive index modification for each VBG. The experimental measurements show that the effective thickness of the grating is approximately constant for all direct laser writing parameters (equal to 160±7 µm for the first transmission order compared to 162±9 µm for the second transmission order). Such effective thickness represents the homogeneous part of the refractive index modification that contributes efficiently to diffraction. We can notice that the axial length of the Gaussian-Bessel beam of the fluorescence images for excitation at 365 nm (Figure IV-22(a)) depends on the laser inscription parameters. In fact, the thickness of the Δn_{AC} zone could be different than the axial length of the fluorescence for some laser inscription conditions. Indeed, silver clusters that mostly contribute to the refractive index modification may not be those being excited at 365 nm. Note that the lateral homogeneity of the line-by-line inscribed and associated periodicity is demonstrated *a posteriori* by the highly-efficient Bragg diffraction measurements and the great agreement between the experimental data and the model.

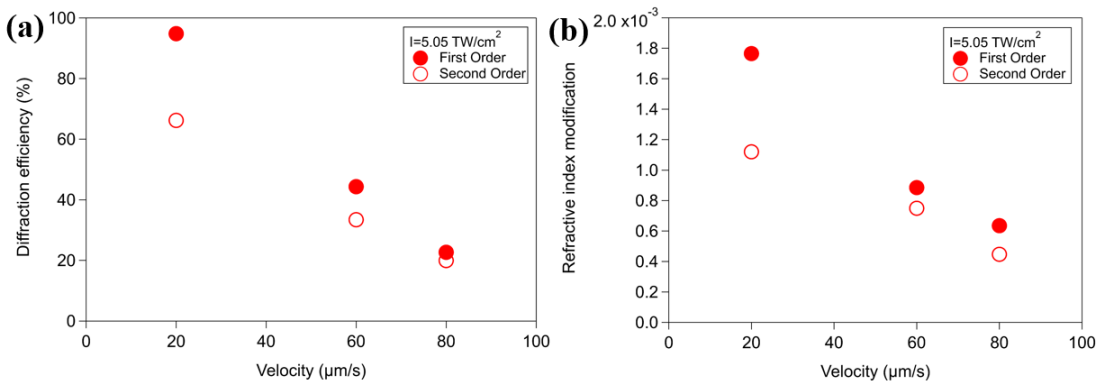

Figure IV-24: (a) Peak diffraction efficiency measured for the first two Bragg orders of the inscribed VBGs at different writing speeds. (b) Their corresponding average refractive index modification extracted from the numerical simulations.

The spectral transmission dip of the zero-order beam results from the first and second diffraction orders of the inscribed grating at 20 $\mu m/s$ and 5.05 TW/cm^2 (as the VBG in Figure IV-20). Such spectral dips are presented in Figure IV-25(a-b) for a VBG orientation at the Bragg angle determined at 632.8 nm. The value of the first- and second-order diffraction efficiencies were obtained from the dip of the zero-order transmission spectrum, giving a diffraction efficiency of around 88.5% and 65.5%, respectively. The experimental result presents a good agreement with the simulation spectrum of the first and second diffraction orders, by assuming the same parameters as those used in Figure IV-23(a-b).

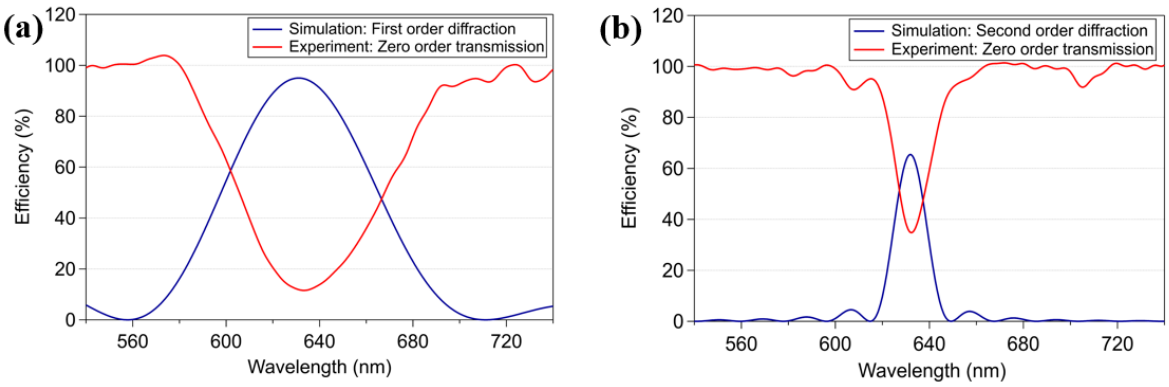

Figure IV-25: Measured transmission dip of the zero-order in the case of (a) the first and (b) the second Bragg order. Simulation of the diffraction spectra for the corresponding orders of the VBG.

Figure IV-26(a,b) represents a photograph of the first and second diffraction orders, respectively, which is measured with the broadband supercontinuum white light laser source (Sambda-450, Leukos). Such orders are depicted for a VBG orientation at the Bragg angle for the 632.8 nm wavelength.

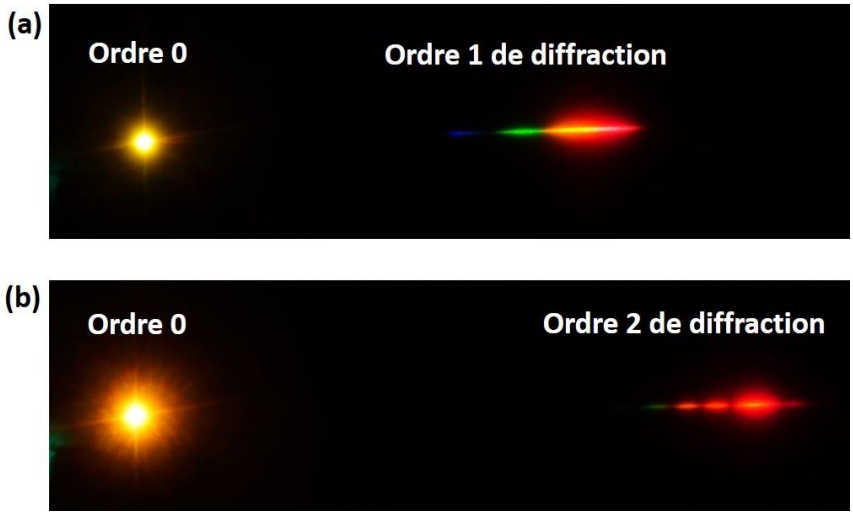

Figure IV-26: Photographs of diffraction of white light laser source by the grating pattern for an orientation at the Bragg angle for the 632.8 nm wavelength for (a) the first-order and (b) second-order diffraction orientations.

Finally, the diffraction efficiency has also been investigated for a Bragg angle adjusted to the wavelength of a 1.55 µm laser (see Figure IV-27(a)). The first-order transmission spectrum of the inscribed grating at 20 $\mu m/s$ and 5.05 TW/cm^2 (as the VBG in Figure IV-23(a)) showed a diffraction efficiency of ~17%. By fitting the angular spectrum, we were able to infer an effective thickness of 150 µm and a peak Δn_{AC} value of 1.37×10^{-3}. Such an effective length at the 1.55 µm wavelength is somehow very similar to the typical 160 µm effective thicknesses for diffraction of the 632.8 nm radiation wavelength. Accordingly, both the maximal

diffraction efficiency and the photo-induced refractive index modulation decreased at a 1.55 µm wavelength. Theoretically, simulating the Bragg diffraction efficiency at 1.55 µm using the parameters extracted in Figure IV-23(a) would have yielded a diffraction efficiency of 28.5%, instead of the measured 17% diffraction efficiency. Thus, one can conclude that most of the observed decrease in diffraction efficiency is inherently due to the increase in the tested wavelength since it accounts for 85% of the relative diffraction efficiency drop. Indeed, by increasing the wavelength of investigation while keeping the same number of periods, the grating tends to become optically thinner and thus less efficient, from the measured ~95% diffraction efficiency at 632.8 nm down to the expected 28.5% value at 1.55 µm. The residual diffraction drop from 28.5% down to 17% accounts for 15% of the residual relative diffraction efficiency drop, which results from the refractive index modification, shows only a weak dispersion decrease from 1.78×10^{-3} at 633 nm down to 1.37×10^{-3} at 1.55 µm. Theoretically, Kramers Kroning equation shows the dispersion of the refractive index change. From Kramers Kroning equation, we can estimate a refractive index change at 1.55 µm around 0.76 x 10^{-3} which gives a diffraction efficiency of about 5%. Thus, we can conclude that the refractive index change extracted from the experimental measurements is higher than the one estimated by Kramers Kroning equation (see Figure IV-27(b)).

Thus, the high refractive index modulation largely persists in the near-infrared range. However, longer gratings around 360 or 460 µm should further be designed and investigated in the future to obtain higher diffraction efficiencies in the infrared range. Still, these results of low spectral dispersion of Type-A refractive index modifications are promising for perspectives in the near-IR applications: it is the first time that we report on a Δn measurement for such a long wavelength, and even longer wavelengths appear accessible within the spectral range of transparency of these photosensitive oxide glasses.

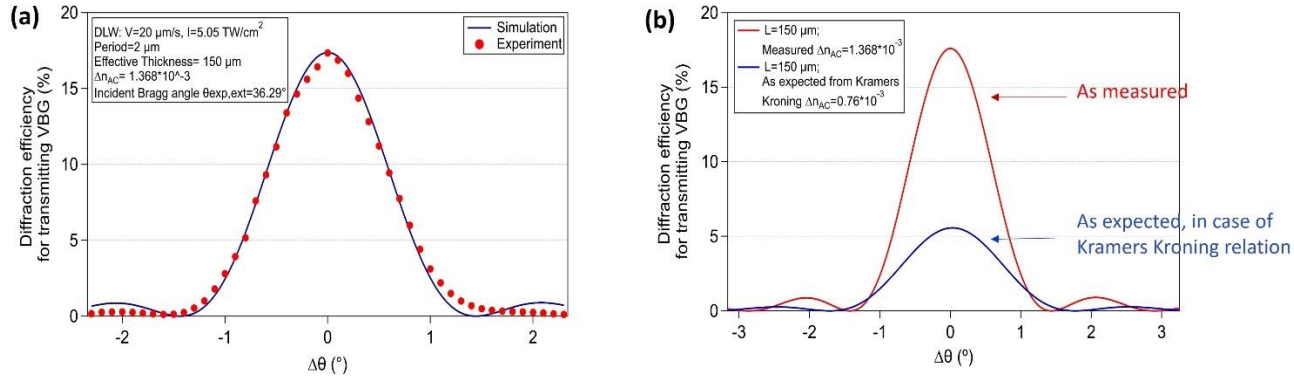

Figure IV-27: (a) Experimental and simulation angular dependence of the first-order diffraction efficiency from the Bragg angle of the transmitting Bragg grating for λ=1.55 µm. (b) First-order diffraction efficiency simulation as expected in the case of constant refractive index modification and as experimentally measured.

IV.9.3. Glass modification and characterization of VBGS using the light-sheet method

As mentioned in section IV.7.3, we generated a light-sheet of 900x24x900 μm^3 at 1030 nm wavelength, using the astigmatic system based on orthogonal cylindrical lenses. Figure IV-28(a) represents the experimental image profile of this beam around the focal plane of the last cylindrical lens. This figure was captured utilizing a beam profiler while employing z-stages to manipulate the focal plane's position. Line profiles were extracted along the horizontal and vertical cross section of Figure IV-28(a) and are represented in Figure IV-28(b-c) respectively. From the experimental measurement, we can extract a light-sheet of 1 mm x 50 µm. Probably, this experiment measurement was not taken exactly around the focal plane.

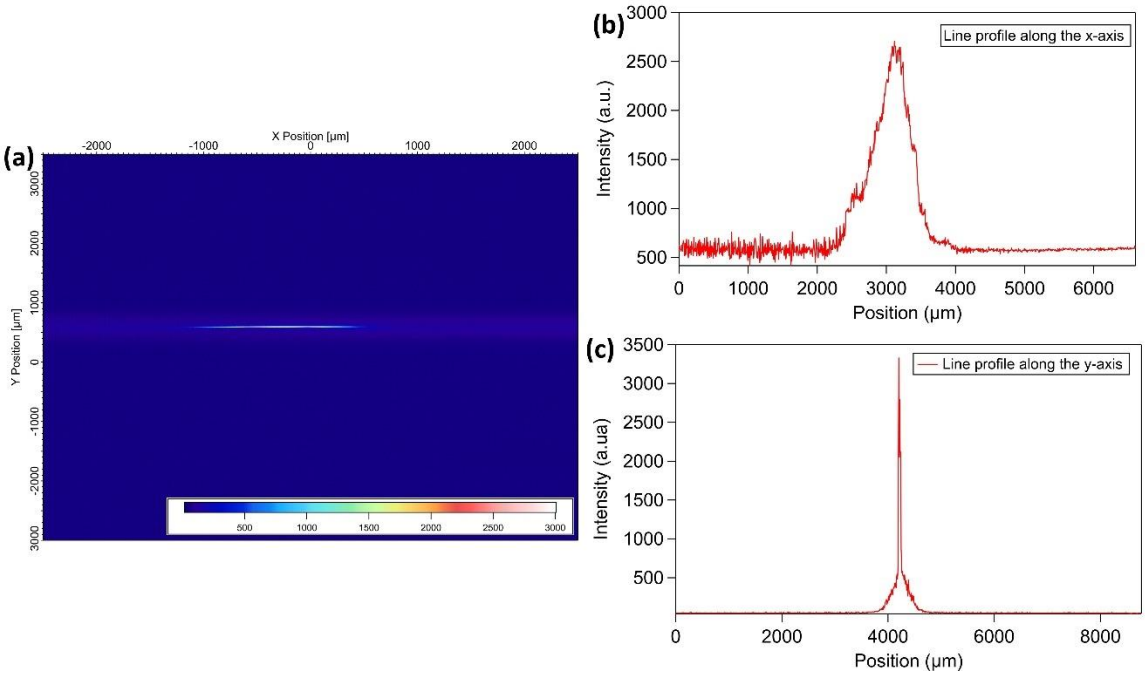

Figure IV-28: (a) Experimental image profile of the produced light-sheet beam. Intensity distribution along the (b) x-axis and (c) y-axis.

To investigate the glass modification created inside the glass using this method, a cartography of light-sheets was written as shown in Figure IV-29(a). The laser irradiance was tested during the writing at 8.82, 9.44, and 9.63 TW/cm^2, while the number of pulses was varied between 100 000 and 800 000 deposited pulses. Top-view fluorescent images under 365 nm excitation reveal the written structures (Figure IV-29(a)). The fluorescence intensity of the written structures exhibits a variation as a function of the laser parameters which was also previously reported by our group [156]: the higher the laser irradiance and/or the number of pulses, the greater the resulting fluorescence intensity. It can be seen also that thermal effects appear when the number of pulses is higher than 400 000 deposited pulses. For this reason, the VBG was written with 9.44 TW/cm^2 and 400 000 deposited pulses with only one single layer. The writing process was achieved within 33 min for a transverse length

of 500 μm and a periodicity of 7.5 μm. Figure IV-29(b) shows the fluorescence image of the inscribed VBG using the light sheet, where the periodic modification is composed of silver clusters. The white circle shows the creation of double lines due to the thermal effect.

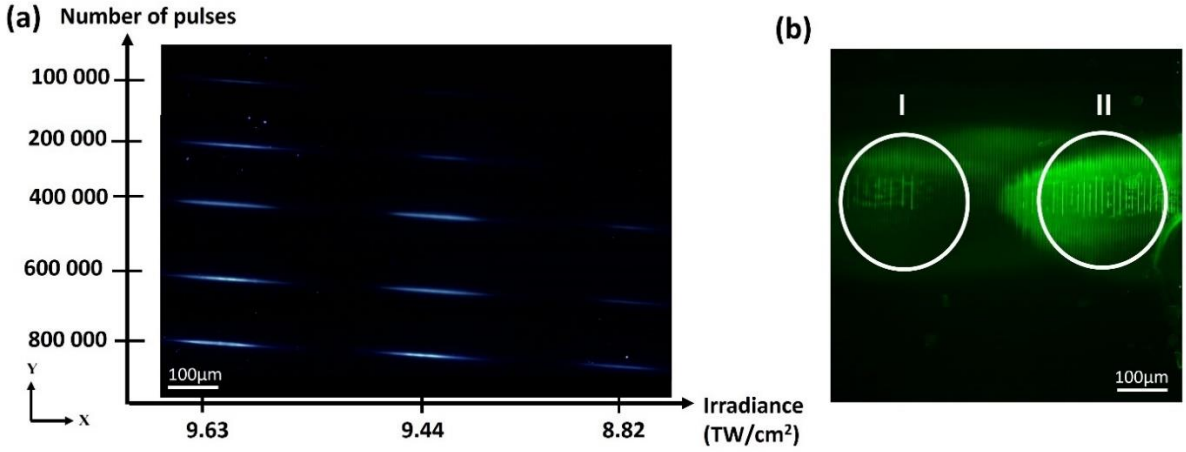

Figure IV-29: (a) Fluorescence images of the written cartography; Writing irradiances are presented along the horizontal axis while the number of pulses appears along the vertical axis. (b) VBG inscribed using the light-sheet method (DLW parameters: irradiance = 9.44 TW/cm² – number of pulses=400 000) where zone I shows the normally written periodicity (Λ=7.5 μm) while zone II presents the area in which the double lines were created.

Furthermore, the angular characterization of this VBG was measured in transmission at 632.8 nm using a He-Ne laser. Figure IV-30 shows the diffraction patterns of the gratings for zones I and II at normal incidence. One can see the appearance of several orders (up to orders ±3) in zone I, as presented in Figure IV-30(a). The first-order diffraction efficiency was about 3.4%, even at normal incidence. Therefore, this grating behaves as a planar-type grating rather than volume type gratings. Planar-type gratings are equivalent to optically thin gratings that exhibit multiple diffracted orders rather than a single diffracted order characteristic of volume-type gratings. Figure IV-30(b) shows the appearance of double orders (those circled in white color) associated with the presence of the double lines in the inscription process in zone II. Further optimizations are required to inscribe relevant VBGs and thus to demonstrate higher efficiencies with Type-A refractive index modifications using the light-sheet method. Although insufficient to achieve efficient VBGs at this stage, these results are the first observation of Type A refractive index change under light-sheet illumination.

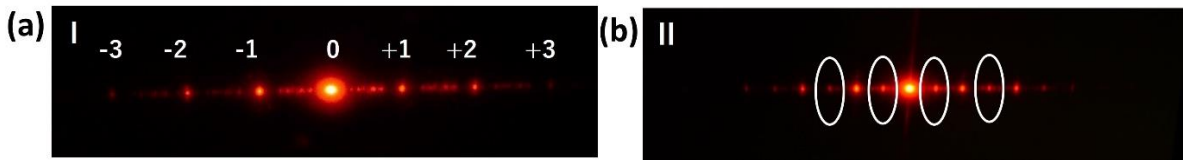

Figure IV-30: Photographs of diffraction orders of He-Ne laser at normal incidence of the grating pattern for (a) zone I and (b) zone II.

IV.9.4. Glass modification and characterization of VBGs using the phase mask technique

This section presents the results of VBGs inscribed using the phase mask technique using the Ti-Saphire laser (1 kHz repetition rate) at the COPL laboratory.

Figure IV-31 shows the two inscribed samples with different laser parameters. Sample 1 has been exposed (from right to left) during 40, 20, 10, and 5 seconds for the same laser irradiance of 4.07 TW/cm^2, corresponding to a writing speed of 6.25, 12.5, 25, and 50 µm/s, respectively. Then, the inscription process was fixed to 1 minute while changing the laser irradiance to 3.44, 4.07, 4.70, and 5.35 TW/cm^2. The produced yellow color inside the glass sample indicates the generation mostly of color centers. Sample 2 has been exposed first to several irradiances below the appearance of filament effect (2.66, 2.94, 3.52, 4.17, 4.74 TW/cm^2) for 30 minutes. However, we were able to see only the yellow color inside the glass sample. Moreover, VBGs were inscribed using a higher irradiance of 4.07 TW/ cm^2 allowing the filament effect to take place. The writing speed, thus the number of deposited pulses, was changed to 4.1, 1.7, 0.83, 0.6, 0.27, and 0.14 µm/s. This corresponds to a recording process duration of 1, 2.5, 5, 7, 15, and 30 minutes, respectively. As shown in Figure IV-31(b), VBGs are written approximately over the whole glass thickness: The VBGs in sample 1 are inscribed intensely and homogeneously along half of the glass thickness while most of the VBGs created in sample 2 seem to be inscribed homogeneously along the full glass thickness.

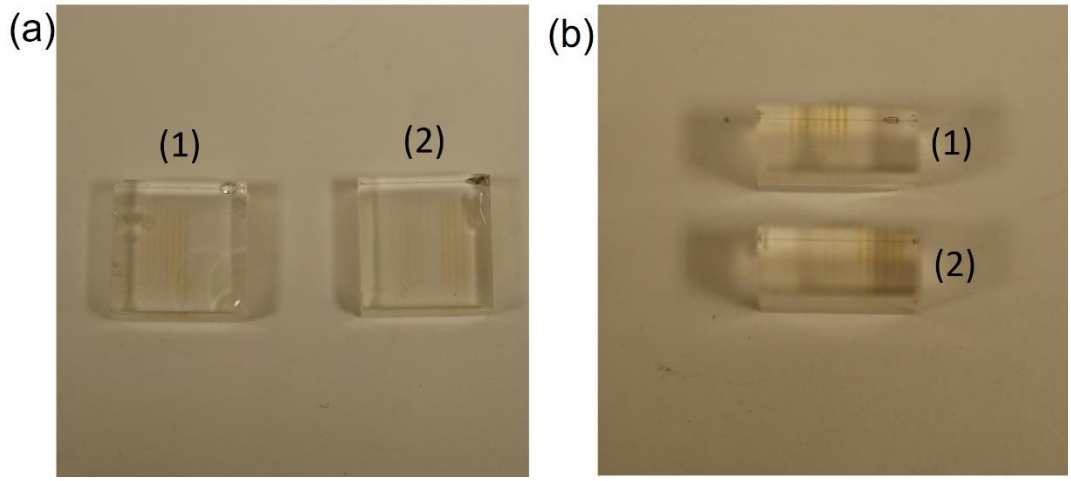

Figure IV-31: (a) Image of the glass samples showing a yellow inscription color indicating the creation of color centers. (b) Side view image of the samples showing modifications along its thickness.

Figure IV-32 shows a fluorescence image of one of the inscribed VBGs with excitation light at 365 nm. It demonstrates the periodic modification produced by the phase mask (Λ_{PM} = 14 µm), corresponding to its half-periodicity ($\Lambda_{Fringes}$ = 7 µm) and represents the traces of fluorescence composed of silver clusters, which is not shown very well here due to the quality of the image.

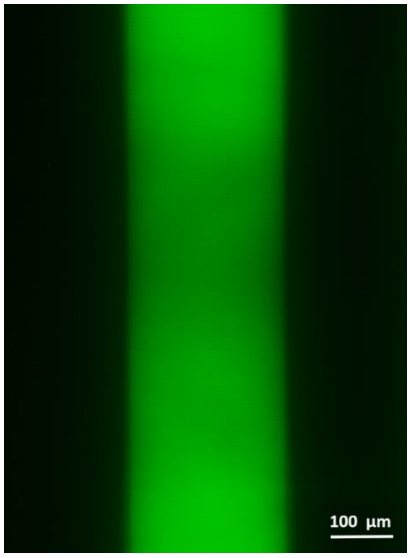

Figure IV-32: Microscopy fluorescence image (excitation at 365 nm) of VBG induced with the phase mask technique with a low repetition rate TiSa laser at 1 kHz (DLW parameters: irradiance = 4.07 TW/cm^2, velocity = 6.25 µm/s corresponding to an inscription time of 40 s for a globally modified volume of ~ 0.125 x 8 x 2 mm^3).

Indeed, using this low repetition rate of 1 kHz, we generate mostly non-stable species namely hole-trap silver species Ag^{2+} in addition to a small number of silver clusters. In fact, the time separating two pulses must be shorter than the lifetime of the intermediate species Ag^0, which stands in the µs scale. The presence of sufficient electron traps Ag^0 from one pulse to another is a necessary step to further allow for the creation of silver clusters, as discussed

in chapter II (sectionII.3.3.b) and as shown in Figure IV-33.

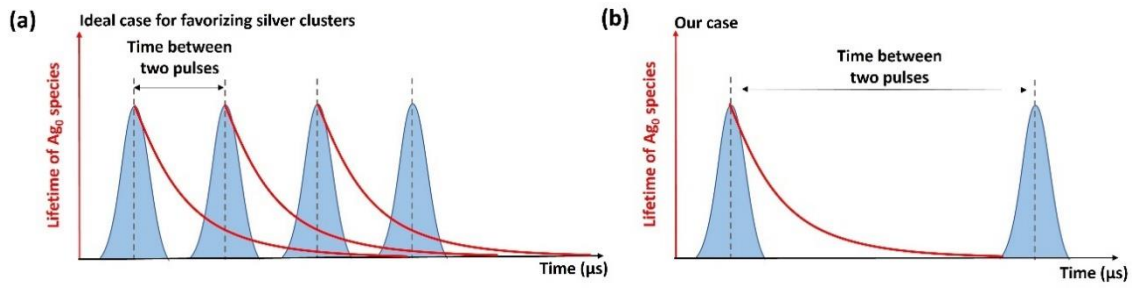

Figure IV-33: Diagram illustrating the decay in the lifetime of Ag^0 species versus the time interval between pulses: (a) an ideal case that promotes the formation of silver clusters, (b) the case observed in our experiment.

In addition, the diffraction efficiencies of the inscribed VBGs were measured in transmission using a TEM_{00} He-Ne laser (632.8 nm wavelength) at the Bragg condition. The gratings exhibit very low diffraction efficiencies. The highest diffraction efficiency was about 0.5% corresponding to the VBG inscribed in 1 minute and for 4.07 TW/ cm^2, which originates from a very low modulation of the refractive index Δn_{AC}. Moreover, the glass sample containing this VBG was heated at 100°C for 30 minutes. Then, we observed that the diffraction efficiency decreases after thermal treatment, indicating that charge compensation and de-trapping processes were at the origin of the canceling of non-stable species (mostly the reduction of the hole traps such as Ag^{2+}) related to the canceling of shallow-trap color centers. The growth of silver species up to metallic nanoparticles showing surface plasmon resonance is completely unlikely as (i) laser irradiation did not even lead to the creation of a significant amount of large silver clusters, and (ii) the post-irradiation thermal treatment is much below the glass transition temperature which prevents any sufficient thermal activation of mobility nor any nucleation/growth process of metallic nanoparticles. It should be noted that the image of this sample (Figure IV-31(b)) is taken after the heat treatment.

IV.10.Conclusion

This chapter presents fs-written Type-A Volume Bragg gratings in silver-containing phosphate glasses, which are fabricated using several techniques.

In the first part of the chapter, VBGs are defined along with some of their applications. In addition, a brief overview of the recording materials used to inscribe VBGs is presented and the state of art of the several fabrication techniques is reported.

In the second part of the chapter, several experimental techniques were presented for the inscribed Type-A VBGs. First, inscribing multi-layer gratings using the Gaussian beam is

discussed. Although the diffraction efficiency is quite low, the measurement demonstrated a significant effective refractive index modification, about a few 10^{-3}. However, the inherent instability problems and lack of nanoscale position accuracy of the inscribed period are critical for the fabrication of higher efficient gratings. To avoid these issues, the VBGs were inscribed with femtosecond Gaussian-Bessel laser pulses with only a single layer. Thus, we report on what we believe to be the first Type-A VBG inscription in a commercial silver-containing glass (AG01®, from Argolight). We demonstrated VBGs reaching high diffraction efficiency up to 95% at 632.8 nm with a period of 2 µm, and a 150 µm effective thickness indicating a $1.78x10^{-3}$ refractive index modulation according to simulations (in great agreement with the experimental data). This approach led to long modification lengths, allowing to speed up the inscription process and optimize the period homogeneity over the grating depth. The spectral characteristics also exhibited good agreement with the numerical simulation. Moreover, our gratings were successfully investigated at 1.55 µm, showing that the refractive index modification remains high enough (with a very moderate spectral normal dispersion) to achieve efficient diffraction in the near-infrared region. Larger wavelengths within the transparency range of the glass appear thus accessible in future experiments. Then, we investigate the formation of the light-sheet beam to attain high throughput inscription process. Experimental angular characterization of the inscribed grating shows that it behaves like a surface grating (namely an optically thin grating) rather than a volume Bragg grating. Finally, another convenient and widespread method was considered to achieve a high period stability, by using a two-beam interference pattern generated by a phase mask. This method demonstrates the need for a higher repetition rate laser (>1 kHz) to promote further the creation of silver clusters. It also confirmed that we can inscribe Type-A-based periodic structures in silver-containing glasses using the phase mask technique. Further optimizations are needed to demonstrate higher diffraction efficiencies with Type-A refractive index modifications using the combination of the light-sheet method and the phase mask approach.
In summary, Table IV-3 illustrates a comparison of results for Type-A Volume Bragg Gratings (VBGs) achieved through various experimental techniques. This table involves parameters such as periodicity, volume of the VBGs, experimental diffraction efficiency, and the throughput of the inscription process.

Table IV-3: A summarized comparison of the characteristics of the most efficient VBGs inscribed using the several experimental techniques.

Technique	Bragg period (µm)	Diffraction efficiency at 632.8 nm (%)	Thickness (µm)	Inscribed surface ($µm^2$)	Inscription time (hours)	Throughput of process (mm^3/h)
Gaussian beam	2	24.7	100 (19 planes)*	500 x 500	6.6	0.0038
Gaussian-Bessel beam	2	~95	150 (1 plane)*	400 x 400	1	0.024

Light sheet	7.5	3.4	900 (1 plane)**	500 x 900	0.55	0.73
Phase mask	7	0.5	~2000 (1 plane)**	125 x 8000	0.012	167

**The mentioned thickness here is the effective one, extracted from the fitting of the experimental diffraction efficiency distribution.*

***The mentioned thickness here is the calculated (theoretical one). In these cases, we couldn't extract an effective thickness since we couldn't obtain an angular diffraction efficiency distribution.*

Indeed, Table IV-3 emphasizes the objective of this work for producing Type-A VBGs using several techniques to demonstrate the direction of progress and the potential achievements to speed up the inscription process and attain high throughput processes together with high efficiencies. Thus, this chapter demonstrates, for the first time, fs-written Type-A VBGs, paving the way for industrial applications.

General conclusion and perspectives

The objective of this research project is to develop innovative optical components by using the benefits obtained through femtosecond inscription in silver-containing glasses.

We demonstrated that femtosecond direct laser writing (DLW) in photosensitive silver-containing glass allows for implementing a 3D fluorescent structure formed by the aggregation of silver ions and silver atoms within the glass volume. In such glasses, the silver ions act as photosensitive agents and trigger an exotic material modification based solely on the silver ion photochemistry. Furthermore, this leads to physical modifications of the material, including changes in refractive index, as well as new physical properties, in particular fluorescence. When translating the writing laser beam, the resulted modification is a positive refractive index change as a result of the formation of silver-chemical bonds. This distinct modification is categorized as Type-A modification, after *Argentum*, and results from the laser-induced photochemistry of silver ions without significantly affecting the glass matrix. Hence, this research considers the investigation of photo-induced silver clusters for two distinct applications.

Chapter III focuses on exploring the potential of silver clusters for X-ray spatially resolved dosimetry. These clusters are created within phosphate glasses containing a high concentration of silver oxide using the femtosecond direct laser writing technique. Then, X-ray irradiation experiments are conducted in order to combine radiophotoluminescence and femtosecond inscription to estimate the potential of those laser-inscribed structures as local probes of the deposited doses. For this study, similar fs-silver clusters have been inscribed inside three glass compositions: ARGO (silver-containing zinc phosphate glass), ARGO3 (silver-containing magnesium-phosphate glass) and GPN2 (silver-containing gallo-sodo-phosphate glass). Moreover, the depth-dependent deposited dose within the glass thickness was evaluated using a Monte Carlo Geant4 simulation. We have explored the production of silver species within the pristine glasses subjected to X-ray irradiation, investigating the development of Ag^{2+} hole traps (color centers) as well as Ag_m^{x+} silver clusters. As a consequence, various optical properties of the glass matrix are influenced. Concerning the ARGO glass sample, these effects include the creation of radiation-induced absorption and emission bands, alongside a minor reduction in the glass's refractive index. Consequently, indirect changes in the spectroscopic properties of the silver clusters following X-ray exposure are primarily attributed to modifications in the surrounding glass environment rather than the direct changes in the silver clusters themselves. These changes in the silver species' glass

environment are, in turn, influenced by the generation of color centers as a consequence of irradiation. Additionally, it is pertinent to highlight the presence of additional X-ray-induced silver clusters in the front surface, depending on the deposited dose, as indicated by the micro-absorption measurements. Also, the stability of the fluorescence lifetime of the irradiated laser-inscribed silver clusters, show their resilience to X-rays in both depths at the considered doses. This series of experiments underscores the robustness of laser-induced silver clusters, that serve as localized indicators of the depth-dependent deposited doses. In the case of the ARGO3 glass sample, we observed a similar behavior to what was described for the ARGO glass sample. However, there are two notable differences after irradiation. Firstly, the lifetime amplitudes exhibit variations compared to their pre-irradiation state, which likely impacts their luminescence properties and leads to an additional decrease in the amplitude of fluorescence. Additionally, the refractive index variation in the inscribed structures on the rear surface remains comparable to the pre-irradiation state, assuming that the surroundings of these structures are not influenced by the received dose at this level. Regarding the GPN2 glass sample, noticeable changes emerge after X-ray irradiation. These changes have been characterized by an augmentation of the fluorescence amplitude and fluorescence lifetime. Our proposition is that irradiation has impacted and partially canceled some non-radiative energy relaxations. This estimation is supported by the observed elevation in the measured fluorescence lifetime, coupled with a concurrent increase in fluorescence amplitude subsequent to irradiation. Additionally, it's worth noting that X-ray irradiation doesn't appear to affect the surrounding matrix of the induced-silver species, thus leaving the refractive index change in this sample unaffected. It's important to highlight that the photo-induced species in the ARG03 and GPN2 glass samples exhibit slightly distinct responses compared to those inscribed in the ARGO glass sample after irradiation. In-depth experiments have revealed that the silver species written in these glasses display lower resilience to X-rays when compared to those in the ARGO glass sample. Moreover, an in-depth analysis of recent findings involving silver-containing sodo-gallophosphate glass GPN1 has been conducted. These findings enable us to estimate depth-dependent profiles of the linear absorption coefficient in absolute values. The assessment of the dosimetry capabilities of the ARGO and GPN1 glass sample was carried out by examining the fluorescence amplitude ratio of bands associated with color centers and/or inscribed silver clusters. In the case of the ARGO3 glass sample, it is more suitable to focus on extracting dosimetry information using amplitude lifetimes. Indeed, with these local probes, it is possible to adapt the dynamic and the linearity range of the detector at differentiated dose ranges, giving the interest of spatially-resolved dosimeter. In particular, GPN demonstrated excellent linearity of its sensing behavior across a dose range of 2–357 Gy. In contrast, the ARGO glass sample exhibited a higher sensitivity to X-ray doses, particularly for doses within the range of below 2 Gy.

On the basis of the results presented, this approach could be further extended to combine laser inscription in photosensitive meter-scale fibers for the purpose of integrated dosimeters showing spatially-distribution sensitivity. By extrapolating the behavior of the ARGOi* glass sample, one may expect an accessible dosimeter response for 0–2 mGy using a 0.55 m long fiber, or even a 20 µGy scale being reached with a 55 m long fiber. Concerning the GPNi*, a fiber of 0.16 m or 160 m length could be considered to show a linear dosimeter behavior in the 2–356 mGy or 2–356 µGy scale, respectively.

These fs-induced silver clusters can also be considered as highly responsive probes, such probes appearing thus for conducting real-time fluorescence or absorption dosimetry within the material. For this purpose, we conducted real-time X-ray irradiation experiments to analyze how femtosecond-written silver clusters react to X-ray exposure, allowing us to monitor dose rates and doses in real-time. Radioluminescence and radiation-induced attenuation investigations were carried out with silver-sustained waveguides, both produced by 1-pass and 5-pass laser inscription, and the outcomes were compared with experiments on the irradiated pristine glass sample. These examinations uncovered that the radioluminescent signals detected were a result of the irradiated glass matrix rather than the silver clusters themselves. Consequently, these inscribed silver patterns exhibit remarkable resilience to X-ray irradiation, on the one hand, but they do not emit radioluminescence, on the other hand. Thus, silver clusters were unfortunately shown to be unsuitable for real-time luminescence dosimetry applications as they do not show fluorescence emission under X-ray excitation. Furthermore, there is no discernible difference in radiation-induced attenuation between the 5-pass and 1-pass waveguides. To draw a reliable conclusion, further optimization is required when comparing the RIA on the fs-inscribed structures with that of the irradiated bulk glass.

Still, preliminary observations suggest the feasibility of obtaining an *in-situ* radiophotoluminescent signal from the inscribed waveguides. However, this outcome was affected by the instability of the UV laser diode and potentially the saturation of the photomultiplier tube. Further refinements and optimizations are necessary to successfully achieve this goal.

Chapter four focuses on the femtosecond laser inscription of Type-A volume Bragg gratings in silver-containing phosphate glasses. A range of experimental techniques for inscribing these volume Bragg gratings are implemented. Initially, we explored the fabrication of multi-layer gratings using Gaussian beams, which, despite yielding relatively low diffraction efficiency, demonstrated a substantial effective refractive index modification of around a few 10^{-3} and a relatively thin grating of 100 µm. However, this process has a throughput of only 0.0038 mm^3/h, presenting inherent issues and lacking the nanoscale positional accuracy required for

precise control of the inscribed period. This precision implies significant challenges, particularly for achieving highly efficient gratings. As an alternative approach to circumvent these challenges, utilizing a Gaussian-Bessel could potentially enhance the fabrication process. This adaptation enabled the creation of thicker structures while simultaneously diminishing the need for stacking numerous layers. Through the utilization of femtosecond Gaussian-Bessel laser pulses and a single-layer plane, we achieved remarkable results. These VBGs exhibited exceptional diffraction efficiency of up to 95% at 632.8 nm, with a period of 2 µm and an effective thickness of 150 µm, resulting in a refractive index modulation of $1.78x10^{-3}$. Importantly, this approach enabled the creation of VBGs with long modification lengths while enhancing period homogeneity throughout the grating depth, achieving a throughput of 0.024 mm^3/h. The use of the Gaussian-Bessel approach led thus to a six-fold improvement of the laser processing throughput. Our findings also showcased diffraction efficiency at 1.55 µm in the near-infrared region, with minimal spectral dispersion of the high refractive index modification. In pursuit of optimizing the inscription process, we explored the formation of a light-sheet beam for enhanced throughput up to 0.73 mm^3/h, which corresponds thus to a very significant additional thirty-fold improvement of the laser processing throughput compared to the Gaussian-Bessel approach. Further optimizations are needed in this experiment which revealed that the inscribed grating behaved as an optically thin surface grating, rather than a volume Bragg grating. Additionally, we investigated an alternative method using the phase mask approach and achieving a high throughput of 167 mm^3/h. This approach highlighted the importance of a higher repetition rate laser (>1 kHz) to facilitate the creation of silver clusters and reaffirmed the feasibility of inscribing Type-A-based periodic structures in silver-containing phosphate glasses using the phase mask technique. However, higher repetition rates thus require higher average laser powers. In conclusion, this chapter marks a significant innovation in the field of volume Bragg gratings by showcasing the direction of progress and the potential achievements in speeding up the inscription process and attaining high-throughput capabilities. We have successfully demonstrated the creation of the first Type-A VBGs, opening access to various industrial applications. Furthermore, the potential for extending these gratings to larger wavelengths within the glass transparency range requires longer grating, which promises exciting prospects for future experiments.

In the future, inscribing these Type A–based periodic structures in the recently synthesized silver-doped gallo-germanate glasses exhibiting enhanced transmission into the mid-infrared (MIR) range offers new insights and advantages for the fabrication of VBGs into the MIR range. The most efficient grating using the Gaussian-Bessel was recorded in ~1 hour at a writing speed of 20 $\mu m/s$. Also, switching to a higher repetition rate with faster velocities is very promising for high throughput. Furthermore, using the multi-scan approach would increase the refractive index modification of the inscribed VBGs. In addition, recent lasers

with higher repetition rates (up to the GHz regime) in burst mode and higher average power (in the order of 50-100 W) would still allow for reaching the Type-A-modification irradiance threshold while shortening the VBGs' writing time by delivering the needed multi-pulse energy deposition to inscribe efficient VBGs. As previously discussed, it is evident that further optimization efforts are necessary, particularly concerning the phase mask approach, to achieve the desired level of effectiveness in volume Bragg gratings.

Conclusion générale et perspectives

L'objectif de ce projet de recherche est de développer des composants optiques innovants en utilisant les avantages obtenus grâce à l'inscription femtoseconde dans des verres contenant de l'argent.

Nous avons démontré que l'écriture laser directe femtoseconde dans un verre photosensible contenant de l'argent permet de créer une structure fluorescente en 3D formée par l'agrégation d'ions d'argent et d'atomes d'argent à l'intérieur du volume du verre. Dans de tels verres, les ions d'argent agissent comme des agents photosensibles et déclenchent une modification du matériau exotique basée uniquement sur la photochimie des ions d'argent. De plus, cela entraîne des modifications physiques du matériau, notamment des changements d'indice de réfraction, ainsi que de nouvelles propriétés physiques, en particulier la fluorescence. Lors de la translation du faisceau laser d'écriture, la modification résultante est un changement d'indice de réfraction positif résultant de la formation de liaisons chimiques argentées. Cette modification distincte est catégorisée comme une modification de Type-A, d'après Argentum, et résulte de la photochimie des ions d'argent induite par le laser sans affecter significativement la matrice vitreuse. Par conséquent, cette recherche se penche sur l'étude des agrégats d'argent photo-induits pour deux applications distinctes.

Le chapitre III se concentre sur l'exploration du potentiel des agrégats d'argent pour la dosimétrie des rayons X résolue spatialement. Ces agrégats sont créés dans des verres de phosphate contenant une concentration élevée d'oxyde d'argent à l'aide de la technique d'écriture laser directe femtoseconde. Ensuite, des expériences d'irradiation par des rayons X sont menées afin de combiner la radiophotoluminescence et l'inscription femtoseconde pour estimer le potentiel de ces structures inscrites au laser en tant que sondes locales des doses déposées. Pour cette étude, des agrégats d'argent similaires ont été inscrits dans trois compositions de verre : ARGO (verre de phosphate de zinc contenant de l'argent), ARGO3 (verre de phosphate de magnésium contenant de l'argent) et GPN2 (verre de gallium-sodium-phosphate contenant de l'argent). De plus, la dose déposée à l'intérieur de l'épaisseur du verre a été évaluée en fonction de la profondeur à l'aide d'une simulation Monte-Carlo Geant4. Nous avons exploré la production d'espèces d'argent au sein des verres non-inscrits soumis à une irradiation aux rayons X, étudiant le développement de pièges à trous Ag^{2+} (centres colorés) ainsi que des clusters d'argent Ag_m^{x+}. Par consequent à l'irradiation, diverses propriétés optiques de la matrice du verre sont influencées par les rayons X. Concernant l'échantillon de verre ARGO, ces effets comprennent la création de

bandes d'absorption et d'émission induites par le rayonnement, ainsi qu'une légère réduction de l'indice de réfraction du verre. Par conséquent, les changements indirects dans les propriétés spectroscopiques des agrégats d'argent après l'exposition aux rayons X sont principalement attribués à des modifications de l'environnement du verre plutôt qu'à des changements directs des agrégats d'argent eux-mêmes. Ces changements dans l'environnement des espèces d'argent sont, à leur tour, influencés par la génération de centres colorés suite à l'irradiation. De plus, il convient de souligner la présence d'agrégats d'argent induits par les rayons X supplémentaires en surface avant, en fonction de la dose déposée, comme l'indiquent les mesures de micro-absorption. En outre, la stabilité de la durée de vie de fluorescence des clusters d'argent inscrits au laser irradiés montre leur résilience aux rayons X à toutes les doses considérées, quelle que soit la profondeur. Cette série d'expériences souligne la robustesse des agrégats d'argent induits par le laser, qui servent d'indicateurs localisés des doses déposées en fonction de la profondeur. Dans le cas de l'échantillon de verre ARGO3, nous avons observé un comportement similaire à celui décrit pour l'échantillon de verre ARGO. Cependant, deux différences notables sont apparues après l'irradiation. Premièrement, les amplitudes de durée de vie présentent des variations par rapport à leur état pré-irradiation, ce qui impacte probablement leurs propriétés de luminescence et entraîne une diminution supplémentaire de l'amplitude de fluorescence. De plus, la variation de l'indice de réfraction dans les structures inscrites dans la face arrière reste comparable à l'état avant irradiation, ce qui propose que l'environnement de ces structures qui ne sont pas influencés par la dose reçue à ce niveau. En ce qui concerne l'échantillon de verre GPN2, des changements notables sont apparus après l'irradiation aux rayons X. Ces changements ont été caractérisés par une augmentation de l'amplitude de fluorescence et de la durée de vie de fluorescence. Notre proposition est que l'irradiation a impacté et partiellement annulé certaines relaxations d'énergie non radiatives. Cette estimation est corroborée par les observations vues suite à l'irradiation. De plus, il convient de noter que l'irradiation aux rayons X ne semble pas affecter la matrice environnante des espèces d'argent induites, laissant ainsi inchangée la variation de l'indice de réfraction dans cet échantillon. Il est important de souligner que les espèces photo-induites dans les échantillons de verre ARG03 et GPN2 présentent des réponses légèrement différentes par rapport à celles inscrites dans l'échantillon de verre ARGO après irradiation. Des expériences approfondies ont révélé que les espèces d'argent inscrites dans ces verres présentent une résistance plus faible aux rayons X par rapport à celles de l'échantillon de verre ARGO. De plus, une analyse approfondie des résultats récents concernant le verre de sodo-gallophosphate contenant de l'argent GPN1 a été réalisée. Ces résultats nous permettent d'estimer les profils dépendant de la profondeur du coefficient d'absorption linéaire en valeurs absolues. L'évaluation des capacités de dosimétrie de l'échantillon de verre ARGO et GPN1 a été réalisée en examinant le rapport d'amplitude de fluorescence des bandes associées aux centres colorés et/ou aux agrégats d'argent inscrits. Dans le cas de l'échantillon de verre

ARGO3, il est plus approprié de se concentrer sur l'extraction d'informations de dosimétrie en utilisant les durées de vie d'amplitude. En effet, avec ces sondes locales, il est possible d'adapter la dynamique et la plage de linéarité du détecteur à des gammes de doses différenciées, compte tenu de l'intérêt de la dosimétrie spatialement résolue. En particulier, GPN a démontré une excellente linéarité de son comportement de détection sur une plage de doses de 2 à 357 Gy. En revanche, l'échantillon de verre ARGO a montré une sensibilité plus élevée aux doses de rayons X, en particulier pour les doses inférieures à 2 Gy.

Sur la base des résultats présentés, cette approche pourrait être étendue pour combiner l'inscription laser dans des fibres photosensibles à l'échelle du mètre dans le but de créer des dosimètres intégrés présentant une sensibilité spatialement distribuée. En extrapolant le comportement de l'échantillon de verre ARGOi*, on peut s'attendre à une réponse de dosimètre accessible pour 0 à 2 mGy à l'aide d'une fibre longue de 0.55 m, voire à atteindre une échelle de 20 µGy avec une fibre longue de 55 m. En ce qui concerne le GPNi*, une fibre de 0.16 m ou de 160 m de longueur pourrait être considérée pour montrer un comportement linéaire de dosimètre dans la plage de 2 à 356 mGy ou de 2 à 356 µGy, respectivement.

Ces agrégats d'argent induits par impulsion laser femtosecondes peuvent également être considérés comme des sondes en temps réel basées sur la fluorescence ou l'absorption à l'intérieur du matériau. Pour ce contexte, nous avons mené des expériences d'irradiation sous rayons X pour analyser la réaction des agrégats d'argent inscrits au laser femtoseconde, ce qui doit permettre de suivre les débits de dose et les doses en temps réel. Des investigations de radioluminescence et d'atténuation induite par le rayonnement ont été réalisées avec des guides d'onde enterrées contenant des agrégats d’argent, produits à la fois par inscription laser à 1 passage et 5 passages, et les résultats ont été comparés à des expériences sur l'échantillon de verre irradié non-inscrit. Ces examens ont révélé que les signaux de radioluminescence détectés étaient le résultat de la matrice vitreuse irradiée plutôt que des agrégats d'argent eux-mêmes. Par conséquent, ces motifs d'argent inscrits se sont révélés remarquablement résistants aux rayons X d'une part, mais ils n'émettent pas de radioluminescence d'autre part. Ainsi, les agrégats d'argent se sont malheureusement révélés inadaptés aux applications de dosimétrie par luminescence en temps réel, car ils n'émettent pas de fluorescence sous excitation aux rayons X. De plus, il n'y a pas de différence discernable dans l'atténuation induite par le rayonnement entre les guides d'onde à 5 passes et à 1 passage. Pour parvenir à une conclusion fiable, une optimisation supplémentaire est nécessaire lors de la comparaison de l'atténuation induite par le rayonnement sur les structures inscrites au laser femtoseconde avec celle du verre vierge irradié.

Néanmoins, les observations préliminaires suggèrent l’obtention possible d’un signal radiophotoluminescent in situ à partir des guides d'onde inscrits. Cependant, ce résultat a été

affecté par l'instabilité de la diode laser UV et potentiellement par la saturation du tube photomultiplicateur. Des raffinements et des optimisations supplémentaires sont nécessaires pour atteindre avec succès cet objectif.

Le chapitre quatre se concentre sur l'inscription laser femtoseconde des réseaux de Bragg volumique de Type-A dans des verres phosphates contenant de l'argent. Une gamme de techniques expérimentales pour inscrire ces réseaux de Bragg volumique est mise en œuvre. Initialement, nous avons exploré la fabrication de réseaux multicouches à l'aide de faisceaux Gaussiens, qui, malgré une efficacité de diffraction relativement faible, ont démontré une modification efficace de l'indice de réfraction d'environ quelques 10^{-3} et un réseau relativement mince de 100 µm. Cependant, ce processus présente un débit de fabrication seulement 0.0038 mm^3/h, présentant des problèmes inhérents et ne disposant pas de la précision de positionnement nanométrique requise pour un contrôle précis de la période inscrite. Cette précision implique des défis importants, en particulier pour la réalisation de réseaux très efficaces. Comme alternative pour contourner ces défis, l'utilisation d'un faisceau Gaussien-Bessel pourrait potentiellement améliorer le processus de fabrication. Cette adaptation a permis la création de structures plus épaisses tout en réduisant simultanément le besoin d'empiler de nombreuses couches. En utilisant des impulsions laser femtoseconde Gaussiennes-Bessel et une seule couche plane, nous avons obtenu des résultats remarquables. Ces réseaux de Bragg ont présenté une efficacité de diffraction exceptionnelle allant jusqu'à 95 % à 632.8 nm, avec une période de 2 µm et une épaisseur effective de 150 µm, résultant en une modulation de l'indice de réfraction de $1,78x10^{-3}$. Cette approche a permis la création des réseaux de Bragg volumiques avec de grandes longueurs de modification tout en améliorant l'homogénéité de la période dans toute la profondeur du réseau, atteignant un débit de 0.016 mm^3/h. L'utilisation de l'approche Gaussienne-Bessel a ainsi permis une amélioration du traitement laser de quatre fois. Nos résultats ont également montré une efficacité de diffraction à 1.55 µm dans la région du proche infrarouge, avec une dispersion spectrale minimale de la modification de l'indice de réfraction élevée. Dans le but d'optimiser le processus d'inscription, nous avons exploré la formation d'un faisceau en forme de feuillet de lumière pour un débit amélioré allant jusqu'à 0.81 mm^3/h, correspondant ainsi à une amélioration supplémentaire très significative de cinquante fois du débit de traitement laser par rapport à l'approche Gaussienne-Bessel. Des optimisations supplémentaires sont nécessaires dans cette expérience qui a révélé que le réseau inscrit se comportait comme un réseau de surface optiquement mince, plutôt que comme un réseau de Bragg de volume. De plus, nous avons exploré une méthode alternative en utilisant l'approche du masque de phase et en obtenant un débit élevé de 125 mm^3/h. Cette approche a souligné l'importance d'une plus grande fréquence de répétition laser (> 1 kHz) pour faciliter la création de clusters d'argent et a confirmé la faisabilité d'inscrire des structures périodiques basées sur le Type-A dans des verres de phosphate contenant de l'argent en utilisant la technique du masque de

phase. Cependant, des fréquences de répétition plus élevées nécessitent des puissances laser moyennes plus élevées. En conclusion, ce chapitre marque une innovation significative dans le domaine des réseaux de Bragg volumique en présentant la direction du progrès et les réalisations potentielles pour accélérer le processus d'inscription et atteindre des capacités de traitement à haut débit. Nous avons réussi à créer les premiers réseaux de Bragg de volume de Type-A, ouvrant ainsi l'accès à diverses applications industrielles. De plus, la possibilité d'étendre ces réseaux à des longueurs d'onde plus grandes dans la plage de transparence du verre ouvre de nouvelles perspectives pour les expériences futures.

Dans le futur, l'inscription de ces structures périodiques basées sur le Type A dans les verres de gallium-germanate récemment synthétisés dopés à l'argent, présentant une transmission améliorée dans la plage du moyen infrarouge (MIR), offre de nouvelles perspectives et avantages pour la fabrication de réseaux de Bragg de volume dans la plage MIR. Le réseau le plus efficace utilisant le faisceau Gaussien-Bessel a été enregistré en ~1 heure à une vitesse d'écriture de 20 µm/s. De plus, le passage à une fréquence de répétition plus élevée avec des vitesses plus rapides est très prometteur pour un débit élevé. De plus, l'utilisation de l'approche multi-passage augmenterait la modification de l'indice de réfraction des VBG inscrits. En outre, les lasers récents avec des fréquences de répétition plus élevées (jusqu'à la gamme des GHz) en mode burst et une puissance moyenne plus élevée (de l'ordre de 50-100 W) permettraient toujours d'atteindre le seuil d'irradiance de modification de Type-A tout en raccourcissant le temps d'écriture des VBG pour inscrire des VBG efficaces. Comme discuté précédemment, il est évident que des efforts d'optimisation supplémentaires sont nécessaires, en particulier en ce qui concerne l'approche du masque de phase, pour atteindre le niveau d’efficacité souhaité dans les réseaux de Bragg de volume.

Appendix

A. Theory of guided optics

In this section, we present a small overview of the waveguiding theory, as they will be crucial for comprehending the subjects discussed in Chapter III.

Figure A-1 depicts a planar dielectric waveguide situated within a medium with a lower refractive index. When light travels from one medium to another with different refractive indices, n_1 and n_2, with $n_2 < n_1$ there is a critical angle of incidence determined using the snell law as:

$$\bar{\theta_c} = cos^{-1}\left(\frac{n_2}{n_1}\right) \qquad \text{A-1}$$

if $\theta < \bar{\theta_c}$, the light is reflected back into the first medium: thus the light propagates inside the waveguide by the Total Internal Reflection (TIR) principle.
The waveguide consists of two parts: the core and the cladding. Light travels within the core of the waveguide, at various angles θ with respect to the z-axis, as illustrated in Figure A-1, following many multiple internal reflections.

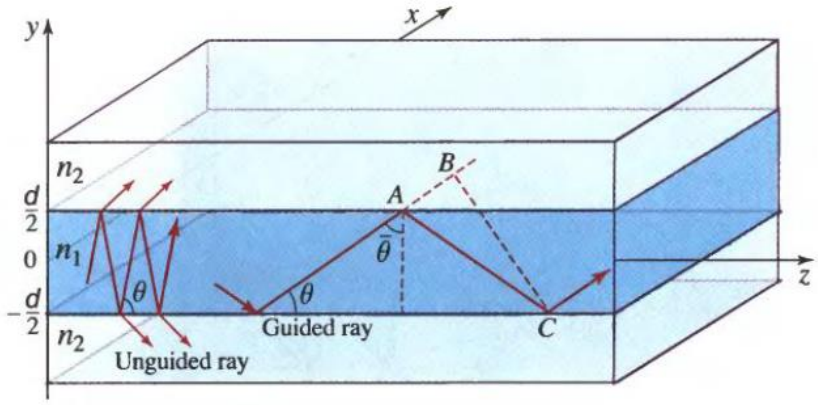

Figure A-1: Schematic representation of guided and unguided rays in a planar dielectric waveguide. Taken from [332]

Light propagates within the waveguide in the form of modes, which can be characterized using the self-consistency condition. These modes maintain a consistent transverse spatial distribution and polarization throughout their passage along the waveguide's propagation axis. The self-consistency condition serves to determine both the quantity of propagating modes within a waveguide and the angles of propagation for these modes, especially in the case of multimode waveguides. While this manuscript does not delve into further details on

this topic, interested readers are encouraged to refer to chapter 8 of the following reference [332] for a more comprehensive understanding.

Optical fibers, known as 3D dielectric waveguiding structures, are capable of transporting light over remarkable distances. The guiding mechanism in dielectric waveguide fibers is primarily based on total internal reflection (TIR), as illustrated in Figure A-1. To be guided within the fiber or waveguide, an incident light beam must have an angle θ with respect to the fiber axis that is smaller than $\overline{\theta_c}$. The difference in the refractive index between the core and the cladding is sufficient to confine light within the core. The difference in the refractive index between the core and the cladding defines the Numerical Aperture (N.A.) of the fiber. N.A. describes the acceptance cone of the fiber, representing the range of angles at which incoming light will experience total internal reflection within the core, thus allowing it to propagate along the entire length of the fiber. The formula for N.A. is as follows:

$$N.A. = sin\theta_\alpha = \sqrt{n_{core}^2 - n_{cladding}^2} \quad \text{A-2}$$

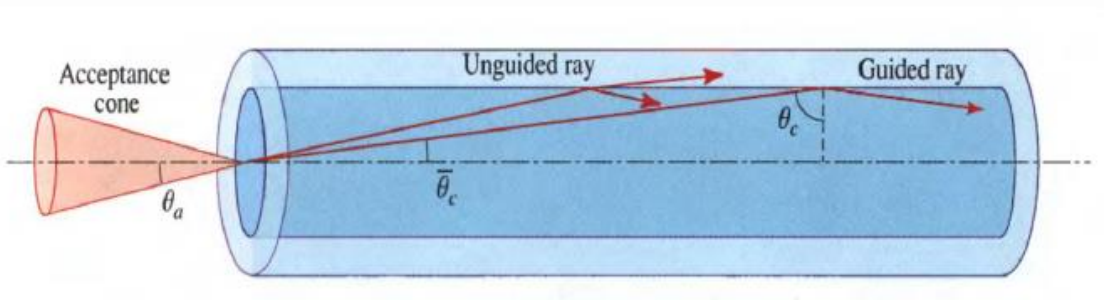

Figure A-2: Schematic representation of an optical fiber with rays within the acceptance cone (defining by the NA) being guided within the fiber by total internal reflection. Taken from [332].

In that case, the fiber is characterized by a characteristic equation expressed using Bessel functions instead of a self-consistency equation. For more details, the reader is invited to read chapter 9 of the following reference [332].

To establish the number of modes propagating within the waveguide (in the case of a circular one), the parameter 'V' is employed to distinguish between single-mode and multimode behavior of the waveguide or fiber at a specific wavelength. This determination is made as follows:

$$V = 2\pi \frac{a}{\lambda} NA \quad \text{A-3}$$

where a is the dimension of the waveguide. Single-mode waveguides or fibers exist in the region where 'V' is less than 2.405. Beyond this threshold, waveguides or fibers exhibit a multimode behavior [28], allowing for the propagation of numerous modes in addition to the fundamental mode.

B. Calculation of the estimated depth-dependent profiles in absolute values of the linear absorption coefficient at 405 nm

From Figure III-17(a), a differential equation of the intensity is used, having a depth-dependent linear absorption coefficient.

$$\frac{\Delta I}{\Delta Z} = -\alpha_{estimated}(z)I(z) \quad \text{B-1}$$

where $\alpha_{estimated}(z)$ is the estimated depth-dependent absorption coefficient at 405 nm.

$$\alpha_{estimated}(z) = cA(z) \quad \text{B-2}$$

where $A(z)$ is the amplitude of the local absorption coefficient profile proportional to the fluorescence intensity profile (Figure III-17(a)) using an exponential fitting equation and c is a proportionality constant.

The proportionality constant c is adjusted by hand in order to have the same value between the effective absorption coefficient measured thanks to the UV/VIS transmission spectroscopy of the irradiated sample at 405 nm (Figure III-16(a)) and the calculated one by integration of Equation (B-1). The calculated effective absorption coefficient is given by:

$$\alpha_{effective,calculated} = \frac{-1}{L}\ln\left(\frac{I(z)}{I(0)}\right) \quad \text{B-3}$$

where $I(0)$ and $I(z)$ is the result (from Equation B-1) of the integrated equation for the initial intensity and for that at a corresponding depth, respectively; L is the thickness of the glass sample (1 mm).

Once c is adjusted, Equation (B-3) allows to trace the estimated depth-dependent profiles of the linear absorption coefficient at 405 nm, as shown in Figure III-18.

C. Calculation of the local differential linear absorption coefficient

From Lambert–Beer equation, the intensity of the excitation source is given by:

$$I_1(\lambda) = I_0(\lambda)e^{-\alpha(\lambda)H} \quad \text{C-1}$$

where $I_0(\lambda)$ is the initial intensity of the incident laser beam corresponding to the experimental wavelength sampling, H is the thickness of the laser-modified area that contains the silver clusters (given in cm), $\alpha(\lambda)$ is the local differential linear absorption coefficient (given in cm^{-1}).

The local differential linear absorption coefficient $\alpha(\lambda)$ is thus calculated using equation:

$$\alpha(\lambda) = \frac{-1}{H} \ln\left(\frac{I_1(\lambda)}{I_0(\lambda)}\right) \qquad \text{C-2}$$

where the intensities are calculated using the transmitted power as follows:

$P_R = SI_0$ is the reference transmitted power and $P_A = S_A I_1 + \overline{S_A} I_0$ is the absorbed transmitted power, where S is the total surface of the scanning beam; at the laser-inscribed structures, one can separate this scanning beam as $S = S_a + \overline{S_a}$ with S_a the absorbing surface of the laser-inscribed structure and $\overline{S_a}$ the complementary non-absorbing surface of these structures.

This calculation takes into account the filling rate of the inscribed structure. Each laser pass is characterized by two lines, each having a thickness of approximately 400 nm, which corresponds to the absorbing surface. The interline between each laser pass for our structures is 5 µm. Thus, the filling rate of the structures is the fraction between the absorbed and the total surface for each laser passage, equal to $\tau = \frac{0.8}{5} = 0.16$. Using the oscilloscope, the power is measured in voltage in direct and alternative current. The alternative current, AC, is the comparison between two modulated signals: a scan between an inscribed zone and a non-inscribed zone compared to that in a non-inscribed zone. The reference and attenuated powers are respectively calculated by $P_R = DC + \frac{AC}{2}$ and $P_A = DC - \frac{AC}{2}$.

List of communications

Scientific papers:

- **Femtosecond Direct Laser Writing of Silver Clusters in Phosphate Glasses for X-ray Spatially-Resolved Dosimetry**
  J. Harb, T. Guérineau, A. Morana, A. Meyer, G. Raffy, A. Del Guerzo, Y. Ouerdane, A. Boukenter, S. Girard, T. Cardinal, Y. Petit, L. Canioni.
  Chemosensors 2022, 10, 110. DOI: 10.3390/chemosensors10030110

- **Demonstration of Type-A Volume Bragg Gratings inscribed with a femtosecond Gaussian-Bessel laser beam**
  J. Harb, L. Talbot, Y. Petit, M. Bernier, L. Canioni.
  Optics Express, 2023, 31, 10, DOI: 10.1364/OE.483722

- **Three-dimensional laser creation of near-IR laser-gain medium based on hydride donor/acceptor complexes made of coupled laser-induced silver clusters with Ytterbium ions**
  F. Alassani, G. Raffy, M. Carpentier, J. Harb, V. Jubera, A. Del Guerzo, L. Canioni, T. Cardinal, Y. Petit.
  Ongoing progress

International conferences:

- **Direct Laser Writing in Photosensitive Glasses: Application to Optical Systems for the Creation of High-Sensitivity Dosimeters**
  J. Harb, Petit. Y, T. Guérineau, T. Cardinal, L. Canioni.
  OPAL' 2021, The 4TH International Conference on Optics, Photonics, and Laser
  Corfu, Greece - October 2022 - ***Oral***

- **Inscription laser femtoseconde d'agrégats d'argents dans des verres de phosphate : Application à la dosimétrie résolue spatialement des rayons X**
  J. Harb, T. Guérineau, A. Morana, A. Meyer, G. Raffy, A. Del Guerzo, Y. Ouerdane, A. Boukenter, S. Girard, T. Cardinal, Y. Petit, L. Canioni.
  89e Congrès de l'Acfas, 619-Le verre Reflet de société, fenêtre sur les sociétés technologiques
  Québec, Canada - May 2022 – ***Online Oral***

- **3D localization beyond diffraction limit of near-IR emission excited by resonant energy transfers from silver clusters in phosphate glasses**
  F. Alassani, G. Galleani, G. Raffy, J. Harb, ASS. de Camargo, V. Jubera, L. Canioni, T. Cardinal, Y. Petit.
  International Conference on Physics of Non-Crystalline Solids
  University of Kent, July 2022 – ***Oral***

- **First demonstration of Type-A Volume Bragg Gratings for VIS-NIR applications**
  J. Harb, L. Talbot, Y. Petit, M. Bernier, L. Canioni.
  SPIE - Photonics West
  *San Francisco, California, USA, January –February 2023 -**Oral***

- **Femtosecond laser writing of multi-scale architecture and optical functionalities in photosensitive glass**
  Y. Petit, J. Harb, Loi. L, L. Talbot, M. Bernier, T. Cardinal, L. Canioni.
  Progress in Ultrafast Laser Modifications of Materials
  *Nikko, Japan – June 2023 - **Oral***

- **First Demonstration of Type-A Femtosecond-Written Volume Bragg Gratings using a Gaussian-Bessel Laser Beam.**
  J. Harb, L. Talbot, Y. Petit, M. Bernier, L. Canioni.
  CLEO EUROPE – EQEC 2023: Conference on Lasers and Electro-optics/Europe- European Quantum Electronics Virtual Conferences
  *Munich,Germany - June 2023 – **Oral***

- **Femtosecond Inscription of Type-A Volume Bragg Gratings in Silver-Containing Phosphate Glasses**
  J. Harb, L. Talbot, Y. Petit, M. Bernier, L. Canioni.
  CLEO EUROPE – EQEC 2023: Conference on Lasers and Electro-optics/Europe- European Quantum Electronics Virtual Conferences
  *Munich,Germany - June 2023 – **Poster***

References

[1] "Optical Manufacturing: Femtosecond-laser direct-written waveguides produce quantum circuits in glass," Laser Focus World. Accessed: Oct. 08, 2023. [Online]. Available: https://www.laserfocusworld.com/lasers-sources/article/16550196/optical-manufacturing-femtosecondlaser-directwritten-waveguides-produce-quantum-circuits-in-glass

[2] H. Roggendorf, "J. Zarzycki (Ed.): Glasses and Amorphous Materials, Vol. 9 of Materials Science and Technology, (Eds. R. W. Cahn, P. Haasen, E. J. Kramer) VCH, Weinheim, 1991, hardcover, DM 430.– (DM 360.- subscription price), 797 pp., ISBN 3–527–26822–7," *Advanced Materials*, vol. 4, no. 3, pp. 246–246, 1992, doi: 10.1002/adma.19920040321.

[3] S. R. Elliott, *Physics of amorphous materials*, 2nd ed. Harlow, Essex, England: Longman Scientific & Technical, 1990.

[4] A. K. Varshneya, *Fundamentals of inorganic glasses: Arun K. Varshneya*. Boston: Academic Press, 1994.

[5] U. Schubert, "Introduction to glass science and technology. Von J. E. Shelby. Royal Society of Chemistry, Cambridge, 1997. 244 S., Broschur, 18.95 £.—ISBN 0-85404-533-3," *Angewandte Chemie*, vol. 109, no. 22, pp. 2637–2637, 1997, doi: 10.1002/ange.19971092243.

[6] A. B. Sabiha, A. Kheloufi, N. Boutarek, and K. Fouad, "Valorization of Algerian Sand for Photovoltaic Application," *Acta Physica Polonica A*, vol. 130, pp. 133–137, Jul. 2016, doi: 10.12693/APhysPolA.130.133.

[7] P. G. Debenedetti, *Metastable Liquids: Concepts and Principles*. Princeton University Press, 1996.

[8] W. H. Zachariasen, "THE ATOMIC ARRANGEMENT IN GLASS," *J. Am. Chem. Soc.*, vol. 54, no. 10, pp. 3841–3851, Oct. 1932, doi: 10.1021/ja01349a006.

[9] V. M. Goldschmidt, "Die Gesetze der Krystallochemie," *Naturwissenschaften*, vol. 14, no. 21, pp. 477–485, May 1926, doi: 10.1007/BF01507527.

[10] A. Smekal and W. Klemm, "Mechanische Messung chemischer Bindefestigkeiten," *Monatshefte für Chemie*, vol. 82, no. 3, pp. 411–421, May 1951, doi: 10.1007/BF00900835.

[11] K.-H. Sun, "Fundamental Condition of Glass Formation*," *Journal of the American Ceramic Society*, vol. 30, no. 9, pp. 277–281, 1947, doi: 10.1111/j.1151-2916.1947.tb19654.x.

[12] J. E. Shelby, *Introduction to Glass Science and Technology, 3rd Edition*. Royal Society of Chemistry, 2020.

[13] T. Guerineau, "Synthèse et caractérisation de verres pour l'impression 3D par laser : verres phosphates et d'oxydes lourds à l'argent," phdthesis, Université de Bordeaux, 2020. Accessed: Sep. 05, 2023. [Online]. Available: https://theses.hal.science/tel-03311678

[14] L. Francis, "Melt Processes," 2016, pp. 105–249. doi: 10.1016/B978-0-12-385132-1.00003-3.

[15] J. D. Musgraves, J. Hu, and L. Calvez, *Springer handbook of glass*, no. Part A. Springer, 2019.

[16] J. A. Savage and S. Nielsen, "Chalcogenide glasses transmitting in the infrared between 1 and 20 μ — a state of the art review," *Infrared Physics*, vol. 5, no. 4, pp. 195–204, Dec. 1965, doi: 10.1016/0020-0891(65)90023-0.

[17] B. Karasu, T. Idinak, E. ERKOL, and A. Yanar, "Chalcogenide Glasses," *El-Cezeri Fen ve Mühendislik Dergisi*, vol. 6, pp. 428–457, Sep. 2019, doi: 10.31202/ecjse.547060.

[18] J.-L. Adam and B. Boulard, "Verres - Propriétés et applications," *Optique Photonique*, Apr. 2018, doi: 10.51257/a-v2-af3601.

[19] L. Bressel *et al.*, "Femtosecond laser induced density changes in GeO_2 and SiO_2 glasses: fictive temperature effect [Invited]," *Opt. Mater. Express, OME*, vol. 1, no. 4, pp. 605–613, Aug. 2011, doi: 10.1364/OME.1.000605.

[20] T. H. Maiman, "Stimulated Optical Emission in Fluorescent Solids. I. Theoretical

Considerations," *Phys. Rev.*, vol. 123, no. 4, pp. 1145–1150, Aug. 1961, doi: 10.1103/PhysRev.123.1145.
[21] M. G. Littman and H. J. Metcalf, "Spectrally narrow pulsed dye laser without beam expander," *Appl. Opt., AO*, vol. 17, no. 14, pp. 2224–2227, Jul. 1978, doi: 10.1364/AO.17.002224.
[22] R. N. Hall, G. E. Fenner, J. D. Kingsley, T. J. Soltys, and R. O. Carlson, "Coherent Light Emission From GaAs Junctions," *Phys. Rev. Lett.*, vol. 9, no. 9, pp. 366–368, Nov. 1962, doi: 10.1103/PhysRevLett.9.366.
[23] "Ultra-violet Gas Laser at Room Temperature | Nature." Accessed: Aug. 21, 2023. [Online]. Available: https://www.nature.com/articles/200667a0
[24] V. Fortin, M. Bernier, J. Carrier, and R. Vallée, "Fluoride glass Raman fiber laser at 2185 nm," *Opt. Lett., OL*, vol. 36, no. 21, pp. 4152–4154, Nov. 2011, doi: 10.1364/OL.36.004152.
[25] P. Emma *et al.*, "First lasing and operation of an ångstrom-wavelength free-electron laser," *Nature Photon*, vol. 4, no. 9, Art. no. 9, Sep. 2010, doi: 10.1038/nphoton.2010.176.
[26] J. J. Rocca, V. Shlyaptsev, F. G. Tomasel, O. D. Cortázar, D. Hartshorn, and J. L. Chilla, "Demonstration of a discharge pumped table-top soft-x-ray laser," *Phys Rev Lett*, vol. 73, no. 16, pp. 2192–2195, Oct. 1994, doi: 10.1103/PhysRevLett.73.2192.
[27] M. Born, E. Wolf, and A. B. Bhatia, *Principles of Optics: Electromagnetic Theory of Propagation, Interference and Diffraction of Light*. Cambridge University Press, 1999.
[28] B. E. A. Saleh and M. C. Teich, *Fundamentals of photonics*. New York: Wiley, 1991. Accessed: Jun. 08, 2023. [Online]. Available: http://catalogue.bnf.fr/ark:/12148/cb373665854
[29] O. Svelto, "Principles of Lasers FIFTH EDITION," 2010.
[30] R. R. Gattass and E. Mazur, "Femtosecond laser micromachining in transparent materials," *Nature Photon*, vol. 2, no. 4, Art. no. 4, Apr. 2008, doi: 10.1038/nphoton.2008.47.
[31] C. B. Schaffer, A. Brodeur, and E. Mazur, "Laser-induced breakdown and damage in bulk transparent materials induced by tightly focused femtosecond laser pulses," *Meas. Sci. Technol.*, vol. 12, no. 11, p. 1784, Oct. 2001, doi: 10.1088/0957-0233/12/11/305.
[32] B. C. Stuart, M. D. Feit, S. Herman, A. M. Rubenchik, B. W. Shore, and M. D. Perry, "Nanosecond-to-femtosecond laser-induced breakdown in dielectrics," *Phys. Rev. B*, vol. 53, no. 4, pp. 1749–1761, Jan. 1996, doi: 10.1103/PhysRevB.53.1749.
[33] S. S. Mao *et al.*, "Dynamics of femtosecond laser interactions with dielectrics," *Appl Phys A*, vol. 79, no. 7, pp. 1695–1709, Nov. 2004, doi: 10.1007/s00339-004-2684-0.
[34] M. Ams *et al.*, "Investigation of Ultrafast Laser-Photonic Material Interactions: Challenges for Directly Written Glass Photonics," *IEEE Journal of Selected Topics in Quantum Electronics*, vol. 14, pp. 1370–1381, Jan. 2008, doi: 10.1109/JSTQE.2008.925809.
[35] F. He *et al.*, "Femtosecond Laser Fabrication of Monolithically Integrated Microfluidic Sensors in Glass," *Sensors (Basel, Switzerland)*, vol. 14, pp. 19402–19440, Oct. 2014, doi: 10.3390/s141019402.
[36] R. W. Boyd, *Nonlinear optics*, 4th ed. San Diego: Academic Press is an imprint of Elsevier, 2019.
[37] A. Royon, Y. Petit, G. Papon, M. Richardson, and L. Canioni, "Femtosecond laser induced photochemistry in materials tailored with photosensitive agents [Invited]," *Opt. Mater. Express*, vol. 1, no. 5, p. 866, Sep. 2011, doi: 10.1364/OME.1.000866.
[38] L. Keldysh, "Concerning the Theory of Impact Ionization in Semiconductors," 1965. Accessed: Aug. 21, 2023. [Online]. Available: https://www.semanticscholar.org/paper/Concerning-the-Theory-of-Impact-Ionization-in-Keldysh/425845d82738c1046f453bd88cf2560b6637d60a
[39] S. M. Eaton, G. Cerullo, and R. Osellame, "Fundamentals of Femtosecond Laser Modification of Bulk Dielectrics," in *Femtosecond Laser Micromachining: Photonic and Microfluidic Devices in Transparent Materials*, R. Osellame, G. Cerullo, and R. Ramponi, Eds., in Topics in Applied Physics. , Berlin, Heidelberg: Springer, 2012, pp. 3–18. doi:

10.1007/978-3-642-23366-1_1.
[40] M. Lenzner *et al.*, "Femtosecond Optical Breakdown in Dielectrics," *Phys. Rev. Lett.*, vol. 80, no. 18, pp. 4076–4079, May 1998, doi: 10.1103/PhysRevLett.80.4076.
[41] K. Bourhis, "Photostructuration par laser infrarouge femtoseconde de verres photosensibles de phosphates de zinc, d'argent et de gallium," Theses, Université Sciences et Technologies - Bordeaux I, 2011. Accessed: Oct. 25, 2022. [Online]. Available: https://tel.archives-ouvertes.fr/tel-00661392
[42] Y. Petit *et al.*, "On the femtosecond laser-induced photochemistry in silver-containing oxide glasses: mechanisms, related optical and physico-chemical properties, and technological applications," *Advanced Optical Technologies*, vol. 7, no. 5, pp. 291–309, 2018, doi: 10.1515/aot-2018-0037.
[43] S. Gross *et al.*, "Ultrafast Laser Inscription in Soft Glasses: A Comparative Study of Athermal and Thermal Processing Regimes for Guided Wave Optics," *International Journal of Applied Glass Science*, vol. 3, no. 4, pp. 332–348, Dec. 2012, doi: 10.1111/ijag.12005.
[44] Papon, G., "Nanostructuration des propriétés optiques linéaires et non-linéaires d'un verre photosensible par laser femtoseconde," Bordeaux University, France, 2012.
[45] Abou khalil, A., "Direct laser writing of a new type of optical waveguides and components in silver containing glasses," Bordeaux University, France, 2018.
[46] C. B. Schaffer, J. F. García, and E. Mazur, "Bulk Heating of Transparent Materials Using a High-Repetition-Rate Femtosecond Laser," *Applied Physics A*, vol. 76, pp. 351–354, Mar. 2003, doi: 10.1007/s00339-002-1819-4.
[47] S. M. Eaton *et al.*, "Heat accumulation effects in femtosecond laser-written waveguides with variable repetition rate," *Opt. Express, OE*, vol. 13, no. 12, pp. 4708–4716, Jun. 2005, doi: 10.1364/OPEX.13.004708.
[48] H. Zhang, S. Eaton, J. Li, and P. R. Herman, "Heat accumulation during high repetition rate ultrafast laser interaction: Waveguide writing in borosilicate glass," *Journal of Physics: Conference Series*, vol. 59, p. 682, May 2007, doi: 10.1088/1742-6596/59/1/144.
[49] "Laser : Fundamentals - Spatial characteristics of the emitted laser beam." Accessed: Aug. 22, 2023. [Online]. Available: http://www.optique-ingenieur.org/en/courses/OPI_ang_M01_C01/co/Contenu_09.html
[50] J. Squier and M. Müller, "High resolution nonlinear microscopy: A review of sources and methods for achieving optimal imaging," *Review of Scientific Instruments*, vol. 72, no. 7, pp. 2855–2867, Jul. 2001, doi: 10.1063/1.1379598.
[51] J. Durnin, J. Miceli, and J. H. Eberly, "Diffraction-free beams," *Phys Rev Lett*, vol. 58, no. 15, pp. 1499–1501, Apr. 1987, doi: 10.1103/PhysRevLett.58.1499.
[52] Z. Li, K. B. Alici, H. Caglayan, and E. Ozbay, "Generation of an Axially Asymmetric Bessel-Like Beam from a Metallic Subwavelength Aperture," *Phys. Rev. Lett.*, vol. 102, no. 14, p. 143901, Apr. 2009, doi: 10.1103/PhysRevLett.102.143901.
[53] F. O. Fahrbach and A. Rohrbach, "Propagation stability of self-reconstructing Bessel beams enables contrast-enhanced imaging in thick media," *Nature Communications*, vol. 3, no. 1, p. 632, Jan. 2012, doi: 10.1038/ncomms1646.
[54] C. Shi, M. Dubois, Y. Wang, and X. Zhang, "High-speed acoustic communication by multiplexing orbital angular momentum," *Proceedings of the National Academy of Sciences*, vol. 114, no. 28, pp. 7250–7253, Jul. 2017, doi: 10.1073/pnas.1704450114.
[55] P. L. Marston, "Scattering of a Bessel beam by a sphere," *The Journal of the Acoustical Society of America*, vol. 121, no. 2, pp. 753–758, 2007.
[56] M. K. Bhuyan *et al.*, "Laser micro-and nanostructuring using femtosecond Bessel beams," *The European Physical Journal Special Topics*, vol. 199, pp. 101–110, 2011.
[57] J. H. McLeod, "Axicons and Their Uses," *J. Opt. Soc. Am., JOSA*, vol. 50, no. 2, pp. 166–169, Feb. 1960, doi: 10.1364/JOSA.50.000166.
[58] R. M. Herman and T. A. Wiggins, "Production and uses of diffractionless beams," *J. Opt. Soc. Am. A, JOSAA*, vol. 8, no. 6, pp. 932–942, Jun. 1991, doi: 10.1364/JOSAA.8.000932.

[59] A. Vasara, J. Turunen, and A. T. Friberg, "Realization of general nondiffracting beams with computer-generated holograms," *J. Opt. Soc. Am. A, JOSAA*, vol. 6, no. 11, pp. 1748–1754, Nov. 1989, doi: 10.1364/JOSAA.6.001748.
[60] J. A. Davis, E. Carcole, and D. M. Cottrell, "Nondiffracting interference patterns generated with programmable spatial light modulators," *Appl. Opt., AO*, vol. 35, no. 4, pp. 599–602, Feb. 1996, doi: 10.1364/AO.35.000599.
[61] J. Turunen, A. Vasara, and A. T. Friberg, "Holographic generation of diffraction-free beams," *Appl Opt*, vol. 27, no. 19, pp. 3959–3962, Oct. 1988, doi: 10.1364/AO.27.003959.
[62] J. Amako, D. Sawaki, and E. Fujii, "Microstructuring transparent materials by use of nondiffracting ultrashort pulse beams generated by diffractive optics," *Journal of the Optical Society of America B Optical Physics*, vol. 20, pp. 2562–2568, Dec. 2003, doi: 10.1364/JOSAB.20.002562.
[63] S. N. Khonina *et al.*, "Rotation of microparticles with Bessel beams generated by diffractive elements," *Journal of Modern Optics*, vol. 51, no. 14, pp. 2167–2184, Sep. 2004, doi: 10.1080/09500340408232521.
[64] "(10) Generation of controllable nondiffracting beams using multimode optical fibers | Request PDF." Accessed: Aug. 22, 2023. [Online]. Available: https://www.researchgate.net/publication/234876572_Generation_of_controllable_nondiffracting_beams_using_multimode_optical_fibers
[65] J. K. Kim *et al.*, "Compact all-fiber Bessel beam generator based on hollow optical fiber combined with a hybrid polymer fiber lens," *Opt Lett*, vol. 34, no. 19, pp. 2973–2975, Oct. 2009, doi: 10.1364/OL.34.002973.
[66] F. Courvoisier, "Ultrafast Laser Micro-Nano Structuring of Transparent Materials with High Aspect Ratio," *Handbook of Laser Micro- and Nano-Engineering*, 2021, [Online]. Available: https://api.semanticscholar.org/CorpusID:232092826
[67] H. D. Nguyen *et al.*, "Non-Diffractive Bessel Beams for Ultrafast Laser Scanning Platform and Proof-Of-Concept Side-Wall Polishing of Additively Manufactured Parts," *Micromachines (Basel)*, vol. 11, no. 11, p. 974, Oct. 2020, doi: 10.3390/mi11110974.
[68] G. Papon *et al.*, "Femtosecond single-beam direct laser poling of stable and efficient second-order nonlinear optical properties in glass," *Journal of Applied Physics*, vol. 115, no. 11, 2014.
[69] Ershov, B.G.;, Ionova, G.V., and Kiseleva, A.A., "Silver clusters: calculations of optical transmissions and of the formation and properties of 'magic' positively charged clusters," *Rus. J. Phys. Chem*, vol. 69, p. 239, 1995.
[70] M. V. Shestakov *et al.*, "Lead silicate glass SiO2–PbF2 doped with luminescent Ag nanoclusters of a fixed site," *RSC Adv.*, vol. 4, no. 40, pp. 20699–20703, May 2014, doi: 10.1039/C4RA03144J.
[71] M. Ams, G. d. Marshall, P. Dekker, J. a. Piper, and M. j. Withford, "Ultrafast laser written active devices," *Laser & Photonics Reviews*, vol. 3, no. 6, pp. 535–544, 2009, doi: 10.1002/lpor.200810050.
[72] S. Gross and M. J. Withford, "Ultrafast-laser-inscribed 3D integrated photonics: challenges and emerging applications," *Nanophotonics*, vol. 4, no. 3, pp. 332–352, Nov. 2015, doi: 10.1515/nanoph-2015-0020.
[73] F. Chen and J. R. V. de Aldana, "Optical waveguides in crystalline dielectric materials produced by femtosecond-laser micromachining," *Laser & Photonics Reviews*, vol. 8, no. 2, pp. 251–275, 2014, doi: 10.1002/lpor.201300025.
[74] J.-P. Bérubé, J. Lapointe, A. Dupont, M. Bernier, and R. Vallée, "Femtosecond laser inscription of depressed cladding single-mode mid-infrared waveguides in sapphire," *Opt. Lett., OL*, vol. 44, no. 1, pp. 37–40, Jan. 2019, doi: 10.1364/OL.44.000037.
[75] S. Sowa, W. Watanabe, T. Tamaki, J. Nishii, and K. Itoh, "Symmetric waveguides in poly(methyl methacrylate) fabricated by femtosecond laser pulses," *Opt. Express, OE*, vol. 14, no. 1, pp. 291–297, Jan. 2006, doi: 10.1364/OPEX.14.000291.

[76] J.-S. Boisvert *et al.*, "Photosensitization agents for fs laser writing in PDMS," *Sci Rep*, vol. 12, no. 1, Art. no. 1, Jan. 2022, doi: 10.1038/s41598-022-05366-w.
[77] T. Allsop, M. Dubov, V. Mezentsev, and I. Bennion, "Inscription and characterization of waveguides written into borosilicate glass by a high-repetition-rate femtosecond laser at 800 nm," *Appl. Opt., AO*, vol. 49, no. 10, pp. 1938–1950, Apr. 2010, doi: 10.1364/AO.49.001938.
[78] C. Florea and K. A. Winick, "Fabrication and characterization of photonic devices directly written in glass using femtosecond laser pulses," *J. Lightwave Technol.*, vol. 21, no. 1, pp. 246–253, Jan. 2003, doi: 10.1109/JLT.2003.808678.
[79] S. Nolte, M. Will, J. Burghoff, and A. Tuennermann, "Femtosecond waveguide writing: a new avenue to three-dimensional integrated optics," *Applied Physics A*, vol. 77, no. 1, pp. 109–111, Jun. 2003, doi: 10.1007/s00339-003-2088-6.
[80] J. P. Bérubé, S. H. Messaddeq, M. Bernier, I. Skripachev, Y. Messaddeq, and R. Vallée, "Tailoring the refractive index of Ge-S based glass for 3D embedded waveguides operating in the mid-IR region," *Opt. Express, OE*, vol. 22, no. 21, pp. 26103–26116, Oct. 2014, doi: 10.1364/OE.22.026103.
[81] J. Lapointe and R. Kashyap, "A simple technique to overcome self-focusing, filamentation, supercontinuum generation, aberrations, depth dependence and waveguide interface roughness using fs laser processing," *Sci Rep*, vol. 7, no. 1, Art. no. 1, Mar. 2017, doi: 10.1038/s41598-017-00589-8.
[82] A. Podlipensky, A. Abdolvand, G. Seifert, and H. Graener, "Femtosecond laser assisted production of dichroitic 3D structures in composite glass containing Ag nanoparticles," *Applied Physics A*, vol. 80, no. 8, pp. 1647–1652, May 2005, doi: 10.1007/s00339-004-3090-3.
[83] Y. Dai, B. Zhu, J. Qiu, H. Ma, B. Lu, and B. Yu, "Space-selective precipitation of functional crystals in glass by using a high repetition rate femtosecond laser," *Chemical Physics Letters*, vol. 443, no. 4, pp. 253–257, Aug. 2007, doi: 10.1016/j.cplett.2007.06.076.
[84] Y. Cheng, K. Sugioka, M. Masuda, K. Shihoyama, K. Toyoda, and K. Midorikawa, "Optical gratings embedded in photosensitive glass by photochemical reaction using a femtosecond laser," *Opt. Express, OE*, vol. 11, no. 15, pp. 1809–1816, Jul. 2003, doi: 10.1364/OE.11.001809.
[85] M. Masuda *et al.*, "3-D microstructuring inside photosensitive glass by femtosecond laser excitation," *Applied Physics A*, vol. 76, no. 5, pp. 857–860, Mar. 2003, doi: 10.1007/s00339-002-1937-z.
[86] K. Miura, J. Qiu, T. Mitsuyu, and K. Hirao, "Space-selective growth of frequency-conversion crystals in glasses with ultrashort infrared laser pulses," *Opt. Lett., OL*, vol. 25, no. 6, pp. 408–410, Mar. 2000, doi: 10.1364/OL.25.000408.
[87] A. Dias *et al.*, "Femtosecond laser writing of photonic devices in borate glasses compositionally designed to be laser writable," *Opt. Lett., OL*, vol. 43, no. 11, pp. 2523–2526, Jun. 2018, doi: 10.1364/OL.43.002523.
[88] T. T. Fernandez *et al.*, "Ultrafast laser inscribed waveguides in tailored fluoride glasses: an enabling technology for mid-infrared integrated photonics devices," *Sci Rep*, vol. 12, no. 1, Art. no. 1, Aug. 2022, doi: 10.1038/s41598-022-18701-y.
[89] S. Wong *et al.*, "Direct Laser Writing of Three- Dimensional Photonic Crystals with a Complete Photonic Bandgap in Chalcogenide Glasses," *Advanced Materials*, vol. 18, no. 3, pp. 265–269, 2006, doi: 10.1002/adma.200501973.
[90] L. B. Fletcher, J. J. Witcher, N. Troy, S. T. Reis, R. K. Brow, and D. M. Krol, "Direct femtosecond laser waveguide writing inside zinc phosphate glass," *Opt. Express, OE*, vol. 19, no. 9, pp. 7929–7936, Apr. 2011, doi: 10.1364/OE.19.007929.
[91] J.-P. Bérubé *et al.*, "Femtosecond laser direct inscription of mid-IR transmitting waveguides in BGG glasses," *Opt. Mater. Express, OME*, vol. 7, no. 9, pp. 3124–3135, Sep. 2017, doi: 10.1364/OME.7.003124.
[92] A. A. Unal, A. Stalmashonak, G. Seifert, and H. Graener, "Ultrafast dynamics of silver nanoparticle shape transformation studied by femtosecond pulse-pair irradiation," *Phys. Rev.*

B, vol. 79, no. 11, p. 115411, Mar. 2009, doi: 10.1103/PhysRevB.79.115411.
[93] A. A. Unal, A. Stalmashonak, H. Graener, and G. Seifert, "Time-resolved investigation of laser-induced shape transformation of silver nanoparticles," *Phys. Rev. B*, vol. 80, no. 11, p. 115415, Sep. 2009, doi: 10.1103/PhysRevB.80.115415.
[94] A. Crespi, R. Osellame, and F. Bragheri, "Femtosecond-laser-written optofluidics in alumino-borosilicate glass," *Optical Materials: X*, vol. 4, p. 100042, Dec. 2019, doi: 10.1016/j.omx.2019.100042.
[95] M. Haque, K. K. C. Lee, S. Ho, L. A. Fernandes, and P. R. Herman, "Chemical-assisted femtosecond laser writing of lab-in-fibers," *Lab on a Chip*, vol. 14, no. 19, pp. 3817–3829, 2014, doi: 10.1039/C4LC00648H.
[96] J. Lapointe, M. Gagné, M.-J. Li, and R. Kashyap, "Making smart phones smarter with photonics," *Opt. Express, OE*, vol. 22, no. 13, pp. 15473–15483, Jun. 2014, doi: 10.1364/OE.22.015473.
[97] A. Arriola *et al.*, "Mid-infrared astrophotonics: study of ultrafast laser induced index change in compatible materials," *Opt. Mater. Express, OME*, vol. 7, no. 3, pp. 698–711, Mar. 2017, doi: 10.1364/OME.7.000698.
[98] T. Meany *et al.*, "Laser written circuits for quantum photonics," *Laser & Photonics Reviews*, vol. 9, no. 4, pp. 363–384, Jul. 2015, doi: 10.1002/lpor.201500061.
[99] A. Royon *et al.*, "Silver Clusters Embedded in Glass as a Perennial High Capacity Optical Recording Medium," *Advanced Materials*, vol. 22, no. 46, pp. 5282–5286, 2010, doi: 10.1002/adma.201002413.
[100] J. Zhang, M. Gecevičius, M. Beresna, and P. G. Kazansky, "Seemingly Unlimited Lifetime Data Storage in Nanostructured Glass," *Phys. Rev. Lett.*, vol. 112, no. 3, p. 033901, Jan. 2014, doi: 10.1103/PhysRevLett.112.033901.
[101] D. Homoelle, S. Wielandy, A. L. Gaeta, N. F. Borrelli, and C. Smith, "Infrared photosensitivity in silica glasses exposed to femtosecond laser pulses," *Opt. Lett., OL*, vol. 24, no. 18, pp. 1311–1313, Sep. 1999, doi: 10.1364/OL.24.001311.
[102] O. M. Efimov *et al.*, "Waveguide writing in chalcogenide glasses by a train of femtosecond laser pulses," *Optical Materials*, vol. 17, no. 3, pp. 379–386, Aug. 2001, doi: 10.1016/S0925-3467(01)00062-3.
[103] D. K. Y. Low, H. Xie, Z. Xiong, and G. C. Lim, "Femtosecond laser direct writing of embedded optical waveguides in aluminosilicate glass," *Appl. Phys. A*, vol. 81, no. 8, pp. 1633–1638, Dec. 2005, doi: 10.1007/s00339-005-3324-z.
[104] T. Pertsch *et al.*, "Discrete diffraction in two-dimensional arrays of coupled waveguides in silica," *Opt. Lett., OL*, vol. 29, no. 5, pp. 468–470, Mar. 2004, doi: 10.1364/OL.29.000468.
[105] A. M. Kowalevicz, V. Sharma, E. P. Ippen, J. G. Fujimoto, and K. Minoshima, "Three-dimensional photonic devices fabricated in glass by use of a femtosecond laser oscillator," *Opt. Lett., OL*, vol. 30, no. 9, pp. 1060–1062, May 2005, doi: 10.1364/OL.30.001060.
[106] A. Martinez, M. Dubov, I. Khrushchev, and I. Bennion, "Direct Writing of Fibre Bragg Gratings by Femtosecond Laser," *Electronics Letters*, vol. 40, pp. 1170–1172, Oct. 2004, doi: 10.1049/el:20046050.
[107] K. Kawamura, N. Sarukura, M. Hirano, and H. Hosono, "Holographic encoding of fine-pitched micrograting structures in amorphous SiO2 thin films on silicon by a single femtosecond laser pulse," *Applied Physics Letters*, vol. 78, no. 8, pp. 1038–1040, Feb. 2001, doi: 10.1063/1.1347007.
[108] W. Cai, A. R. Libertun, and R. Piestun, "Polarization selective computer-generated holograms realized in glass by femtosecond laser induced nanogratings," *Opt. Express, OE*, vol. 14, no. 9, pp. 3785–3791, May 2006, doi: 10.1364/OE.14.003785.
[109] W. Watanabe, T. Toma, K. Yamada, J. Nishii, K. Hayashi, and K. Itoh, "Optical seizing and merging of voids in silica glass with infrared femtosecond laser pulses," *Opt. Lett., OL*, vol. 25, no. 22, pp. 1669–1671, Nov. 2000, doi: 10.1364/OL.25.001669.
[110] E. N. Glezer and E. Mazur, "Ultrafast-laser driven micro-explosions in transparent

materials," *Applied Physics Letters*, vol. 71, no. 7, pp. 882–884, Aug. 1997, doi: 10.1063/1.119677.
[111] P. Zijlstra, J. W. M. Chon, and M. Gu, "Five-dimensional optical recording mediated by surface plasmons in gold nanorods," *Nature*, vol. 459, no. 7245, Art. no. 7245, May 2009, doi: 10.1038/nature08053.
[112] C.-H. Park, Y. Petit, L. Canioni, and S.-H. Park, "Five-Dimensional Optical Data Storage Based on Ellipse Orientation and Fluorescence Intensity in a Silver-Sensitized Commercial Glass," *Micromachines (Basel)*, vol. 11, no. 12, p. 1026, Nov. 2020, doi: 10.3390/mi11121026.
[113] Y. Shimotsuma, P. G. Kazansky, J. Qiu, and K. Hirao, "Self-Organized Nanogratings in Glass Irradiated by Ultrashort Light Pulses," *Phys. Rev. Lett.*, vol. 91, no. 24, p. 247405, Dec. 2003, doi: 10.1103/PhysRevLett.91.247405.
[114] C. Hnatovsky *et al.*, "Pulse duration dependence of femtosecond-laser-fabricated nanogratings in fused silica," *Applied Physics Letters*, vol. 87, no. 1, p. 014104, Jun. 2005, doi: 10.1063/1.1991991.
[115] S. Juodkazis *et al.*, "Laser-Induced Microexplosion Confined in the Bulk of a Sapphire Crystal: Evidence of Multimegabar Pressures," *Phys. Rev. Lett.*, vol. 96, no. 16, p. 166101, Apr. 2006, doi: 10.1103/PhysRevLett.96.166101.
[116] M. Ams, G. D. Marshall, D. J. Spence, and M. J. Withford, "Slit beam shaping method for femtosecond laser direct-write fabrication of symmetric waveguides in bulk glasses," *Opt. Express, OE*, vol. 13, no. 15, pp. 5676–5681, Jul. 2005, doi: 10.1364/OPEX.13.005676.
[117] M. Will, S. Nolte, B. N. Chichkov, and A. Tünnermann, "Optical properties of waveguides fabricated in fused silica by femtosecond laser pulses," *Appl. Opt., AO*, vol. 41, no. 21, pp. 4360–4364, Jul. 2002, doi: 10.1364/AO.41.004360.
[118] L. Shah, A. Y. Arai, S. M. Eaton, and P. R. Herman, "Waveguide writing in fused silica with a femtosecond fiber laser at 522 nm and 1 MHz repetition rate," *Opt. Express, OE*, vol. 13, no. 6, pp. 1999–2006, Mar. 2005, doi: 10.1364/OPEX.13.001999.
[119] A. M. Streltsov and N. F. Borrelli, "Study of femtosecond-laser-written waveguides in glasses," *J. Opt. Soc. Am. B, JOSAB*, vol. 19, no. 10, pp. 2496–2504, Oct. 2002, doi: 10.1364/JOSAB.19.002496.
[120] J. W. Chan, T. R. Huser, S. H. Risbud, and D. M. Krol, "Modification of the fused silica glass network associated with waveguide fabrication using femtosecond laser pulses," *Appl Phys A*, vol. 76, no. 3, pp. 367–372, Mar. 2003, doi: 10.1007/s00339-002-1822-9.
[121] D. J. Little, M. Ams, P. Dekker, G. D. Marshall, and M. J. Withford, "Mechanism of femtosecond-laser induced refractive index change in phosphate glass under a low repetition-rate regime," *Journal of Applied Physics*, vol. 108, no. 3, p. 033110, Aug. 2010, doi: 10.1063/1.3468490.
[122] J. W. Chan, T. Huser, S. Risbud, and D. M. Krol, "Structural changes in fused silica after exposure to focused femtosecond laser pulses," *Opt. Lett., OL*, vol. 26, no. 21, pp. 1726–1728, Nov. 2001, doi: 10.1364/OL.26.001726.
[123] P. Dekker, M. Ams, G. D. Marshall, D. J. Little, and M. J. Withford, "Annealing dynamics of waveguide Bragg gratings: evidence of femtosecond laser induced colour centres," *Opt. Express, OE*, vol. 18, no. 4, pp. 3274–3283, Feb. 2010, doi: 10.1364/OE.18.003274.
[124] Q.-Z. Zhao, J.-R. Qiu, X.-W. Jiang, Q.-L. Zhou, C.-J. Zhao, and C.-S. Zhu, "Temperature dependence of femtosecond laser induced refractive index change in Nd3+-doped phosphate glass," *Optical Materials*, vol. 27, no. 6, pp. 1159–1162, Mar. 2005, doi: 10.1016/j.optmat.2004.09.011.
[125] L. Sudrie, M. Franco, B. Prade, and A. Mysyrowicz, "Writing of permanent birefringent microlayers in bulk fused silica with femtosecond laser pulses," *Optics Communications*, vol. 171, no. 4, pp. 279–284, Dec. 1999, doi: 10.1016/S0030-4018(99)00562-3.
[126] M. Lancry, B. Poumellec, J. Canning, K. Cook, J.-C. Poulin, and F. Brisset, "Ultrafast nanoporous silica formation driven by femtosecond laser irradiation," *Laser & Photonics*

Reviews, vol. 7, no. 6, pp. 953–962, 2013, doi: 10.1002/lpor.201300043.
[127] S. Richter, M. Heinrich, S. Döring, A. Tünnermann, and S. Nolte, "Formation of femtosecond laser-induced nanogratings at high repetition rates," *Appl. Phys. A*, vol. 104, no. 2, pp. 503–507, Aug. 2011, doi: 10.1007/s00339-011-6489-7.
[128] F. Liang, R. Vallée, and S. L. Chin, "Mechanism of nanograting formation on the surface of fused silica," *Opt. Express, OE*, vol. 20, no. 4, pp. 4389–4396, Feb. 2012, doi: 10.1364/OE.20.004389.
[129] C. Hnatovsky *et al.*, "Fabrication of microchannels in glass using focused femtosecond laser radiation and selective chemical etching," *Appl. Phys. A*, vol. 84, no. 1, pp. 47–61, Jul. 2006, doi: 10.1007/s00339-006-3590-4.
[130] A. Marcinkevičius *et al.*, "Femtosecond laser-assisted three-dimensional microfabrication in silica," *Opt. Lett., OL*, vol. 26, no. 5, pp. 277–279, Mar. 2001, doi: 10.1364/OL.26.000277.
[131] Y. Bellouard, A. Said, M. Dugan, and P. Bado, "Fabrication of high-aspect ratio, micro-fluidic channels and tunnels using femtosecond laser pulses and chemical etching," *Opt. Express, OE*, vol. 12, no. 10, pp. 2120–2129, May 2004, doi: 10.1364/OPEX.12.002120.
[132] E. N. Glezer *et al.*, "Three-dimensional optical storage inside transparent materials," *Opt. Lett., OL*, vol. 21, no. 24, pp. 2023–2025, Dec. 1996, doi: 10.1364/OL.21.002023.
[133] S. Juodkazis *et al.*, "Application of femtosecond laser pulses for microfabrication of transparent media," *Applied Surface Science*, vol. 197–198, pp. 705–709, Sep. 2002, doi: 10.1016/S0169-4332(02)00397-5.
[134] B. Poumellec, M. Lancry, A. Chahid-Erraji, and P. G. Kazansky, "Modification thresholds in femtosecond laser processing of pure silica: review of dependencies on laser parameters [Invited]," *Opt. Mater. Express, OME*, vol. 1, no. 4, pp. 766–782, Aug. 2011, doi: 10.1364/OME.1.000766.
[135] Y. Petit *et al.*, "On the femtosecond laser-induced photochemistry in silver-containing oxide glasses: mechanisms, related optical and physico-chemical properties, and technological applications," vol. 7, no. 5, Art. no. 5, 2018, doi: 10.1515/aot-2018-0037.
[136] N. G. Boetti, D. Pugliese, E. Ceci-Ginistrelli, J. Lousteau, D. Janner, and D. Milanese, "Highly Doped Phosphate Glass Fibers for Compact Lasers and Amplifiers: A Review," *Applied Sciences*, vol. 7, no. 12, Art. no. 12, 2017, doi: 10.3390/app7121295.
[137] J. H. Campbell and T. I. Suratwala, "Nd-doped phosphate glasses for high-energy/high-peak-power lasers," *Journal of Non-Crystalline Solids*, vol. 263–264, pp. 318–341, Mar. 2000, doi: 10.1016/S0022-3093(99)00645-6.
[138] MOHAMED MESNAOUI, M. MAAZAZ, C. PARENT, B. TANGUY, and G. LE FLEM, "Spectroscopic properties of Ag ions in phosphate glasses of NaPO3-AgPO3 system," *Spectroscopic properties of Ag ions in phosphate glasses of NaPO3-AgPO3 system*, vol. 29, no. 6, pp. 1001–1013, 1992.
[139] R. K. Brow, "Review: the structure of simple phosphate glasses," *Journal of Non-Crystalline Solids*, vol. 263–264, pp. 1–28, Mar. 2000, doi: 10.1016/S0022-3093(99)00620-1.
[140] R. K. Brow, "Nature of Alumina in Phosphate Glass: I, Properties of Sodium Aluminophosphate Glass," *Journal of the American Ceramic Society*, vol. 76, no. 4, pp. 913–918, 1993, doi: 10.1111/j.1151-2916.1993.tb05315.x.
[141] Bourhis, K., "Photostructuration par laser infrarouge femtoseconde de verres photosensible de phosphate de zinc, d'argent et de gallium," Bordeaux University, France, 2011.
[142] J.-C. Desmoulin, "Synthèse et caractérisation de verres d'oxyde d'argent : évolution sous rayonnements ionisants et structuration multi-échelle par laser femtoseconde," These de doctorat, Bordeaux, 2016. Accessed: Sep. 05, 2023. [Online]. Available: https://www.theses.fr/2016BORD0334
[143] P. Ebeling, D. Ehrt, and M. Friedrich, "X-ray Induced Effects in Phosphate Glasses," *Optical Materials*, vol. 20, pp. 101–111, Sep. 2002, doi: 10.1016/S0925-3467(02)00052-6.
[144] U. Natura, T. Feurer, and D. Ehrt, "Kinetics of UV laser radiation defects in high performance glasses," *Nuclear Instruments and Methods in Physics Research Section B: Beam*

Interactions with Materials and Atoms, vol. 166–167, pp. 470–475, May 2000, doi: 10.1016/S0168-583X(99)00698-9.
[145] I. Belharouak, C. Parent, B. Tanguy, G. Le Flem, and M. Couzi, "Silver aggregates in photoluminescent phosphate glasses of the `Ag2O–ZnO–P2O5' system," *Journal of Non-Crystalline Solids*, vol. 244, no. 2, pp. 238–249, Mar. 1999, doi: 10.1016/S0022-3093(99)00014-9.
[146] Guérineau, T.; *et al.*, "Structural influence on the femtosecond laser ability to create fluorescent patterns in silvercontaining sodium-gallium phosphate glasses," *OPTICAL MATERIALS EXPRESS*, vol. 8, pp. 3748–60, 2018, doi: 10.1364/OME.8.003748.
[147] A. Abou Khalil, "Direct laser writing of a new type of optical waveguides and components in silver containing glasses," Université de Bordeaux; Université Laval (Québec, Canada), 2018.
[148] K. Bourhis *et al.*, "Femtosecond laser structuring and optical properties of a silver and zinc phosphate glass," *Journal of Non-Crystalline Solids*, vol. 356, pp. 2658–2665, Oct. 2010, doi: 10.1016/j.jnoncrysol.2010.03.033.
[149] Marquestaut, N.;, Petit, Y,;, Royon, A.;, Mounaix, P.;, Cardinal, T., and Canioni, L., "Three-Dimensional Silver Nanoparticle Formation Using Femtosecond Laser Irradiation in Phosphate Glasses: Analogy with Photography," *Adv Funct Mater*, vol. 24, pp. 5824–5832, 2014, doi: 10.1002/adfm.201401103.
[150] M. Bellec *et al.*, "3D Patterning at the Nanoscale of Fluorescent Emitters in Glass," *The Journal of Physical Chemistry C*, vol. 114, pp. 15584–15588, Aug. 2010, doi: 10.1021/jp104049e.
[151] M. Bellec *et al.*, "Beat the diffraction limit in 3D direct laser writing in photosensitive glass," *Opt. Express, OE*, vol. 17, no. 12, pp. 10304–10318, Jun. 2009, doi: 10.1364/OE.17.010304.
[152] E. Smetanina *et al.*, "Modeling of cluster organization in metal-doped oxide glasses irradiated by a train of femtosecond laser pulses," *Phys. Rev. A*, vol. 93, no. 1, p. 013846, Jan. 2016, doi: 10.1103/PhysRevA.93.013846.
[153] J.-C. Desmoulin *et al.*, "Femtosecond laser structuring of silver-containing glass: Silver redistribution, selective etching, and surface topology engineering," *Journal of Applied Physics*, vol. 118, no. 21, Dec. 2015, doi: 10.1063/1.4936233.
[154] G. Papon *et al.*, "Fluorescence and second-harmonic generation correlative microscopy to probe space charge separation and silver cluster stabilization during direct laser writing in a tailored silver-containing glass," *Optical Materials Express*, vol. 3, Nov. 2013, doi: 10.1364/OME.3.001855.
[155] J. Choi *et al.*, "Three-dimensional direct femtosecond laser writing of second-order nonlinearities in glass," *Opt Lett*, vol. 37, no. 6, pp. 1029–1031, Mar. 2012, doi: 10.1364/OL.37.001029.
[156] A. Abou Khalil *et al.*, "Direct laser writing of a new type of waveguides in silver containing glasses," *Scientific reports*, vol. 7, no. 1, pp. 1–9, 2017.
[157] A. Abou Khalil, W. Gebremichael, Y. Petit, and L. Canioni, "Refractive index change measurement by quantitative microscopy phase imaging for femtosecond laser written structures," *Optics Communications*, vol. 485, p. 126731, Apr. 2021, doi: 10.1016/j.optcom.2020.126731.
[158] P. P. Rajeev *et al.*, "Memory in Nonlinear Ionization of Transparent Solids," *Phys. Rev. Lett.*, vol. 97, no. 25, p. 253001, Dec. 2006, doi: 10.1103/PhysRevLett.97.253001.
[159] L. Loi, Y. Petit, and L. Canioni, "High refractive index change in Type A laser modification using a multi-scan approach," *Opt. Mater. Express*, vol. 12, no. 6, p. 2297, Jun. 2022, doi: 10.1364/OME.457655.
[160] J. Lapointe, J.-P. Bérubé, S. Pouliot, and R. Vallée, "Control and enhancement of photo-induced refractive index modifications in fused silica," *OSA Continuum, OSAC*, vol. 3, no. 10, pp. 2851–2862, Oct. 2020, doi: 10.1364/OSAC.406247.
[161] A. Abou Khalil *et al.*, "Comparative study between the standard type I and the type A femtosecond laser induced refractive index change in silver containing glasses," *Opt. Mater.*

Express, OME, vol. 9, no. 6, pp. 2640–2651, Jun. 2019, doi: 10.1364/OME.9.002640.
[162] T. Guérineau *et al.*, "Laser Direct Writing of Silver Clusters-Based Subwavelength Periodic Structures Embedded in Mid-Infrared Gallo-Germanate Glass," *Advanced Photonics Research*, vol. 3, no. 10, p. 2200032, 2022, doi: 10.1002/adpr.202200032.
[163] A. Abou Khalil, P. Lalanne, J.-P. Bérubé, Y. Petit, R. Vallée, and L. Canioni, "Femtosecond laser writing of near-surface waveguides for refractive-index sensing," *Optics Express*, vol. 27, no. 22, p. 31130, 2019, doi: 10.1364/OE.27.031130.
[164] R. Laberdesque *et al.*, "Three-dimensional femtosecond laser inscription of Type A-based high-efficiency first-order waveguide Bragg gratings," *J. of Advanced Optical Technologies*, vol. to appear in press, 2023.
[165] E. Marom, O. G. Ramer, and S. Ruschin, "Relation between normal-mode and coupled-mode analyses of parallel waveguides," *IEEE Journal of Quantum Electronics*, vol. 20, pp. 1311–1319, Dec. 1984, doi: 10.1109/JQE.1984.1072326.
[166] S. Lacroix, F. Gonthier, and J. Bures, "Modeling of symmetric 2 × 2 fused-fiber couplers," *Appl Opt*, vol. 33, no. 36, pp. 8361–8369, Dec. 1994, doi: 10.1364/AO.33.008361.
[167] C.-H. Park, "Study on nonlinear multi-dimensional direct laser writing by using ultrashort high power laser," phdthesis, Université de Bordeaux ; Yonse Taehakkyo, 2020. Accessed: Sep. 26, 2023. [Online]. Available: https://theses.hal.science/tel-02945362
[168] A. Le Camus, "Conception et élaboration de composants photoniques pour l'infrarouge moyen inscrits par impulsions ultra brèves," phdthesis, Université de Bordeaux ; Université Laval (Québec, Canada), 2020. Accessed: Sep. 26, 2023. [Online]. Available: https://theses.hal.science/tel-02992064
[169] L. Loi, "Femtosecond laser inscription of type A-based high index contrast waveguides and Bragg gratings," These de doctorat, Bordeaux, 2022. Accessed: Sep. 05, 2023. [Online]. Available: https://www.theses.fr/2022BORD0291
[170] M. Ams, P. Dekker, S. Gross, and M. J. Withford, "Fabricating waveguide Bragg gratings (WBGs) in bulk materials using ultrashort laser pulses," *Nanophotonics*, vol. 6, no. 5, pp. 743–763, Sep. 2017, doi: 10.1515/nanoph-2016-0119.
[171] "1990 Recommendations of the International Commission on Radiological Protection," *Ann ICRP*, vol. 21, no. 1–3, pp. 1–201, 1991.
[172] S. Girard *et al.*, "Radiation Effects on Silica-Based Optical Fibers: Recent Advances and Future Challenges," *IEEE Transactions on Nuclear Science*, vol. 60, no. 3, pp. 2015–2036, Jun. 2013, doi: 10.1109/TNS.2012.2235464.
[173] B. Brichard, O. V. Butov, K. M. Golant, and A. Fernandez Fernandez, "Gamma radiation-induced refractive index change in Ge- and N-doped silica," *Journal of Applied Physics*, vol. 103, no. 5, p. 054905, Mar. 2008, doi: 10.1063/1.2885116.
[174] E. J. Friebele, M. E. Gingerich, and K. J. Long, "Radiation damage of optical fiber waveguides at long wavelengths," *Appl. Opt., AO*, vol. 21, no. 3, pp. 547–553, Feb. 1982, doi: 10.1364/AO.21.000547.
[175] H. T. Zubair *et al.*, "Recent Advances in Silica Glass Optical Fiber for Dosimetry Applications," *IEEE Photonics Journal*, vol. 12, no. 3, pp. 1–25, Jun. 2020, doi: 10.1109/JPHOT.2020.2985857.
[176] Schulman, J.H.;, Ginther, R.J.;, Klick, C.C.;, Alger, R.S., and Levy, R.A., "Dosimetry of X-Rays and Gamma-Rays by Radiophotoluminescence," *Journal of Applied Physics*, vol. 22, pp. 1479–1487, 1951, doi: https://doi.org/10.1063/1.1699896.
[177] T. Guérineau *et al.*, "Silver centers luminescence in phosphate glasses subjected to X-Rays or combined X-rays and femtosecond laser exposure," *Int J Appl Glass Sci.*, vol. 11, pp. 1–12, 2019, doi: 10.1111/ijag.13957.
[178] J. Harb *et al.*, "Femtosecond Direct Laser Writing of Silver Clusters in Phosphate Glasses for X-ray Spatially-Resolved Dosimetry," *Chemosensors*, vol. 10, p. 110, Mar. 2022, doi: 10.3390/chemosensors10030110.
[179] "X-rays | ARPANSA." Accessed: Sep. 22, 2023. [Online]. Available:

https://www.arpansa.gov.au/understanding-radiation/what-is-radiation/ionising-radiation/x-ray
[180] "Laboratoire National Henri Becquerel – Laboratoire national de métrologie dans le domaine des rayonnements ionisants." Accessed: Sep. 22, 2023. [Online]. Available: http://www.lnhb.fr/en/
[181] AlHelou, N., "Etude de verres pour la dosimétrie fibrée de rayonnements ionisants," Lille University, France, 2018.
[182] T. Kahan, "Discussion de formules et courbes theoriques relatives aux rayons γ," *J. Phys. Radium*, vol. 10, no. 10, pp. 430–434, 1939, doi: 10.1051/jphysrad:019390010010043000.
[183] W. Abdel-Rahman and E. Podgorsak, "Energy transfer and energy absorption in photon interactions with matter revisited: A step-by-step illustrated approach," *Radiation Physics and Chemistry - RADIAT PHYS CHEM*, vol. 79, pp. 552–566, May 2010, doi: 10.1016/j.radphyschem.2010.01.007.
[184] M. L. Taylor, R. D. Franich, J. V. Trapp, and P. N. Johnston, "The effective atomic number of dosimetric gels," *Australas. Phys. Eng. Sci. Med.*, vol. 31, no. 2, pp. 131–138, Jun. 2008, doi: 10.1007/BF03178587.
[185] W. V. Mayneord, "The significance of the roentgen," *Acta Int Union Against Cancer*, vol. 2, p. 271, 1937.
[186] S. Girard, V. De Michele, and A. Morana, "Spectroscopic Studies of Radiation Effects on Optical Materials," in *Spectroscopy for Materials Characterization*, John Wiley & Sons, Ltd, 2021, pp. 229–251. doi: 10.1002/9781119698029.ch8.
[187] D. L. Griscom, "Nature Of Defects And Defect Generation In Optical Glasses," in *Radiation Effects on Optical Materials*, SPIE, Dec. 1985, pp. 38–59. doi: 10.1117/12.975358.
[188] S. Girard *et al.*, "Overview of radiation induced point defects in silica-based optical fibers," *Reviews in Physics*, vol. 4, p. 100032, Nov. 2019, doi: 10.1016/j.revip.2019.100032.
[189] N. Al Helou *et al.*, "Radioluminescence and Optically Stimulated Luminescence Responses of a Cerium-Doped Sol-Gel Silica Glass Under X-Ray Beam Irradiation," *IEEE Transactions on Nuclear Science*, vol. 65, no. 8, pp. 1591–1597, Aug. 2018, doi: 10.1109/TNS.2017.2787039.
[190] Y. Liu, "Photoluminescence Mechanism and Applications of Graphene Quantum Dots," 2017.
[191] T. Rivera, "Thermoluminescence in medical dosimetry," *Applied Radiation and Isotopes*, vol. 71, pp. 30–34, Dec. 2012, doi: 10.1016/j.apradiso.2012.04.018.
[192] A. S. Pradhan, J. I. Lee, and J. L. Kim, "Recent developments of optically stimulated luminescence materials and techniques for radiation dosimetry and clinical applications," *J Med Phys*, vol. 33, no. 3, pp. 85–99, 2008, doi: 10.4103/0971-6203.42748.
[193] G. N. Chapman and A. J. Walton, "Triboluminescence of glasses and quartz," *Journal of Applied Physics*, vol. 54, no. 10, pp. 5961–5965, Oct. 1983, doi: 10.1063/1.331773.
[194] S. Robin, "Effet Tcherenkov (Cerenkov)," *J. Phys. Radium*, vol. 11, no. 5, p. S1, 1950, doi: 10.1051/jphysrad:0195000110501700.
[195] M. Aznar, "Real-time in vivo luminescence dosimetry in radiotherapy and mammography using Al2O3:C," 2005.
[196] J. C. Polf, S. W. S. McKeever, M. S. Akselrod, and S. Holmstrom, "A Real-time, Fibre Optic Dosimetry System Using Al2O3 Fibres," *Radiation Protection Dosimetry*, vol. 100, no. 1–4, pp. 301–304, Jul. 2002, doi: 10.1093/oxfordjournals.rpd.a005873.
[197] H. E. Hamzaoui, M. Bouazaoui, and B. Capoen, "Chapter 14 - Sol–gel materials for optical fibers," in *Sol-Gel Derived Optical and Photonic Materials*, A. Martucci, L. Santos, R. Estefanía Rojas Hernández, and R. Almeida, Eds., in Woodhead Publishing Series in Electronic and Optical Materials. , Woodhead Publishing, 2020, pp. 315–346. doi: 10.1016/B978-0-12-818019-8.00014-4.
[198] J. Vidalot, "Dosimétrie par fibre optique d'installations d'irradiation expérimentales," These de doctorat, Saint-Etienne, 2022. Accessed: Dec. 09, 2023. [Online]. Available: https://www.theses.fr/2022STET0045

[199] J. Izewska and G. Rajan, *Radiation dosimeters*. International Atomic Energy Agency (IAEA): IAEA, 2005. [Online]. Available: http://inis.iaea.org/search/search.aspx?orig_q=RN:36071459
[200] Ž. Knežević, L. Stolarczyk, I. Bessieres, J. M. Bordy, S. Miljanić, and P. Olko, "Photon dosimetry methods outside the target volume in radiation therapy: Optically stimulated luminescence (OSL), thermoluminescence (TL) and radiophotoluminescence (RPL) dosimetry," *Radiation Measurements*, vol. 57, pp. 9–18, Oct. 2013, doi: 10.1016/j.radmeas.2013.03.004.
[201] J. Vidalot, "Dosimétrie par fibres optiques d'installations d'irradiation expérimentales," These en préparation, Saint-Etienne, 2019. Accessed: Oct. 08, 2023. [Online]. Available: https://www.theses.fr/s237548
[202] Schulman, J.H.;, Shurcliff, W.;, Ginther, R.J., and Attix, F.H., "RADIOPHOTOLUMINESCENCE DOSIMETRY SYSTEM OF THE U.S. NAVY Radiophotoluminescence dosimetry system of the U.S.," *Nucleonics (U.S.) Ceased publication*, vol. 5, 1953.
[203] Piesch, E, and Burgkhardt, B., "Photoluminescence dosimetry: the alternative in personnel monitoring.," *Radioprotection*, vol. 29, pp. 39–67, 1994, doi: 10.1051/radiopro/1994021.
[204] Piesch, E, and Burgkhardt, B., "One-element phosphate glass dosimetry systems for the simultaneous indication of different dose quantities in individual and area dosimetry," *Radioprotection*, vol. 17, pp. 63–66, 1986.
[205] Perry, J.A., "RPL dosimetry. Radiophotoluminescence in health physics," vol. 19, 1987.
[206] Yamamoto, T., "RPL Dosimetry: Principles and Applications," in *AIP Conference proceedings*, 2011, pp. 217–230. doi: https://doi.org/10.1063/1.3576169.
[207] Kodaira, S.;, Yanagida, Y.;, Kawashima, H.;, Kitamua, H.;, Kurani, M., and Ogura, K., "Note: Complementary approach for radiation dosimetry with Ag+-activated phosphate glass," *Review of Scientific Instruments*, vol. 89, pp. 1–3, 2018, doi: https://doi.org/10.1063/1.5058697.
[208] McKeever, S.W.W.;, Sholom, S.;, Shrestha, N., and Klein, D.M., "An in-situ, fiber-optic system for sub-surface, environmental dose measurements using radiophotoluminescence from Ag-doped alkali-phosphate glass," *Radiation Measurements*, vol. 132, 2020, doi: 10.1016/j.radmeas.2020.106273.
[209] Miyamoto, Y.; *et al.*, "Radiophotoluminescence from silver-doped phosphate glass," *Radiation Measurements*, vol. 46, pp. 1480–1483, 2011, doi: 10.1016/j.radmeas.2011.05.048.
[210] Bourhis, K.; *et al.*, "Formation and thermo-assisted stabilization of luminescent silver clusters in photosensitive glasses," *Materials Research Bulletin*, vol. 48, 2013, doi: 10.1016/j.materresbull.2013.01.003.
[211] Kurobori,T.;, Zheng, W.;, Miyamoto, Y.;, Nanto, H., and Yamamoto, T., "The role of silver in the radiophotoluminescent properties in silver-activated phosphate glass and sodium chloride crystal.," *Optical Materials*, vol. 32, pp. 1231–1236, a 2010, doi: https://doi.org/10.1016/j.optmat.2010.04.004.
[212] Kurobori,T.;, Zheng, W., and Zhao, C., "Silver-activated radiophotoluminescent glass: band assignments and a novel readout system using a modulated UV laser diode," *IOP Conference Series: Materials Science and Engineering*, vol. 15, pp. 1–8, b 2010.
[213] McKeever, S.W.W.;, Sholom, S., and Shrestha, N., "Observations regarding the build-up effect in radiophotoluminescence of silver-doped phosphate glasses," *Radiation Measurements*, vol. 123, pp. 13–20, 2019, doi: https://doi.org/10.1016/j.radmeas.2019.02.009.
[214] McKeever, S.W.W.;, Sholom, S.;, Shrestha, N.;, and Klein, D.M., "Build-up of radiophotoluminescence (RPL) in Ag-doped phosphate glass in real-time both during and after exposure to ionizing radiation: A proposed model," *Radiation Measurements*, vol. 132, 2020, doi: 10.1016/j.radmeas.2020.106246.

[215] H. Kawamoto, "Recent developments in radio photoluminescence dosimeters," *Kagaku Kogyo*, vol. 74, no. 2, pp. 96–102, 2023.
[216] Dmitryuk, A.V.;, Paramzina, S.E.;, Perminov, A.S.;, Solov'eva, N.D., and Timofeev, N.T., "The influence of glass composition on the properties of silver-doped radiophotoluminescent phosphate glasses," *Journal of Non-Crystalline Solids*, vol. 202, pp. 173–177, 1996, doi: https://doi.org/10.1016/0022-3093(96)00175-5.
[217] Yokota, R. and Imagawa, H., "Radiophotoluminescent Centers in Silver-Activated Phosphate Glass," *J. Phys. Soc. Jap*, vol. 23, pp. 1038–1048, 1966, doi: https://doi.org/10.1143/JPSJ.23.1038.
[218] Miyamoto, Y.; *et al.*, "Emission mechanism of radiophotoluminescence in Ag-doped phosphate glass," *Radiation Measurements*, vol. 45, 2010.
[219] Zheng, W. and Kurobori,T., "Assignments and optical properties of X-ray-induced colour centres in blue and orange radiophotoluminescent silver-activated glasses," *Journal of Luminescence*, vol. 131, pp. 36–40, 2011, doi: https://doi.org/10.1016/j.jlumin.2010.08.024.
[220] Maki, D;, Nagai, T.;, Sato, F.;, Kato, Y., and Iida, T., "Microscopic dose measurement with thin radiophotoluminescence glass plate," *Radiation Measurements*, vol. 46, pp. 1543–1546, 2011, doi: https://doi.org/10.1016/j.radmeas.2011.05.051.
[221] Maurel, C.; *et al.*, "Luminescence properties of silver zinc phosphate glasses following different irradiations," *Journal of Luminescence*, vol. 129, pp. 1514–1518, 2009, doi: https://doi.org/10.1016/j.jlumin.2008.12.023.
[222] Kurobori,T.;, Itoi, H.;, Yanagida. T., and Chen, Y.Q., "Time resolved dose evaluation in an X-and gamma-ray-irradiated silver-activated glass detector for three-dimensional imaging applications.," *Nuclear Instruments and Methods in Physics Research A*, vol. 793, pp. 6–11, 2015, doi: DOI:10.1016/J.NIMA.2015.04.062.
[223] T. Yamamoto, Y. Yanagida-Miyamoto, T. Iida, and H. Nanto, "Current status and future prospect of RPL glass dosimeter," *Radiation Measurements*, vol. 136, p. 106363, Aug. 2020, doi: 10.1016/j.radmeas.2020.106363.
[224] Y. Miyamoto *et al.*, "Radiophotoluminescence from silver-doped phosphate glass," *Radiation Measurements*, vol. 46, no. 12, pp. 1480–1483, Dec. 2011, doi: 10.1016/j.radmeas.2011.05.048.
[225] Hsu, S.M.;, Yeh, S.H.;, Lin, M.S,;, and Chen, W.L.;, "Comparison on characteristics of radiophotoluminescent glass dosemeters and thermoluminescent dosemeters," *Radiation Protection Dosimetry*, vol. 119, pp. 327–331, 2006, doi: https://doi.org/10.1093/rpd/nci510.
[226] Ihara,Y.; *et al.*, "Acompact system for measurement of radiophotoluminescence of phosphate glass dosimeter," *Radiation Measurements*, vol. 43, pp. 542–545, 2008, doi: https://doi.org/10.1016/j.radmeas.2007.11.045.
[227] Ranogajek-Komor, M., "Solid state dosimeters in environmental monitoring," in *Proc. of The 3rd Inter.Workshop on Individual Monitoring of Ionizing Radiation*, 2007, pp. 53–75.
[228] K.-E. Peiponen and E. M. Vartiainen, "Kramers-Kronig relations in optical data inversion," *Phys. Rev. B*, vol. 44, no. 15, pp. 8301–8303, Oct. 1991, doi: 10.1103/PhysRevB.44.8301.
[229] W. Primak, "Fast-Neutron-Induced Changes in Quartz and Vitreous Silica," *Phys. Rev.*, vol. 110, no. 6, pp. 1240–1254, Jun. 1958, doi: 10.1103/PhysRev.110.1240.
[230] L. Remy, G. Cheymol, A. Gusarov, A. Morana, E. Marin, and S. Girard, "Compaction in Optical Fibres and Fibre Bragg Gratings Under Nuclear Reactor High Neutron and Gamma Fluence," *IEEE Transactions on Nuclear Science*, vol. 63, no. 4, pp. 2317–2322, Aug. 2016, doi: 10.1109/TNS.2016.2570948.
[231] M. Hajek, M. Sugiyama, G. Kolb, D. M. Tucker, and M. Pinak, "CHARACTERISATION OF RADIOPHOTOLUMINESCENCE DOSIMETRY SYSTEM FOR INDIVIDUAL MONITORING," *Radiation Protection Dosimetry*, vol. 190, no. 1, pp. 66–70, Aug. 2020, doi: 10.1093/rpd/ncaa077.
[232] M. Ranogajec-Komor, Ž. Knežević, S. Miljanić, and B. Vekić, "Characterisation of radiophotoluminescent dosimeters for environmental monitoring," *Radiation Measurements*,

vol. 43, no. 2–6, pp. 392–396, Feb. 2008, doi: 10.1016/j.radmeas.2007.11.020.
[233] E. G. Yukihara and F. Assenmacher, "Performance of a radiophotoluminescence (RPL) system in environmental and area monitoring," *Radiation Measurements*, vol. 140, p. 106514, Jan. 2021, doi: 10.1016/j.radmeas.2020.106514.
[234] F. Sato *et al.*, "Development of Human Hand Phantom Containing Radiophotoluminescence Material," *Radiation Measurements*, vol. 85, Dec. 2015, doi: 10.1016/j.radmeas.2015.12.006.
[235] Ž. Knežević, N. Beck, Đ. Milković, S. Miljanić, and M. Ranogajec-Komor, "Characterisation of RPL and TL dosimetry systems and comparison in medical dosimetry applications," *Radiation Measurements*, vol. 46, no. 12, pp. 1582–1585, Dec. 2011, doi: 10.1016/j.radmeas.2011.05.042.
[236] T. Hashimoto, F. Sato, S. Tamaki, S. Kusaka, H. Miyamaru, and I. Murata, "Fabrication of radiophotoluminescence dosimeter with 3D-printing technology," *Radiation Measurements*, vol. 124, Apr. 2019, doi: 10.1016/j.radmeas.2019.04.012.
[237] C. Figueira *et al.*, "Medical staff extremity dosimetry in CT fluoroscopy: an anthropomorphic hand voxel phantom study," *Phys. Med. Biol.*, vol. 58, no. 16, p. 5433, Jul. 2013, doi: 10.1088/0031-9155/58/16/5433.
[238] Kurobori,T., "Performance characterisation of a real-time fiber dosimetry system using radiophotoluminescent glasses," *Jpn J Appl Phys*, vol. 57, pp. 1–7, 2018, doi: 10.7567/JJAP.57.106402.
[239] F. Sato *et al.*, "Development of radiophotoluminescence glass dosimeter usable in high temperature environment," *Radiation Measurements*, vol. 53–54, pp. 8–11, Jun. 2013, doi: 10.1016/j.radmeas.2013.03.016.
[240] Gautier, P., "Nanostructuration des propriétés optiques linéaires et non-linéaires d'un verre photosensible par laser femtoseconde," Bordeaux University, France, 2012.
[241] Poludniowski, G., Omar, A.;, Bujila, R.;, and Pedro, A., "Technical Note: SpekPy v2.0-a software toolkit for modeling x-ray tube spectra," *Med Phys*, vol. 48, pp. 3630–3637, 2021, doi: DOI: 10.1002/mp.14945.
[242] Bujila, R.;, Artur, O.;, and Poludniowski, G.;, "A validation of SpekPy: A software toolkit for modelling X-ray tube spectra," *Physica Medica*, vol. 75, pp. 44–54, 2020, doi: DOI: 10.1016/j.ejmp.2020.04.026.
[243] Allison, J. et al., "Recent developments in GEANT4," *Nuclear Instruments and Methods in Physics Research A*, vol. 835, pp. 186–225, 2016.
[244] K. Philippe, "Etudes préliminaires pour le dépôt localisé de nanoparticules sur des verres photosensibles structurés par laser femtosecondeapport de stage Master II Mention Chimie," Stage Master II, Université de Bordeaux, 2014.
[245] Royon, A.;, Bourhis, K.;, Béchou, L.;, Cardinal, T.;, Canioni, L., and Deshayes, Y, "Durability study of a fluorescent optical memory in glass studied by luminescence spectroscopy," *Microelectronics Reliability,Elsevier*, vol. 53, pp. 1514–1518, 2013, doi: 10.1016/j.microrel.2013.07.110.
[246] A. Meyer *et al.*, "X-Ray Radioluminescence in Diversely Doped Multimode Silica-Based Optical Fibers," *IEEE Transactions on Nuclear Science*, vol. 69, no. 7, pp. 1625–1632, Jul. 2022, doi: 10.1109/TNS.2022.3140392.
[247] T. Allanche, "Effect of high radiation doses (MGy) on light Emitting Diodes and optical glasses," These de doctorat, Lyon, 2020. Accessed: Oct. 08, 2023. [Online]. Available: https://www.theses.fr/2020LYSES039
[248] N. Kerboub *et al.*, "Radiation Induced Attenuation and Luminescence study in Radioluminescent Optical Fibres," *IEEE Transactions on Nuclear Science*, vol. 70, no. 8, pp. 1917–1924, Feb. 2023, doi: 10.1109/TNS.2023.3246239.
[249] O. M. Efimov, L. B. Glebov, L. N. Glebova, K. C. Richardson, and V. I. Smirnov, "High-efficiency Bragg gratings in photothermorefractive glass," *Appl. Opt.*, vol. 38, no. 4, p. 619, Feb. 1999, doi: 10.1364/AO.38.000619.
[250] L. B. Glebov, "Volume Holographic Elements in a Photo-Thermo-Refractive Glass," *Journal*

of Holography and Speckle, vol. 5, no. 1, pp. 77–84, Apr. 2009, doi: 10.1166/jhs.2009.011.
[251] M. SeGall, I. Divliansky, C. Jollivet, A. Schülzgen, and L. B. Glebov, "Holographically encoded volume phase masks," *OE*, vol. 54, no. 7, p. 076104, Jul. 2015, doi: 10.1117/1.OE.54.7.076104.
[252] O. Andrusyak, V. Smirnov, G. Venus, V. Rotar, and L. Glebov, "Spectral Combining and Coherent Coupling of Lasers by Volume Bragg Gratings," *Selected Topics in Quantum Electronics, IEEE Journal of*, vol. 15, pp. 344–353, May 2009, doi: 10.1109/JSTQE.2009.2012438.
[253] A. L. Glebov, O. Mokhun, A. Rapaport, S. Vergnole, V. Smirnov, and L. B. Glebov, "Volume Bragg gratings as ultra-narrow and multiband optical filters," in *Micro-Optics 2012*, SPIE, May 2012, pp. 42–52. doi: 10.1117/12.923575.
[254] N. G. Boetti, D. Pugliese, E. Ceci-Ginistrelli, J. Lousteau, D. Janner, and D. Milanese, "Highly Doped Phosphate Glass Fibers for Compact Lasers and Amplifiers: A Review," *Applied Sciences*, vol. 7, no. 12, p. 1295, Dec. 2017, doi: 10.3390/app7121295.
[255] S. D. Stookey, "Photosensitive Glass," *Ind. Eng. Chem.*, vol. 41, no. 4, pp. 856–861, Apr. 1949, doi: 10.1021/ie50472a042.
[256] D. Kliukin, *Femtosecond laser modification of photo-thermo-refractive glass with volume bragg gratings*. Itä-Suomen yliopisto, 2018. Accessed: Apr. 26, 2023. [Online]. Available: https://erepo.uef.fi/handle/123456789/20042
[257] L. Siiman, "Ultrashort Laser Pulse Interaction With Photo-thermo-refractive Glass," University of Central Florida, Orlando, Florida, 2008. [Online]. Available: https://stars.library.ucf.edu/etd/3725
[258] A. Sevian, O. Andrusyak, I. Ciapurin, V. Smirnov, G. Venus, and L. Glebov, "Efficient power scaling of laser radiation by spectral beam combining," *Opt. Lett., OL*, vol. 33, no. 4, pp. 384–386, Feb. 2008, doi: 10.1364/OL.33.000384.
[259] D. Richter *et al.*, "Minimizing residual spectral drift in laser diode bars using femtosecond-written volume Bragg gratings in fused silica," *Opt. Lett.*, vol. 42, no. 3, p. 623, 2017, doi: 10.1364/OL.42.000623.
[260] Igor V. Ciapurin, Leonid B. Glebov, and Vadim I. Smirnov, "Spectral combining of high-power fiber laser beams using Bragg grating in PTR glass," Jun. 2004, pp. 116–124. doi: 10.1117/12.533740.
[261] A. Glebov *et al.*, "Novel volume Bragg grating notch filters for ultralow-frequency Raman measurements".
[262] A. Rapaport *et al.*, "Very Low Frequency Stokes and Anti-Stokes Raman Spectra Accessible with a Single Multichannel Spectrograph and Volume Bragg Grating Optical Filters," *AIP Conference Proceedings*, vol. 1267, no. 1, pp. 808–809, Aug. 2010, doi: 10.1063/1.3482824.
[263] I. Divliansky, "Volume Bragg Gratings: Fundamentals and Applications in Laser Beam Combining and Beam Phase Transformations," in *Holographic Materials and Optical Systems*, IntechOpen, 2017. doi: 10.5772/66958.
[264] K.-H. Liao, M.-Y. Cheng, E. Flecher, V. I. Smirnov, L. B. Glebov, and A. Galvanauskas, "Large-aperture chirped volume Bragg grating based fiber CPA system," *Opt. Express*, vol. 15, no. 8, p. 4876, 2007, doi: 10.1364/OE.15.004876.
[265] E. Slobodchikov and P. F. Moulton, "1-GW-Peak-Power, Cr:ZnSe Laser," in *CLEO:2011 - Laser Applications to Photonic Applications*, in OSA Technical Digest (CD). Baltimore, Maryland: Optica Publishing Group, May 2011, p. PDPA10. doi: 10.1364/CLEO_SI.2011.PDPA10.
[266] A. Glebov *et al.*, "Angle Selective Enhancement of Beam Deflection in High-Speed Electrooptic Switches," *Photonics Technology Letters, IEEE*, vol. 19, pp. 701–703, Jun. 2007, doi: 10.1109/LPT.2007.895066.
[267] L. H. Lin, "Method of Characterizing Hologram-Recording Materials*," *J. Opt. Soc. Am.*, vol. 61, no. 2, pp. 203–208, Feb. 1971, doi: 10.1364/JOSA.61.000203.
[268] R. J. Collier, C. B. Burckhardt, and L. H. Lin, *Optical holography*. New York: Academic

Press, 1971.
[269] B. J. Chang and C. D. Leonard, "Dichromated gelatin for the fabrication of holographic opticalelements," *Appl. Opt.*, vol. 18, no. 14, pp. 2407–2417, Jul. 1979, doi: 10.1364/AO.18.002407.
[270] W. S. Colburn and K. A. Haines, "Volume Hologram Formation in Photopolymer Materials," *Appl. Opt., AO*, vol. 10, no. 7, pp. 1636–1641, Jul. 1971, doi: 10.1364/AO.10.001636.
[271] S.-D. Wu and E. N. Glytsis, "Holographic grating formation in photopolymers: analysis and experimental results based on a nonlocal diffusion model and rigorous coupled-wave analysis," *J. Opt. Soc. Am. B*, vol. 20, no. 6, pp. 1177–1188, Jun. 2003, doi: 10.1364/JOSAB.20.001177.
[272] F. S. Chen, J. T. LaMacchia, and D. B. Fraser, "HOLOGRAPHIC STORAGE IN LITHIUM NIOBATE," *Applied Physics Letters*, vol. 13, no. 7, pp. 223–225, Oct. 2003, doi: 10.1063/1.1652580.
[273] S I Stepanov, "Applications of photorefractive crystals," *Reports on Progress in Physics*, vol. 57, no. 1, p. 39, Jan. 1994, doi: 10.1088/0034-4885/57/1/002.
[274] S. Dewra and A. Grover, "Fabrication and Applications of Fiber Bragg Grating- A Review".
[275] L. B. Glebov, "Kinetics modeling in photosensitive glass," *Optical Materials*, vol. 25, no. 4, pp. 413–418, May 2004, doi: 10.1016/j.optmat.2003.10.005.
[276] O. M. Efimov, L. B. Glebov, and V. I. Smirnov, "High-frequency Bragg gratings in a photothermorefractive glass," *Opt. Lett.*, vol. 25, no. 23, pp. 1693–1695, Dec. 2000, doi: 10.1364/OL.25.001693.
[277] O. M. Efimov, L. B. Glebov, and V. I. Smirnov, "Diffractive optical elements in photosensitive inorganic glasses," in *Inorganic Optical Materials III*, SPIE, 2001, pp. 39–47.
[278] D. Richter, C. Voigtländer, R. G. Krämer, J. U. Thomas, A. Tünnermann, and S. Nolte, "Femtosecond laser pulse written Volume Bragg Gratings," *MATEC Web of Conferences*, vol. 8, p. 06014, 2013, doi: 10.1051/matecconf/20130806014.
[279] J. Lumeau, "Photosensitive Materials: Optical properties and applications," thesis, Aix Marseille Université, 2012. Accessed: May 28, 2023. [Online]. Available: https://hal.science/tel-01274421
[280] K. M. Davis, K. Miura, N. Sugimoto, and K. Hirao, "Writing waveguides in glass with a femtosecond laser," *Opt Lett*, vol. 21, no. 21, pp. 1729–1731, Nov. 1996, doi: 10.1364/ol.21.001729.
[281] K. Yamada, W. Watanabe, K. Kintaka, J. Nishii, and K. Itoh, "Volume Grating Induced by a Self-Trapped Long Filament of Femtosecond Laser Pulses in Silica Glass," *Jpn. J. Appl. Phys.*, vol. 42, no. 11R, p. 6916, Nov. 2003, doi: 10.1143/JJAP.42.6916.
[282] C. Voigtländer, D. Richter, J. Thomas, A. Tünnermann, and S. Nolte, "Inscription of high contrast volume Bragg gratings in fused silica with femtosecond laser pulses," *Appl. Phys. A*, vol. 102, no. 1, pp. 35–38, Jan. 2011, doi: 10.1007/s00339-010-6065-6.
[283] D. Grobnic, S. J. Mihailov, C. W. Smelser, M. Becker, and M. W. Rothhardt, "Femtosecond laser fabrication of Bragg gratings in borosilicate ion-exchange waveguides," *IEEE Photonics Technology Letters*, vol. 18, no. 13, pp. 1403–1405, Jul. 2006, doi: 10.1109/LPT.2006.877230.
[284] L. Ye *et al.*, "NUV femtosecond laser inscription of volume Bragg gratings in poly(methyl)methacrylate with linear and circular polarizations," *Laser Phys.*, vol. 23, no. 12, p. 126004, Nov. 2013, doi: 10.1088/1054-660X/23/12/126004.
[285] D. Liu *et al.*, "High-speed uniform parallel 3D refractive index micro-structuring of poly(methyl methacrylate) for volume phase gratings," *Appl. Phys. B*, vol. 101, no. 4, pp. 817–823, Dec. 2010, doi: 10.1007/s00340-010-4205-5.
[286] Y. Matushiro, S. Juodkazis, K. Hatanaka, and W. Watanabe, "Regenerated volume gratings in PMMA after femtosecond laser writing," *Opt. Lett., OL*, vol. 42, no. 8, pp. 1632–1635, Apr. 2017, doi: 10.1364/OL.42.001632.
[287] L. Talbot, D. Richter, M. Heck, S. Nolte, and M. Bernier, "Femtosecond-written volume

Bragg gratings in fluoride glasses," *Opt Lett*, vol. 45, no. 13, pp. 3625–3628, Jul. 2020, doi: 10.1364/OL.396022.
[288] H. Kogelnik, "Coupled wave theory for thick hologram gratings," *The Bell System Technical Journal*, vol. 48, no. 9, pp. 2909–2947, Nov. 1969, doi: 10.1002/j.1538-7305.1969.tb01198.x.
[289] D. Paipulas, M. Mikutis, V. Sirutkaitis, and S. Juodkazis, "Volumetric modifications in fused silica using Gaussian and Bessel femtosecond laser beams," J. Shao, T. Jitsuno, and W. Rudolph, Eds., Shanghai, P. R. China, Jul. 2013, p. 87860D. doi: 10.1117/12.2020258.
[290] D. G. MacLachlan, R. R. Thomson, C. R. Cunningham, and D. Lee, "Mid-Infrared Volume Phase Gratings Manufactured using Ultrafast Laser Inscription," *Opt. Mater. Express, OME*, vol. 3, no. 10, pp. 1616–1624, Oct. 2013, doi: 10.1364/OME.3.001616.
[291] A. S. Chernikov, R. V. Chkalov, and D. G. Vasilchenkova, "Volume Bragg Grating Fabrication by Femtosecond Laser Pulses," in *2020 International Conference Laser Optics (ICLO)*, Nov. 2020, pp. 1–1. doi: 10.1109/ICLO48556.2020.9285461.
[292] H. Wang, F. Zhang, K. Ding, and J. Duan, "Non-diffraction-length Bessel-beam femtosecond laser drilling of high-aspect-ratio microholes in PMMA," *Optik*, vol. 229, p. 166295, Mar. 2021, doi: 10.1016/j.ijleo.2021.166295.
[293] P. Birch, I. Ituen, R. Young, and C. Chatwin, "Long-distance Bessel beam propagation through Kolmogorov turbulence," *J. Opt. Soc. Am. A*, vol. 32, no. 11, Art. no. 11, Nov. 2015, doi: 10.1364/JOSAA.32.002066.
[294] F. Courvoisier, "Ultrafast laser micro-nano structuring of transparent materials with high aspect ratio," 2020, pp. 1–37. doi: 10.1007/978-3-319-69537-2_33-1.
[295] P. A. Brandão and D. G. Pires, "Transmission and reflection of vector Bessel beams through an interface between dielectrics," *Physics Letters A*, vol. 381, no. 8, pp. 813–816, Feb. 2017, doi: 10.1016/j.physleta.2016.12.049.
[296] S. Nemoto, "Waist shift of a Gaussian beam by plane dielectric interfaces," *Appl. Opt.*, vol. 27, no. 9, pp. 1833–1839, May 1988, doi: 10.1364/AO.27.001833.
[297] K. Liao, W. Wang, X. Mei, J. Cui, M. Li, and X. Li, "An analytical model to predict the sizes of modified layer in glass with femtosecond Bessel beam," *Optik*, vol. 185, pp. 232–241, May 2019, doi: 10.1016/j.ijleo.2019.03.071.
[298] "Bessel Beam Generation," Photon Engineering. Accessed: Oct. 06, 2022. [Online]. Available: https://photonengr.com/fred-software/application-examples/bessel-beam/
[299] M. Mikutis, T. Kudrius, G. Šlekys, D. Paipulas, and S. Juodkazis, "High 90% efficiency Bragg gratings formed in fused silica by femtosecond Gauss-Bessel laser beams," *Opt. Mater. Express, OME*, vol. 3, no. 11, pp. 1862–1871, Nov. 2013, doi: 10.1364/OME.3.001862.
[300] Y. J. Zhang, G. D. Zhang, C. L. Chen, R. Stoian, and G. H. Cheng, "Transmission volume phase holographic gratings in photo-thermo-refractive glass written with femtosecond laser Bessel beams," *Opt. Mater. Express, OME*, vol. 6, no. 11, pp. 3491–3499, Nov. 2016, doi: 10.1364/OME.6.003491.
[301] W. Watanabe, "Regeneration of a Grating in PMMA Inscribed by Femtosecond Laser Bessel Beam," *Journal of Laser Micro/Nanoengineering*, vol. 12, pp. 102–106, Sep. 2017, doi: 10.2961/jlmn.2017.02.0010.
[302] N. Abdukerim, D. Grobnic, R. Lausten, C. Hnatovsky, and S. J. Mihailov, "Complex diffraction and dispersion effects in femtosecond laser writing of fiber Bragg gratings using the phase mask technique," *Opt Express*, vol. 27, no. 22, pp. 32536–32555, Oct. 2019, doi: 10.1364/OE.27.032536.
[303] C. Dix and P. F. McKee, "High accuracy electron-beam grating lithography for optical and optoelectronic devices," *Journal of Vacuum Science & Technology B: Microelectronics and Nanometer Structures Processing, Measurement, and Phenomena*, vol. 10, no. 6, pp. 2667–2670, Nov. 1992, doi: 10.1116/1.586022.
[304] A. Swanton, D. J. Armes, K. J. Young-Smith, C. Dix, and R. Kashyap, "Use of e-beam written, reactive ion etched, phase masks for the generation of novel photorefractive fibre

gratings," *Microelectronic Engineering*, vol. 30, no. 1, pp. 509–512, Jan. 1996, doi: 10.1016/0167-9317(95)00297-9.
[305] W. C. Cheng, L. A. Wang, and C. Y. Hsieh, "Phase masks fabricated by interferometric lithography for working in 248 nm wavelength," *Microelectronic Engineering*, vol. 67–68, pp. 63–69, Jun. 2003, doi: 10.1016/S0167-9317(03)00060-1.
[306] T. Kjellberg and R. Schatz, "The effect of stitching errors on the spectral characteristics of DFB lasers fabricated using electron beam lithography," *Journal of Lightwave Technology*, vol. 10, no. 9, pp. 1256–1266, Sep. 1992, doi: 10.1109/50.156877.
[307] J. Carrier, "ÉCRITURE DE RÉSEAUX DE BRAGG PAR LASER FEMTOSECONDE À 400 NM".
[308] M. Bernier, "Inscription de réseaux de Bragg à fibre optique à l'aide d'impulsions brèves et applications aux lasers à fibre," 2010, Accessed: Sep. 26, 2023. [Online]. Available: http://hdl.handle.net/20.500.11794/22133
[309] V. Gâté *et al.*, *New low-cost high-efficiency solar module: Diffracting deflector module*, vol. 8438. 2012. doi: 10.1117/12.921366.
[310] D. N. Erschens, K. Buchwald, and V. Gratings, "Pulse front tilting with transmission gratings," 2019.
[311] E. Wikszak, J. Thomas, S. Nolte, and A. Tünnermann, "Inscribing fiber Bragg gratings using IR-fs pulses and a phase-mask scanning technique: potential and applications," in *Commercial and Biomedical Applications of Ultrafast Lasers VII*, SPIE, Mar. 2007, pp. 157–164. doi: 10.1117/12.711993.
[312] C. W. Smelser, D. Grobnic, and S. J. Mihailov, "Generation of pure two-beam interference grating structures in an optical fiber with a femtosecond infrared source and a phase mask," *Opt. Lett., OL*, vol. 29, no. 15, pp. 1730–1732, Aug. 2004, doi: 10.1364/OL.29.001730.
[313] C. W. Smelser *et al.*, "Multiple-beam interference patterns in optical fiber generated with ultrafast pulses and a phase mask," *Opt. Lett., OL*, vol. 29, no. 13, pp. 1458–1460, Jul. 2004, doi: 10.1364/OL.29.001458.
[314] S. Mihailov, D. Grobnic, C. Smelser, P. Lu, R. Walker, and H. Ding, "Bragg grating inscription in various optical fibers with femtosecond infrared lasers and a phase mask," *Optical Materials Express*, vol. 1, Aug. 2011, doi: 10.1364/OME.1.000754.
[315] J. Thomas *et al.*, "Inscription of fiber Bragg gratings with femtosecond pulses using a phase mask scanning technique," *Appl. Phys. A*, vol. 86, no. 2, pp. 153–157, Feb. 2007, doi: 10.1007/s00339-006-3754-2.
[316] K. Kawamura, M. Hirano, T. Kurobori, D. Takamizu, T. Kamiya, and H. Hosono, "Femtosecond-laser-encoded distributed-feedback color center laser in lithium fluoride single crystals," *Applied Physics Letters*, vol. 84, no. 3, pp. 311–313, Jan. 2004, doi: 10.1063/1.1640784.
[317] C. Grivas and R. W. Eason, "Fabrication of reflective volume gratings in pulsed-laser-deposited Ti:sapphire waveguides with UV femtosecond laser pulses," *Appl. Phys. A*, vol. 93, no. 1, pp. 219–223, Oct. 2008, doi: 10.1007/s00339-008-4673-1.
[318] T. Elsmann *et al.*, "Generation of volume Bragg gratings by 400nm femtosecond laser pulses with Talbot-type interferometer in S-TIH53 glass," *Optik*, vol. 124, no. 20, pp. 4519–4521, Oct. 2013, doi: 10.1016/j.ijleo.2013.03.022.
[319] J. Martin and F. Ouellette, "Novel writing technique of long and highly reflective in-fibre gratings," *Electronics Letters*, vol. 30, no. 10, pp. 811–812, May 1994.
[320] A. Saliminia, J.-P. Bérubé, and R. Vallée, "Refractive index-modified structures in glass written by 266nm fs laser pulses," *Opt. Express*, vol. 20, no. 25, pp. 27410–27419, Dec. 2012, doi: 10.1364/OE.20.027410.
[321] M. V. Shishova, S. Odinokov, A. Zherdev, D. Lushnikov, and V. Markin, "Recording of the multiplexed Bragg diffraction gratings using the phase mask for the near-eye display," in *Holography: Advances and Modern Trends VII*, SPIE, Apr. 2021, p. 1177408. doi: 10.1117/12.2589121.
[322] L. Talbot and M. Bernier, "Femtosecond writing of intra-phase-mask volume Bragg

gratings," *Opt. Lett., OL*, vol. 48, no. 7, pp. 1954–1957, Apr. 2023, doi: 10.1364/OL.483894.
[323] M. P. Siems, D. Richter, T. A. Goebel, R. G. Krämer, and S. Nolte, "Realization of Chirped Volume Bragg Gratings in Fused Silica by Femtosecond Phase Mask Inscription," in *Optica Advanced Photonics Congress 2022 (2022), paper BW5A.5*, Optica Publishing Group, Jul. 2022, p. BW5A.5. doi: 10.1364/BGPPM.2022.BW5A.5.
[324] O. Andrusyak, "Dense spectral beam combining with volume Bragg gratings in photo-thermo-refractive glass," Mar. 2009. Accessed: May 28, 2023. [Online]. Available: https://www.semanticscholar.org/paper/Dense-spectral-beam-combining-with-volume-Bragg-in-Andrusyak/3cd6b04096aedca31c0f390f8b1cc0c9c7f80498
[325] R. Laberdesque *et al.*, "Three-dimensional femtosecond laser inscription of type a-based high-efficiency first-order waveguide Bragg gratings," *Adv. Opt. Technol*, vol. 12, p. 1237679, Jul. 2023, doi: 10.3389/aot.2023.1237679.
[326] T. de Castro *et al.*, "Femtosecond laser micro-patterning of optical properties and functionalities in novel photosensitive silver-containing fluorophosphate glasses," *Journal of Non-Crystalline Solids*, p. 51, Aug. 2019, doi: 10.1016/j.jnoncrysol.2019.04.012.
[327] J. Harb, L. Talbot, Y. Petit, M. Bernier, and L. Canioni, "Demonstration of Type A Volume Bragg Gratings inscribed with a femtosecond Gaussian-Bessel laser beam," *Optics Express*, vol. 31, Apr. 2023, doi: 10.1364/OE.483722.
[328] Bellec, M.; *et al.*, "Beat the diffraction limit in 3D direct laser writing in photosensitive glass," *OPTICS EXPRESS*, vol. 17, p. 10305, 2009.
[329] T. Guérineau *et al.*, "Laser Direct Writing of Silver Clusters-Based Subwavelength Periodic Structures Embedded in Mid-Infrared Gallo-Germanate Glass," *Advanced Photonics Research*, vol. 3, no. 10, p. 2200032, 2022, doi: 10.1002/adpr.202200032.
[330] A. Abou Khalil, W. Gebremichael, Y. Petit, and L. Canioni, "Refractive index change measurement by quantitative microscopy phase imaging for femtosecond laser written structures," *Optics Communications*, vol. 485, p. 126731, Apr. 2021, doi: 10.1016/j.optcom.2020.126731.
[331] C. W. Smelser, S. J. Mihailov, and D. Grobnic, "Characterization of Fourier components in type I infrared ultrafast laser induced fiber Bragg gratings," *Opt. Lett.*, vol. 32, no. 11, pp. 1453–1455, Jun. 2007, doi: 10.1364/OL.32.001453.
[332] B. E. A. Saleh and M. C. Teich, *Fundamentals of photonics*, Third edition. in Wiley series in pure and applied optics. Wiley, 2007.

Title: Femtosecond-laser-written Type-A modifications: Application to X-ray spatially-resolved dosimetry and volume Bragg gratings

Abstract: Direct Laser Writing (DLW) has seen remarkable growth as a research field over the past two decades, based on the process of multiphoton absorption. This technique, known for its reliability and efficiency, enables the formation of permanent and confined modification in glasses, inducing complex three-dimensional (3D) optical structures down to sub-micrometer dimensions. Over the years, researchers have delved deeply into femtosecond direct laser writing across a diverse range of glass material families. In particular, the phosphate glass family presents numerous advantageous characteristics, especially with the addition of photosensitive substances, such as silver. Thus, the femtosecond interaction enables the clustering of silver ions, inducing the creation of fluorescent silver clusters Ag_m^{x+} at the vicinity of the interaction voxel. Based on silver clusters, a distinct type of refractive index modification was demonstrated, labeled as Type-A (with A referring to Argentum). In this project, we take advantage of Type-A modifications to create new types of optical components through their fluorescence and refractive index change properties. The research presented in this manuscript has a dual objective.
On one hand, we investigate the potential of the 3D distributed fluorescent structures created by laser inscription in spatially-distributed X-ray dosimetry. Within this context, a novel technique combining radiophotoluminescence and femtosecond laser irradiation is employed in our glasses. Our study shows that the ensemble of the spectroscopic experiments highlights the resilience of laser-induced silver clusters, these species acting as local probes of the depth-dependent deposited doses. Additionally, in-situ measurements were carried out on waveguides supporting femtosecond-induced silver clusters distribution.
On the other hand, this work reports on the fabrication of periodic optical gratings based on Type-A refractive index change which have been exploited for the realization of transmission Volume Bragg Gratings (VBGs). The Type-A VBGs are presented using several techniques, from multi-layer using standard Gaussian beam geometry to the phase mask approach. Consequently, Type-A VBGs have been successfully realized for the very first time. A noteworthy outcome of this research is the inscription of a single plane grating inscribed with a Gaussian-Bessel femtosecond beam. This approach yielded a remarkable and high diffraction efficiency of 95%. Thus, this work opens the avenue for highly effective femtosecond-written VBGs suitable for industrial applications.

Keywords: Femtosecond laser inscription, silver-containing glasses, silver clusters, Type-A modifications, X-ray irradiation, spatially-resolved dosimetry, volume Bragg gratings.

Titre: Inscription laser femtoseconde des modifications de Type-A: Application à la dosimétrie résolue spatialement des rayons X et aux réseaux de Bragg volumiques.

Résumé: L'inscription laser directe a connu une croissance remarquable en tant que domaine de recherche au cours des deux dernières décennies, basée sur le processus d'absorption multiphoton. Cette technique, connue pour sa fiabilité et son efficacité, permet la formation de modifications permanentes et confinées dans les verres, induisant des structures optiques trois-dimensionnelles (3D) complexes jusqu'à des dimensions sub-micrométriques. Au fil des ans, les chercheurs se sont engagés profondément dans l'inscription laser directe femtoseconde sur une gamme diversifiée de familles de verres. En particulier, la famille des verres de phosphate présente de nombreuses caractéristiques avantageuses, notamment avec l'ajout de substances photosensibles, telles que l'argent. Ainsi, l'interaction femtoseconde permet le regroupement des ions d'argent, induisant la création des agrégats d'argent fluorescents Ag_m^{x+} à proximité du voxel d'interaction. Sur la base de ces agrégats d'argent, un type distinct de modification de l'indice de réfraction a été démontré, désigné sous le nom de Type-A (avec A faisant référence à Argentum). Dans ce projet, nous tirons parti des modifications de Type-A afin de créer de nouveaux types de composants optiques grâce à leurs propriétés de fluorescence et de changement d'indice de réfraction. Le travail rapporté et présenté dans ce manuscrit a un double objectif.
D'une part, nous explorons le potentiel des structures fluorescentes distribuées en 3D créées par inscription laser pour la dosimétrie résolue spatialement des rayons X. Dans ce contexte, une nouvelle technique combinant la radiophotoluminescence et l'irradiation laser femtoseconde est utilisée dans nos verres. Notre étude montre que l'ensemble des expériences spectroscopiques met en évidence la résilience des agrégats d'argent induite par le laser, ces espèces agissant comme des sondes locales des doses déposées dépendant de la profondeur. De plus, des mesures in situ ont été réalisées sur des guides d'ondes supportant la distribution des agrégats d'argent induite par des impulsions femtosecondes.
D'autre part, ce travail rend compte de la fabrication de réseaux optiques périodiques basés sur la modification de l'indice de réfraction de Type-A, qui ont été exploités pour la réalisation de réseaux de Bragg volumique de transmission (VBG). Les VBGs de Type-A sont présentés en utilisant plusieurs techniques, allant de la multicouche à l'utilisation de la géométrie du faisceau gaussien standard à l'approche du masque de phase. Par conséquent, les VBGs de Type-A ont été réalisés avec succès pour la toute première fois. Un résultat notable de cette recherche est l'inscription d'un réseau de plan unique inscrit avec un faisceau femtoseconde Gaussien-Bessel. Cette approche a donné une efficacité de diffraction remarquablement élevée de 95%. Ainsi, ce travail ouvre la voie à des VBGs inscrites en femtoseconde hautement efficaces et adaptées aux applications industrielles.

Mots clés: Inscription laser femtoseconde, verres contenant de l'argent, agrégats d'argent, modifications de Type-A, irradiation aux rayons X, dosimétrie résolue spatialement, réseaux de Bragg volumique.

Unité de recherche : UMR5026 ICMCB, 33608 PESSAC cedex, France.